



Oberaargletscher. Picture: Jürgen Strub

## **The snow and glacier melt components of the streamflow of the River Rhine and its tributaries considering the influence of climate change**

**Final report to the International Commission for the Hydrology of the Rhine basin (CHR)**

**English version, March 2017**

**Kerstin Stahl<sup>1</sup>, Markus Weiler<sup>1</sup>, Daphné Freudiger<sup>1</sup>, Irene Kohn<sup>1</sup>  
Jan Seibert<sup>2</sup>, Marc Vis<sup>2</sup>,  
Kai Gerlinger<sup>3</sup>, Mario Böhm<sup>3</sup>**

<sup>1</sup>University of Freiburg

<sup>2</sup>University of Zurich

<sup>3</sup>HYDRON GmbH Karlsruhe

## Contents

<i>List of abbreviations</i> .....	3
<i>Summary</i> .....	7
<b>1 Background and objectives</b> .....	<b>11</b>
1.1 Streamflow components and climate variability .....	11
1.2 Data, analyses, and models: Outline of the project and the report .....	13
<b>2 Reconstruction of daily climate input grids for the period 1901–1950</b> .....	<b>16</b>
2.1 Objectives .....	16
2.2 Analogue method .....	16
2.3 Results .....	19
2.4 Compilation and validation of climate input datasets 1901–2006 .....	24
2.5 Conclusions for the use as input data for hydrological models .....	25
<b>3 Alpine catchments: statistical data analyses</b> .....	<b>27</b>
3.1 Introduction and objectives .....	27
3.2 Seasonal climate sensitivity of alpine streamflow .....	27
3.3 Streamflow trends .....	33
3.4 Glacier coverage in the headwater catchments of the River Rhine .....	35
3.5 Conclusions for the modelling of the glacierized headwater catchments .....	38
<b>4 Streamflow components: definitions and modelling</b> .....	<b>41</b>
4.1 Background and objectives .....	41
4.2 Methodical approaches for quantifying streamflow components .....	43
4.3 Application and intercomparison .....	45
4.4 Conclusions for the realisation within the project modelling framework .....	51
<b>5 Modelling of the glacierized headwater catchments</b> .....	<b>52</b>
5.1 Objectives .....	52
5.2 Delineation and model setup .....	52
5.3 Specific developments for glacierized headwater catchment models .....	54
5.4 Model application and multi-criteria-calibration .....	58
5.5 Modelled components of streamflow (1901–2006) .....	66
5.6 Modelled streamflow components in selected extreme years .....	70
5.7 Long-term behaviour of modelled streamflow components .....	79
5.8 Conclusions .....	85
<b>6 Modelling of the entire Rhine basin</b> .....	<b>87</b>
6.1 Objectives and description of the LARSIM model .....	87
6.2 Model adaptations and extensions .....	91
6.3 Modelled components of streamflow (1901–2006) .....	100
6.4 Modelled streamflow components in low flow years .....	108
6.5 Temporal changes of streamflow components .....	119
6.6 Conclusions .....	121
<b>7 Model validation and uncertainty analyses</b> .....	<b>123</b>
7.1 Validation of selected modelling results .....	123
7.2 Model parameter uncertainty .....	128
7.3 Conclusions .....	136
<b>8 Conclusions from the project considering climate change</b> .....	<b>137</b>
<i>References</i> .....	139
<i>Acknowledgement</i> .....	145

## List of abbreviations

ASG Rhine	The snow and glacier melt components of the streamflow of the River Rhine and its tributaries considering the influence of climate change (title of the project, in German: “Abflussanteile aus Schnee- und Gletscherschmelze im <b>Rhein</b> und seinen Zuflüssen vor dem Hintergrund des Klimawandels”)
AVLR	“Amt der Vorarlberger Landesregierung”: office of the government of the federal state of Vorarlberg (Austria)
BfG	German Federal Institute of Hydrology (“Bundesanstalt für Gewässerkunde”), see: <a href="http://www.bafg.de">www.bafg.de</a>
BMLFUW	Austrian Federal Ministry of Agriculture, Forestry, Environment and Water Management (“Bundesministerium für Land- und Forstwirtschaft, Umwelt und Wasserwirtschaft”)
BOKU	University of Natural Resources and Life Sciences, Vienna (“Universität für Bodenkultur”)
CH	Switzerland
CH 1903	Swiss coordinate system
CHR/KHR	International Commission for the Hydrology of the Rhine basin, see: <a href="http://www.chr-khr.org">www.chr-khr.org</a>
CRU	University of East Anglia Climate Research Unit, see: <a href="http://www.cru.uea.ac.uk">www.cru.uea.ac.uk</a>
DEM	Digital elevation model
DHM25	Digital elevation model based on the Swiss National Map 1:25000 and available from swisstopo; the report refers to the DHM25 matrix model (25 m resolution) , which has been used for analyses within the project
DWD	“Deutscher Wetterdienst”, Germany’s national meteorological service, see: <a href="http://www.dwd.de">www.dwd.de</a>
ELA	equilibrium-line altitude
ECA&D	European Climate Assessment & Dataset, see: <a href="http://eca.knmi.nl">http://eca.knmi.nl</a>
EZG	catchment from German: “Einzugsgebiet”
FOEN	Swiss Federal Office for the Environment, see: <a href="http://www.bafu.admin.ch">www.bafu.admin.ch</a>
FOWG	Swiss Federal Office of Water and Geology (merged in 2006 with the SAEFL to the present FOEN)
GAP	HBV-light tool for automatic model calibration (genetic algorithm for parameter optimization)
GEWISS	“Gewässerinformationssystem der Schweiz” geodata portal supplying the Swiss government maps about waters in Switzerland (since 2015 integrated in Topic Water)
GMD	Format of the “Gesellschaft für Mathematik und Datenverarbeitung (GMD)” (merged in 2001 with the Fraunhofer Society), one of the usable data formats for LARSIM simulations

HBV	Hydrologiska Byråns Vattenbalansavdelning, conceptual hydrological model, originally by Sten Bergström in the 1970s and since then developed at the Swedish Meteorological and Hydrological Institute (SMHI), see: <a href="http://www.smhi.se/forskning/forskningsomraden/hydrologi/hbv-1.1566">www.smhi.se/forskning/forskningsomraden/hydrologi/hbv-1.1566</a>
HBV-EC	Model version based on HBV, embedded into the modelling environment Green Kenue™ (previously EnSim™), which available from the National Research Council Canada
HBV-light	Model version based on HBV that is currently developed at the University of Zurich, see: <a href="http://www.geo.uzh.ch/de/units/h2k/services/hbv-model">www.geo.uzh.ch/de/units/h2k/services/hbv-model</a>
HVZ	Flood forecasting centre. From German: “Hochwasservorhersagezentrale”
HYRAS	From German: “HYdrologische RASterdaten”: gridded hydrometeorological dataset (daily values 1951–2006, resolution 5 km, partially 1 km) as reference (climatology) dataset for river basins in Central Europe, developed by the DWD within the research programme KLIWAS (“Auswirkungen des Klimawandels auf Wasserstraßen und Schifffahrt – Entwicklung von Anpassungsoptionen”: Impacts of climate change on waterways and navigation – Searching for options of adaptation) of the German Federal Ministry of Transport and Digital Infrastructure, data available from DWD/BfG
HYRAS-REC	Within the ASG Rhine project reconstructed gridded hydrometeorological dataset for the period 1901–1950 based on the HYRAS data and the analogue method and to be used as model input, see Chapter 2.
ICPR	International Commission for the Protection of the Rhine
KALA	From German: “Kartenformat LARSIM”, format of gridded data that was developed by the “LARSIM-developer community” in 2015. This has been the predominantly used format of gridded data in LARSIM simulations since then.
KHR/CHR	International Commission for the Hydrology of the Rhine basin (“Internationale Kommission für die Hydrologie des Rheingebietes”), see: <a href="http://www.chr-khr.org/en">www.chr-khr.org/en</a>
LARSIM	Large Area Runoff Simulation Model, a software for a water balance model initially developed by Bremicker (2000), see: <a href="http://larsim.info">http://larsim.info</a>
LARSIM-Hochrhein	Term used specifically in the ASG Rhine project to refer to four different 1x1km <sup>2</sup> LARSIM-models, which were combined for the modelling of the Rhine basin upstream of Basel: the LARSIM models for the Swiss Rhine basin and the German tributaries to the Hochrhein and Lake Constance (setup adopted from that licenced to the LUBW) and the LARSIM model for the Bregenzerach basin (setup adopted from that of the AVRL)
LARSIM-ME	Model based on LARSIM for Central Europe (ME: “Mitteleuropa”) at a resolution of 5km developed by the BfG (partially using different approaches as the LARSIM-Hochrhein model version)
LARSIM-ME-Rhein	LARSIM-ME model for the Rhine basin
LILA	From German: “Listenformat LARSIM”, data format that was developed by the “LARSIM-Entwicklergemeinschaft” in 2015 and has been the pre-

	dominantly used format for spatially discrete data in LARSIM simulations since then
LOESS	Locally weighted scatterplot smoothing
LUBW	Institute for the Environment, Measurements, and Nature Conservation of the federal state of Baden-Württemberg (“Landesanstalt für Umwelt, Messungen und Naturschutz Baden-Württemberg”), see: <a href="http://www.lubw.baden-wuerttemberg.de">www.lubw.baden-wuerttemberg.de</a>
MAE	Mean absolute error
Max	Maximum
MB	Mixing tank, conceptual container used for the modelling of the different components of streamflow in the ASG Rhine project, see Chapter 4
MB <sub>elem</sub>	MB as attached to each spatial modelling unit (LARSIM-region $\hat{=}$ either 1x1km <sup>2</sup> or 5x5km <sup>2</sup> LARSIM grid cell) for the modelling of the different components of streamflow in the ASG Rhine project
MB <sub>lake</sub>	MB as attached to each lake or reservoir included in LARSIM for the modelling of the different components of streamflow in the ASG Rhine project
ME	Central Europe (from German: “Mitteleuropa”)
MeteoSwiss	Swiss Federal Office of Meteorology and Climatology MeteoSwiss, see: <a href="http://www.meteoswiss.admin.ch">www.meteoswiss.admin.ch</a>
Min	Minimum
MixZone	Newly introduced model parameter in HBV-light used to limit the size of the conceptual MB the modelling of the different components of streamflow in the ASG Rhine project is based on
MRE	Mean relative error
NSE	Nash-Sutcliffe Efficiency
Q <sub>I</sub>	Modelled streamflow component (fraction) resulting from the contribution of ice melt input according to explanations in Section 4.1
Q <sub>R</sub>	Modelled streamflow component (fraction) resulting from the contribution of rain input according to explanations in Section 4.1
Q <sub>S</sub>	Modelled streamflow component (fraction) resulting from the contribution of snowmelt input according to explanations in Section 4.1
RhiresD	Gridded data product from MeteoSwiss: daily precipitation sums for the period 1961–2013 for the spatial domain of Switzerland at a resolution of 1.25°
RMSE	Root mean square error
SCA	Fractional snow covered area
OSHD-SLF	From German: “Operationeller schneehydrologischer Dienst”, operational snow hydrological service at the SLF
SAEFL	Swiss Agency for the Environment, Forests and Landscape (merged in 2006 with sections of the FOWG to the present FOEN)

SLF	WSL Institute for Snow and Avalanche Research (from German : “Schnee- und Lawinenforschung”), see: <a href="http://www.slf.ch">www.slf.ch</a>
SWE	Sow water equivalent
swisstopo	Swiss Federal Office for Topography swisstopo, see: <a href="http://www.swisstopo.admin.ch">www.swisstopo.admin.ch</a>
WGMS	World Glacier Monitoring Service, see: <a href="http://wgms.ch">http://wgms.ch</a>
WHM	Water balance model (from German: “Wasserhaushaltsmodell”)
WSL	Swiss Federal Institute for Forest, Snow and Landscape Research, see: <a href="http://www.wsl.ch">www.wsl.ch</a>

## Summary

In the year 2012, the International Commission for the Hydrology of the Rhine basin (KHR/CHR) initiated the research project “The snow and glacier melt components of the streamflow of the River Rhine and its tributaries considering the influence of climate change” (ASG Rhine). The **objective** of the project was to determine the daily and monthly fractions of rain, snowmelt, and glacier ice melt that comprised the streamflow of the River Rhine during the study period 1901–2006. One particular interest was the analysis of the flow composition during extreme low flow conditions in the mid and lower reaches of the River Rhine based on the modelled daily streamflow components. The long study period may elucidate trends and changes in streamflow as a result of a combined influence of climate change, glacier retreat, and an increase in reservoir storage and regulation during the 20<sup>th</sup> Century. The governing idea for the study was that all analyses and modelling should be based on as observed data as much as possible.

Hence, the study first assembled a long-term **dataset** of water cycle observations and gridded (interpolated) data products for the Rhine basin. Amongst these, the HYRAS data, a gridded dataset of interpolated meteorological variables provided by the German Weather Service (DWD) and the Federal Institute of Hydrology (BfG) provided an important input. However, as HYRAS only covers the period 1951–2006, a first important development in the project was a **climate reconstruction** for the early part of the study period 1901–1950. This HYRAS-REC dataset was obtained by resampling daily grids from HYRAS based on daily weather analogues determined from a selection of available long-term data records in the study area. The combination of HYRAS-REC and HYRAS then provided consistent meteorological input to the project’s hydrological modelling experiments.

Besides the meteorological variables, the project’s dataset of observations also includes long time series of streamflow along the Rhine River and its tributaries. In particular, all available streamflow records from smaller scale glacierized headwater catchments in the Alps were included, even if the measurements only covered a few years within the study period. Further data assembled include snow water equivalent information, glacier length, glacier area, and thickness distributions at various times in the past. While many of these data were made available to the project from other researchers or from the agencies, glacier extents at the start of the study period had to be digitized manually from the Swiss “Siegfried maps”. This additional layer of areal extent of glaciers in the early 1900s then provided the initial conditions for the hydrological modelling over the entire 20<sup>th</sup> Century.

Before the modelling, the project carried out a **statistical analysis of climate sensitivity and trends of streamflow** based on a set of 25 long-term streamflow observations from alpine catchments across Switzerland. Most of the selected catchments are relatively unregulated and partially glacierized, but some were selected to serve as non-glacierized references. The empirical analysis investigated these long-term streamflow records together with long-term climate data observations for different subperiods of the study period. The climate sensitivity, which was defined by the contribution of climate variables to the variability of weekly flows, was calculated by regression models. The resulting coefficients from all 25 records showed clear relations to catchment glacier coverage and mean catchment elevation. Below an elevation of ca. 1000–1500 m a.s.l. flow variability in winter is strongly dominated by precipitation, whereas above 1500–2000 m a.s.l. flow variability in summer is driven by temperature. The sign of the temperature control depends on the presence of a glacier, i.e. a dominance of evapotranspiration processes reduces flow with temperature, while the dominance of ice melt increases flow with temperature.

The empirical analyses showed how important a correct description of runoff generation mechanisms is particularly in mountain headwater catchments. Hence, in the setup of hydrological models for the project particular attention was paid to the determination of climate variable lapse rates as well as to basin glacier coverage and its changes with time. The analysis further showed a negative trend for July

and August in streamflow for the last few decades in several basins with small glacier coverage. These trends suggest that the temporary increase of ice melt that is generally expected in a warming climate may have already passed its peak.

Considering these findings, a **model chain** was developed for the Rhine basin. Glacierized headwater catchments were modelled with the semi-distributed conceptual HBV-light model that allows a coupling of rainfall-runoff hydrology with glacier mass balance and glacier change simulation. The entire Rhine basin was then modelled with different distributed LARSIM water balance models ("LARSIM-Hochrhein" at 1km resolution and "LARSIM-ME-Rhein" at 5km resolution).

All models required substantial **adaptations** to be suitable for the project's challenge of modelling the long time period of over 100 years. A particularly interesting modelling task was the **accounting of the fractions of rain, snowmelt and glacier ice melt** from runoff generation (input) through the conceptualized hydrological modelling system into the modelled output (streamflow). Several options to account for and follow these runoff contributions through the various models' soil and groundwater storages, lakes, and along the river network were developed and tested. Finally, a method with storage-corresponding mixing tanks was employed. In each spatial model element, all input fluxes are perfectly mixed with previously present components in a storage-corresponding mixing tank and then passed on to the next model unit according to the unit's water balance. The method can be implemented separately for each model store (soil, groundwater, lakes) or as one integrative mixing tank per spatial model unit (LARSIM grid box at the respective resolution). The mixing tanks hence serve as a model run parallel to the hydrological model in order to calculate the mixing of the input components with the previously stored mix and release the components accordingly. Subsequent the LARSIM models then separately routes these components along the river network.

As a result of a perfect and complete mixing in the Rhine's rather large lakes and groundwater reservoirs, however, flow components became almost constant year-round. Therefore, the mixing tanks' capacities were limited compared to the hydrological models' maximum storage capacities. This step was necessary for the models to allow the study to answer the question of quantitative effects of changes in the input components, e.g. a reduced snow and ice melt input, on the streamflow response considering runoff generation, runoff concentration and routing in the basin. Sensitivity analyses showed that the limited mixing tank approach can achieve this objective.

Another requirement for the long-term modelling was to correctly simulate the **coupled glacier change and streamflow change**. To avoid any long-term accumulation of snow outside real glacier accumulation areas, a new snow redistribution method was implemented in HBV-light. The glacier area adjustment with the so-called "delta-h-Method" had to be modified to account for glacier growth in the early 20<sup>th</sup> Century besides the commonly modelled retreat of glaciers thereafter. Further model developments include a seasonally varying melt factor and glacier reservoir outflow coefficient.

Finally, HBV-light's multiple criteria model calibration features were extended. The objective function that was specifically designed for the project weighs the differences between modelled and observed snow water equivalent and snow cover area, glacier volume change between available observations, and streamflow dynamics at various temporal scales. For the modelling of ungauged basins, a parameter regionalisation was combined with a recalibration to available snow and glacier observations. The automatic calibration with many parameter sets in HBV-light allowed the determination of the range of parameter uncertainty. In the end, only the results of the 'best' simulation, i.e., the rain, snowmelt, and ice melt component of streamflow were eventually transferred from the modelled headwater basin as lateral input into the LARSIM model grid.

Modifications in the LARSIM models also concerned the snow routine, as well as an additional elevation discretization scheme in the lower resolution LARSIM-ME model, to improve snow modelling and other elevation-dependent processes. The increasing reservoir storage for hydropower generation throughout the 20<sup>th</sup> century was incorporated through the implementation of lumped reservoirs, each

representing a number of smaller reservoirs upstream. Reservoir capacities change throughout the modelling period according to a generalized timeline of historical hydropower development. The regulation of several pre-alpine lakes is also considered in the model.

Modelled streamflow components were then assessed at three different spatial scales: the glacierized headwater catchments of the Rhine basin, modelled by HBV-light, the basin of the Alpine Rhine and High Rhine upstream of the gauging station in Basel (CH), modelled by LARSIM-Hochrhein, and the Rhine basin below Basel (without the delta region) down to the gauging station of Lobith (NL), modelled by LARSIM-ME.

The “**glacierized headwater catchments**” hereby represent a model and project-specific delineation of high-elevation, subbasins with considerable glacier cover at the start of the study period. The total area covered by these headwater basins is only 4152km<sup>2</sup>. However, an analysis at this scale, which corresponds to the hydrological meso-scale, allows a comparison with many other studies at similar scales. In addition, it is the scale where glacier melt water contributions are locally important for hydropower generation.

For the entire period 1900–2006, **modelled ice melt** amounts to a mean fraction of about one tenth of the average annual flow from the aggregated streamflow of all glacierized headwater catchments. In August and September the mean ice melt component is one fifth of the total flow. During warm summers, these fractions have been much higher, for example, in the years of 1921 and 1947 or more recently in 2003. In these years, monthly means of ice melt flow for all the HBV-modelled glacierized headwater catchments together amounted to 160–195 m<sup>3</sup>/s, which corresponded to fractions of up to 50%. When streamflow in such years receded strongly during late summer, the relative contributions of ice melt were higher in September than in August. This result differs from previous studies and can be attributed to the more accurate runoff generation and routing considered in this study.

The separate analysis of the glacierized headwater catchment scale also allowed the spatial mapping of the ice melt contributions within the Rhine basin as well as temporal changes in that contribution. Interestingly, over the long-term period modelled streamflow components indicate little change. The reason glacier retreat is compensated by increased glacier melt. According to the modelled time series, the ice meltwater production at the end of the period requires nearly a doubling of the specific negative glacier mass balance compared to the beginning of the period. It should be noted, however, that the last few years of the modelling period (ca. from 2000 to 2006) showed an increase in the ice melt component of streamflow. Regarding the entire Rhine basin there is no conclusion yet on when the ice melt component of streamflow will finally decline.

The LARSIM models then propagated and modelled the **streamflow components downstream**. The resulting long-term mean of the modelled annual fractions of the ice melt component were estimated at approx. 2% of the streamflow in Basel and approx. 1% of the streamflow in Lobith. These numbers agree well with estimates in previous modelling studies. The mean annual fractions of the snowmelt component are much higher and thus more important. They were estimated at 39% of the streamflow in Basel and at 34% in Lobith. Thanks to the daily resolution of the modelling, for the first time, this study could quantify specifically the ice melt component during extreme low flow years such as 1921, 1947, 2003. These events were characterised by spatially coherent summer heat and drought conditions in western and central Europe affecting the Rhine from the alpine headwaters all the way down to the mouth.

The summer peak of the glacier melt season coincides with or closely follows the overall peak of the annual streamflow regimes upstream of Basel, whereas the downstream reaches of the Rhine have hydrological regimes with late summer to autumn low flows. Hence, in the lower Rhine this coincidence of the peak glacier melt with the time of recession to lower flows results in relatively high fractions of ice melt from August to October. While the long-term mean of the ice melt component in August and September was estimated at 4.5%/6% in Basel and 2.6%/4.2% in Lobith, maximum daily

fractions in the aforementioned record years were much higher. In the hot summer of 2003, for example, the maxima of the ice melt component were a quarter in Basel and still 17% in Lobith.

Hydrological modelling always has **uncertainties** stemming from a number of sources from measurement errors to parameter uncertainties. The project considered in particular model parameter uncertainty but concluded that it did not affect the main conclusions of the study. This can mainly be attributed to the consideration of the observations of glacier changes and the dynamics of snow cover and streamflow, which effectively helped to constrain the models. Therefore, the model chain developed in the project provides a reliable tool to follow the effect of runoff contributions from rain, snowmelt, and ice melt through the basin and to determine the consequent changes in the respective streamflow components. This tool also provides the potential to test scenarios of future climate change and water use and regulation.

## 1 Background and objectives

### 1.1 Streamflow components and climate variability

In the year 2012, the International Commission for the Hydrology of the Rhine basin (KHR/CHR) initiated the research project “The snow and glacier melt components of streamflow in the River Rhine and its tributaries considering the influence of climate change” (ASG Rhine). Figure 1.1 shows the basin area of the River Rhine, one of the largest rivers in Europe with tremendous significance for navigation and water supply for a variety of water uses (Belz et al., 2007). The hydrological regime of the River Rhine depends on melt water from the Alps and other mountain headwater regions in Central Europe.

As a result of climate warming, particularly since the 1980s (Figure 1.2), snow and glacier ice melt patterns in the Alps have experienced changes. The expectation was therefore that also the composition of the streamflow in the River Rhine, which is comprised of rain, snowmelt and glacier ice melt, will have changed. Several modelling experiments have already predicted a future decline in the glacier ice melt component of streamflow. However, the modelling of the ice melt component in these studies was usually calculated on a monthly or annual basis and the routing of the different contribution sources and their storage within the Rhine basin was strongly simplified. In addition, studies on changes in the glacier contribution to streamflow have so far given little emphasis to the simultaneous changes in the non-glacierized parts of the basin. Considering climate change with its rising temperatures and a potentially increased climate variability, however, requires a combined assessment of changes in all three streamflow components (rain, snowmelt, glacier ice melt). This report describes in detail the work on this challenge that was carried out by a consortium of the Universities of Freiburg and Zürich and the consultant HYDRON GmbH.

The objective of the ASG Rhine research project was to determine the fractions of the three streamflow components of rain, snowmelt and ice melt on a daily basis over the long time period 1901–2006. High-resolution daily modelling and analysis was expected also to elucidate the contributions of these components to extreme events, especially low flows along the River Rhine. The long study period may elucidate trends and changes in streamflow as a result of the combined climatic change, glacier retreat, and the increase in reservoir storage and regulation during the 20<sup>th</sup> century. The governing idea for the study was that all analyses and modelling should be based on as many observed data as possible. Specific aims of the various steps are described in the respective chapters.

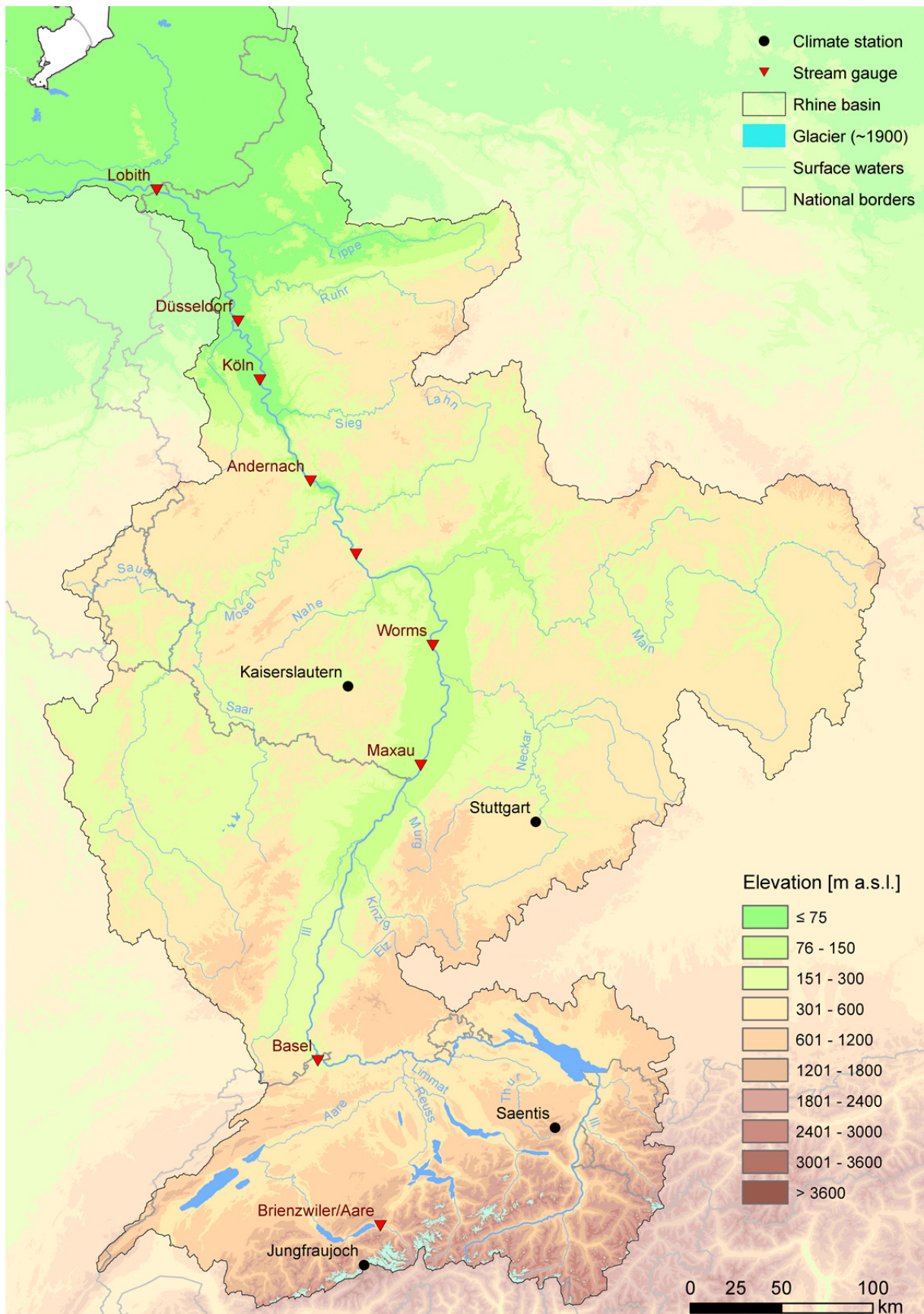


Figure 1.1: Map of the modelling area (Rhine basin of the station at Lobith) with selected gauges and climate stations (see annual mean temperature series of stations in Figure 1.2). Altitude classification based on SRTM 90m Digital Elevation Database v4.1 (Jarvis et al., 2008).

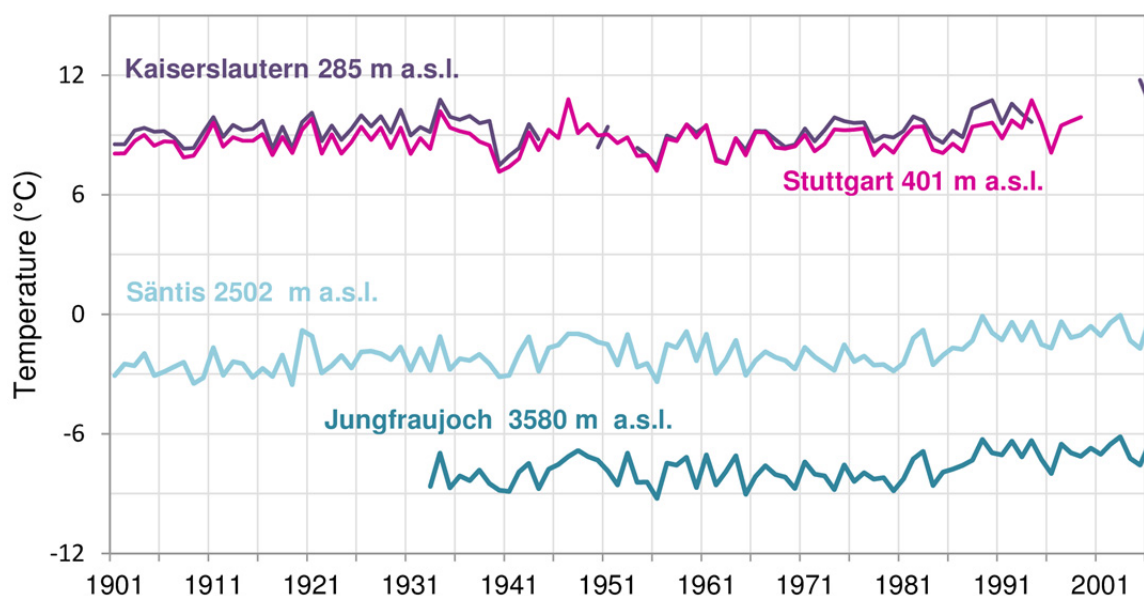


Figure 1.2: Annual mean temperatures in the period 1901–2006 for selected climate stations with long time series within the Rhine basin (for locations see Figure 1.1; data sources: DWD/BfG, MeteoSwiss and European Climate Assessment & Dataset ECA&D).

## 1.2 Data, analyses, and models: Outline of the project and the report

The project consisted of a number of work steps and a complex flow of data and information between them (Figure 1.3). Chapter 2 starts with the description of a key task in the beginning of the project, i.e., the climate model input reconstruction for the early period 1901–1950. The aim was to construct a meteorological input dataset for the project’s hydrological modelling experiments. The input needed to cover the entire study period and be consistent with the German Weather Service’s HYRAS dataset, which only covers the period 1951–2006. Therefore, a new method had to be developed for the resampling of daily grids of meteorological variables for the early period. All daily meteorological data records available in the study area since the beginning of the 20<sup>th</sup> century were used to determine the daily weather analogues this resampling was based on and many were used in the following data analysis of alpine catchments.

Chapter 3 describes a number of different statistical time series analyses of observations of climate variables, streamflow, and glacier change that were carried out prior to the modelling. These analyses were carried out for a set of 25 high-mountain, partially glacierized, catchments with long gauged streamflow records and no reservoir regulation. In addition, different datasets of glacier coverage were assembled and harmonized for the project. These data and analyses provided a framework for necessary model adaptations and developments and any further data needs, such as snow cover information. The results also informed the design of benchmarks for the calibration and validation of hydrological models (Figure 1.3).

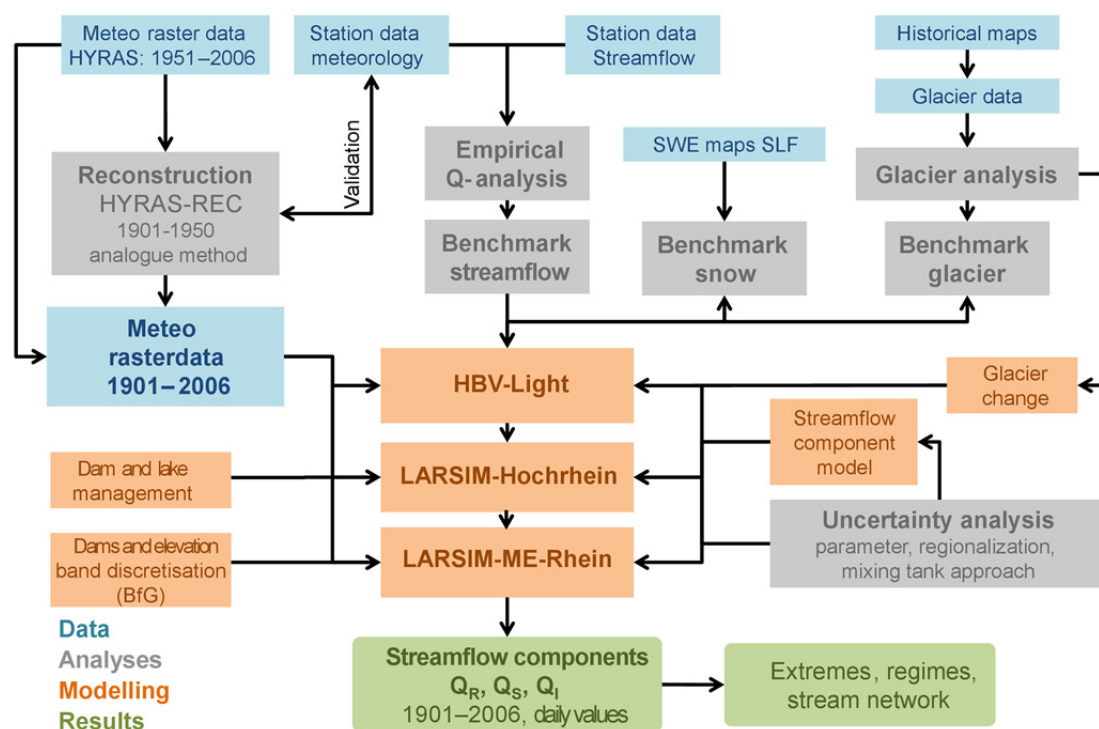


Figure 1.3: Data, analyses and models in the ASG-Rhein-Project. Abbreviations: BfG: Bundesanstalt für Gewässerkunde (Federal Institute of Hydrology); SLF: WSL-Institute for Snow and Avalanche Research, Davos; SWE: snow water equivalent, Q: streamflow;  $Q_R$ : modelled rain component of streamflow;  $Q_S$ : modelled snowmelt component of streamflow;  $Q_I$ : modelled ice melt component of streamflow (details on the definition of streamflow components in Chapter 4).

The hydrological modelling experiments in the project are based on the model chain shown in Figure 1.4. HBV-light was used to model all glacierized headwater catchments at approximately the scale of the most upstream gauging stations. At 39 nodes along the river network, the resulting streamflow components then provided input to the gridded LARSIM Model, which was applied for the remaining Swiss part of the Rhine basin (1x1km). For the basins of the Bregenzerach (Austria) and the German tributaries to the Lake of Constance and the “High Rhine” a similarly high-resolution LARSIM model was used. For the remaining basin area below Basel, the LARSIM-ME model (5x5km) was used. All three models required substantial adaptation and extension.

Chapter 4 explains the method employed to account for and route the runoff contributions from rain, snowmelt, and glacier ice melt through the various model storages to streamflow along the river. Before the decision which to implement into all models a number of different approaches were tested. The following chapters then present in detail the specific model developments and the results of the streamflow component modelling over the period 1901–2006, with Chapter 5 dealing with the HBV-light modelled glacierized headwater catchments and Chapter 6 presenting results for the entire Rhine basin as modelled by LARSIM.

Chapter 7 finally deals with various aspects of model validation and uncertainty analysis. Chapter 8 closes with an assessment of the results regarding climate change.

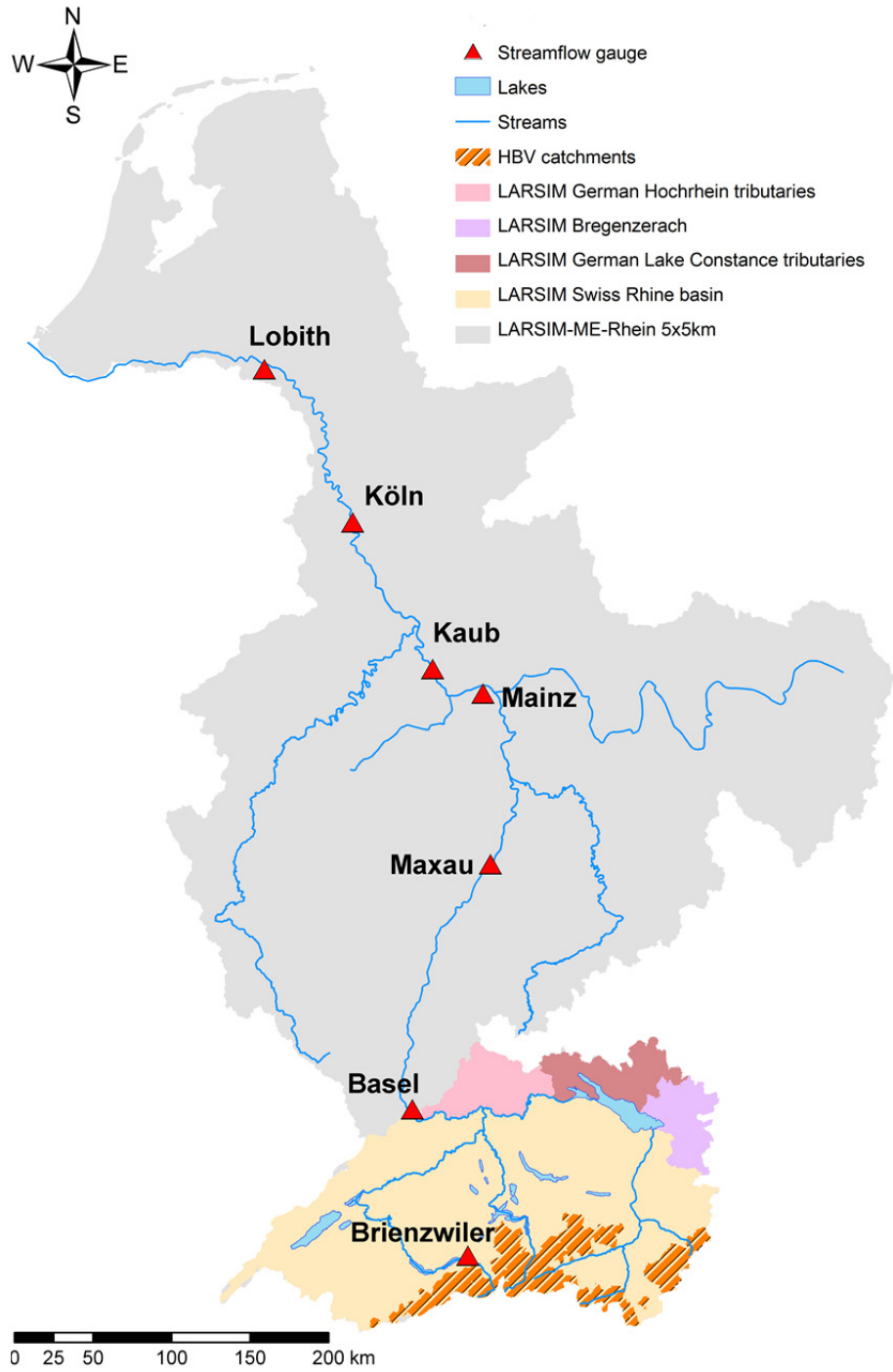


Figure 1.4: Outline map of used model.

## 2 Reconstruction of daily climate input grids for the period 1901–1950

### 2.1 Objectives

A major challenge for the project was the reconstruction of a gridded climate dataset for the period from 1901 to 1950. For this early part of the study period no distributed meteorological data consistent with the later period was available for the entire Rhine basin. All existing climate grid products did not meet the required spatial or temporal resolution for the application of the selected hydrological models. At the same time, in the context of modelling snow and ice melt in particular, it was important that the variables precipitation and temperature were consistent in time and space over the entire period. This requirement refers particularly to the typical variations, sequences and persistence of daily meteorological variables and their spatial gradients, but also to the consistency of the annual averages and sums, and, for example, the exceedance of temperature thresholds such as to distinguish liquid and solid precipitation and to initiate snowmelt.

The hydrological modelling applied in this project was to use the meteorological input of the HYRAS dataset of the DWD (1951–2006; Rauthe et al., 2013; Frick et al., 2014). The HBV models for the glacierized headwater catchments as well as the LARSIM-Hochrhein model (Rhine basin upstream of Basel) are driven at a daily resolution and run at a 1 km spatial resolution, while the LARSIM-ME-Rhein model (Rhine basin below Basel) is modelled at a 5 km spatial resolution. To ensure the spatial and temporal consistency of these highly parameterized models, these same models need to be applied to the entire study period (since 1901). Unfortunately, only a few long time series of observation stations but no appropriate gridded climate data product existed for the early period 1901–1950 for the Rhine basin.

To create a consistent gridded input dataset, a new approach was developed to reconstruct the **HYRAS-REC dataset** (1901–1950) using daily weather analogues resampled from the HYRAS record (1951–2006). Additional variables required to run LARSIM-Hochrhein, such as station observations of humidity, global net radiation, wind speed, and surface pressure, were also reconstructed based on the same daily weather analogues and then interpolated within the LARSIM model.

### 2.2 Analogue method

The reconstruction of the daily climate input grids for the early period 1901–1950 is based on **daily weather analogues** and follows a basic approach developed for synoptic meteorology, that has often been used for the reconstruction of weather conditions in the past (Franke et al., 2011; Zorita & von Storch, 1999). The applied method is based on the assumption that a daily weather analogue exists in the period 1951–2006 for every target day in the period 1901–1950. This daily weather analogue is similar regarding the magnitude and spatial distribution pattern of the meteorological variables. If such a daily weather analogue can be found in the HYRAS record, it can be used to represent the spatial pattern of the different variables on the target day in the HYRAS-REC record (Figure 2.1). The method to determine the daily weather analogue, i.e., to find the most similar day, is based on the maximization of agreement simultaneously for temperature, precipitation, cloud cover, and potential global radiation for all long-term station observations available in and around the Rhine basin.

Several studies have investigated whether the observed trends in temperature and precipitation resulted in changes of the frequency of occurrence of certain weather pattern or in changes of the hydrothermal properties within a specific weather pattern. Fleig et al. (2014) came to the conclusion that the changes in the weather pattern frequencies have a stronger influence in Northwest Europe than in the rest of Europe. In certain seasons and for certain patterns (e.g., dry weather patterns) also hydrothermal changes can be relevant. Particularly in the latter case, the assumption that a daily weather ana-

logue exists may lead to the wrong analogue selection, if the similarity is defined by a relative similarity like a correlation coefficient. Therefore, the method employed here also uses the absolute similarity to define daily weather analogues. However, if certain meteorological conditions of the reconstruction period, like extremely hot, cold, or wet conditions, did not exist in the HYRAS period, the assumption would prevent finding an appropriate analogue. Lacking alternatives, the applied method has to be considered a pragmatic solution to a severe lack of appropriate data in the early period.

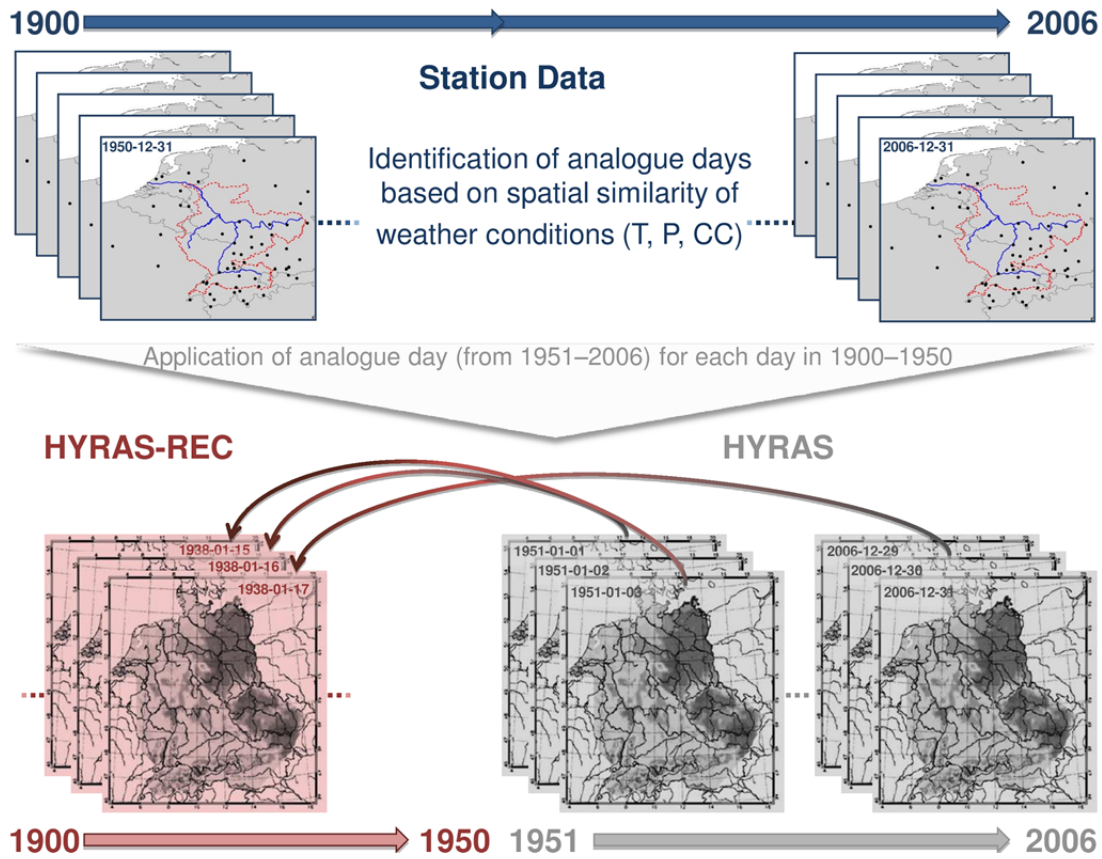


Figure 2.1: Schematic illustration of the method for the reconstruction of climate input grids (HYRAS-REC) for the period 1901–1950 by means of daily weather analogues in HYRAS (bottom) based on long observation time series from climate stations (top).

For the purpose of the determination of daily weather analogues, we defined 14 similarity criteria based on the four available observed variables precipitation, temperature, cloud cover, and potential global radiation. Each similarity criterion was scaled between 0 (no agreement) and 1 (complete agreement) to allow a simple relative comparison (Table 2.1). From all available long-term station observations for the target day and for the potential daily weather analogue, we calculated:

- the rank correlation coefficient after Spearman,  $r$ ,
- the proportion of stations with valid data,  $p_{valid}$
- the proportion of stations whose values are within a predefined deviation (as defined in Table 2.1) between the target and analogue day,  $p_{range}$ ,
- the mean absolute deviation scaled to the maximum deviation for all potential daily weather analogues,  $MAEn$ ,
- and the proportion of stations with matching signs of the temperature (above and below zero),  $p_{sign}$ .

Table 2.1: Criteria to determine the similarity between a target day to potential analogue days.

	Precipitation	Temperature	Cloud Cover	Pot. Radiation
$r$	✓	✓	✓	
$p_{valid}$	✓	✓	✓	
$p_{range}$	[2.5 mm, 2.5 mm]	[-2.5 °C, 2.5 °C]	[-25 %, 25 %]	
$MAEn$	✓	✓	✓	✓
$p_{sign}$		✓		

Initial applications showed a systematic underestimation of precipitation using daily weather analogues due to the generally right-skewed distribution of precipitation values. Therefore, the probability to select a day with less precipitation is higher than that to select a day with the same or more precipitation. Therefore, a correction factor (separately for summer and winter) for each station was defined for determining the daily weather analogues. The correction factor is defined as the ratio of the average observed precipitation to the average precipitation from the determined daily weather analogues without correction. The search for the best daily weather analogues was then repeated with the correction factor. It has to be noted that the factor only modifies the search for the best daily weather analogues but not the precipitation of the target day. The daily weather analogues are then used without a correction factor.

The climate stations used to determine the analogue days were selected to have correspondingly long observation time series in the relevant period (1900–2006) and to spatially cover the Rhine basin without excessive clustering in some regions. Particular focus was on a good representation of the different elevation zones in the alpine region of the Rhine basin. The stations finally used (with slight differences depending on the variable) are shown in Figure 2.2. The average of all 14 similarity criteria defined in Table 2.1 comprises the overall similarity of two days for the study area. Thus, one similarity value was calculated between each target day for the period 1901–1950 and all potential daily weather analogues from the period 1951–2006. Then the most similar day, defined as the day with the highest similarity measure, was selected as the daily weather analogue and the corresponding HYRAS data of this day are used for the target day in HYRAS-REC.

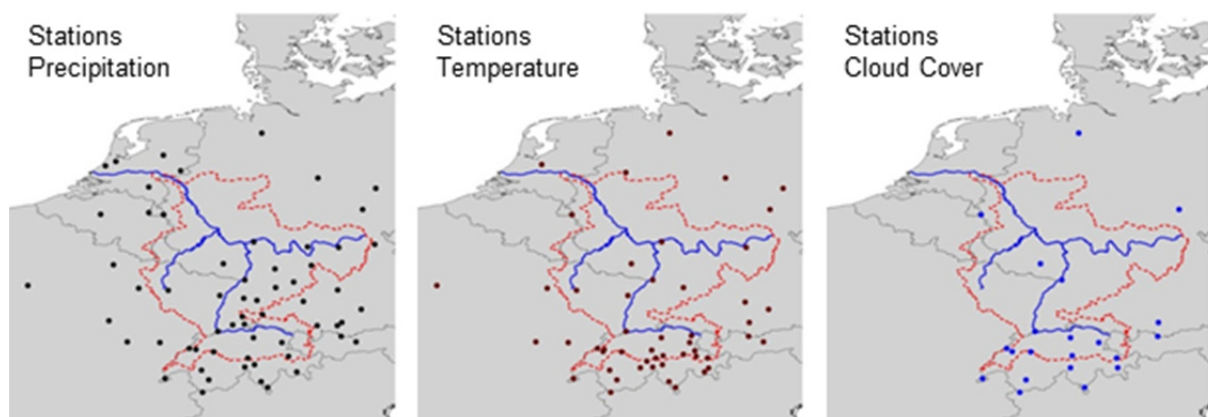


Figure 2.2: Climate stations with long time series that were used for the identification of the daily weather analogues.

To evaluate the quality of the generated reconstructed climate input grids, various statistical measures were calculated comparing the variables of the reconstructed time series at the stations with the real

observed variables for the time period 1901–1950. We selected the following statistical measures: the mean annual absolute and relative error of the daily values, the absolute and relative errors of the mean monthly values, the temporal changes over the reconstruction period, and the values for the 5 and 50 year return period values for one-day and three-day rainfall totals as well as for the distribution of wet and dry spell durations (estimated with the general extreme value distribution). Furthermore, additional precipitation records starting in the 1920s and 1930s that were not used in the analogue search could be used for an independent validation of the precipitation reconstruction.

## 2.3 Results

For six selected stations, which cover a large elevation difference in the Rhine basin (Säntis, Andermatt, Engelberg, Chur, Stuttgart, Kaiserslautern), the various statistical measures illustrate the difference between the observations and the reconstruction in the period 1901–1950. In addition, the most important and hydrologically relevant error statistics are presented as box-whisker plots to show the mean and the variance of the statistical measures of all stations.

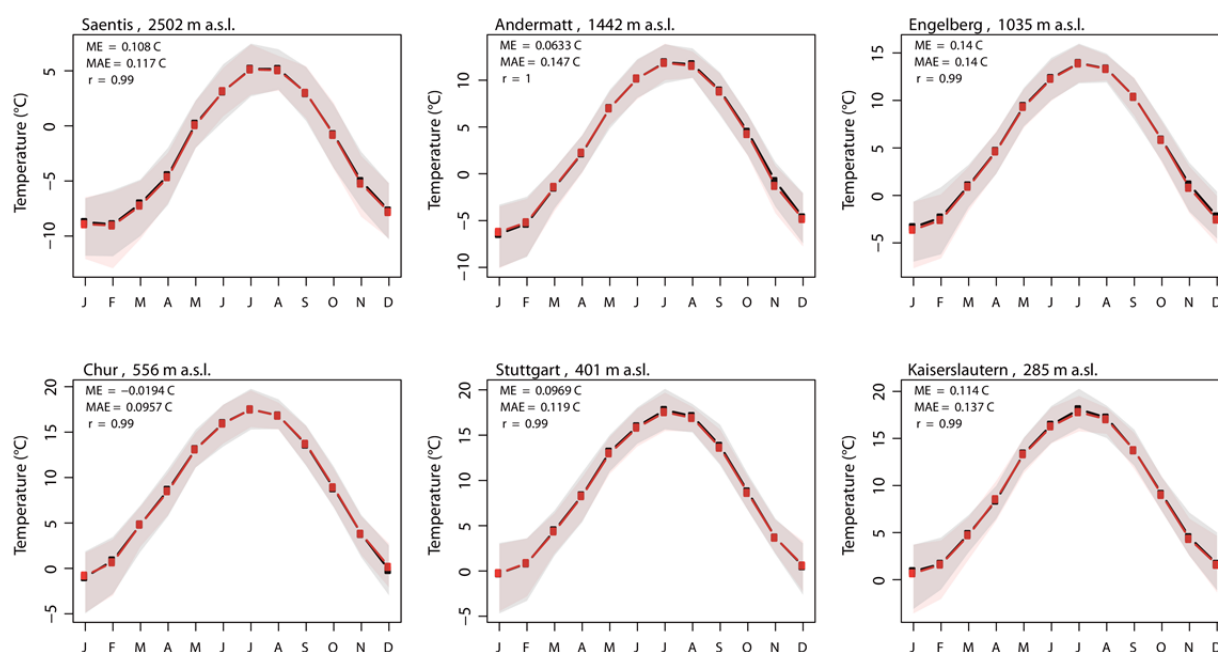


Figure 2.3: Mean monthly temperature regimes of selected stations for observed (black) and reconstructed (red) data from 1901–1950. Shaded areas show the 25–75 percentile ranges. Additionally, summary statistics are given: mean error (ME), mean absolute error (MAE), and correlation coefficient ( $r$ ).

Based on the exemplary results of the six stations the mean monthly air temperature calculated from the reconstructed daily values shows only very small deviations from the observations regardless of the location of the station (Figure 2.3). All stations show a fairly similar picture for the daily mean error on a monthly and annual basis (Figure 2.4). The average error of the daytime temperatures varies depending on the year and station between  $-0.7$  and  $+0.8$  °C, the mean absolute error between  $0.8$  and  $1.9$  °C (Figure 2.4). The reconstructed temperatures generally underestimate the observed values in July, August, and November with the absolute error being lower in summer. The reconstructed winter temperatures overestimate the observed temperatures. One explanation for this effect could be related to climatic warming, as the pool of potential cold daily weather analogues in the winter may be limited

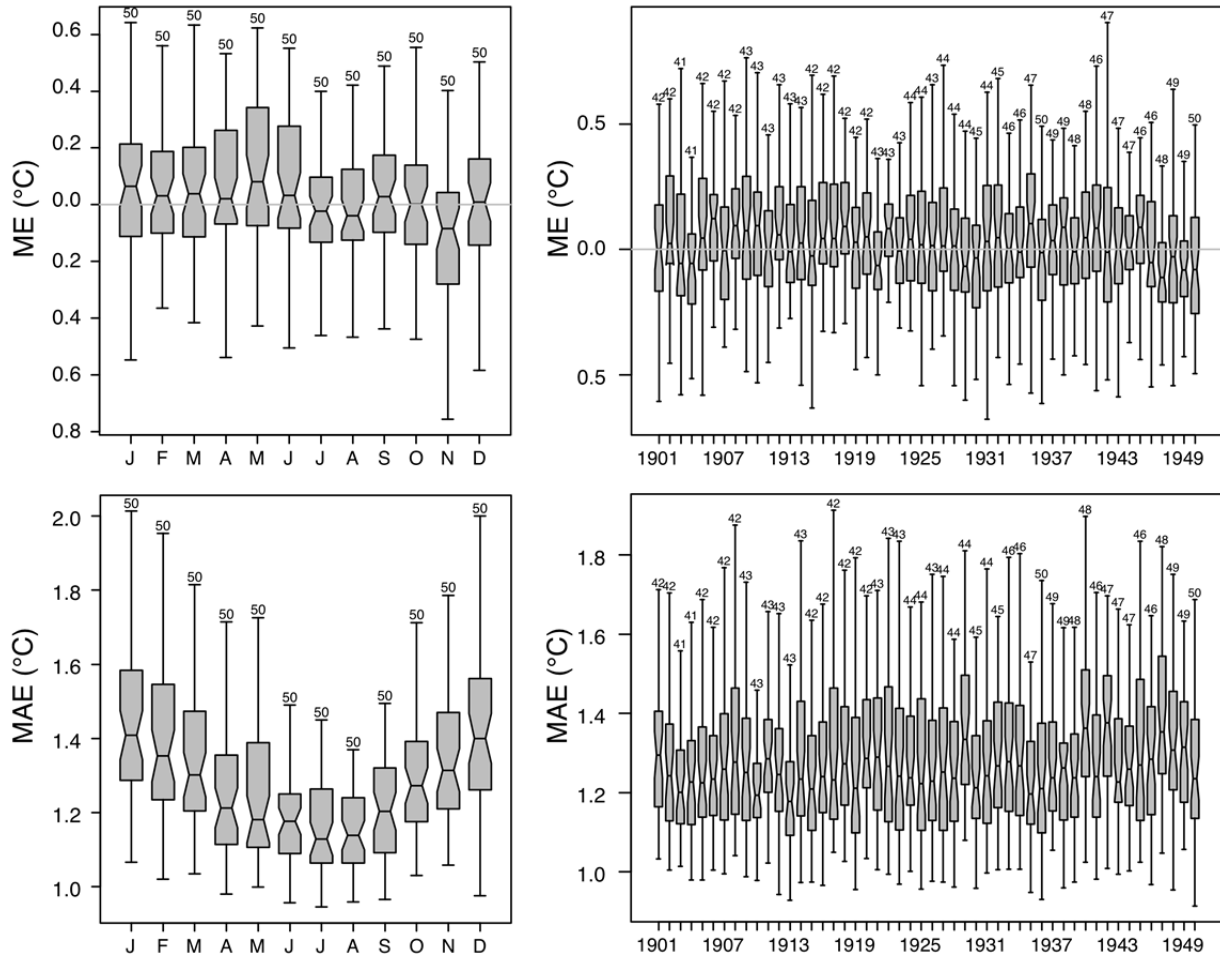


Figure 2.4: Distributions of the mean errors (ME) (reconstructed–observed) (upper panel) and the mean absolute errors (MAE) (lower panel) of the daily temperatures for all stations and all months and all years in 1901–1950; numbers on top of bars denote the number of underlying stations for each year.

in the warmer period 1951–2006 and thus potentially warmer days may have been selected causing the overestimation. The variations from year to year show no noticeable pattern and no long-term trend. Therefore, we conclude that the quality of the reconstruction is similar over the entire period.

The mean relative errors (MRE) of the precipitation reconstruction for all stations and for the validation with independent additional stations are generally smaller than 10% and therefore within the range of the commonly expected measurement uncertainty of precipitation (Figure 2.5 and Figure 2.6). The reconstructed monthly sums of precipitation tend to overestimate the observations in the winter and to underestimate them in the summer. These patterns are similar for the stations used for the determination of the analogues and for the independent validation stations. The reconstruction is better for the alpine area than for the remaining part of the Rhine basin, where the spatial low station density results in lower precipitation during the summer months, probably due to missing convective precipitation events (Figure 2.5). Due to the negative climatic water balance during summer in this region, the effect of potentially underestimating streamflow in the lower part of the Rhine basin due to this bias, however, is assumed to be low.

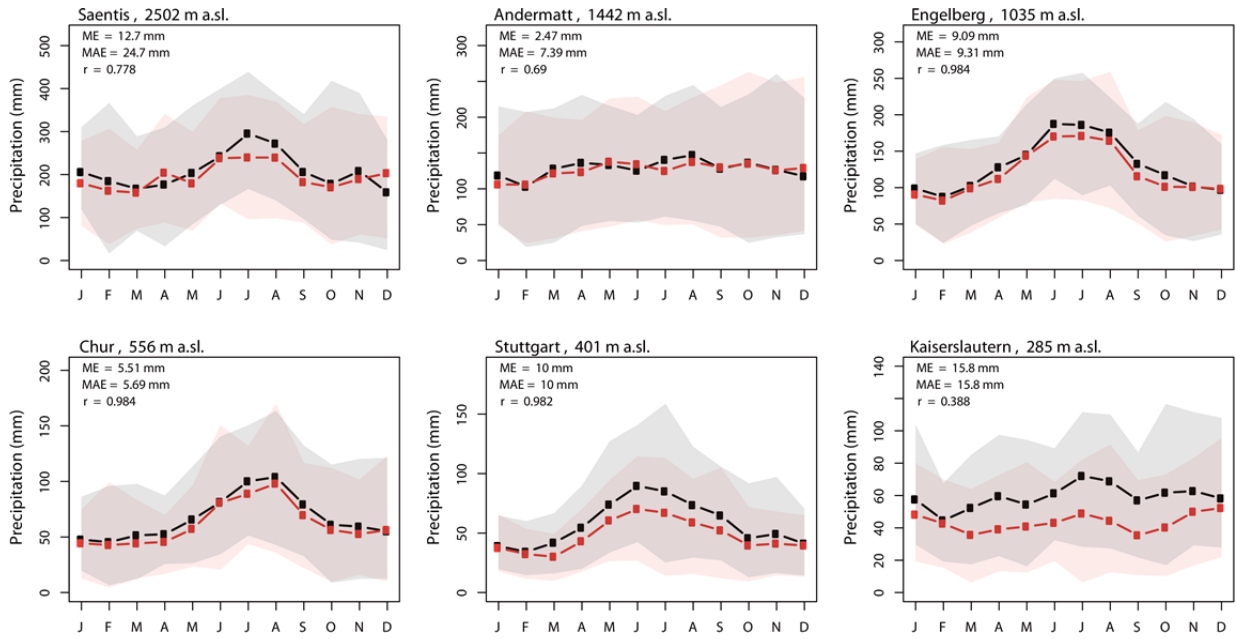


Figure 2.5: Mean monthly precipitation regimes of selected stations based on observed (black) and reconstructed (red) data from 1901–1950. Corresponding transparent areas show the 25–75 percentile ranges. Additionally, summary statistics are given: mean error (ME), mean absolute error (MAE), and correlation coefficient (r).

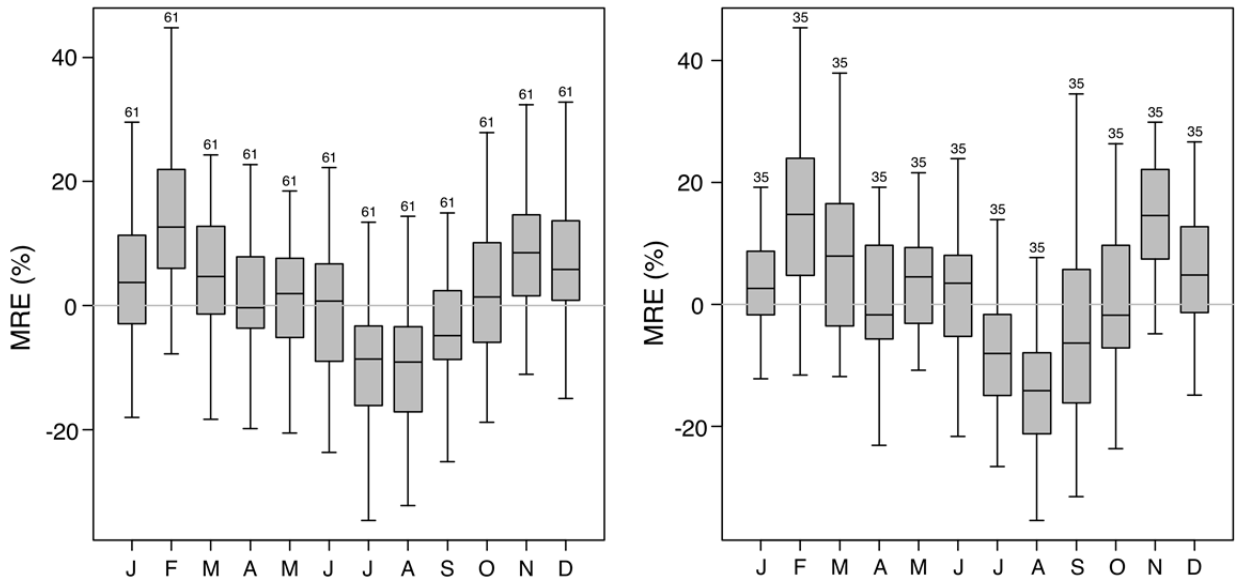


Figure 2.6: Distributions of the mean relative errors (MRE) (reconstructed–observed) of the reconstructed monthly precipitation sums for all 61 stations (left hand) and for 35 stations used for independent validation (right hand).

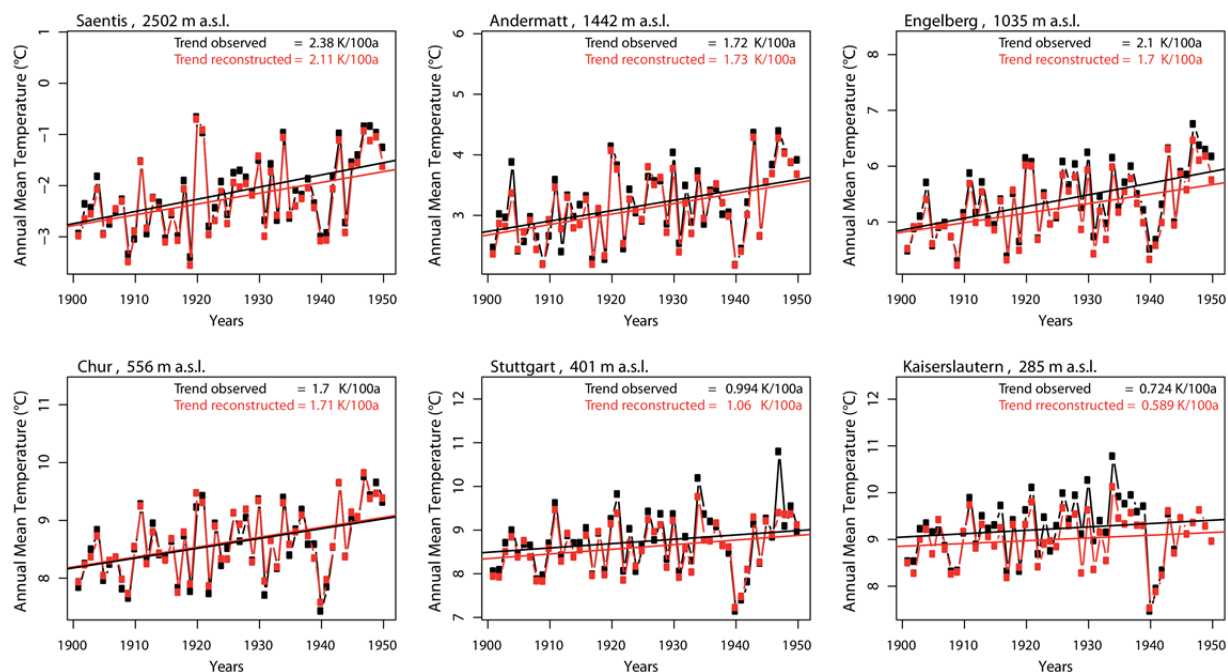


Figure 2.7: Annual mean temperatures of selected stations for the observed (black) and reconstructed (red) data from 1901–1950. Lines show linear regression trends with slopes in Kelvin per 100 years.

The annual variations of precipitation over the 50-year period, similar to the temperatures, show neither a striking pattern nor a temporal change in the reconstruction quality. However, the relative mean error for some specific years and for a few stations is relatively high with over 30% (no figure). Also the long-term temporal pattern is preserved in the reconstruction. To test this, we performed a trend analysis using a linear regression for the observed and the reconstructed annual data series. The slopes of the respective regression lines are addressed as the "trend" in the discussion below. We also distinguish between significant and non-significant trends (significance level  $\alpha = 0.05$ ) trends.

The trends of the observed and reconstructed annual temperatures for the period 1901 to 1950 are positive for all six sample stations and generally decrease from higher stations to lower stations (Figure 2.7). The observed and reconstructed trends are quite similar, often the observed trends are slightly larger. The inter-annual variations of the mean temperatures are usually slightly lower for the reconstructed than for the observed time series, but extremely cold and warm years are well reproduced. The observed and reconstructed trends of the mean annual temperatures are positive for all stations except one. The largest trends of the reconstructed time series are slightly underestimated (Figure 2.8). As already mentioned for the sample stations, the trends in the reconstructed data are often slightly lower, but the statistical significance of reconstructed and observed trends generally agree. The observed and reconstructed trends for the summer season are almost all significantly positive and agree well, but also with slightly lower trends in the reconstructed data. The trends for the winter season are almost all not significant. A closer look at the trend analysis shows that the underestimation of the reconstructed temperature trends is especially strong for urban weather stations. The observed trends of these stations are potentially influenced by the "urban heat island" effect. The generally low station density for the long time series, however, did not allow their removal from the sample.

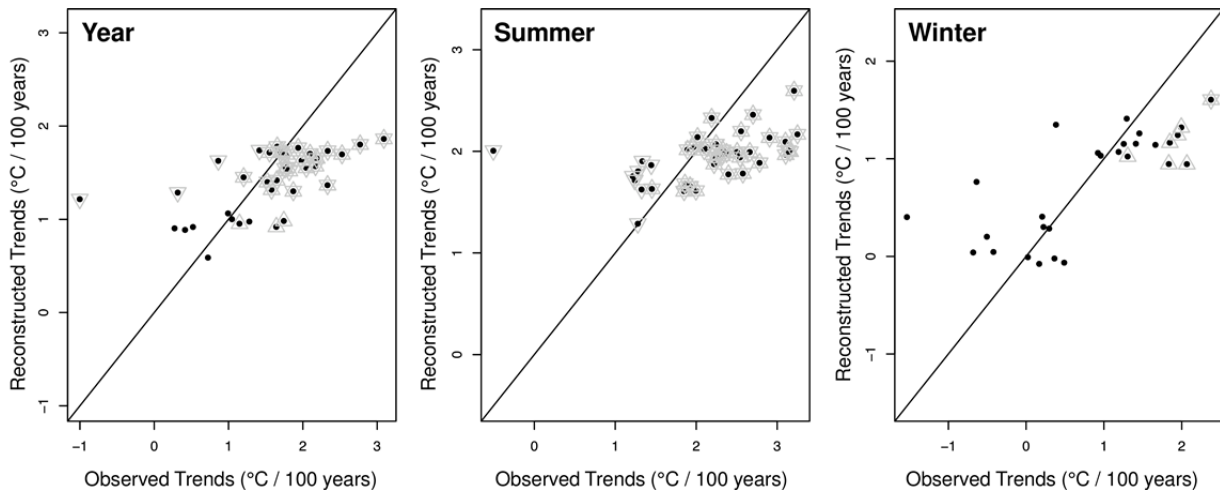


Figure 2.8: Comparison of observed vs. reconstructed trends of the temperatures at the climate stations over the period 1901–1950 for the entire year (left hand) for the summer season (centre) and for the winter season (right hand). Triangles indicate significant trends in the observation time series; upside down triangles indicate significant trends in the reconstructed time series.

Compared to the trends in temperature, the identified trends in precipitation of the period 1901–1950 are variable with more positive trends, but rarely significant (no figure). The same can be observed for the precipitation trends for summer and winter. Comparing the observed and reconstructed trends, the directions of the trends generally agree, but the size of the trends are often quite different. However, the precipitation trends in the reconstruction period are relatively small and not significant overall.

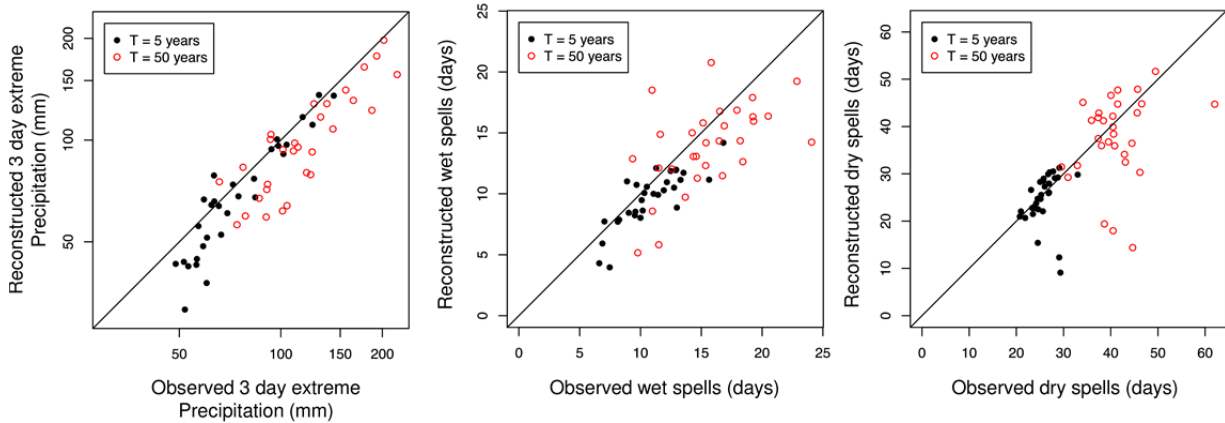


Figure 2.9: Comparison of the extreme values for the 3-day precipitation sums (left hand), wet spells (centre), and dry spells, each with return periods (T) of 5 and 50 years.

Furthermore, extreme rainfall events that can trigger high runoff events as well as the distribution of the durations of wet and dry spells are hydrologically relevant meteorological characteristics. The comparison of the statistical distribution of the multi-day rainfall and the durations of wet and dry spells therefore represents a relevant validation of the analogue method with respect to the persistence of meteorological situations over several days. Figure 2.9 shows that the reconstructed 3-day rainfall totals of the 5-year return period is slightly underestimated in particular for stations with lower absolute values. The same applies to the 50-year return period. The durations of the wet spells spread uniformly around the 1:1 line, with larger differences for the 50-year return period. The reconstructed durations of dry spells slightly overestimate those of the observations. In summary, all reconstructed

extreme meteorological events are well reproduced and therefore the approach is suited to produce long-term climate datasets for hydrological modelling.

## 2.4 Compilation and validation of climate input datasets 1901–2006

Using the derived table of dates of the daily weather analogues from the period 1951–2006, we could generate the HYRAS-REC climate input grids for the period 1901–1950. The relational data base linking the daily weather analogues of the two periods were used to generate the following datasets:

### *HYRAS dataset*

- Precipitation → HYRAS 2.0, 1x1km-grid for the entire Rhine basin
- Temperature → HYRAS 1.01, 1x1km-grid for the entire Rhine basin
- Relative humidity → HYRAS 1.01, 1x1km-grid for the Rhine basin upstream of Basel
- Global radiation → HYRAS 0.21, 5x5km-grid (derived only for LARSIM-ME)

**Station datasets** were derived for the following three variables and were used for the LARSIM-Hochrhein model upstream of Basel to interpolate the relevant daily fields:

- Wind speed → 206 stations from MeteoSwiss
- Barometric pressure → 162 stations from MeteoSwiss
- Sunshine duration → 108 stations from MeteoSwiss

Thus, consistent climate input grids were generated for the various hydrological models for the continuous period from 1901–2006.

The newly generated HYRAS-REC and the available HYRAS precipitation data ( $P_{\text{HYRAS}}$ ) were also compared with the CRU precipitation ( $P_{\text{CRU}}$ ) product (TS3.23 Precipitation, source: University of East Anglia Climatic Research Unit, Jones & Harris, 2008) for the entire period (1901 to 2006). Since  $P_{\text{CRU}}$  is only available with a spatial resolution of  $0.5^\circ$  and a temporal resolution of one month,  $P_{\text{HYRAS}}$  was aggregated accordingly in time and space. We selected four CRU grid cells as test areas within the

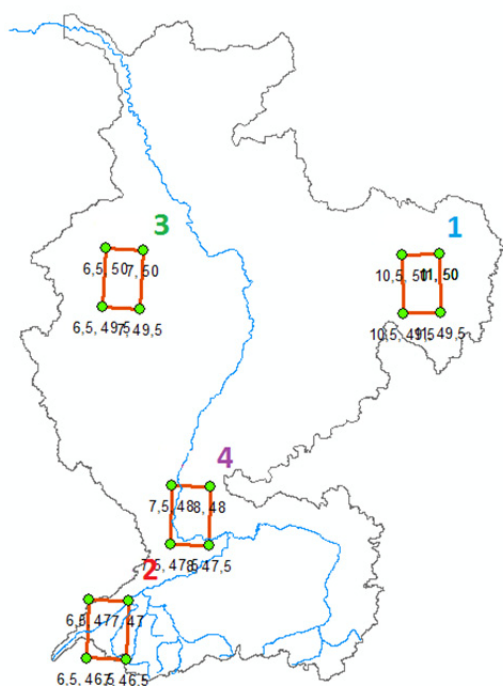


Figure 2.10: Location of selected 4 CRU grid cells in the Rhine basin.

Rhine basin for comparison (Figure 2.10). These test areas were selected to cover different characteristic parts of the Rhine basin, while avoiding areas with high relief, which would be incomparable due to different DEM resolutions and thus elevations. For comparison, all daily  $P_{\text{HYRAS}}$  data within a CRU grid cell were averaged and the absolute deviations ( $P_{\text{CRU}} - P_{\text{HYRAS}}$ ) for annual sums calculated.

Figure 2.11 shows the annual deviations for the four test areas of the two datasets over the whole period. The differences are sometimes quite large. Since none of the products can be assumed to be better, we are particularly interested in whether the deviations were larger for the reconstructed period (1901–1950) than afterwards. In the areas 1, 2, and 3, the deviations in the reconstruction period are even smaller than in the time after 1950, only for area 4 it is larger. This comparison reveals that the deviations changes in some areas in particular starting in the 1960s. However, this change cannot be attributed to the reconstruction of HYRAS-REC, which was applied until 1950, but rather to a change

of the precipitation sums in the HYRAS product in the 1960s. Possible explanations for these changes are real changes in the precipitation climate or a systematic error in the HYRAS product. A systematic error could be generated from changes in station availabilities and densities used to derive the grid product. A possible increase in stations at higher elevation with higher annual precipitation could result in such a change.

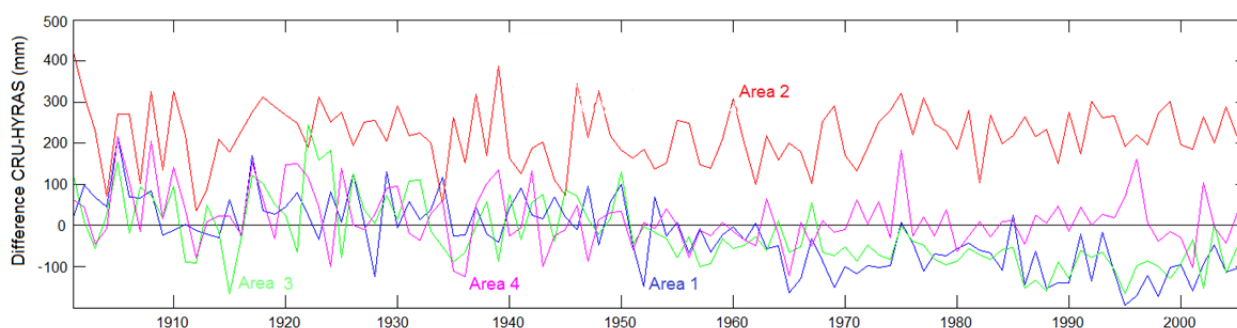


Figure 2.11: Differences between the annual precipitation sums (in mm) of the CRU- and the HYRAS- (HYRAS-REC and HYRAS) datasets for the 4 selected CRU grid cells (Area 1-4) in the Rhine basin (see Figure 2.10).

## 2.5 Conclusions for the use as input data for hydrological models

The aim of reconstructing daily climate input grids for the period 1901–1950 was to obtain consistent input data for the hydrological modelling of the 106 years. For this purpose, the general methodology of a reconstruction via analogues was further developed to the usage of a combined similarity measure based on various climate variables and similarity criteria. Additional tests to use the only existing long-term weather type classification for Central Europe, the circulation patterns by Hess & Brezowsky (Werner & Gerstengarbe, 2010) in combination with the other measures to define daily weather analogues did not improve the results and was hence not included. The selection of daily weather analogues finally used the similarity in precipitation, temperature, cloud cover, and season. Without access to additional suitable data, which do not exist to our best knowledge, an even better selection of daily weather analogues won't be possible. The development of the method and in particular its application to reconstruct all climate records was overall rather complex but it was necessary as no alternative climate grid at a daily resolution and at a high spatial resolution of 1 km exists. The developed method can be seen as a pragmatic solution for this project, but the approach is generally of interest as it can be used for any other data products, or be easily modified for other periods alike.

In most cases the error of the reconstructed time series are in the range of the measurement uncertainty. Generally, they are smaller in the Alps and the central mountain region due to a higher station density with long time series in these areas. At a few stations, especially at the edges or outside of the Rhine basin, where the station density is low, the errors for some climate variables are larger. Precipitation amounts are generally underestimated outside the Alps and especially during summer, although this bias was reduced to some extent by the introduction of a correction factor for the search of analogues. The underestimation may be due to the fact that in summer convective precipitation events occur, which are not captured by the low station density of the long-term observations in this area. Strong temporal trends and wet and dry extremes in the reconstruction period are usually well reproduced.

An independent validation of the long-term precipitation grids over a period of 106 years with the CRU data product shows the general limitation of grid-based data products based on varying numbers

and density of underlying station data available for generating the grid products. In addition, a comparison of climate grids with different spatial and temporal resolution is always problematic. For the purpose of this project, it will be important to assess HYRAS-REC in its role as climate input data for the long-term hydrological modelling, i.e., how well the input data allows to reproduce the observed streamflow records for the two time periods before and after 1950.

## 3 Alpine catchments: statistical data analyses

### 3.1 Introduction and objectives

Previous studies have analysed the sensitivity of runoff generation from snow and glacier melt and the resulting changes of the streamflow mainly based on model experiments. Fewer studies have used empirical analysis of time series observations. Nevertheless, the investigation of time series can help to detect and quantify the signals of climate sensitivity and to attribute the processes causing certain changes. A correct representation of the signals and the cause and effect relations is crucial for the use of hydrological models for the attribution of climate change impacts. Therefore, in a first step the ASG Rhine project statistically analysed relevant time series data.

The aim of this empirical analysis was an improved understanding of the relative influences of precipitation and temperature on the temporal and spatial variability of runoff generation in high-mountain headwater catchments. The study focused particularly on the analysis of the differences of these sensitivities for different elevation ranges and different catchment glacier coverage. Changes in the glacier coverage over the study period were therefore studied and characterized intensively based on a number of observation datasets for different time periods. This information was then available to help the explanation of the long-term development of streamflow since the beginning of the 20<sup>th</sup> Century. The findings about sensitivity and temporal changes also served the development of modelling benchmarks, e.g., criteria for calibration or validation of the models used in the project.

### 3.2 Seasonal climate sensitivity of alpine streamflow

#### 3.2.1 Data and methods

A special dataset was assembled, consisting of streamflow records from gauged catchments at the hydrological meso-scale that include a range of elevations and glacier coverages. The criteria for the selection of these study catchments was the availability of long time series of hydrometric data that are relatively unregulated, i.e., in particular free of reservoir storage and substantial water transfers, as well as the availability of catchment characteristics metadata. Each streamflow record was paired with a long-term climate record from the closest available station (see Chapter 2). The resulting set of 25 Swiss test catchments was assembled with the support of the Swiss FOEN. Most of the catchments are partially glacierized (Figure 3.1.), but some were selected to serve as non-glacierized references. This dataset allows an analysis with respect to systematic gradients with catchment elevation and glacier cover.

The statistical analysis of the sensitivity of streamflow variability to climatic influences was then based on this dataset. For each catchment, daily time series of the climate variables, temperature  $T$  (°C), precipitation sums  $P$  (mm/d), and streamflow, which was related to catchment area and expressed as catchment runoff  $q$  (mm/d), were aggregated to averages for each calendar week ( $t$ ). A weekly aggregation integrates typical time scales of snowmelt phases or precipitation events and corresponds to the time scale of runoff concentration in these meso-scale catchments. Previous studies on the analysis of streamflow variability in snow and glacier dominated mountain catchments have found this time scale useful (e.g., Déry et al., 2009).

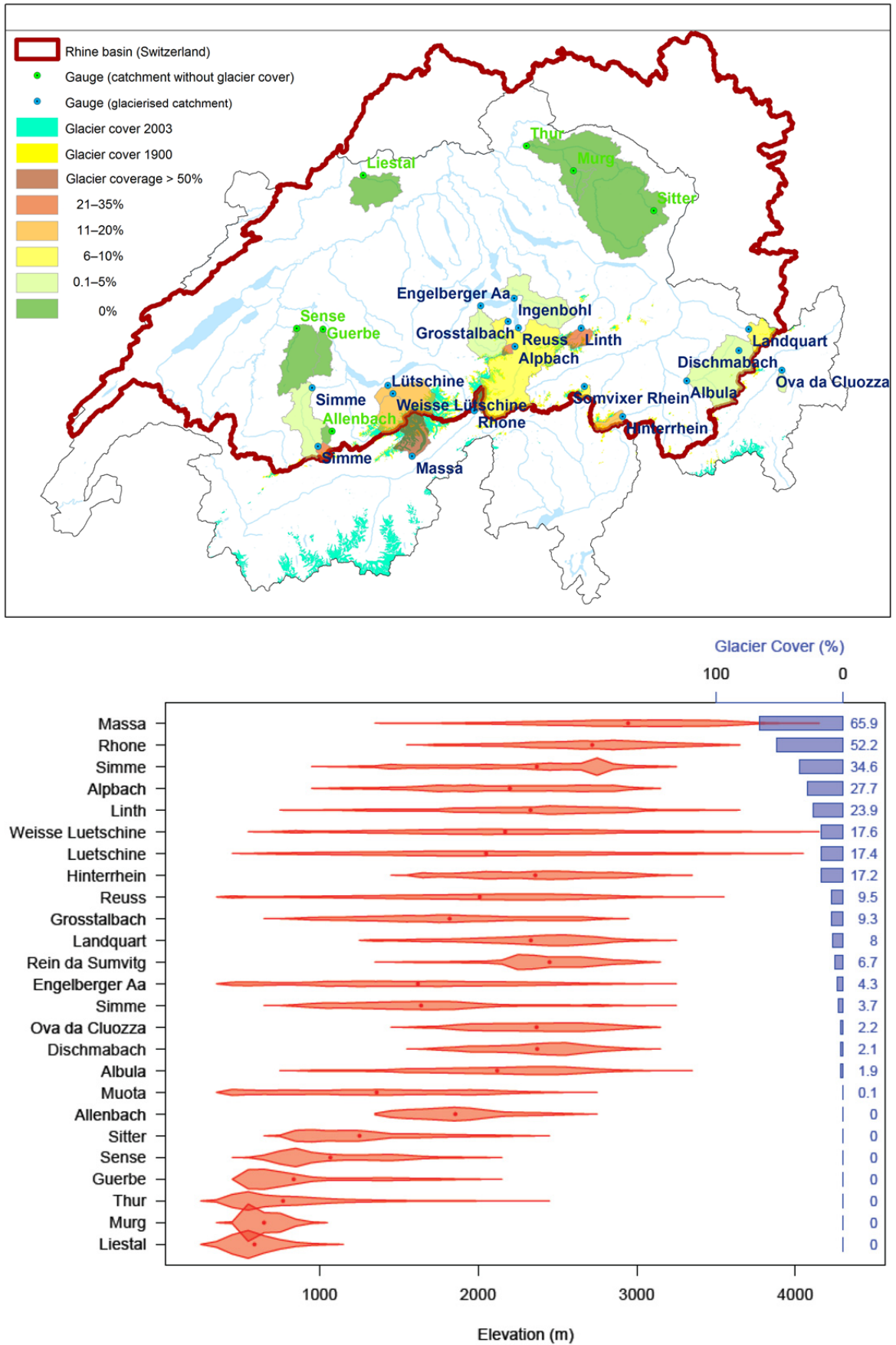


Figure 3.1: Location (top graph), hypsography, and glacier coverage (bottom graph) of the 25 study catchments.

The analysis of the climate sensitivity of the weekly runoff is based on the analysis of the contribution of the climate variables to the runoff variability from year to year. This relation can best be described by the multiple linear regression model in equation 3.1.

$$q(t) = a + b_T T(t) + b_P P(t) + b_q q(t-1) \quad (3.1)$$

where, in addition to precipitation ( $P$ ) and temperature ( $T$ ), runoff ( $q$ ) of the preceding week acts as a third predictor variable. The effect of this predictor in the model is that of a lag-1 autocorrelation, which has previously been used as a proxy for storage level in the catchment system (e.g., Stahl & Moore, 2006). The respective regression coefficients in equation 3.1 are  $b_T$ ,  $b_P$ , and  $b_q$ ;  $a$  is the intercept. The relative contributions of the three predictors to the total variance was calculated based on the approach by Grömping (2007), whereby the partial coefficients of determination sum up to the total variance explained ( $R^2$ ).

Hence, the regression coefficients  $b_T$ ,  $b_P$ , and  $b_q$  indicate direction and magnitude of the influence of the climate variables and the storage over the year. They can be expressed as absolute sensitivities  $b_T$  and  $b_P$  in mm runoff change as a response to a change of temperature in °C and a change of precipitation in mm, respectively. Alternatively, they can be expressed as a relative sensitivity  $S$  by relating the changes to the mean runoff as in equation 3.2.

$$S_P = b_P / \bar{q} \text{ and } S_T = b_T / \bar{q} \quad (3.2)$$

Figure 3.2 shows the partial coefficients of determination and the fitted regression coefficients  $b_T$  and  $b_P$  for two example catchments. The Weisse Lüttschine catchment has a glacier coverage of 17%. Thus, temperature is the variable that dominates the summer streamflow variability as indicated by the positive values of  $b_T$  and high partial  $R^2$  values during the snow and ice melt season. Runoff variability of the lower elevation, non-glacierized Sitter catchment is dominated by direct rainfall-runoff processes as indicated by the generally high  $R^2$  for precipitation and positive values of the sensitivity  $b_P$ . During summer, the Sitter catchment runoff also indicates temperature sensitivity, however, with an opposite sign. Thus, the coefficient indicates a reduction of runoff with increasing temperature as a result of increased evapotranspiration.

The climate sensitivities for all of the 25 catchments can then be used to derive a general regional relation between climate sensitivity and catchment elevation and glacier coverage. This relation was quantified for temperature sensitivity  $S_T$  and precipitation sensitivity  $S_P$  by fitting a linear regression model with the predictors ‘mean catchment elevation’  $H$  (m a.s.l.) and ‘glacier coverage’  $G$  (%) to the data of the sample of 25 catchments:

$$S_T = a + b_H H + b_G G \quad (3.3)$$

$$S_P = a + b_H H + b_G G \quad (3.4)$$

The results can be used to visualize the annual cycle of regional elevation-dependent temperature sensitivity  $S_T(H)$  or precipitation sensitivity  $S_P(H)$ , e.g., without glacier coverage, assuming  $G=0$  in equation 3.3 or 3.4, or with elevation-dependent glacier coverage, assuming an increasing glacier coverage with the mean catchment elevation. Based on the data of the 25 catchments, this increase amounts to  $G = 0.033 \cdot H$  (for mean catchment elevations  $>1660$  m a.s.l.) from a regression with  $R^2 = 0.48$  and  $p = 0.0014$ .

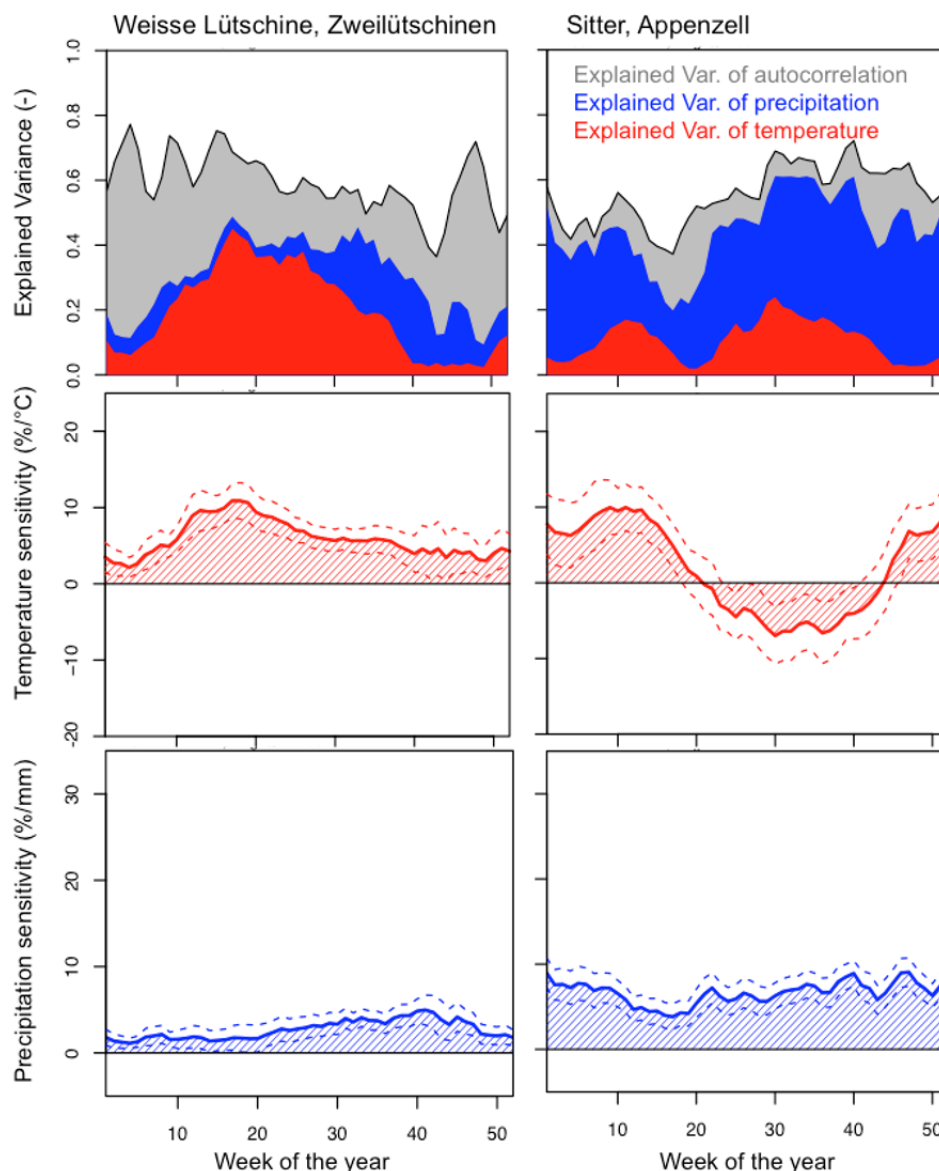


Figure 3.2: Examples of regression analysis results for the runoff from the “Weisse Lütschine” catchment with a glacier coverage of 17% (left hand panel) and the non-glacierized “Sitter” catchment (right hand panel). Seasonal patterns of the explained variance ( $R^2$ ) by the regression models for weekly catchment runoff (black line) and the corresponding coefficients of determination for the predictors  $T$  (red area),  $P$  (blue area), and runoff of the preceding week  $q(t-1)$  (grey area). Seasonal distributions of the resulting  $S_T$  (centre graphs) and  $S_P$  (bottom graphs).

### 3.2.2 Results: regional climate sensitivity of streamflow

The variance of catchment runoff explained by the regression models ranges between 60% and 90% for different calendar weeks and different catchments. Temperature explains between 0% (e.g., in January in strongly glacierized, high-elevation catchments) and 60% (e.g., during the peak ice melt period in glacierized catchments); precipitation also explains between 0% (see temperature) and 60% (e.g. in autumn in high elevation catchments or year round in lower elevation rain-dominated catchments). In high-elevation catchments  $q(t-1)$  can explain up to 80% of the streamflow variability in January and February. Catchments showing high contributions of this predictor, which essentially describes the release from storage below a continuous snow cover, to the variability of winter streamflow include the Hinterrhein and Rhein da Sumvitg (Somvixer Rhein), Landquart, Albula, Dischma,

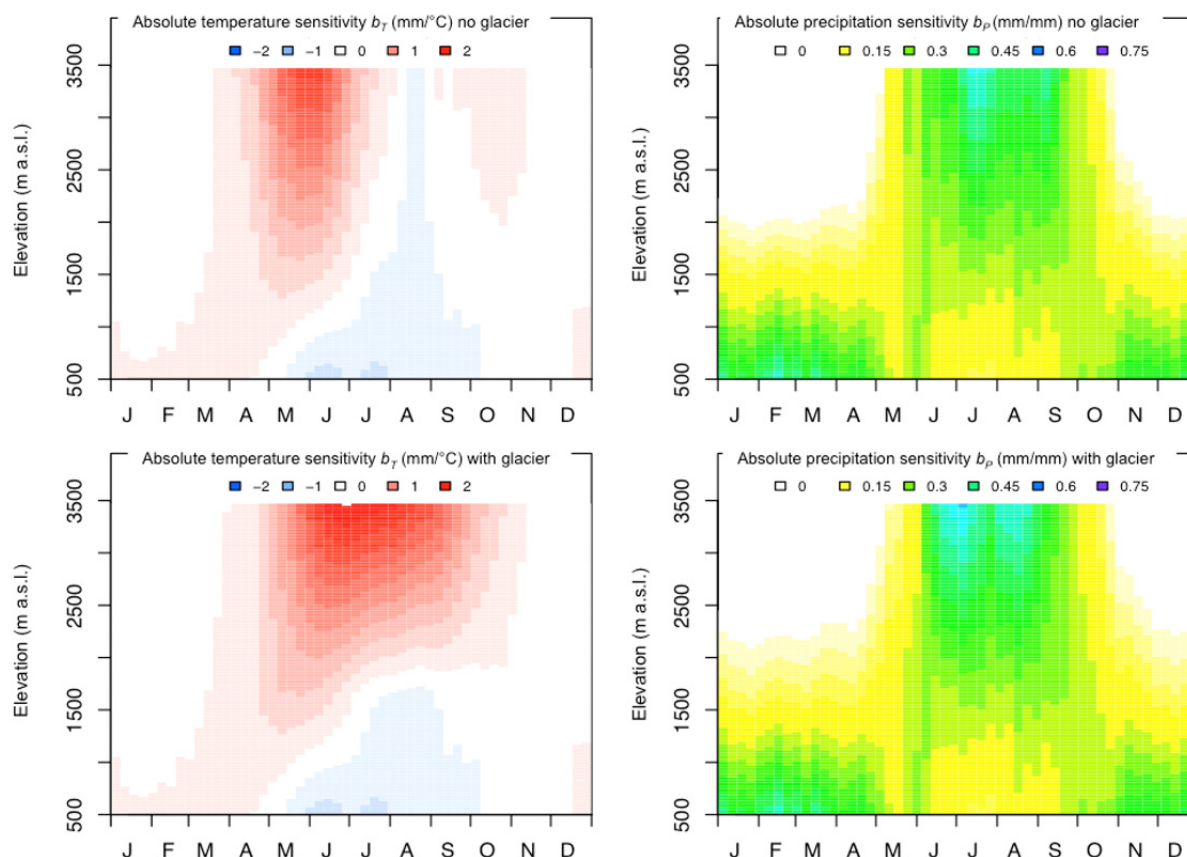


Figure 3.3: Regional climate sensitivity of weekly catchment runoff: temperature sensitivity (left hand) and precipitation sensitivity (right hand) when assuming no glacier coverage  $G=0\%$  (top) and elevation-dependent glacier coverage as derived from the study catchment sample (bottom).

and Ova da Cluoza. The catchments Albula, Dischma, Engelberger Aaa, Simme, and Allenbach have year-round relatively high contributions of this predictor.

The visualisation of the weekly absolute temperature and precipitation sensitivity versus elevation under the assumption of ‘no glacier coverage’ (Figure 3.3 upper) or ‘elevation-dependent glacier coverage’ (Figure 3.3 lower) allows a quantitative interpretation of the drivers of the hydrological regime in these alpine catchments. The calculated temperature sensitivity of runoff is positive from April to July in catchments with mean elevations above 1500 m a.s.l. assuming ‘no glacier coverage’ (Figure 3.3 upper left). These positive temperature sensitivities generally show an increasing influence of snowmelt on catchment runoff with increasing temperature. This relation is often used in hydrological models as degree-day (or temperature index) approach for snowmelt modelling. The 1–2 mm/°C values derived in this sensitivity analysis are lower than the values used in most degree-day models. During the annual snowmelt period the temperature sensitivity shows an increase with elevation and increases seasonally until late May and decreases thereafter. In lower elevation catchments increasing temperature sensitivity can be found even earlier in the year but with lower magnitudes. Below approx. 1000 m a.s.l. the temperature sensitivity becomes negative as early as in the end of May; above 2000 m a.s.l. it is negative only for about 2 weeks in August, indicating only a short period when evapotranspiration directly influences the runoff variability. Under the assumption of elevation-dependent glacier coverage the temperature sensitivity of runoff remains positive throughout the summer. In the catchments with the highest mean elevations above 2500 m a.s.l. weak positive temperature sensitivities of runoff last into early November. Only the lowest elevation catchments in the sample show weak positive temperature sensitivities over the entire winter.

The precipitation sensitivities of runoff over the year indicate the increasing probability of a snow cover with increasing elevation (Figure 3.3 right). A low value of precipitation sensitivity from November to May in catchments with mean elevations above 2000 m a.s.l. suggests that precipitation is stored as snow, i.e., there is no direct response of runoff to precipitation in this period of the year. In lower elevations, where snow cover is rarely persistent over long periods of time, precipitation sensitivity of runoff is much higher during the same season. The pattern abruptly changes in May; over the summer, until about the end of October, precipitation sensitivity of runoff is strongly positive in high-elevation catchments. Low precipitation sensitivities in low elevation catchments may indicate that rain events in summer first replenish storage depleted from climatic water deficits. This effect appears to be less important above 2000 m a.s.l. and, indeed, the derived summer precipitation sensitivity values increase to the highest catchments. In July and August, with the assumption of ‘elevation-dependent glacier coverage’ the precipitation sensitivity in the highest elevation catchments increases further.

Figure 3.4 summarizes the dependence of the climate sensitivities of runoff on catchment elevation and glacier coverage. It shows that elevation positively influences temperature sensitivity of runoff from April to July with highest values in May and June. From mid-July to October, glacier coverage dominates the temperature sensitivity of runoff. From December to February the influence of elevation on temperature sensitivity is small negative but significant, i.e., temperature sensitivity declines with elevation. The same applies to precipitation sensitivity during winter and can be explained by the dominance of storage outflow during the period of snow cover. From mid-May to mid-October there is no significant gradient of the precipitation sensitivity of runoff with either elevation or glacier coverage.

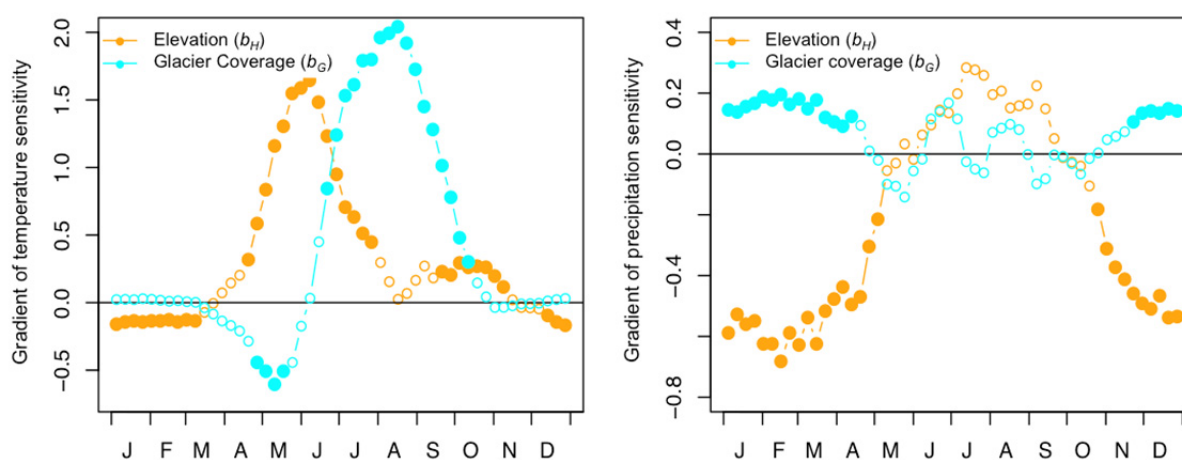


Figure 3.4: Influence of elevation and glacier coverage on the climate sensitivity of (weekly) catchment runoff for temperature sensitivity (left hand) and precipitation sensitivity (right hand). For better comparability, gradients of elevation and glacier coverage were normalised based on the whole range of elevations and glacier coverages given by the sample of study catchments. Hence, the shown gradients are quantified in relative terms with respect to this elevation and glacier coverage range. Filled dot symbols indicate a statistically significant gradient ( $\alpha$  level = 5 %).

Similar approaches have previously been employed to quantify the relative influences of climate on seasonal runoff and to compare the sensitivities across catchments or different time periods to help the attribution of differences and changes in runoff components from glacierized catchments (Collins, 2006; Stahl & Moore, 2006). Information on the temperature sensitivity of summer runoff may provide indications of the peak water changes expected in glacierized catchments affected by climate warming, i.e., whether the ice melt component of catchment runoff is increasing or has already peaked

(Hock, 2005; Moore et al., 2009). This study expanded the method from previous application to the streamflow of specific summer months to the analysis of year-round sensitivities at a weekly resolution. Thus, this data analysis elucidates further drivers of the runoff generation and, e.g., also indicates which catchments show an influence of evapotranspiration on runoff in summer and which have substantial influence of catchment storage on streamflow variability.

The data analysis carried out proves the complexity of the drivers of streamflow composition variability of alpine, and in particular of partially glacierized, catchments. In general, two different main aspects of climate drivers emerged as most relevant. In the studied catchments, precipitation is the dominant driver of runoff in winter in catchments with mean elevations below 1000–1500 m a.s.l., whereas in catchments with mean elevations above 1500–2000 m a.s.l. temperature is the dominant driver of runoff in spring and summer. Transitions were found in between. These results suggest that the modeling and model calibration and validation of the hydrological changes in the Rhine basin should pay particular attention to runoff generation in the headwater catchments between 1000 and 2000 m a.s.l. The analysis also showed considerable differences among the catchments, particularly about the direct influences of climate versus effects of storage. The assumption of ‘no glacier coverage’ gives an impression how the temperature driver of summer runoff may weaken or flip. Hence, a correct description of catchment glacier coverage and climate lapse rates is important for the quantification of runoff composition in high mountain catchments.

### 3.3 Streamflow trends

#### 3.3.1 Data and methods

In the Alps, climate change effects are documented particularly by increasing temperatures and the retreat of glaciers over the past decades. Consequently, the response of streamflow from alpine catchments to these changes is a main question. To elucidate the temporal response, streamflow trends were investigated for four subperiods, 1900–1925, 1925–1954, 1955–1984, and 1985–2012. These subperiods refer to particular phases of glacier change and are described in detail in Section 3.4.1. For the earliest period only few streamflow observation records are available; within the other periods data availability also varied resulting in slight variations of start and end dates for individual records.

Of interest for this study were the potential trends in the runoff generation processes rather than the trends in total streamflow. Therefore, the trends were analysed for the catchment runoff  $q_i$  of each calendar week, i.e., separately for  $i = (1, 52)$ . A further aim was then, to compare the trend in the observations with the trend from the runoff reconstructed by application of the regression models (Equation 3.1) for the same calendar week. This analysis is essentially equivalent to the analysis of trends in the residuals of the regression analyses and described, e.g., by Stahl & Moore (2006). It serves the detection of changes (or alternatively the stability) of the climate sensitivity of runoff in snow and glacier melt dominated regimes and hence the detection of changes to these runoff generation processes.

In order to minimize the influence of outliers the trend over each subperiod was estimated by the „Sen-Slope“ or „Kendall-Theil Robust Line“ (Theil, 1952), i.e., by the median of all possible pairs  $q_i$  and  $year$ . The Mann-Kendall test was applied to test for statistical significance at  $p \leq 0.05$  (Mann, 1945; Kendall, 1975).

#### 3.3.2 Results

The analyses show different seasonal trends for the three subperiods, though data coverage is incomplete for the period 1925–1954. Figure 3.5 shows the trends per week for the same examples as in Figure 3.1, the Weisse Lüttschine (glacierized) and the Sitter (no glacier coverage), and in addition for the Alpbach (glacierized). The figure shows the trend magnitudes obtained, on the one hand, from the

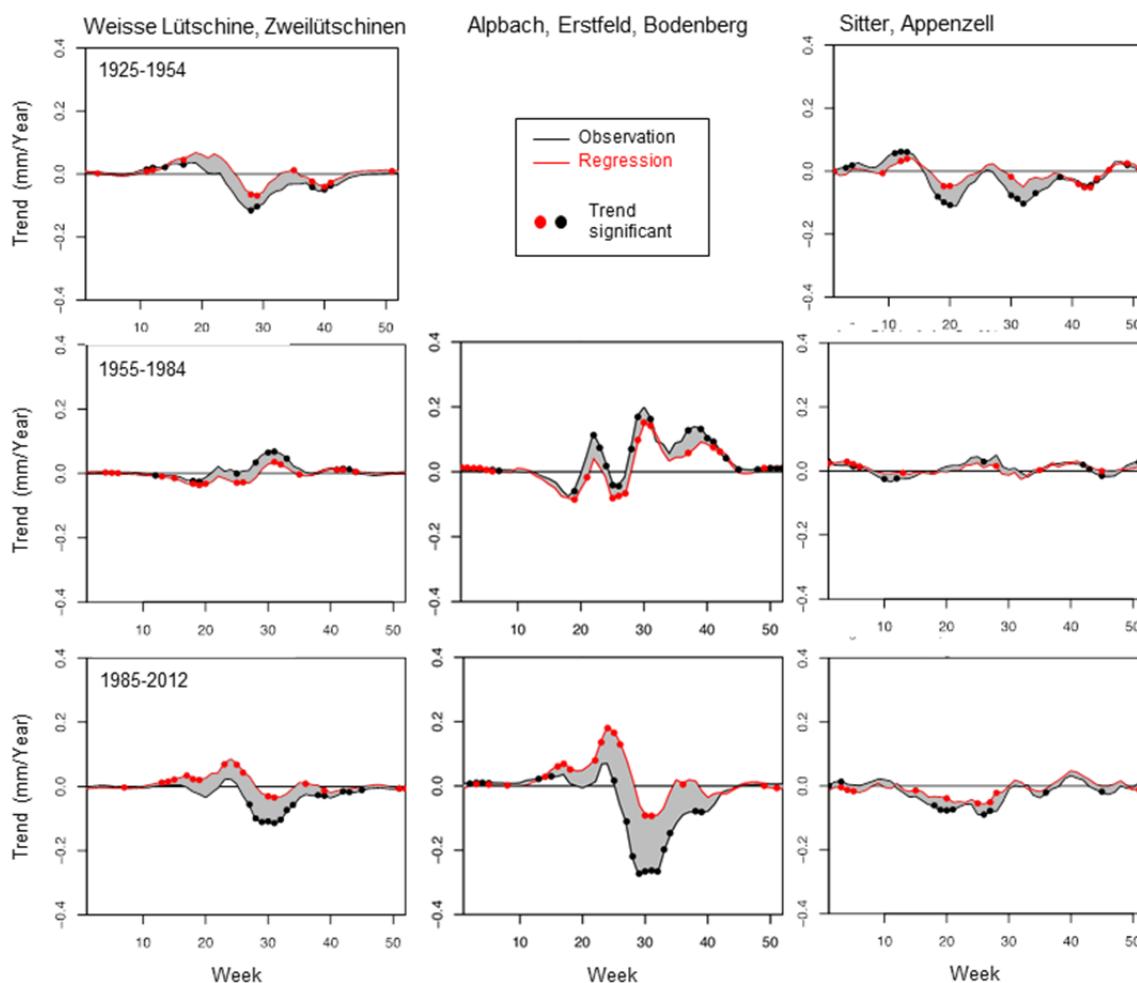


Figure 3.5: Trends of daily means of runoff over the year for the three sub-periods: Weisse Lüttschine (left hand), Albach (centre), and Sitter (right hand). Due to differing data availability the exact start and end dates of the time series may deviate slightly from those of the complete time period.

observed runoff and, on the other, from the runoff estimated from the regression model. Trends are given as the slope in the daily mean runoff for each calendar week. So a trend value of  $0.1 \text{ mm d}^{-1}\text{year}^{-1}$  amounts to an increase of 21 mm of runoff during this calendar week over the 30-year period. A consistent trend of  $0.1 \text{ mm d}^{-1}\text{year}^{-1}$  throughout the year would mean an increase of approx. 1000 mm over the 30-year period.

During the period of negative glacier mass balances from 1925–1954, spring time runoff trends (ca. Week 15–20) are predominantly positive, whereas summer trends are predominantly negative (ca. Week 25–30) in the high-elevation catchments (see, e.g., the Weisse Lüttschine in Figure 3.5). In lower elevation catchments trends are often negative – although small – around Week 20 and Week 30. Trends in the observed data tend to be larger than those in the time series reconstructed by the regression models. During the period of nearly stationary glacier mass balances 1955–1984 trends are generally small and rather similar for the respective observed and reconstructed series. For the following period with predominantly negative glacier mass balances 1985–2012 some positive trends were found again during spring-time. Throughout the summer most catchments with substantial glacier coverage first show negative trends (ca. Week 25–35, i.e., July–August). In mid-August trends change to smaller negative, or even positive, values. The positive trend in spring is overestimated systematically by the regression model-reconstructed runoff trend, whereas the negative summer trend is underestimated by the reconstructed runoff trend. This discrepancy between observed and reconstructed trends points at a change in the temperature and precipitation sensitivity of runoff generation. The

difference in summer trends in particular suggests that the calculated amount of observed summer snow and ice melt runoff generation per temperature increase does not keep pace with the rate derived from the calculated climate sensitivity. Besides the examples of Weisse Lutschine and Alpbach shown in Figure 3.5, this effect (i.e., the underestimation of the negative summer trend) is also detected for the Rhône, the Somvixer Rhein, and the Hinterrhein. The losses of glacier area in these catchments were high in relative terms but did not specifically exceed those of other catchments.

Table 3.1: Trends in summer catchment runoff (approximately Weeks 28–31) for the period 1985–2012 based on observed streamflow time series and the loss in glacier coverage 1973–2003 (based on the glacier inventories). Due to differing data availability the exact start and end dates of the time series may deviate slightly from those of the complete time period.

Stream	Gauge station	Runoff trends in summer		Loss of glacier cover 1973 to 2003	
		Observation	Regression model	%	km <sup>2</sup>
Massa	Blatten bei Naters	unclear/pos. Week 35	unclear/pos.	13.1	17.9
Rhône	Gletsch	neg.	less neg.	15.2	3.1
Simme	Oberried/lenk	slightly pos.	slightly pos.	25.5	3.0
Alpbach	Erstfeld, Bodenberg	neg.	much less neg.	17.8	1.0
Linth	Tierfehd	no data	no data	19.7	3.1
Weisse Lutschine	Zweilutschinen	neg.	less neg.	13.6	4.1
Luetschine	Gsteig	neg.	keiner	16.6	12.1
Hinterrhein	Hinterrhein	neg.	less neg.	50.9	4.9
Reuss	Seedorf	neg.	less neg.	22.3	17.2
Grosstalbach	Isenthal	pos.	less pos.	21.0	0.8
Landquart	Klosters	pos.	less pos.	39.0	3.1
Somvixer Rhein	Somvix, Encardens	neg.	less neg.	46.8	0.6
Engelberger Aa	Buochs, Flugplatz	neg.	no trend	25.5	2.2
Simme	Oberwil	no trend	no trend	26.3	3.1
Dischmabach	Davos	neg.	less neg.	62.5	0.7
Albula	Tiefencastel	hardly	hardly	60.5	3.8
Muota	Ingenbohl	neg.	no trend	72.5	0.2

red: pattern most distinct

In catchments with no glacier coverage trends from observed and regression model-reconstructed runoff are more similar and overall smaller. Rain-dominated catchments with high estimated precipitation sensitivities throughout the year (see Figure 3.2) only show negative runoff trends in the spring-time.

### 3.4 Glacier coverage in the headwater catchments of the River Rhine

#### 3.4.1 Glacier datasets

The project required data about glacier changes during the study period for the interpretation of the observed runoff dynamics and trends as well as for the hydrological modelling of the glacierized headwater catchments. For the modelling it was particularly important to set the initial conditions at the start of the modelling period and to define the status of the glaciers at certain times during and at the end of the modelling period (see Chapter 5). In general, glacier change is documented by mass balance measurements, observations of glacier length changes, and glacier area changes.

As was already noted before the beginning of the project, glaciological and hydrological observation networks are largely decoupled with the exception of some rather small highly glacierized research catchments, such as the Vernagt in Austria or the Gletsch in Switzerland – both not in the Rhine basin. This means that hardly any of the rivers below the few glaciers that have long-term mass balance

measurements have streamflow observations that are long-term and relatively free of regulation. Hence, the database did not allow an empirical analysis on joint observed glaciological and hydrological time series. For the validation of the modelled mass balance by the HBV-light model, however, two long-term observational mass balance records were available (Silvretta and Clariden glaciers) (see Chapter 7).

Another possibility is the use of glacier length change observations, which are much more frequent and available. All available time series in the Rhine basin were obtained from the inventory of the World Glacier Monitoring Service (WGMS) (56 glaciers with different resolution of the data, of which 11 had lengths over 4 km and 24 had lengths from 2–4 km around the year 1900). Figure 3.6 shows that for the study area of the project the retreat of the glaciers began between 1910 and 1920 with a delayed response of the longer (larger) glaciers. Based on these data and the available hydrological data different phases of glacier change were defined for the analysis of subperiods in this study. Other studies have delineated similar phases (cf., e.g., Aellen & Funk, 1999; Zemp et al., 2008; Huss, 2012):

- **Phase 1: 1901–1924** with predominantly stable glaciers or positive mass balances (esp. in the 1910s positive) with exceptions such as the year 1921 in particular,
- **Phase 2: 1925–1954** with an increased frequency of warm and dry years, predominantly negative glacier mass balances and glacier retreat,
- **Phase 3: 1955–1984** with predominantly steady or even positive mass balances and respective stagnation or growth of glaciers
- **Phase 4: the period after 1985:** predominantly negative glacier mass balances and glacier retreat as a consequence of warming temperatures.

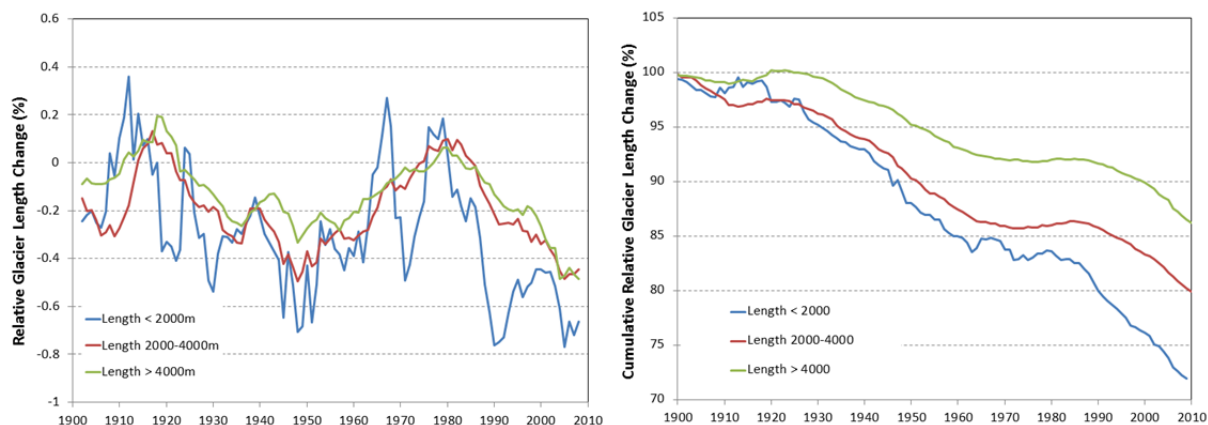


Figure 3.6: Glacier length changes (median) of monitored glaciers in the Rhine basin differentiated into three general length classes. Left hand: relative length change per year (smoothed). Right hand: Cumulative relative length changes from 1900–2010. Data source: WGMS (<http://wgms.ch>), see WGMS (2013).

For the modelling of the individual glacierized headwater catchments of the Rhine basin, however, knowing the exact geographical location and areal extent of the glaciers is crucial. Table 3.2 provides an overview over the assembled spatial-temporal data of glacier evolution in the Rhine basin. It contains data about glacier area for four key points in time: after the little ice age ca. 1850, in the beginning of the 20<sup>th</sup> Century ca. 1900-1940, in 1973, and recently in 2003 and 2010. They stem from different sources and were determined with different methods.

Table 3.2: Compilation of available datasets on glacier cover for different survey dates and from different sources.

Year (ca.)	Method	Source/Reference
1850	Aerial photography (reconstruction from moraine extends)	Maisch et al. (2000)
1900	Digitisation of historical maps (1892-1944)	swisstopo
1940		
1973	Aerial photography from September 1973	Müller et al. (1976); Maisch et al. (2000)
2003	Landsat imageries acquired in Autumn 2003	Paul et al. (2011)
2010	Aerial ortho-imagery acquired between 2008 and 2011	Fischer et al. (2014)

The glacier extents of the years 1850 and 1973 were provided by Max Maisch (University of Zurich) in form of a geo-referenced gridded dataset. Glacier areas of the year 1973 had been derived from aerial photography from September 1973; areas of the year 1850 had been reconstructed from the combined information of the 1973 areas and knowledge about the extent of the glacial moraines. The other datasets were available in form of geo-referenced polygons of the glacier areas. The glacier areas of the year 2003 had also been derived from satellite imageries and were provided by Frank Paul (University of Zurich) to the ASG Rhine project. The glacier extents of 2010 are based on the glacier inventory from Fischer et al. (2014) and were provided by Matthias Huss (University of Fribourg/ETH Zurich). In addition, as a joint effort of the ASG Rhine project and the scholarship funded PhD project by Daphné Freudiger (University of Freiburg), glacier areas of the years 1900 and 1940 were digitized from the so-called “Siegfried maps”. The Siegfried maps were provided by the Federal Office of Topography (Swisstopo) and cover the entire Swiss Alps (including the small glacierized part of the Rhine basin in Italy and Austria). These maps consist of a collection of historical maps from the years 1892–1918 and 1925–1940. For sake of simplicity, the digitized glacier areas were assigned to the years 1900 and 1940 for all analyses within the project. Due to the different data sources and to the different methodologies the glacier areas of the different years were derived with, systematic errors have to be considered in their combined use. Uncertainties will likely be higher for earlier glacier extents.

### 3.4.2 Changes in glacier cover since 1900

For the modeling with the HBV-light model and its coupled glacier routine (see Chapter 5), all headwater catchments with glacier coverage around the year 1900 had to be identified and delineated. This was done based on the new dataset. With the exception of one larger catchment (Albula), all glacierized headwater catchments delineated for use with HBV-light have a catchment area between ca. 20 km<sup>2</sup> and 220 km<sup>2</sup>. The glacierized area of each headwater catchment was calculated on the basis of the available datasets for the years 1900, 1940, 1973, 2003, and 2010. The relative glacier coverage in these catchments around the year 1900 ranges from 2% to 50%.

The glacier retreat in the 49 headwater catchments is represented in Figure 3.7 with catchments ordered by their glacier coverage. Retreat was calculated as the relative difference between the glacierized area of the years 1940, 1973, 2003, and 2010 and the glacierized area of the year 1900. These relative differences in glacier coverage tend to be greater for headwater catchments with a low glacier coverage and smaller for headwater catchments with a high glacier coverage. However, some exceptions can be observed as faster or slower glacier retreat is the result of complex interactions between several different factors. Along with the meteorological conditions, the glacier aspect and the specific topography around the glacier play an important role, with snow redistribution influencing the snow accumulation on and around the glacier and shading influencing the intensity of solar radiation and therefore the melting of snow and ice. On average, the headwater catchments have lost between 40%

and 60% of their glacier areas, some catchments have even lost up to 80–90% of their glacier areas (especially the most eastern headwater catchments, which already had small glacier areas in 1900). Between 1900 and 1940, the glacier area of most catchments retreated only slightly and for few catchments, the glacier area even increased. Until 1973 important glacier retreat took place and most catchments have lost at least 30–50% of their glacier area. This was followed by a smaller decrease of glacierized area between 1973 and 2003. The decrease of the glacier areas between 2003 and 2010 was again notably higher.

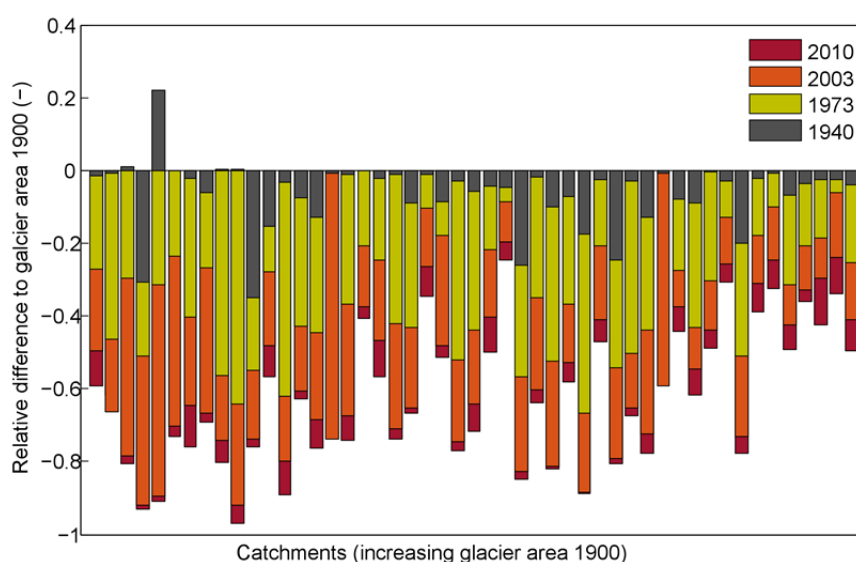


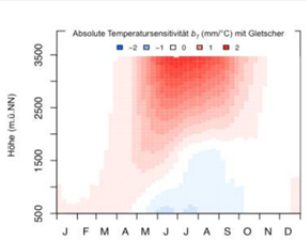
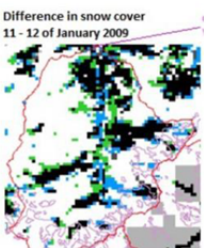
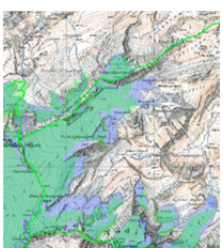
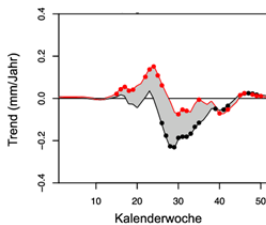
Figure 3.7: Cumulative changes in the glacier areas of the 49 glacierized headwater catchments. Changes for the years with glacier datasets are given relative to the glacier areas in 1900 (see Figure 5.1).

### 3.5 Conclusions for the modelling of the glacierized headwater catchments

The results of the data analyses of the glacier and streamflow series and the derived climate sensitivity of runoff provide important information for the design of benchmarks for the modelling of high mountain catchments in the Alps. Such benchmarks aim to control the correct modelling of runoff generation processes. They can be implemented indirectly through the consideration of model development and adaptation or they can be used directly in a multi-criteria calibration or in the model validation. Table 3.3 provides some schematic examples how the findings were used to develop modelling benchmarks in this study.

The data analysis of the seasonally varying climate sensitivity of runoff suggests that different criteria need to be considered in the modelling of the runoff generation and dynamics. In the catchments with snow and glacier ice melt dominated runoff, the investigated temperature sensitivity, which can also be interpreted as an empirically derived degree-day factor, varies with season, elevation and glacier coverage. Thus, the spatial and temporal discretization of the modelling should consider these differences. Consequently, the extensions to the HBV-light model used in this study, for example, employed a seasonally varying degree-day factor (see Chapter 5). In addition, seasonal differences in sensitivity can be considered by varying the weights in a multi-criteria calibration. Finally, weekly climate sensitivities can be calculated again from the streamflow simulated using HBV and compared to the empirically derived values to validate the internal consistency of processes.

Table 3.3: Derived benchmarks for the modelling of the glacierized headwater catchments (abbreviations: SLF – WSL Institute for Snow and Avalanche Research, SWE – snow water equivalent, SCA – fraction of snow covered area).

Data analysis	Result	Benchmark (examples)
	<p>Climate sensitivity of seasonal runoff (empirically derived regression coefficients; partial variance explained)</p>	<p>Parametrisation: seasonal variation of melt factors            Calibration: seasonal weighting of objective function            Validation: comparison of empirically derived with modelled climate sensitivities</p>
	<p>Climate sensitivity of runoff: variability of runoff generation from snow melt is high and dependent on elevation            SLF snow map data: interpolation of observed snow data and empirical relations</p>	<p>Calibration: fit of modelled to observed SWE and SCA of SLF snow maps</p>
	<p>3 phases of long-term change of glacier area (and estimated glacier volume) influences runoff generation</p>	<p>Parametrisation: initial conditions of glacier coverage around the year 1900            Calibration: comparison of modelled and observed glacier change from 1900 to 1973 and 2003</p>
	<p>Seasonal trends in runoff</p>	<p>Validation: comparison of trend directions and time periods with significant trends in modelled and observed time series</p>

The data analysis of the climate sensitivity showed a particularly high climate sensitivity of the runoff generation from snowmelt. The modelling of the headwater catchments therefore introduced calibration criteria based on snow water equivalent (SWE) and snow covered area (SCA) from daily snow map information (See Chapter 5). The snow map data made available to the project were the ‘SWE map series 1972–2012’ produced by the WSL Institute for Snow and Avalanche Research (SLF). This grid product at 1 km resolution was derived from daily observations of snow depth and their empirical relations to physiographic factors and covers the winters 1971/72 to 2011/12. The dataset and the underlying empirical analyses are described in detail in Jonas et al. (2009), OSHD-SLF (2013), and Jörg-Hess et al. (2014). For the purpose of modelling the glacierized headwater catchments in the project, the information of the data product is considered best for the elevation range 2000–2500 m a.s.l. where most snow observations take place. The sensitivity analysis of runoff suggested that also snow information between 1000 and 2000 m a.s.l. would be important. The project’s decision to use the snow product in the suggested elevation range for model calibration is also based on the results of a side project on the “Analysis of the uncertainty of precipitation in the alpine Rhine basin through compari-

son of the HYRAS and RhiresD (MeteoSwiss) climate data and the SLF SWE maps” (Freudiger et al., 2014).

The data analysis illustrated the strong influence of catchment glacier coverage on the climate sensitivity of runoff dynamics. In addition, differences in the changes of the glaciers in a catchment affect the runoff evolution. Consequently, developments and adaptations made to the HBV model paid particular attention to the elevation-dependent description of the glacierization and its change over time (see Chapter 5). The glacier volume changes derived from the comparison of different data for different times throughout the study period were used in the calibration of the parameters of the mass balance and glacier change routine in the model. Finally, trends derived from the modelled catchment runoff can be compared to those in the observed streamflow.

## 4 Streamflow components: definitions and modelling

### 4.1 Background and objectives

For the quantification by a hydrological model the rain, snowmelt, and ice melt components of streamflow need to be well defined. The challenge related to the definition is that rain, snowmelt, and ice melt, as inputs to the hydrological system, do not immediately contribute to streamflow, but first pass through various hydrological systems (snow cover, glaciers, soil, groundwater, rivers, lakes). In the model, these systems are conceptualized as storages, from which streamflow is finally generated. The question then is, for instance, whether rain that fell on snow ultimately counts towards the rain component or to the snowmelt component of streamflow. In this study we follow the definition that the type of input (rain, snowmelt, ice melt) to the system of model storages counts towards the respective output component of the system, i.e. to streamflow, regardless of the path it takes. One exception is rain that refreezes within the snow cover, which according to the concept of the snow model, is added to the snow cover storage and can then ultimately contribute to the snowmelt component of streamflow or it may be converted to firn and ice in the glacier model and can then contribute to the ice melt component of streamflow.

Most existing hydrological models do not allow to follow the rain, snowmelt, and ice melt input contributions separately through the model at modelling time step and thus also cannot differentiate between their individual resulting components of streamflow output at the temporal resolution of the modelling time step. Instead, what model often allow to distinguish is either the components of streamflow that originate from particular spatial units (for example, water from a spatial model unit “glacier”) or the components of streamflow that are generated from different runoff generation processes represented by storage outflows in the model (for example: direct runoff, interflow, groundwater runoff, glacier runoff). But rainwater falling on a glacier, for instance, is an example of an input contribution that few models would allow tracking from its input to the streamflow output. This runoff contribution should be accounted for as a part of the “rain component of streamflow”, following the aim of the project, and not as “runoff from a glacier”. The same applies to rain-on-snow events or snowmelt percolating through the soil and groundwater storage. The ASG Rhine project thus took care to develop transparent definitions and methods for following the input contributions through the system to the desired output “components of streamflow” within the HBV and LARSIM models used. The terms “components” of rain, snowmelt or ice melt of streamflow and “fractions” of rain, snowmelt or ice melt of streamflow will thereby be used interchangeably.

Glacier contributions to streamflow, defined as consisting either of ice melt or of snowmelt on the glacier or both, have already been investigated in various studies (Huss, 2011; Bookhagen & Burbank, 2010; Weber et al., 2010; Engelhardt et al., 2014). Almost all of these studies quantified the resulting streamflow components at a monthly or annual resolution and often simplified their estimation by directly transferring the rain, snowmelt, and ice melt input contribution into respective streamflow output components. Hence, the streamflow components are equal to the long-term averages of the input contributions. Thereby, the effect of evapotranspiration on the individual contributions is often neglected. This simplification may be a valid assumption for most glacier runoff contributions to streamflow, but it may be quite relevant for runoff contributions from the non-glacierized parts of the catchment. In addition, the model simulation of streamflow components at a higher temporal resolution, e.g. daily, is not possible with this transfer approach. The ASG Rhine project however was specifically interested in the question, which input contribution was directly responsible for a specific streamflow response or initiation of streamflow at the same time scale. As an example, snowmelt floods are generated by runoff from snowmelt, but also by water stored in the catchment, which to-

gether produce the streamflow response. The separation into event water (snowmelt runoff) and pre-event water (water from earlier input contributions released from storage) is not trivial and still a topic of basic research towards a better understanding of flow pathways and water travel times (see also the relevant literature: Pearce et al., 1984; Buttle, 1994).

An appropriate modelling approach for this study therefore needed to correctly simulate the runoff response and to allow tracking the individual input contributions through the model. Tracking runoff contributions through a hydrological system is similar in principle to the simulation of solute concentrations by particle tracking algorithms. Water quality models use this approach to track solutes in a catchment. Hence, the same models could theoretically also be used to track the differently generated water input contributions through the hydrological system by assigning them hypothetical solute concentrations. However, these models simulate the travel time of water particles, which ultimately contribute to streamflow, and these travel times are often very long (several decades) and difficult to parameterize in the model because they are difficult to observe and measure. If the interest of a study is not only the amount of a component but the quantitative composition, i.e. the fraction of each component, also the components' mixture matters. Hence, assumptions of how the different contributions mix in each model storage compartment are also highly relevant. Generally, travel times and mixing assumptions of water in hydrological systems are among the most difficult to determine, even with the help of stable isotopes (e.g., Seibert et al., 2003).

Ultimately, one needs to distinguish between the task of quantifying the actual water particles from the different input sources and the relative fraction each component contributes to the final streamflow output. The former depends on the water travel times and hence the particle velocity, while the latter depends on the response time and the speed of the propagating wave (celerity) through the hydrologic system. In the Rhine, the particle velocity is significantly slower than the celerity as the water passes through large storages such as groundwater aquifers and the large pre-alpine lakes. Due to the resulting long water residence times, the input contributions' particles will reach a certain point along the river (e.g. a gauging station) much more delayed than the streamflow response that was caused by their generation.

For the aim of the ASG Rhine project, however, it is this streamflow response that is of interest. Especially in light of climate change and its influence on the change of the input components, the project is interested in the streamflow amount at a particular location in the stream that is generated with, without or with changing contributions from rain, snowmelt and ice melt. For these reasons, an important part of the ASG Rhine project was to develop a suitable approach to simulate the various input contributions and their respective resulting streamflow components at a high temporal resolution for the HBV-light and LARSIM models. This report will use the symbols  $Q_R$  for the rain component,  $Q_S$  for the snowmelt component and  $Q_I$  for the ice melt component of streamflow.

In the project model chain (Figure 1.4), the glaciers in the glacierized headwater catchments of the Rhine basin are simulated with the model HBV-light. The modelled runoff from the HBV's glacier storage is a combination of rain, snowmelt, and ice melt, with the ice melt component  $Q_I$  being defined as only the bare ice melt (without water from melting snow or firn on the glacier surface). This distinction was made to consider only the effect of the glacier on the streamflow and not the effect of the snow. In future, a glacier may disappear, but there will probably still be snow accumulating on the area of the former glacier, generating runoff from snowmelt to comprise  $Q_S$ . This is an important definition and distinguishes the results of this study from many other studies worldwide, which consider glacier runoff as all streamflow components from a glacierized area thus mixing together runoff from rain, snowmelt and ice melt (e.g., review by La Frenierre & Mark, 2014).

In the HBV-light that was used in the ASG Rhine project for modelling the glacierized headwaters (see Chapter 5), the simulated runoff from the glaciers and thus, the fraction of  $Q_I$ , is added directly to the streamflow at the outlet of the headwater basin. Within the model chain of the project,  $Q_I$  is then passed to the LARSIM model and then further transported in the river and lakes. Thus, for this study the question how to best track and mix the streamflow components mainly concerns the rainfall and snowmelt components  $Q_R$  and  $Q_S$ .

## 4.2 Methodical approaches for quantifying streamflow components

In order to develop an appropriate modelling approach for the outlined research task, the following approaches were developed, tested and evaluated:

- **Separate Effect Modelling:** a separate simulation of each input by the model. To do so, one or two of the three different input contributions (rain, snowmelt and glacier ice melt) are simply “turned off”, i.e. extracted from the input to the system, or respectively re-added in order to determine the resulting change in the output components of streamflow.
- **Integrative Mixing Tank:** the mixing of the input contributions occurs in one integrative conceptual mixing tank for the whole model unit (headwater catchment or LARSIM grid cell) based on the water balance.
- **Multiple Mixing Tanks:** mixing of the input contributions occurs in all conceptual storages of each **HBV model** unit. These model runs set the benchmark for the other, simplified, approaches.

As a variant to the two mixing tank approaches, the calculation of the streamflow components can also be made using a “Limited Mixing Tank”, i.e. an integrative mixing tank or multiple mixing tanks that are assigned a maximum capacity for the mixing.

### **Separate effect modelling**

The project steering group had suggested to apply and test this simple methodology whereby existing models are used but run separately with and without the rain or snowmelt input to determine the individual streamflow components by the difference between these two runs. The project team implemented the suggestion and tested it with the HBV-light model. The results are illustrated by successively removing each input contribution running a previously calibrated model in an alpine catchment. This removal was also performed in different orders.

### **Integrative mixing tank**

Input from rain and snowmelt initially generates a streamflow response in each model unit that depends on the various runoff generation processes in the soil and groundwater. In accordance with the project objectives the tracking approach for modelling the streamflow components can be simplified by assuming that the input components will completely mix in an integrative mixing tank that represents all the various conceptual storages of the model unit from which the outflow forms the streamflow. The streamflow response will then be altered further as it is routed along the river network and through lakes and reservoirs, where it mixes with the components already present there. Figure 4.1 shows this modelling approach schematically with the integrative mixing tank (right) at its interaction with the associated hydrological modelling unit’s system (left).

In this approach, the storage or storage change per time step is described by the water balance equation for each spatial model unit, i.e. each subbasin (HBV) or each grid cell (LARSIM), depending on the spatial discretization of the model: here the simulated time series of inputs from rain ( $I_R$ ) and snowmelt ( $I_S$ ) and the outputs of actual evapotranspiration (aET) and discharge ( $Q$ ) from the simulations of the original and unaltered hydrological model (see Figure 4.1). These time series allow the calculation of the storage change and, hence, the total storage of the mixing tank ( $S_{MB}$ ) for each time

step t. Tracking the input contributions allows the determination of the fraction of rain and snowmelt in the mixing tank for each time step. Assuming complete mixing, the total amount of  $Q_R$  and  $Q_S$  of the outflow from the mixing tank, which by definition is equal to the simulated discharge of the hydrological model, can be derived. The streamflow of the components  $Q_R$  and  $Q_S$  from the mixing tank of a spatial model unit represent the inflows to the mixing tank of the next spatial model unit. The same calculations are then performed again to simulate the outflow components of this next spatial unit. Thus, any model will generally use the same number of mixing tanks as it has spatial modelling units.

The practical implementation of the integrative mixing tank approach essentially corresponds to a separate model, which does not interfere with the structure of the existing hydrological model and which can be implemented with relatively little effort. It can thus be applied to any conceptual hydrological model. For a single model unit (without routing of the streamflow components) a completely independent calculation of the streamflow components would even be possible after running the hydrological model and by using the simulated time series for the variables  $I_R$ ,  $I_S$ ,  $aET$ , and  $Q$ .

## Hydrological Modelling Unit

(e.g. LARSIM subcatchment =  $1 \times 1 \text{ km}^2$  grid cell)

## Integrative Mixing Tank

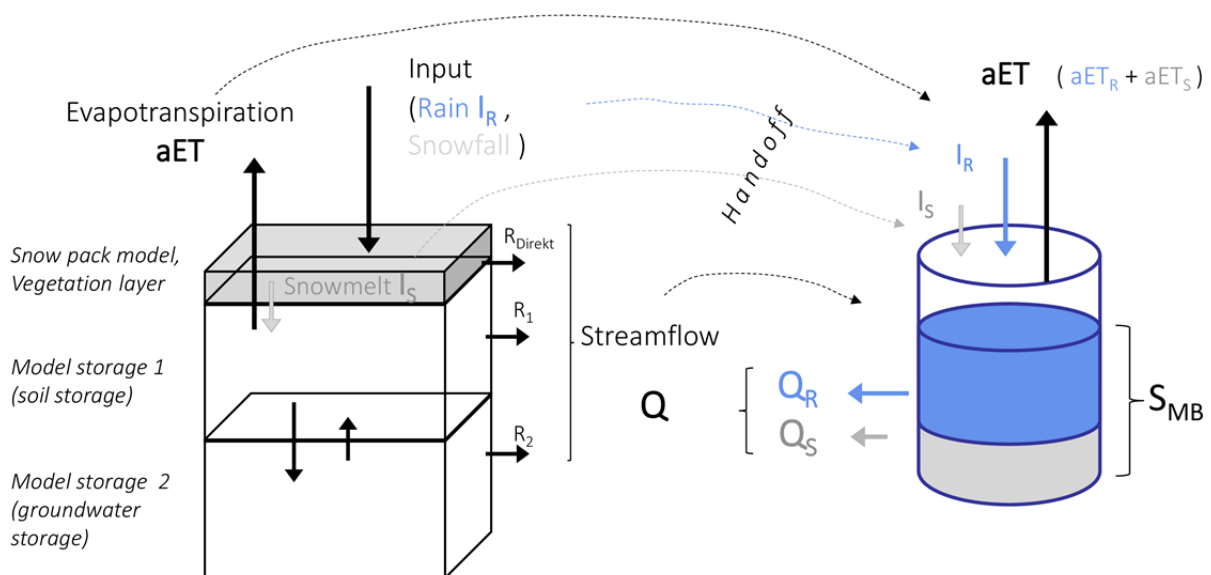


Figure 4.1: Schematic illustration of the streamflow component modelling by one integrative mixing tank. Model storages 1, 2 and runoff  $R_1$ ,  $R_2$ ,  $R_{\text{Direkt}}$  serve only as examples for many potential model structures and runoff generation concepts.

### Multiple mixing tanks

This more complex approach with several mixing tanks per model unit was integrated into the HBV-light model. For each spatial model unit instead of one, a set of several separate mixing tanks are used corresponding to the model's runoff generation process conceptualization with storages and fluxes, including a soil and a groundwater storage, translation and retention in the river, lakes, and reservoirs. Each conceptual storage in the hydrological model can be considered a mixing tank accounting for the fractions of rain and snowmelt. This method has been implemented in the model HBV-light and thus component fractions. This approach represents the most complex and conceptually accurate implementation of tracking streamflow components. Results from this method, implemented in HBV-light, thus serve as a **benchmark** for the test of the other, more simplified, tracking and mixing methods.

**Variant: Effect tracking**

In this variant, the mixing volume of each tank is limited, i.e., a constant mixing volume (mm) is assigned rather than using the actual volume from the corresponding hydrological model. Analogous to the unlimited mixing tank approach, at each time step, the fraction of each streamflow component is calculated from the fraction of the component in the limited mixing tank. This variant represents a further conceptual simplification and was introduced as a tool to intentionally track the effect of the various input components on streamflow dynamics (celerity) rather than the actual water residence times. This approach ensures that modelling of a hydrological system with large storages and long travel times over time does not result in a constant ratio of streamflow component simulations and still conserves the mass balance and the continuity of the hydrological model. This “effect tracking” approach can be implemented for the integrative mixing tank as well as for the multiple mixing tanks approach, limiting mixing volumes in all respective tanks. In this chapter, we present exemplary results of testing the effect tracking for the integrative mixing tank approach.

**4.3 Application and intercomparison****Separate effect modelling**

This approach was tested with the HBV-light model, but can generally be applied with any other hydrological model. We tested the approach on one alpine headwater catchment, the Minster (CH, prealps) and compared the resulting streamflow simulations with those from the benchmark model run with the multiple mixing tanks approach of the same catchment, model parameters, and input time series. The separate effect modelling removed the rain and snowmelt input components in the example in two different orders (Table 4.1).

Table 4.1: Annual mean runoff components resulting from different orders of input component omission in the separate effect modelling approach for the Minster catchment.

Method	Average annual runoff (mm)		
	$Q_R$	$Q_S$	
Benchmark model	742	1281	
Separate effect modelling; Order of components:			
rain	snowmelt	812	1212
snowmelt	rain	658	1366

The resulting streamflow components for these two omission orders differ significantly in terms of the simulated temporal (intra-annual) dynamics of the output components and even in terms of annual mean runoff (Table 4.1). In addition, neither order resulted in the same output component fractions as the benchmark simulation. The reason is that the interaction between storages and fluxes in a hydrological system is highly non-linear and results in different effects when changing the order of omitting input components. These changes concern in particular the evapotranspiration and the outflow from the two conceptual groundwater storages of HBV, as they are dependent on the filling levels of the storages and thus on how these are altered by the input omission. The conclusion from the differences found was that with the demonstrated issues with water balance and streamflow dynamics, this simple approach is not suitable for the project’s objective.

**Comparison of the integrative mixing tank and the multiple mixing tanks**

HBV-light simulations for the catchment of Minster (CH, prealps) are also used to illustrate the differences between the detailed multiple mixing tank approach (benchmark) and the integrative mixing tank approach. For this comparison, the fractions of the two components for the integrative mixing

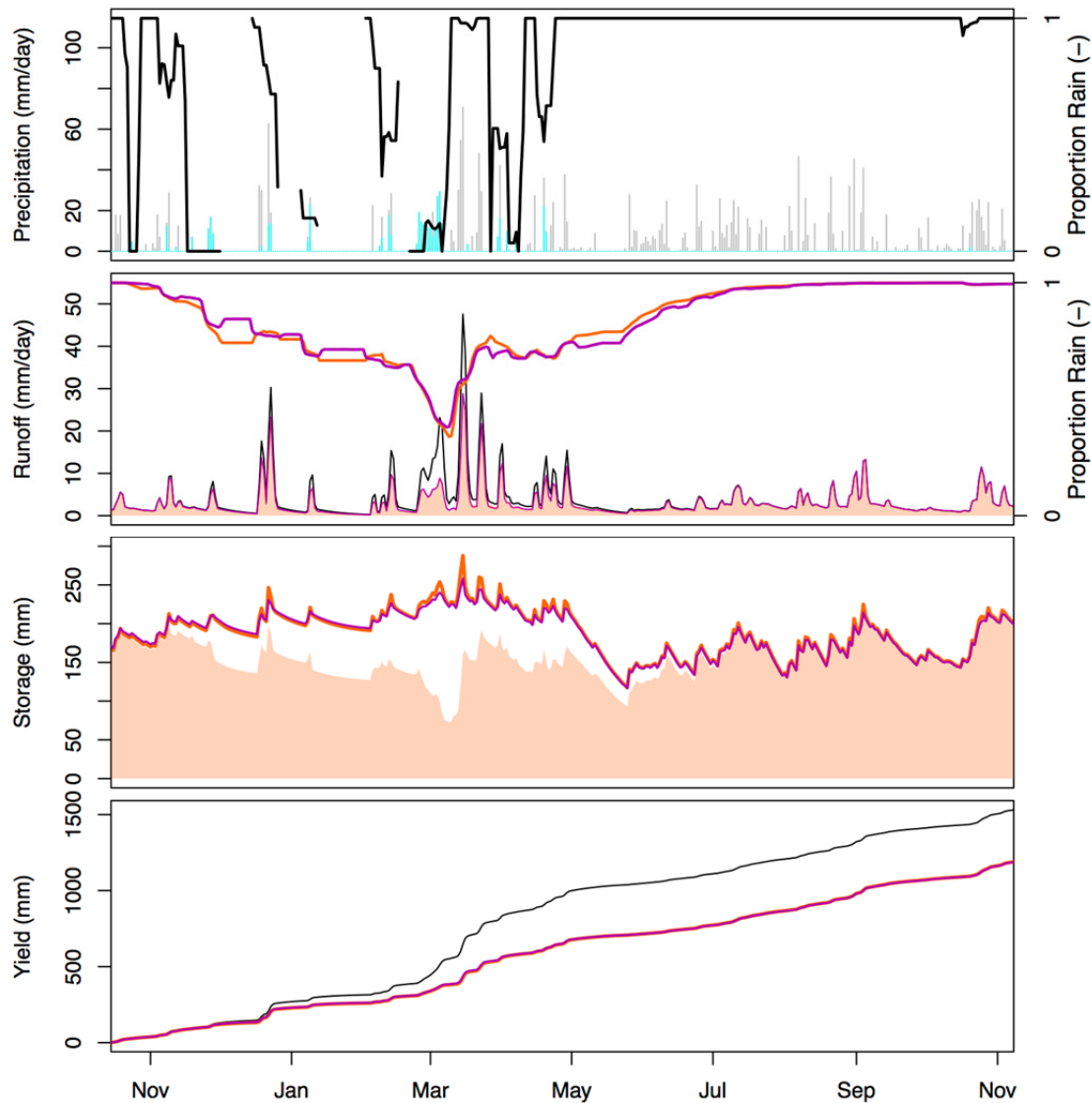


Figure 4.2: Modelled components of runoff and tank storages for the integrative mixing tank approach (orange) and the multiple mixing tanks approach (purple) for the water year 1992 for the Minster catchment (CH). Upper graph: input components  $I_R$  (grey) and  $I_S$  (cyan) as well as the fraction of  $I_R$  (black). Second graph: total simulated runoff (black) and rain component  $Q_R$  (orange area) as well as the relative contributions of  $Q_R$ . Third graph: evolution of total mixing tank storage for the multiple mixing tanks (purple line) and the integrative mixing tank (orange line) and fraction of  $Q_R$  (orange area). Lowest graph: cumulative runoff (yield) (black) and contributions of  $Q_R$  for both methods (note that the results are very similar and, thus, differences between the two curves barely visible).

tank approach were calculated as described in Section 4.2 by using the simulated time series for the variables  $I_R$ ,  $I_S$ ,  $aET$ , and  $Q$ , and storage change from HBV-light. Initial storage of the mixing tank was set to a value that ensured the storage of the integrative mixing tank never to be less than zero.

Figure 4.2 compares the results of the two methods for the hydrological year 1992. Generally, the results show that the snowmelt contribution  $Q_S$  quickly leaves the catchment because the total storage is relatively small (about 200 mm). Nevertheless, during storm events after the end of the snowmelt period, the snowmelt fraction of streamflow is still about 30–50%. The dynamic of the two streamflow components is very similar for the two methodical variants. Only the relative fractions of the components in the streamflow allow to visually detect slight differences, but the overall dynamic and the

sums of the streamflow components are very similar. Likewise, the mean annual rain component of streamflow of 1234 mm for the calculation with the integrative mixing tank is nearly identical to the rain component of 1250 mm for the calculation with the multiple mixing tanks (Figure 4.2 below).

For longer simulation time periods the very similar behaviour of the two approaches is conserved. Figure 4.3 shows that the inter-annual dynamics of the fractions of the streamflow components are almost indistinguishable and the cumulative yields are almost identical. The simulated storage dynamics from the water balance of the integrative mixing tank are also close to the storage dynamics of the multiple stores simulated with the HBV model. It should be noted that the agreement of the absolute values is specific to the comparison experiment, as the initial storage was chosen to be similar to the initial storage of the HBV model.

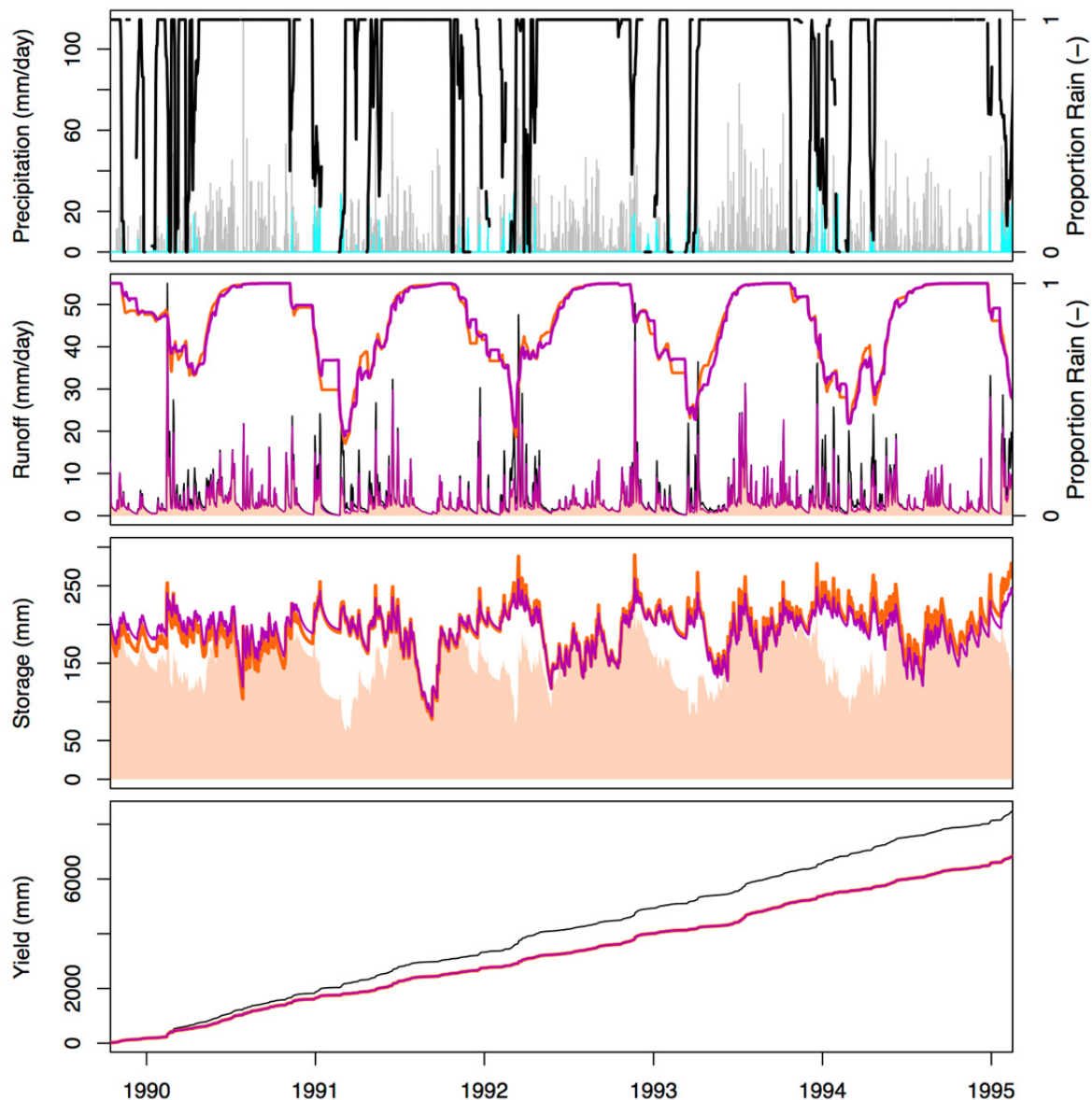


Figure 4.3: Modelled runoff components and tank storages for application of the integrative mixing tank approach (orange) and the multiple mixing tanks approach (purple) for a period of five years for the Minster catchment (CH). Individual graphs see Figure 4.2.

The two approaches were also compared for a number of other catchments and time periods with similar results (not shown). In summary, the comparisons demonstrate that the simplified approach of an integrative mixing tank is able to predict dynamics and a total yield of each streamflow component that are very similar to the results of the more complex multiple mixing tank benchmark model.

### **Results of the effect tracking approach**

Finally, the effect tracking approach with a limited mixing volume was tested, because an application of the regular mixing tank approach to the whole Rhine basin and its subbasins, including the large groundwater resources and lakes and thus large mixing tank storages and long water travel times, was expected to result in nearly time-constant fractions of the Rhine's streamflow components. Chapter 7 discusses the sensitivity of limiting the mixing tank for modeling of the entire Rhine basin in detail, as part of the overall model parameter uncertainty analysis. In this chapter, we illustrate again compare the difference based on the simulation for the Minster catchment as used above. For the experiment the a constant mixing volume of 25 mm and 1000 mm was used to limit component mixing in the integrative mixing tank model.

Figure 4.4 shows the simulation results of the rainfall and snowmelt components in the evapotranspiration flux, in the streamflow, and in the storage for an unlimited integrative mixing tank approach as outlined in the previous section, as well as for the limited mixing tank approach with a constant mixing volume of 25 mm. As intended, the dynamic response of the streamflow components becomes quite rapid using the effect tracking approach with a small mixing volume. Differences between the methods of limited and unlimited mixing tank volume are thus modelled in streamflow but also in the evaporation flux. In the application of the effect tracking approach the simulated streamflow components thus represent more the components generating the streamflow response. Another influence of the effect tracking approach is the much higher variation of the streamflow components from a nearly 100% to only 0% fraction of rain in the streamflow  $Q_R$ . This effect also results in a snowmelt dominated streamflow response during the snowmelt period in spring. Such a pronounced effect may not reflect the general understanding of part of the streamflow being generated by groundwater flow (baseflow), and thus streamflow always being comprised of a mixture of  $Q_R$  and  $Q_S$ , but it may be a necessary compromise for the objective of this project. Although the daily evolutions of the streamflow components are very different, the cumulative rain components  $Q_R$  at the end of the year are almost identical for both approaches. Thus, the long-term conservation of mass of the individual components is satisfied even for the effect tracking approach using a mixing tank with a constant mixing volume.

Figure 4.5 shows the simulation results of the rainfall and snowmelt components as in Figure 4.4 but with a larger constant mixing volume of 1000 mm. As intended, the dynamic of the streamflow components becomes more dampened when the effect tracking approach is applied with a mixing volume that is larger and corresponds approximately to the average annual streamflow yield. This leads to a moderate variation of the fraction of  $Q_R$  between 75% and 95%, meaning that in a catchment with a large mixing volume, streamflow is dominated by water from snowmelt during the whole year. This may be correct in terms of particle tracking in transit time modelling, but the result does not help to understand changes in streamflow components as a response to climate change at a high temporal resolution, which is the aim of the project. As for the case of the smaller constant mixing volume of 25 mm, the cumulative  $Q_R$  of the two variants differ only during the individual events, but the sum is almost identical at the end of each year.

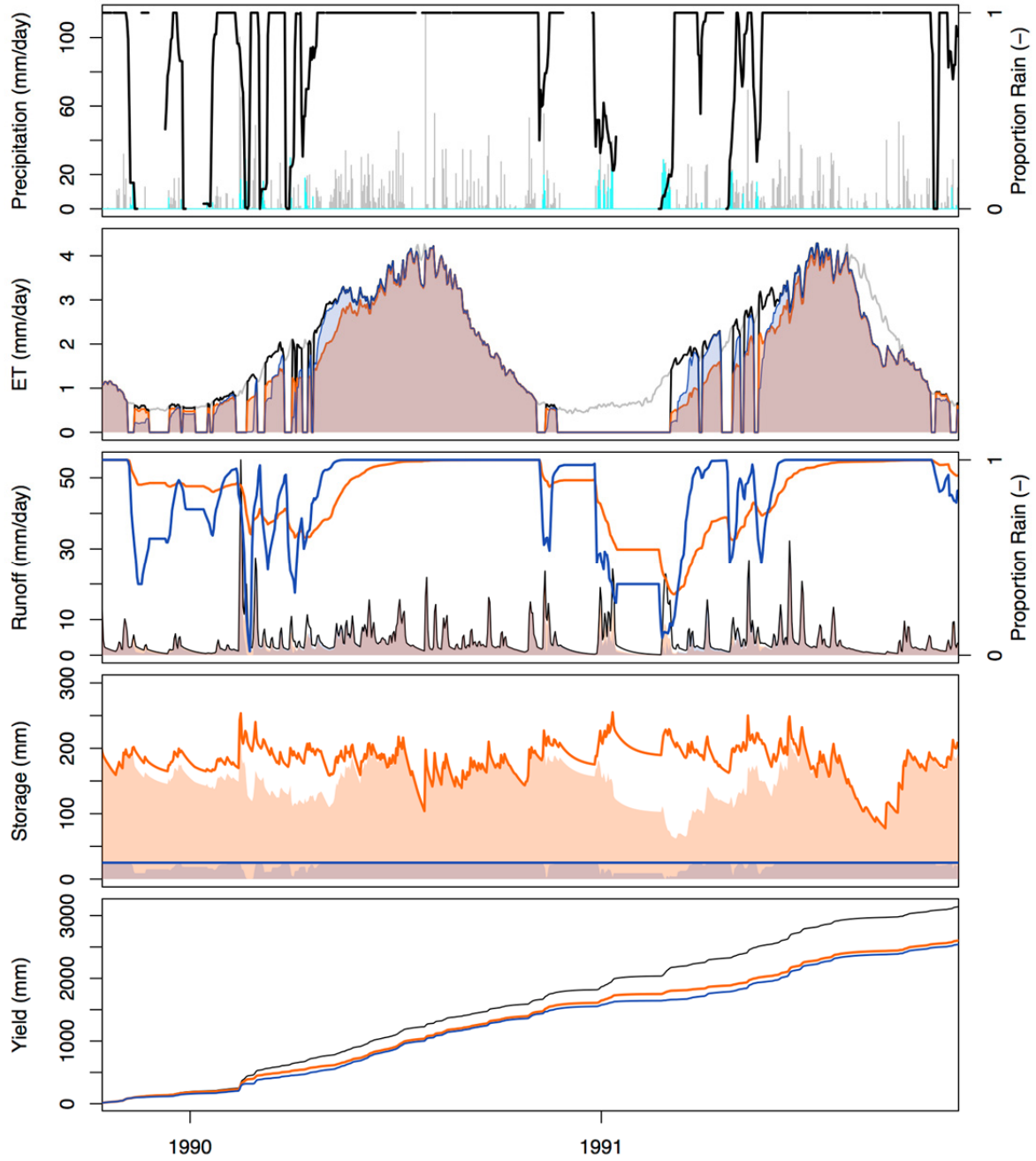


Figure 4.4: Simulated components in the evapotranspiration flux, runoff (streamflow in mm), and storage (mixing tanks) for the methodical variants: integrative Mixing Tank (orange) and Effect Tracking with an integrative mixing tank limited to a volume of 25 mm (blue). Upper graph: input components  $I_R$  (grey) and  $I_S$  (cyan) and fraction of  $I_R$  (black). Second graph: potential evapotranspiration (grey), aET (black), and rain components in evapotranspiration for both variants. Third graph: simulated runoff (black), its rain component (areas), and the fraction of the rain component (lines) for both variants. Fourth graph: temporal storage changes ( $S_{MB}$ ) for both variants (line with rain component as area). Bottom graph: cumulative runoff with rain contribution  $Q_R$  for both variants.

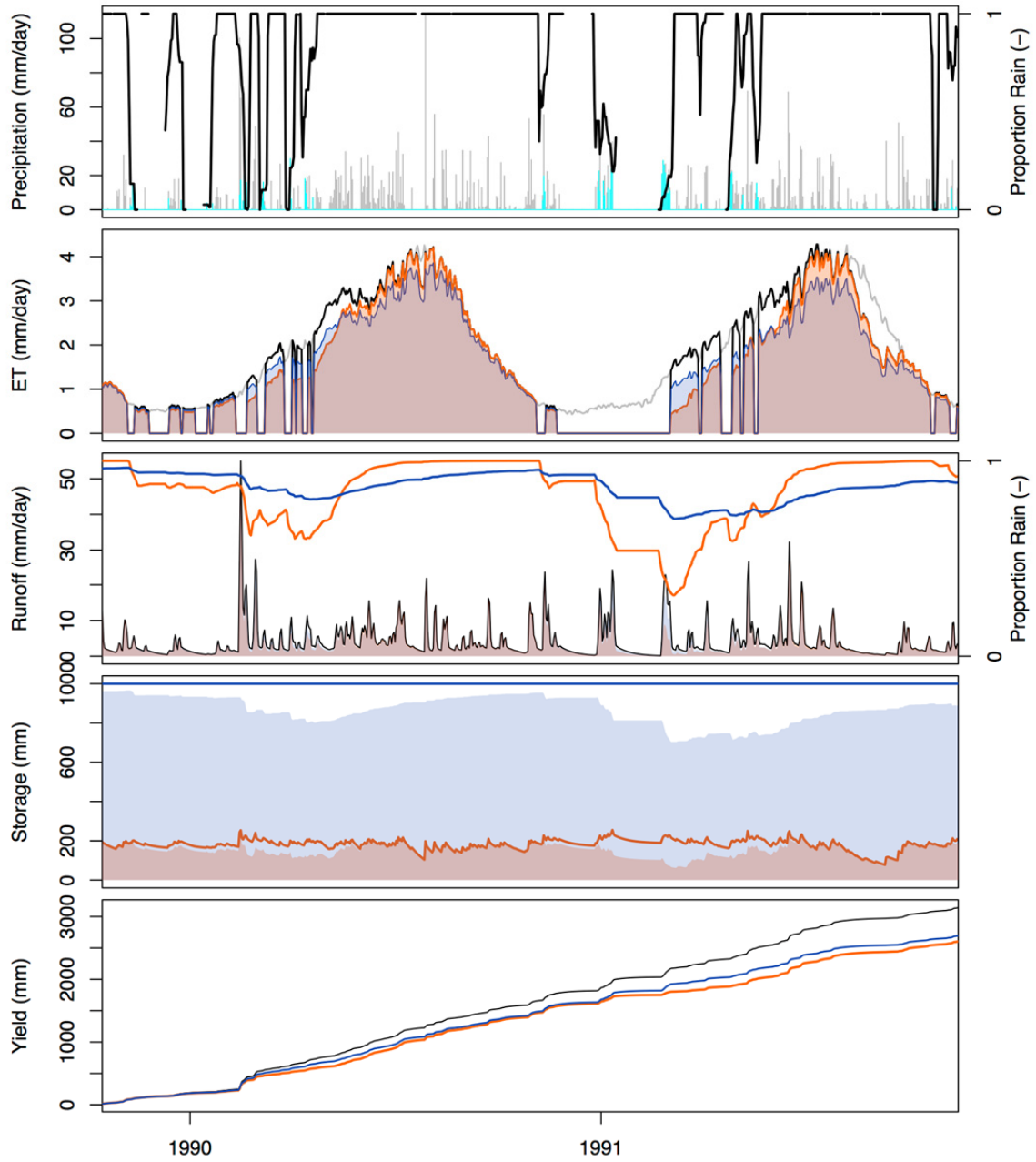


Figure 4.5: Simulated components in evapotranspiration, in runoff, and in the storage (mixing tank) for comparison of the methodical variants with the integrative mixing tank (orange) and the effect tracking with a limited mixing tank of 1000 mm volume (blue). Individual graphs as in Figure 4.4.

#### 4.4 Conclusions for the realisation within the project modelling framework

The results of the method comparison illustrate that the separate effect modelling is not a suitable approach for this project's aims, as the order of omission and adding components leads to significant differences in the fluxes and the water balance. The approaches using the mixing tank(s) are correct regarding the mass balance and, hence, more suited for the objectives of the project. The approach using the multiple mixing tanks directly implemented into the HBV-light model is the most accurate implementation to track input components through a hydrological system. However, the method of the integrative mixing tank is much easier to implement and much faster to calculate. It has the further advantage that the calculation can be carried out independent of the hydrological model and, consequently, potential differences between different models do not matter. The comparison of model variants further highlights that for the purpose of the project objectives, namely the simulation of the streamflow response to the input components, a limitation of the mixing tank to a constant mixing volume is useful or even necessary.

The integrative mixing tank approach using a constant mixing volume (effect tracking) was consequently implemented into the LARSIM model. The integrative mixing tank is used separately for each grid cell in the model and thus allows the streamflow components to be calculated for each grid cell separately. As the results of an integrated mixing tank were found to be similar to the previously implemented multiple mixing tanks with a similar constant mixing volume in HBV-light, it can be expected that the combination of both in the project's model chain won't influence the results for the streamflow components. The main decision is thus to choose a value for the constant mixing volume of the effect tracking approach to insure that the input components of rain, snowmelt, and ice melt are reflected as directly as possible in the streamflow response, in order to answer the research question of the project. In this respect, it must be born in mind that with the chosen approach the simulated streamflow components do not represent the water composition, i.e., the mixture of rainwater and snowmelt water particles in the same sense in, e.g., a usual end member mixing approach. Instead, with the chosen effect tracking approach, e.g. fractions of the snowmelt component of streamflow  $Q_S$  of up to 100%, will mean that the streamflow response, on a short-term perspective, is attributed to snowmelt alone.

The final parameterization of the constant mixing volume, i.e., the dimension of the mixing tank volume limit, was based on the results of sensitivity tests (see Chapter 7) and set to match both model structures (HBV and LARSIM). The constant mixing volume definition was thereby based on the simulated maximum daily runoff as a minimum necessary. Accordingly, the constant mixing volume was finally set to 10 mm for each of the three conceptual tanks in HBV-light and to 25 mm for the integrative mixing tank in LARSIM, as well as to 25 mm for all lakes and reservoirs (modelled by LARSIM) in the Rhine basin.

## 5 Modelling of the glacierized headwater catchments

### 5.1 Objectives

To quantify the rain, snow, and glacial ice melt components of streamflow and their dynamics the application of hydrological models is indispensable. In addition, modelling is required to assess time periods in the past or the future for which observed discharge data are missing as well as to include ungauged catchments lacking any discharge observations. In the first instance, the model simulations for the glacierized headwater catchments aimed to reasonably capture all key processes to restrict the uncertainties of the resulting fractions of  $Q_R$ ,  $Q_S$ , and  $Q_I$  as much as possible. To address the high potential of error compensation (equifinality issues) in modelling snow and glacier dominated catchments (see also Stahl et al., 2008), it is essential to consider internally simulated variables, such as snow water equivalent, snow covered area, glacier mass balances, glacier equilibrium-line altitude, glacier volumes, and glacier coverage (glacier areas) complementary to the use of discharge time series and specific discharge related benchmarks. Within the project this was realised by means of a semi-distributed coupled glacio-hydrological model based on the HBV-light software.

As a result of the impact of temporal variations and evolutions over the course of the unusually long simulation period from 1901 to 2006, the model has to be capable to simulate transient changes of the glaciers (i.e. time-variant glacier coverage) and needs to be parametrised with the use of and validated against observed glacier changes. Hence, a significant goal was to extend and adapt the model to achieve an, as much as possible, realistic representation of the major phases of observed glacier evolution.

Previous modelling studies quantified melt contributions to streamflow mostly on monthly or annual time steps. To enhance the findings from those studies and gain further insights into the dynamics of  $Q_R$ ,  $Q_S$ , and  $Q_I$  a daily-time step model was applied in the project. The main goal of this was to be able to assess the hydrographs and corresponding melt components in individual hydrologically extreme years. Here a specific focus was given to low flow years, in particular low flow events in late summer/autumn typically leading to the well-known impacts on river navigation and further water uses at the middle and lower reaches of the Rhine.

### 5.2 Delineation and model setup

The headwater catchments of the Rhine basin that had a glacier cover around the year 1900 and therefore required to be modelled by the coupled glacio-hydrological HBV-light model were identified based on glacier outlines derived from the “Siegfried maps“(Table 5.1 and Figure 5.1). The exact delineation of the individual catchments considered both, the availability of streamflow observations from gauges representing the glacierized areas (preferably located high up in the basin) and suitable handover nodes for the transfer of the modelled streamflow components into the stream network of the LARSIM model downstream. These considerations resulted in the definition of 49 HBV-light model catchments for 24 of which streamflow observation records are available. Most of those gauged headwater catchments have an area between 20 and 220 km<sup>2</sup>, only one catchment (Albula with 529km<sup>2</sup>) is notably larger. Catchment glacier coverages around the year 1900 range between 2% and 50%.

The initial HBV-light model catchments were set up with the following spatial model unit discretisation. Firstly, the glacierized and non-glacierized catchment area fractions (state at simulation start 1901) were distinguished. Those areas were divided into area fractions per elevation zones (100m), and then further differentiated within each elevation zone into area fractions for 3 aspect classes (north-exposed: 315°–45°, south-exposed: 135°–225°, and indifferent: west-/east-exposed and flat areas).

Table 5.1: Characteristics of the glacierized headwater catchments (HBV-light model catchments). Elevation according to the (recent) Swiss Digital Elevation Model (25x25m) "DHM25", Catchment glacier coverage for the stage around 1900, ordered by decreasing glacier coverage (G).

#	Stream	Gauge station	Elevation (m a.s.l.)			Area (km <sup>2</sup> )	G (%)
			Mean	Min	Max		
1901	Triftwasser		2435	925	3484	46.0	51.3
1800	Aare		2531	1139	4241	162.7	43.9
1100	Simme	Oberried/Lenk	2336	1096	3243	34.7	42.6
1701	Urbachwasser	Unterstock	2289	630	3608	68.4	37.7
4400	Ill		2489	1772	3265	50.5	34.9
2401	Goeschener Reuss	Abfrutt	2376	1064	3623	92.8	32.2
3201	Rein da Vigliuts		2425	1377	3160	18.5	32.0
3700	Hinterrhein	Hinterrhein	2357	1587	3387	53.9	31.8
1302	Oeschibach		2330	1171	3651	30.7	30.4
2201	Alpbach	Erstfeld, Bodenberg	2194	1022	3192	20.7	30.0
2600	Linth	Tierfehd	2321	805	3610	79.9	28.3
1902	Gadmerwasser		2131	926	3497	65.3	27.4
2502	Kaerstelenbach	Hinterbristen	2170	519	3295	116.8	26.3
3500	Valsler Rhein		2497	1861	3370	62.6	25.9
1502	Schwarze Luetschine	Guendlischwand	2059	648	4086	179.9	25.1
1300	Kander	Gasterntal, Staldi	2333	1170	3696	106.4	24.3
1501	Weisse Luetschine	Zweiluetschinen	2149	650	4146	164.9	22.7
1001	Louibach		2167	1245	3242	30.7	19.3
4501	Ferrerabach	Trun	2038	840	3420	19.2	19.0
1601	Rychenbach		2090	595	3698	52.6	18.8
3202	Somvixer Rhein	Somvix, Encardens	2448	1489	3159	21.8	15.9
2302	Schaechen		1952	990	3292	31.2	13.9
3401	Aua Russein		2326	959	3609	54.6	13.6
3302	Medelser Rhein	Disentis	2225	1049	3203	126.7	13.0
2400	Reuss	Andermatt	2260	1072	3581	196.6	12.3
4800	Landquart	Klosters, Auelti	2339	1321	3296	103.4	11.9
3101	Ual da Draus		2121	1046	3021	26.3	11.7
3602	Peilerbach	Vals	2275	1260	3110	32.4	11.3
2101	Grosstalbach	Isenthal	1813	773	2941	43.9	11.3
1401	Gornernwasser	Kiental	2047	930	3621	46.6	10.7
2501	Reuss		1979	519	3397	188.8	10.4
2801	Rosmatter Chlue		1993	862	2911	32.6	10.0
2102	Chlitaler Bach		1768	777	2907	12.3	9.3
3301	Vorderrhein	Sedrun	2149	1048	3319	156.6	8.7
2902	Raminer Bach		2046	962	3088	30.6	8.4
4601	Schmuèrbach	Rueun (Ruis)	2009	726	3420	100.6	7.7
3901	Ual da Niemet		2356	1455	3186	20.1	7.4
4001	Reno di Lei		2367	1560	3192	52.6	7.1
3800	Hinterrhein		2161	1080	3265	161.0	6.4
4101	Oberboda		2408	1716	3103	50.9	6.1
2000	Engelberger Aa	Buochs, Flugplatz	1604	443	3221	228.0	5.9
1201	Engstligenbach	Engstligenalp	2051	1227	3224	28.8	5.8
2301	Hinterschaechen		1933	989	3116	26.7	5.3
4301	Ava da Faller		2446	1460	3390	31.5	4.9
3001	Tamina	Vaettis, Mattlina	2088	940	3204	57.9	4.3
2700	Linth		1634	520	3238	171.4	3.9
2901	Sernft		1937	960	3145	49.8	3.0
4202	Albula	Tiefencastel	2125	837	3407	529.0	2.5
4701	Flem		1977	611	3234	82.3	2.3

Besides this general catchment model setup the initial glacier profile (at a higher resolution) had to be compiled for the transient glacier area adjustment simulation (for details see Section 5.4.2). Overall, compared to other semi-distributed hydrological modelling applications at the meso-scale, a fairly de-

tailed and, given the complex alpine topographic setting, appropriate discretisation of the catchments was realised. Consequently, the model catchments consisted of up to 201 (in case of the Weisse Lütchine catchment) different modelling subunits (“elevation-aspect-classes” in glacierized and non-glacierized parts).

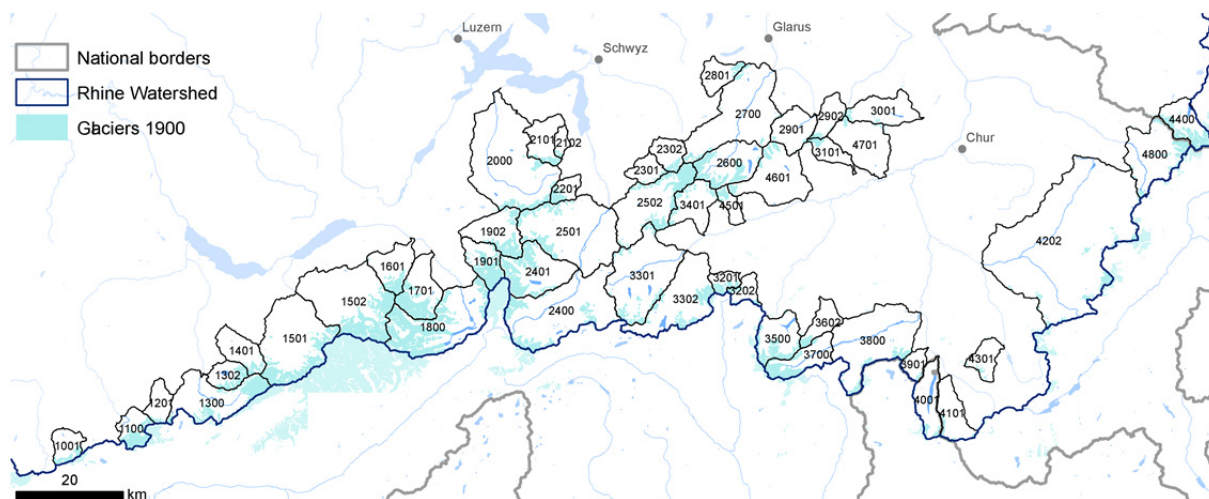


Figure 5.1: Map of all 49 glacierized headwater catchments (HBV-light model catchments), corresponding catchment characteristics in Table 5.1.

### 5.3 Specific developments for glacierized headwater catchment models

The HBV model, which has been developed in Sweden since the 1970s (Lindström et al., 1997), is a widely used semi-distributed conceptual precipitation-runoff model. In the project the HBV-light model version developed further at the University of Zurich (Seibert & Vis, 2012) was applied. Model adaptations and extensions required specifically for the project comprise three main aspects: the development of a conceptual snow-redistribution routine for high-altitude areas, extensions of the HBV glacier routine, and an implementation of a method to differentiate into the components  $Q_R$ ,  $Q_S$ , and  $Q_I$ . The latter is also relevant for the modelling of the entire Rhine basin (using the LARSIM models) and was addressed in the previous chapter. Furthermore, several features were incorporated in HBV-light as part of the final multi-criteria calibration procedure (see also Section 5.4.2).

#### 5.3.1 Snow modelling and snow-redistribution

In HBV-light snow water equivalents (SWE) are computed by a temperature-index model (degree-day factor approach). Snowmelt simulation takes into account different elevation zones and area fractions for three aspect classes (west-/east-exposed and indifferent (flat) areas, north-exposed areas with delayed snowmelt, and south-exposed areas with quicker snowmelt) (see Konz & Seibert, 2010). Within the project, a temporally (sinusoidally) varying degree-day factor was introduced to realise a better representation of the seasonal variability of snowmelt processes (described e.g. by Stahl et al., 2008). As in many similarly conceptual hydrological models, snow-redistribution processes originally had not been represented in HBV-light. Since the modelling aimed at a long-term period over more than 100 years, it was crucial to avoid the common hydrological modelling issue often called the “snow towers” phenomenon. Such an unrealistic accumulation of snow is often modelled in high-elevation areas if summer temperatures are not sufficiently high to completely melt the seasonal snowpack with the degree-day method. Thus during long-term modelling an excessive snowpack (snow tower) can build up. Simultaneously, however, it must be ensured that the snow input particularly in these high

altitudes, representing the glacier accumulation zones, is well captured to derive correct glacier mass balances. To this end the following conceptual snow redistribution representation was incorporated in HBV-light: If the snowpack on non-glacierized areas above a certain elevation *m a.s.l.* (for the project between 2500–2700 *m a.s.l.* depending on the catchment) reaches a certain threshold (for the project defined as 500 mm SWE), any additional snowfall input is evenly distributed to elevation zones located below and to all glacierized elevation zones (Figure 5.2). An even re-distribution means that the distribution of the redistributed snow on the acceptor-elevation-zones corresponds to their relative areas (same amount of redistributed snow in mm SWE in all acceptor elevation zones). Snow redistribution is restricted to the part of the catchment area above 1900 *m a.s.l.* in the model since areas in elevation zones below 1900 *m a.s.l.* are excluded from accepting redistributed snow. Following this approach a conceptual representation of the dominating transport of snow from non-glacierized high-altitude areas (typical “snow erosion sites”) to glacierized areas (preferential accumulation sites) could be obtained whilst the development of snow towers is prevented.

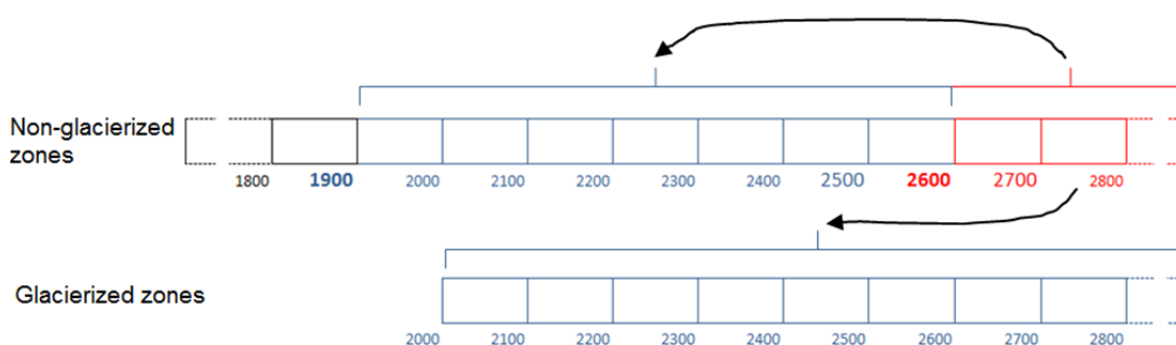


Figure 5.2: Simplified illustration of the newly introduced HBV-light snow-redistribution routine based on the differentiation of glacierized and non-glacierized elevation zones.

### 5.3.2 Enhancements of the glacier routine

The glacier routine implemented in HBV-light by Konz & Seibert (2010) is based on a very simplified depiction of glacio-hydrological processes requiring several enhancements in the context of the project. One issue was to incorporate the effect of the evolution of the annual seasonal sub- and en-glacial drainage system to also enable a **seasonally variable glacier runoff (outflow) response** characterized by an increasingly more efficient and responsive (quicker) glacier runoff generation and concentration during summer. This was realised by using the approach of the Canadian HBV-EC model version as, e.g., described by Stahl et al. (2008). Herein the outflow coefficient of the model glacier reservoir has a calibration parameter which, depending on the decreasing SWE of the snowpack on the glacierized areas, is varied by increasing it from an initial minimum to a maximum value over the melt season.

Another significant enhancement of the model was made regarding the transient **adjustment of glacier coverage (glacier areas) and glacier volumes** based on the computed glacier mass balances in the model. After consideration of different approaches, based on literature review as well as on discussions with scientists from glaciology, the  $\Delta h$ -parametrization approach by Huss et al. (2010) was chosen. The approach basically describes the spatial distribution of the glacier surface elevation change in response to glacier mass balances (changes) as shown in Figure 5.3 as a normalized ice thickness change as a function of the normalized elevation range (relative elevations). For the Alps Huss et al. (2010) derived empirical  $\Delta h$ -parametrizations based on observation from a number of glaciers for three glacier size classes (Figure 5.3b), namely small, medium, and large glaciers. Consequently, glaci-

ier retreat, i.e. the time-variant change of glacier area, in HBV-light is computed according to those empirical  $\Delta h$ -parametrizations, in the following simply referred to as glacier type curves.

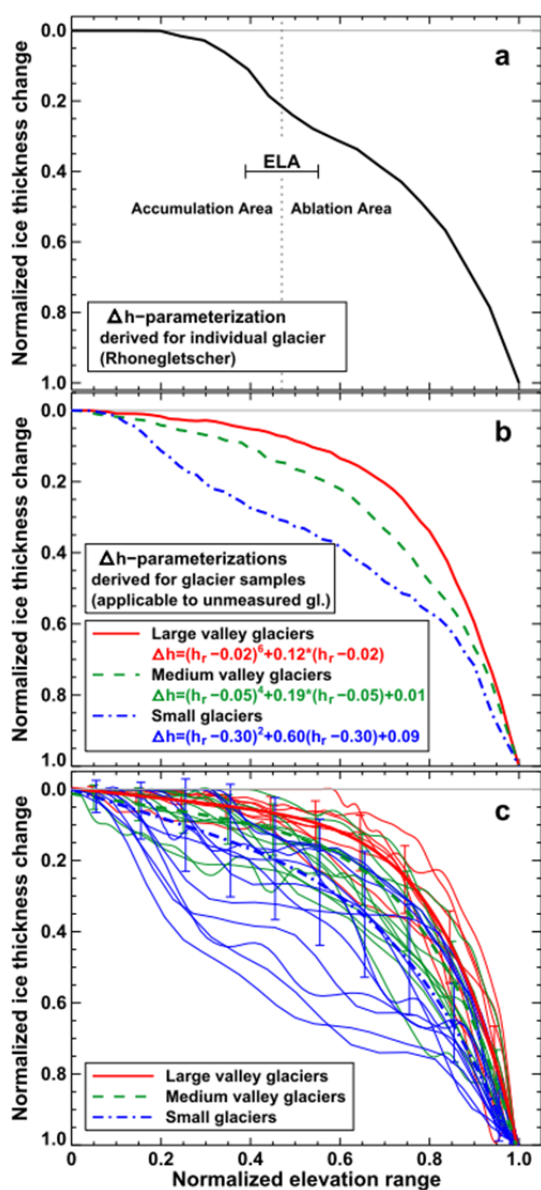


Figure 5.3: a) Parametrization of the normalised distributions of ice thickness changes to the normalised elevation range ( $\Delta h$ -parametrization) for the Rhône glacier based on observed ice thickness changes in the 20<sup>th</sup> century; additionally the variability of the equilibrium altitude line (ELA) is shown. (b) Empirical  $\Delta h$ -parametrizations for three glacier size classes applicable to unmeasured glaciers derived from digital elevation model comparison for 34 glaciers. (c) Empirically approximated  $\Delta h$ -parametrizations (as in b) and individual  $\Delta h$ -parametrizations for all 34 glaciers (thin lines). Error bars are calculated as the standard deviation in each glacier size class. From Huss et al. (2010).

To model the glacierized headwater catchments all glacier-covered areas within a catchment had to be aggregated to a single glacier represented in the model. This is a necessary simplification that implies certain limitations with regards to the resulting glacier change simulations from a glaciological perspective. Yet is likely to be less relevant for uncertainties of the hydrological modelling results (quantification of the glacial ice melt component of streamflow  $Q_I$ ). The selection of the glacier type curve to be applied is based on the initial size of the total glacier area but can also be defined by the user prior to running the model. The selection of the glacier type curve eventually used in the project resulted from assessing the distributions of glacier areas for all individual glaciers at different times (around the year 1900, around 1940, in 1973, and in 2003, see Section 3.4 glacier datasets) for each of the 49 glacierized headwater catchments. In contrast to the spatial discretization of the entire model catchments using elevation bands of 100 m, the model glacier and the simulation of its temporal changes are based on 10 m elevation bands.

The  $\Delta h$ -parameterization has been developed primarily for the description of recently observed glacier retreat (Huss et al., 2010). In the context of the project's objective one shortcoming is that it is not capable of describing the **advancing of glaciers** (as, for instance, partially observed in the 1960s–1980s period). Because glacier volumes and glacier areas are directly linked according to the approach suggested by Huss et al. (2010) a workaround was found for that problem by executing the model runs in two steps: Firstly, the glacier is gradually melted away completely based on the  $\Delta h$ -parameterization and the given initial ice thickness distribution. For that reason it is crucial to define this initial glacier volume (glacier thickness distribution) set at the start of the simulation in 1901 reasonably. In this first glacier melt model run hypothetical series of glacier area distributions (area per elevation band) and corresponding glacier volumes are generated

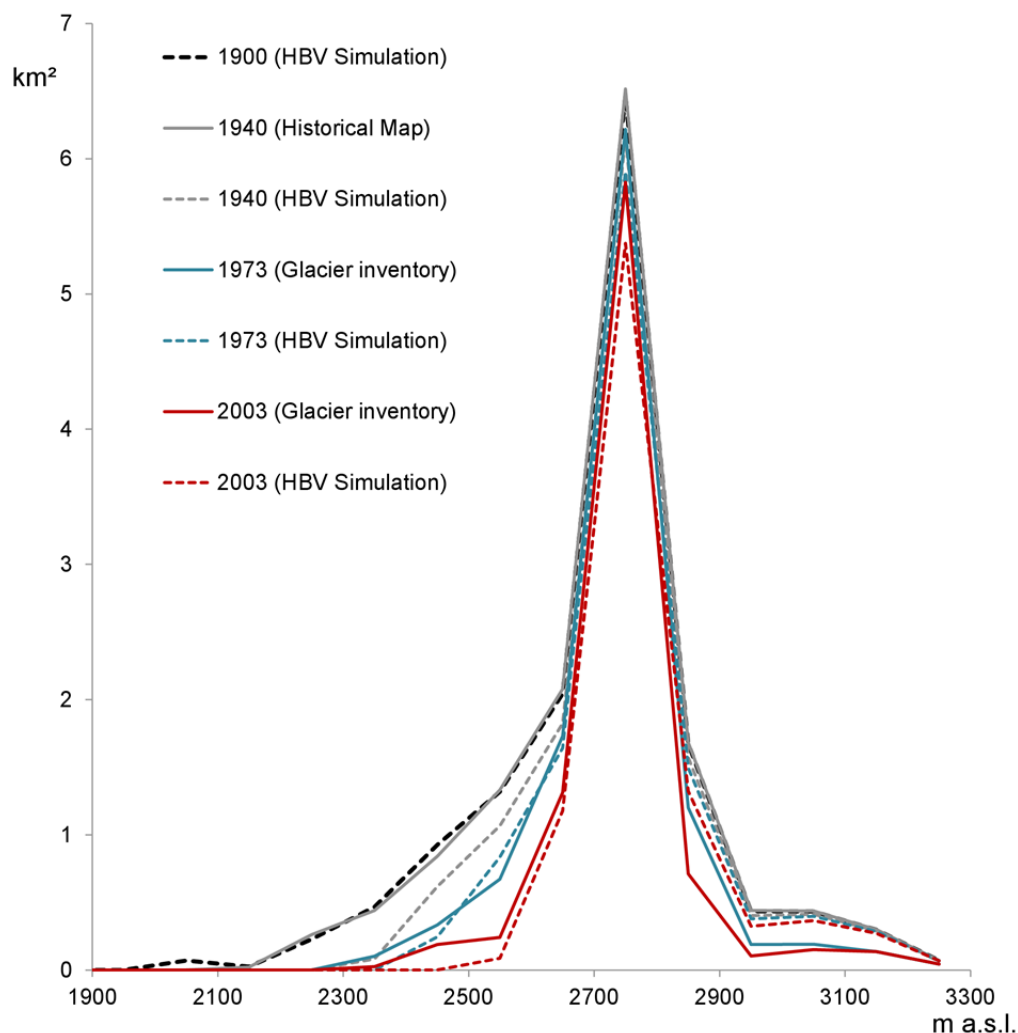


Figure 5.4: Modelled glacier areas (y-axis) for individual elevation zones (x-axis) and observed data from different glacier inventories for the years 1940, 1973, and 2003 in the Simme catchment (catchment # EZG 1100).

and then saved as lookup tables. Afterwards, as second step, the actual model simulation is executed. It is driven by the actual climatological input data and after each hydrological year the computed mass balance is used to derive change in the glacier area fractions for each elevation band from the lookup table. Adjusted glacier area distributions are then used in the simulation of the subsequent hydrological year. By this two-stage model application it is possible to also simulate an advancing glacier (by “going upwards” in the lookup table) as long as it does not outgrow its initial stage at the start of the simulation in 1901.

Finally, it should be noted that a **glacier width scaling function** was introduced as a further modification of the approach for simulating time-variant glacier coverage by Huss et al (2010). Based on a physically-based relation between glacier width (here translated into glacier area per elevation band) and glacier thickness according to Bahr et al. (1997) a transient change of glacier area within an elevation band is determined. This is a necessary adaptation, because effectively the original  $\Delta h$ -parameterization approach is a 2D-model representation referring to average glacier thickness per elevation band. This would only allow a distinction in completely glacier-free or completely glacier-covered elevation bands (and, hence, would lead to step-like retreat simulation patterns of glacier area over elevation bands). Figure 5.4 shows an example of a final glacier area simulation result (incorporating all model enhancements mentioned above) for one of the glacierized headwater catchments.

## 5.4 Model application and multi-criteria-calibration

In addition to the enhancements of the HBV-light model outlined above, the model application for the 49 glacierized headwater catchments (Figure 5.1) required several data processing steps to set up the final models. In summary these mainly concerned the following issues:

- Acquiring and scanning of additional **streamflow observation data series** to be used for model calibration.
- Calculating **potential evapotranspiration** input data (daily values 1901-2006) based on the method proposed by Oudin et al. (2005) and the use of evapotranspiration data by Menzel et al. (1999) for validation.
- Adjusting **precipitation input data** through a combined application of the wind correction method according to Sevruk (1989) and validation with long-term annual mean precipitation sums resulting from the HADES (Hydrologischer Atlas der Schweiz – transl: *Hydrological Atlas of Switzerland*) water balance approach (detailed in Section 5.4.1).
- **Reconstructing initial glacier volumes and glacier thickness distributions for the year 1900** as initial conditions in the models (detailed in Section 5.4.2),
- Developing and integrating an adequate combined objective function incorporating observation data on streamflow, snowpack, and glacier (volume) change as important **benchmarks** for the **multi-criteria calibration** in HBV-light (detailed in Section 5.4.3).
- Developing a method for the **transfer of parameters to ungauged glacierized headwater catchments** (without streamflow records) by an identification of the gauged catchment being the most similar one to the ungauged catchment in question (see also Section 7.2.3).

### 5.4.1 Correction of precipitation input data

The meteorological input to be used to model the streamflow components was the gridded data composed of the HYRAS (1951–2006) and the reconstructed HYRAS-REC (1901–1951) datasets (see Chapter 2). The evaluation of the precipitation series from these products, including the comparative analysis of the available streamflow observation records, demonstrated the presence of a considerable **severe underestimation of precipitation** sums, and thus the necessity of an adequate **correction** as a crucial precondition of the model application. The correction method according to Sevruk (1989) was applied to the gridded input data and subsequent correction factors were identified at the catchments scale based on the water balance approach by Weingartner & Schädler (2001). Correction of precipitation before the modelling thus allowed avoiding calibration of precipitation gradients as part of the model calibration. In practice, the correction method based on Sevruk (1989) was first applied to the original gridded data (1901–2006) by means of the precipitation correction tool implemented in the LARSIM model. Afterwards, using these corrected data, on the one hand, the precipitation-elevation gradients required by the HBV-light model were determined for all glacierized headwater catchments, on the other hand, mean catchment precipitation sums were calculated and the mean annual sums in the period 1961–1990 were compared against values from Weingartner & Schädler (2001).

Weingartner & Schädler (2001) suggested for alpine areas specifically that precipitation input determined based on observed streamflow as remaining term of the water balance, may lead to less uncertain results than interpolation of station data given the poor station density and large measurement errors typical for alpine regions. Weingartner & Schädler (2001) used streamflow records, evapotranspiration data modelled according to Menzel et al. (1999), and estimates on the changes in water storage caused by glaciers (using available mass balance series from monitored glaciers) to derive their

water balances and precipitation terms for catchments covering all of Switzerland. Further details on the procedure by Weingartner & Schädler (2001) are given in the explanatory remarks to the corresponding page of the atlas “HADES” (HADES-Tafel 6.3 “Komponenten des natürlichen Wasserhaushalts”). In some cases (16 out of the 49 glacierized headwater catchments) the delineated HBV model catchment corresponded exactly to one of the catchments assessed by Weingartner & Schädler (2001) or was composed of several of these. Then, a straightforward comparison of the mean annual precipitation totals (1961–1990) from Weingartner & Schädler (2001) and from HYRAS data corrected according to the Sevruk method was possible. The remaining HBV model catchments each represent only a part (headwater area) of one of the study catchments by Weingartner & Schädler (2001). Therefore, the difference in mean elevation between the catchment and its subcatchment and the ascertained precipitation-elevation gradients were used to adjust the precipitation to the smaller HBV model catchment. From the comparison of the mean annual precipitation totals (1961–1990) resulting from the water balance approach by Weingartner & Schädler (2001) and according to the corrected HYRAS data, a specific correction factor for each catchment was derived and finally applied to the series of daily mean catchment precipitation that had been calculated from the gridded data (1901–2006).

Finally, the plausibility of the results was examined based on the spatial patterns of long-term mean precipitation across the catchments and compared with a variety of references (map by Uttinger, 1949; tables in the appendix of Baumgartner et al., 1983; map by Kirchhofer & Sevruk, 1992; and mean catchment precipitation according to the RhiresD dataset by MeteoSwiss). Only a few catchments had evidences of inconsistencies, for instance, where Weingartner & Schädler (2001) indicated a “reduced plausibility” of their water balance (often related to issues caused by anthropogenic impacts on the underlying streamflow data). In these cases the second step of the correction procedure based on correction factors was skipped (or the factor set to 1) and the corrected data according to the Sevruk method was directly used as model input. The correction factors eventually used were, with one exception,  $\geq 1$ . Only for the catchment of the Upper Aare (catchment # EZG 1800) the comparison of the corrected HYRAS precipitation with the precipitation sum from the water balance by Weingartner & Schädler (2001) resulted in a reduction by 10%. Apart from that and the few exceptional cases in which the application of the correction factor was skipped, the corrected HYRAS and HYRAS-REC precipitation sums were increased further, in individual cases by up to 60%. The corrections mostly ranged between only a few % to +25%.

#### 5.4.2 Reconstruction of initial glacier volumes around 1900

The modelling of the glacierized headwater catchments from 1901 onwards required an adequate approach to reconstruct the initial glacier state in terms of areas, volumes, and also glacier profiles, i.e. the glacier thickness distributions over the 10m elevation bands. For that purpose, the glacier thickness distributions for the years of 1973 and 2010 (approximately) were determined for each of the 49 catchments from an unpublished gridded dataset of modelled glacier thickness (25x25m) for Switzerland, which was provided by Matthias Huss (Université de Fribourg). These glacier thickness data were computed based on the physically-based method by Huss & Farinotti (2012) using available ice thickness measurements (from about 35 sites) for model calibration and the inventories of glacier area for both years (1973: Müller et al., 1976; 2010: Fischer et al., 2014). The distributions of glacier areas over the elevation bands could be ascertained for all years, ~1900, ~1940, 1973, 2003, and 2010 for which glacier map products were available (glacier inventories and digitised “Siegfried maps”, see Section 3.4). To reconstruct the total glacier volumes around 1900 for each catchment the widely used relationship between glacier area and glacier volume (glacier volume-area scaling, see e.g. Bahr et al., 1997; Bahr et al., 2015) was applied:

$$V = c \cdot A^\gamma \quad (5.1)$$

where

$V$	glacier volume
$c$	glacier specific scaling parameter
$A$	glacier area
$\gamma$	scaling exponent

By using the known volume-area values for the years of 1973 and 2010 (volumes taken from the gridded glacier thickness datasets) and setting the scaling exponent  $\gamma$  to the theoretically fixed value of 1.375, as described by Bahr et al. (2015), the multiplicative scaling parameter  $c$  for both glacier volume-area pairs of value, for 1973 and 2010, was obtained for each catchment. The average of both values of the multiplicative scaling parameter  $c$  was then used to determine the total glacier volume for the simulation start at 1901 based on the total glacier area from the “Siegfried maps”. In a next step to reconstruct the glacier thickness distributions over the 10m elevation bands, again a physically-based relation from Bahr et al. (1997), namely a proportionality of glacier width and the square root of glacier thickness, is used. For illustration, Figure 5.5 shows the reconstructed glacier thickness profile for one catchment. The underlying glacier thickness distributions for the years 1973 and 2010 were directly obtained from the gridded glacier thickness datasets (provided by Matthias Huss). The profile for the stage around 1900 was reconstructed based on the glacier area distributions according to the “Siegfried maps” and the locally fitted relation between glacier area and volume as described above. As expected, the thickness for the reconstructed profile glacier is generally larger compared to the later/recent profiles, particularly in the lowest and the uppermost parts.

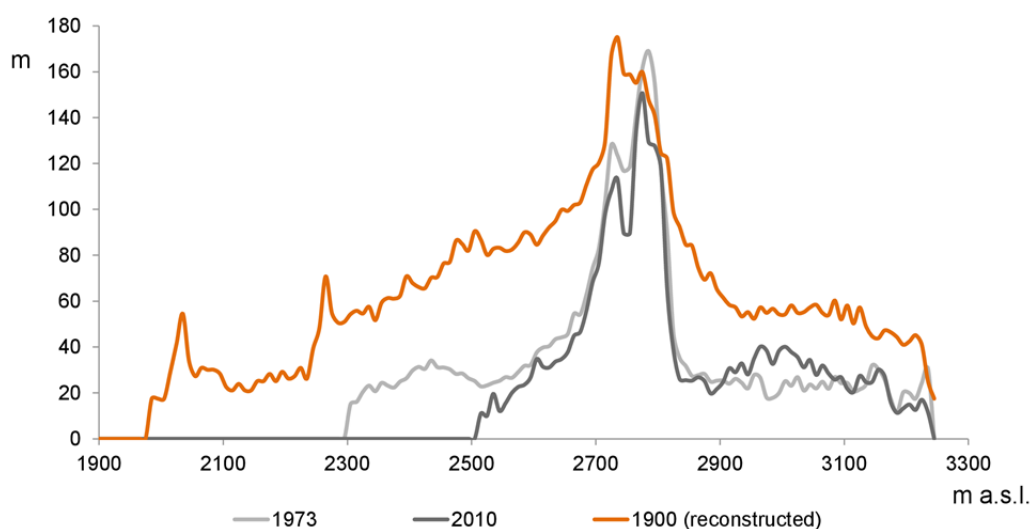


Figure 5.5: Glacier profile, i.e. ice thickness for 10m elevation bands, exemplarily shown for the Simme catchment (catchment # EZG 1100): grey lines: based on a gridded ice thickness dataset for the years 1973 and 2010 provided by Matthias Huss (modelled according to the method by Huss & Farinotti (2012)) and by using available local ice thickness observations in Switzerland and the glacier inventories by Müller et al. (1976) and Fischer et al. (2014)); orange line: reconstructed glacier ice thickness profile that is used as initial glacier state for the HBV-light simulations.

### 5.4.3 Multi-criteria calibration

The overall benefit of using diverse observation datasets and multiple criteria to calibrate conceptual hydrological models complementary to streamflow time series is unquestionable (e.g., Seibert, 2000; Seibert & McDonnell, 2002; Konz & Seibert, 2010). The study by Finger et al. (2015) initially

demonstrated this benefit for selected high-altitude glacierized catchments. For the multi-criteria calibration of all 49 glacierized headwater catchments in the project, in addition to streamflow observations, information (benchmarks) on snow and glaciers, which were derived from several available data products, were then used.

The **calibration of streamflow** principally aimed at incorporating all available discharge observations for the glacierized catchments. Consequently, discharge records from 24 gauges covering the period from 1910 to 2006 but differing in length and timing were used. Only streamflow data (sometimes subrecords for shorter time periods) not or only marginally affected (as far as documented) by water resources management operations, i.e. dams, water diversions and returns, or other stream regulation measures were used. Partially this included streamflow data from hydrometric stations that do not represent the whole model-catchment, i.e. the gauge is situated upstream of the outlet of the modelled catchment, see Figure 5.6). In such cases, streamflow data for the calibration were regionalized, i.e. adjusted by means of specific discharge (in mm) and differences in catchment area. In the specific case of the Schwarze Lutschine catchment, a streamflow record for a period of more than 73 years could be reconstructed from the available streamflow records for the gauge at the outlet of the Weisse Lutschine catchment and for the Lutschine at the gauge Gsteig downstream of the confluence. Streamflow observations from the gauge Gündlischwand (Schwarze Lutschine, record: 1992–1999) provided by the Amt für Wasser und Abfall des Kantons Bern (water authority of the Canton of Berne) were used to validate the reconstructed streamflow data.

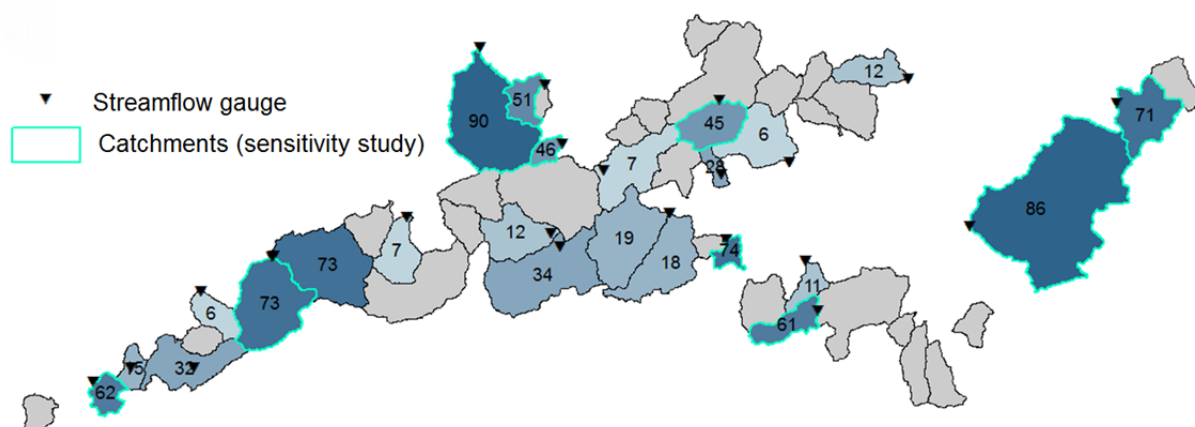


Figure 5.6: Map of the glacierized headwater catchments with streamflow gauges. Among the 49 catchments 24 had streamflow observations suitable for model calibration (blue shaded catchments with indication of available streamflow record length in years), the other 25 catchments (grey) had no streamflow observations. Catchments with relatively long streamflow records and only marginal influence by river regulation, which were included in the climate sensitivity study (see Section 3.2), are highlighted (turquoise frames).

Mainly based on the conclusions from the data analysis of alpine streamflow regimes (see Chapter 3), three **efficiency criteria regarding streamflow** were finally incorporated in model calibration, the Lindstrom measure, the Nash-Sutcliffe Efficiency calculated on logarithmic flows, and a season specific Nash-Sutcliffe Efficiency calculated only on the flows from June to September. The Lindstrom measure (Lindström et al., 1997) represents a variant of the Nash-Sutcliffe Efficiency that takes the volume error of the simulated streamflow (against observed streamflow) into account. Thereby it prevents a systematic overestimation or underestimation of streamflow by the model simulations and constitutes an adequate efficiency criteria particularly in the context of long-term (water balance) modelling studies. The two additional streamflow efficiency criteria were selected mainly because of the distinct seasonality of the streamflow regimes of the glacierized headwater catchments: The use of

the seasonal Nash-Sutcliffe Efficiency for the period from June-1 to September-30 aims at the best possible simulation of the intra-annual peak flows of the glacierized headwaters at the climax of the alpine snow and glacial melt, whereas the Nash-Sutcliffe Efficiency for logarithmic flows ensures a better representation of winter low flows (and thereby a better representation of catchment storage characteristics) which are mostly neglected by other common streamflow efficiency criteria. Exemplary, Figure 5.7 shows the final results of the streamflow calibration (incorporating all three criteria) for the catchment of the Weisse Lütshine. As a consequence of using these different streamflow signatures for calibration, a good agreement of model simulations with observations could be achieved with respect to the intra-annual variability of mean streamflow (water balance focus), the characteristic seasonal patterns of streamflow (regimes of mean daily streamflow including dynamics of typical peak and low flow behaviour), and the dynamics in years of unusually low/high mean flows (years of 1972 and 1999 respectively) as well. Figure 5.7 demonstrates how well the extended HBV-light model represents the various streamflow conditions.

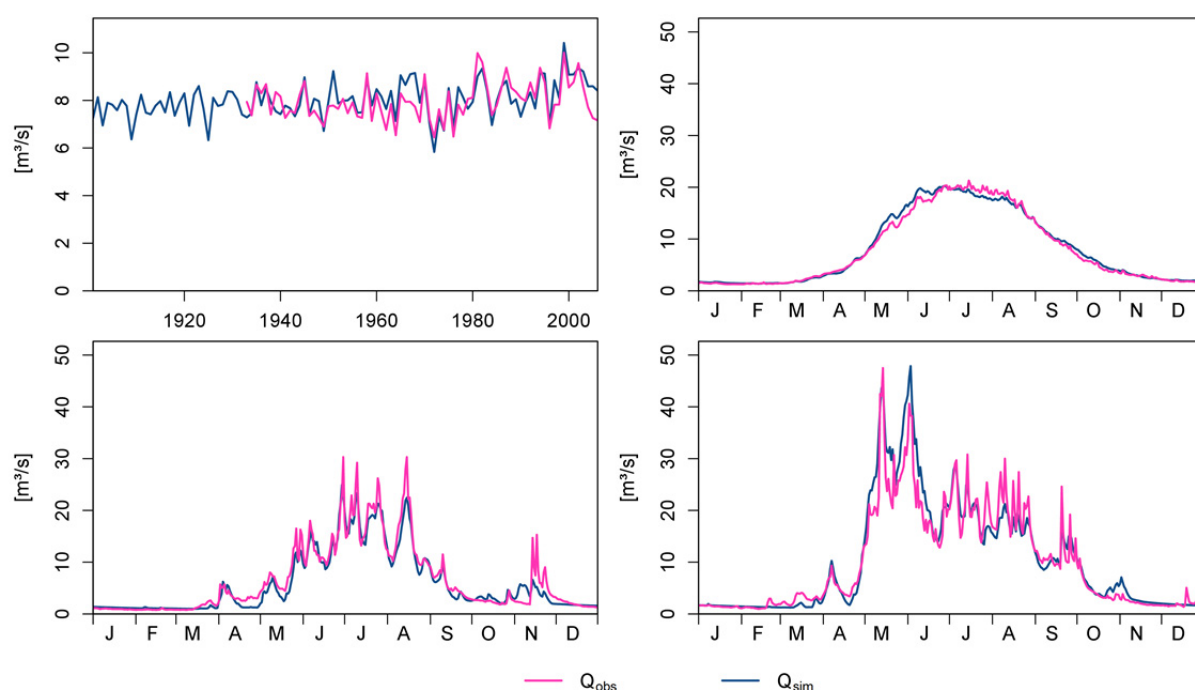


Figure 5.7: Exemplary HBV-light streamflow simulations compared to streamflow observations for the Weisse Lütshine catchment (catchment # EZG1501): a) annual means 1901–2006, b) daily means (period 1933–2006 corresponding to the available streamflow observation record), c) for the year 1972, the year of lowest annual mean streamflow of all years, d) for the year 1999, the year of highest annual mean streamflow of all years.

In contrast to similar studies, model calibration concerning the **snowpack** was not based on observation records from single snow monitoring stations but on the gridded SLF data product “SWE climatology for the winters 1972–2012” (OSHD-SLF, 2013; Jörg-Hess et al., 2014) over a spatial domain covering Switzerland and some bordering areas. Thereby it was possible to apply a consistent procedure for all 49 catchments, a considerable advantage for the project. However, limitations linked to the use of the SLF’s SWE product are its constrained availability to the period 1972–2006 and in particular to the months November to May only (no data available beyond the normal winter season). Also, uncertainties may originate directly from the data product as well as from discrepancies in resolution with a grid cell size of 1km<sup>2</sup> for the SLF data against the relatively detailed discretisation of the catchments for the HBV-light simulation. With respect to the project’s objective of quantifying the

contributions of the melt components from several subbasins, a calibration based on spatially averaged SWE values, matching the mean of SLF data vs. the mean of simulated SWE, has been considered the most effective option to make use of the SLF data.

Further analyses of the SLF data, such as, e.g., the investigation of SWE distributions over elevation zones within the catchments, led to the final decision of using the daily SWE values averaged for the elevation range 2000–2500 m a.s.l. for the snow calibration of each catchment. In this elevation range, the SLF data product is fairly well supported by station data and assumed to be most reliable. The mean absolute error (MAE) served as performance criterion. The option to base the calibration on the fit between SWE averages for certain elevation ranges had to be implemented into HBV-light specifically for this project. Parallel to this adapted SWE calibration, the SLF data product was used for the calibration of the catchments' snow covered area fractions (SCA) using the root mean square error (RMSE) as performance criterion. For the latter, limitations and uncertainties due to the comparatively large grid cell sizes of the SLF product needed to be taken into account as well. Exemplary, Figure 5.8 shows simulations of SCA and SWE for the Alpbach catchments in comparison to the values derived from the SLF data. The SCA dynamics, the increase of SCA in early winter and the decreasing SCA due to snowmelt in spring, are well represented. The intra-annual variability of SWE is mostly well represented, too. The results of both, SCA and SWE, however, reveal minor deficits in the simulation of the snowmelt beyond May, at a time when snow observation data for model calibration were unavailable (SLF data constrained to Nov–May). In the simulation a snow cover can persist over the whole summer in some single modelling subunits with elevations above 2500 m a.s.l., which usually does not occur in reality. Yet, overall a consistent simulation of the accumulation and melt of snow could be achieved over 30 years if the SLF snow data product is taken as reference.

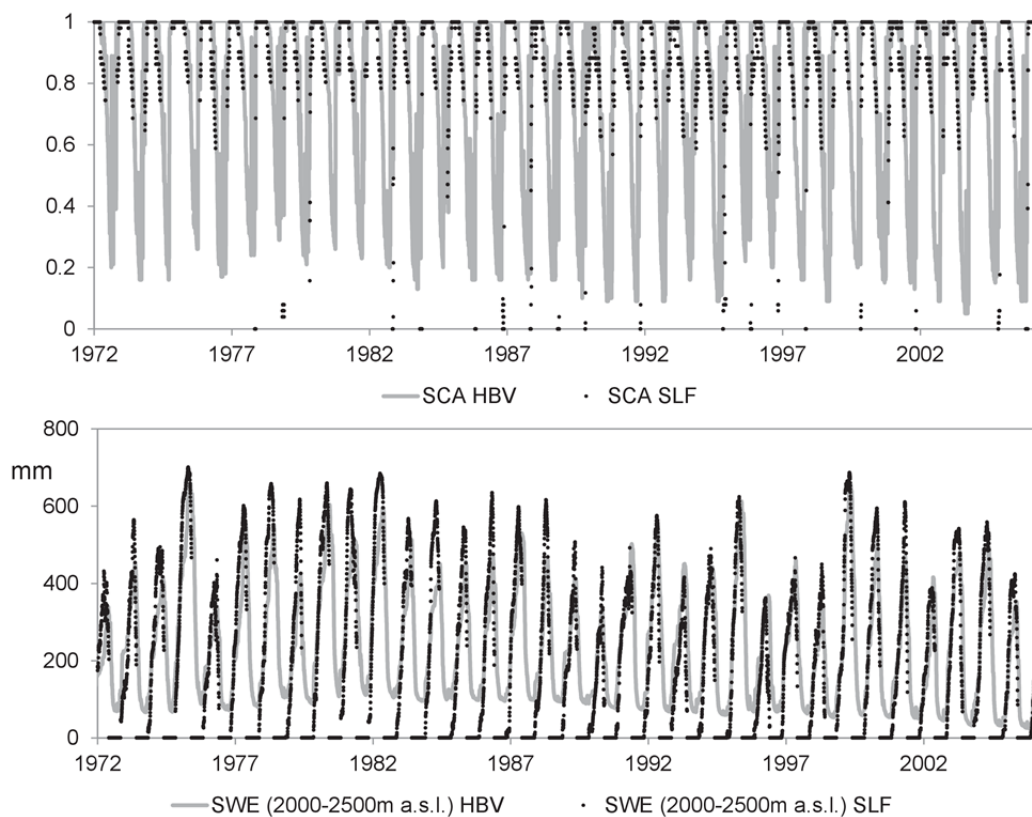


Figure 5.8: HBV-light snowpack simulation (daily values) compared to observation data based on the SLF SWE map product 1972–2006 exemplarily shown for the Alpbach catchment (catchment # EZG 2201). Top graph: fraction of snow covered area (SCA), bottom graph: snow water equivalent (SWE) mean for the elevation range 2000–2500 m a.s.l..

For the calibration of **glacier volume changes** the glacier volumes for the years of 1940, 1973, and 2003 were determined based on the available glacier coverage datasets (Section 3.4) and on the glacier ice thickness datasets from Matthias Huss for the years of 1973 and 2010 (details see Section 5.4.2). Glacier volumes were estimated using the glacier-volume-area-scaling relationships for 1973 and 2010, which had already been derived for the reconstruction of the initial glacier profiles (Section 5.4.2). Those estimates of glacier volume change are clearly subject to uncertainties, yet were incorporated in the model calibration mainly to avoid extreme overestimations and extreme underestimations of glacier retreat over the period 1901–2006, as sometimes had been the case in preliminary test simulations. For this model calibration using benchmarks of glacier volume from three reference years, a further objective function had to be introduced in HBV-light specifically for that purpose. Exemplary, Figure 5.9 shows the final results of the calibration of glacier volumes for the catchment of the Weisse Lutschine.

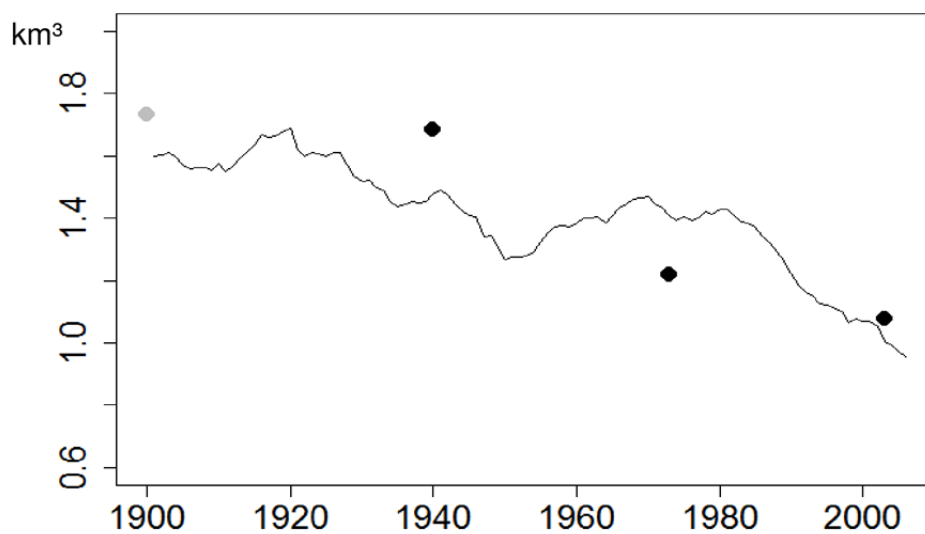


Figure 5.9: Modelled glacier volumes 1901–2006 (line) and glacier volume benchmarks (black dots) derived from the available glacier datasets and used for model calibration for the example of the Weisse Lutschine catchment (catchment # EZG 1501). Determination of volumes: i) for the year 1940: based on glacier areas in the (digitised) historical maps (“Siegfried maps”) and volume-area-scaling, ii) for the year 1973: based on the glacier inventory from Müller et al. (1976) and glacier ice thickness data by Matthias Huss, and iii) for the year 2003: based on the glacier area from Paul et al. (2011) and volume-area-scaling.

While modelling studies commonly intend to explore the transferability to time periods beyond the calibration period, the ASG Rhine project aimed at the best possible simulation of the streamflow in the past. Therefore the final multi-criteria calibration of HBV-light for all 49 glacierized headwater catchments attempted to incorporate all available observational information and was applied over the whole simulation period (1901-1-1 to 2006-12-31) based on the following **weighted objective function** for the glacierized headwater catchments with streamflow observation records:

$$R = 0.20 \cdot R_{Q1} + 0.15 \cdot R_{Q2} + 0.15 \cdot R_{Q3} + 0.15 \cdot R_{SWE} + 0.10 \cdot R_{SCA} + 0.25 \cdot R_G \quad (5.2)$$

and for the ungauged glacierized headwater catchments (without streamflow observations) :

$$R = 0.30 \cdot R_{SWE} + 0.20 \cdot R_{SCA} + 0.50 \cdot R_G \quad (5.3)$$

where

- $R$  Weighted objective function used for parameter optimisation
- $R_{Q1}$  Lindstrom measure (streamflow simulation)
- $R_{Q2}$  Nash-Sutcliffe Efficiency of logarithmic flow (streamflow simulation)
- $R_{Q3}$  Seasonal Nash-Sutcliffe Efficiency for flows from Jun-1 to Sep-30 (streamflow simulation)
- $R_{SWE}$  Performance criterion (MAE) for the simulation of SWE (mean 2000–2500 m a.s.l.)
- $R_{SCA}$  Performance criterion (RMSE) for the simulation of SCA
- $R_G$  Performance criterion for the simulation of glacier volume change

where for all criteria  $R$  the optimum (perfect fit) value = 1

The weights in equation (5.2) and (5.3) respectively were defined in a qualitative assessment through an iterative process including several test simulations with different calibration settings and weights.

A **genetic parameter optimisation algorithm** was applied for the calibration of each catchment using the GAP-tool implemented in HBV-light (see Seibert, 2000). For the final model parameterisation 10 calibrations, with about 3000 model runs each, were realised. Firstly, all 24 catchments with streamflow observation records were calibrated according to equation (5.2). Based on the resulting best parameter sets for those catchments, a **parameter transfer** approach was developed for the remaining 25 ungauged glacierized headwater catchments. For each ungauged catchment the most similar gauged catchment was identified based on several available catchment characteristics. Whereas all HBV model parameters linked to runoff generation processes were then directly taken from the most similar gauged catchment (i.e., fixed to the calibrated parameter values of the most similar gauged catchment), HBV model parameters relevant for snow and glacier simulation were identified using a multi-criteria calibration according to equation (5.3). For this partial parameter calibration the effective parameter ranges were restricted to the range of optimum values from the calibration of all gauged catchments. Again, 10 calibrations, with about 3000 model runs each, were realised. For each of the 49 glacierized headwater catchments the best model parameter set, i.e. the one with the highest value of  $R$ , was used to generate the final streamflow component series to be passed on to the LARSIM-Hochrhein model.

Table 5.2: Summary of HBV-light model performance results including all objective functions applied in model calibration (bold font) as well as additional objective functions (not incorporated in model calibration) for the 24 glacierized headwater catchments for which streamflow observation records were available; optimum value for all objective functions would equal 1.0.

Catchment ID	1100	1201	1300	1401	1501	1502	1701	2000	2101	2201	2400	2401	2502	2600	3001	3202	3301	3302	3602	3700	4202	4501	4601	4800
Glacier cover 1900 (%)	<b>43</b>	6	24	11	23	25	<b>38</b>	6	11	30	12	<b>32</b>	26	29	5	16	9	13	11	<b>32</b>	3	19	8	12
Sum Qsim	1879	1456	1383	1492	1530	1805	2224	1719	1356	2318	1702	2042	2389	2051	1477	2065	1542	1453	1587	1835	968	1397	1323	1654
Sum Qobs	1899	1488	1111	1638	1523	1883	2200	1723	1273	2442	1828	2027	2642	2001	1615	2151	1525	1410	1609	1964	921	1568	1299	1740
Sum P (Precipitation)	1919	1697	1643	1637	1769	1922	2295	2034	1640	2633	2059	2143	2485	2204	1676	2283	1724	1651	1839	2017	1295	1540	1597	1968
Sum AET	118	229	102	145	142	153	114	<b>301</b>	268	136	151	103	142	120	178	100	172	181	153	108	220	142	204	128
Sum PET	367	430	363	430	410	426	365	<b>525</b>	473	378	370	337	389	354	410	334	398	386	377	355	415	420	434	363
Sum Qobs- SumQsim	20	32	-273	146	-8	79	-24	4	-83	124	125	-15	<b>253</b>	-51	138	86	-17	-44	21	130	-47	172	-25	86
Mean difference* -". (% of Qobs)	1	2	-25	9	-1	4	-1	0	-7	5	7	-1	10	-3	9	4	-1	-3	1	7	-5	11	-2	5
Mean difference*	-35	-32	-281	119	-31	64	43	-4	-135	60	110	-40	179	-57	82	75	45	-8	136	95	-47	168	11	54
<b>R</b>	0.85	0.86	0.79	0.84	0.86	0.84	0.83	0.83	0.76	0.85	0.83	0.87	0.80	0.84	0.88	0.79	0.84	0.79	0.79	0.82	0.77	0.80	0.81	0.83
<b>R<sub>Q1</sub> (Lindstrom)</b>	0.89	0.91	0.80	0.85	0.88	0.87	0.84	0.85	0.72	0.85	0.77	0.89	0.74	0.84	0.88	0.74	0.80	0.69	0.79	0.81	0.78	0.83	0.82	0.81
<b>R<sub>Q2</sub> (Eff. ln(Q))</b>	0.89	0.89	0.82	0.91	0.92	0.82	0.90	0.86	0.78	0.89	0.87	0.93	0.89	0.90	0.89	0.81	0.84	0.86	0.75	0.85	0.75	0.88	0.83	0.86
<b>R<sub>Q3</sub> (seasonal)</b>	0.71	0.81	0.50	0.63	0.69	0.70	0.50	0.68	0.59	0.65	0.56	0.65	0.42	0.52	0.79	0.57	0.68	0.55	0.59	0.69	0.62	0.46	0.49	0.57
Nash-Sutcliffe Efficiency	0.89	0.91	0.83	0.86	0.89	0.87	0.84	0.85	0.73	0.86	0.78	0.89	0.75	0.84	0.88	0.75	0.80	0.69	0.80	0.82	0.78	0.84	0.82	0.81
Volume error	0.98	0.98	0.75	0.93	0.98	0.97	0.98	1.00	0.89	0.98	0.94	0.98	0.93	0.97	0.95	0.97	0.97	0.99	0.92	0.95	0.95	0.89	0.99	0.97
MARE Measure	0.63	0.67	0.28	0.74	0.75	0.70	0.66	0.76	0.65	0.62	0.75	0.75	0.70	0.69	0.69	0.57	0.71	0.68	0.56	0.63	0.69	0.72	0.69	0.69
R <sub>SCA</sub>	0.85	0.84	0.84	0.84	0.86	0.88	0.87	0.85	0.85	0.86	0.88	0.86	0.87	0.88	0.88	0.84	0.86	0.85	0.82	0.81	0.85	0.84	0.86	0.86
R <sub>SWE</sub>	0.65	0.58	0.65	0.69	0.70	0.68	0.76	0.63	0.50	0.74	0.80	0.77	0.79	0.79	0.88	0.66	0.79	0.74	0.67	0.65	0.52	0.63	0.72	0.78
<b>R<sub>G</sub></b>	1.00	1.00	1.00	1.00	1.00	1.00	1.00	1.00	1.00	1.00	1.00	1.00	1.00	1.00	0.99	1.00	1.00	1.00	1.00	1.00	1.00	1.00	1.00	1.00

\* Mean difference:  $365/n \cdot \sum (Qobs-Qsim)$ ; n: number of days

The 10 parameter sets resulting from the multiple calibrations for each of the glacierized headwater catchments represent one part of the uncertainty analysis (see Chapter 7). The objective functions obtained for the 24 headwater catchments with streamflow records, which are summarized in Table 5.2, are particularly indicative for an assessment of the model performance. Whereas, as expected, some differences among the catchments and among different variables (or corresponding objective functions) may be noted, overall, the simulation results are in a reasonable range with respect to the project objective. Consequently it can be stated, that the version of the HBV-light model with all described enhancements used by the project enabled an adequate representation of all, streamflow, snowpack, and glacier changes, as required for the purpose of the project.

### 5.5 Modelled components of streamflow (1901–2006)

Figure 5.10 shows the mean streamflow components (1901–2006) from all glacierized headwater catchments as modelled by HBV-light. The Figures 5.11 and 5.12 specifically illustrate the magnitude of the mean ice melt component of streamflow  $Q_I$  stemming from the individual catchments. As expected, the largest contributions of  $Q_I$  are found in the catchment of the Aare River and adjacent catchments with considerable glacier coverages. In contrast,  $Q_I$  contributions from rather sparsely glacierized headwater catchments in the eastern part of the basin (Alpine Rhine basin) seem to be of minor relevance. Overall, the modelling resulted in a mean streamflow from all glacierized headwater catchments over the simulation period (1901–2006) amounting to  $218 \text{ m}^3/\text{s}$  with fractions of  $Q_S = 56\%$  and  $Q_I = 8\%$  (Table 5.3).

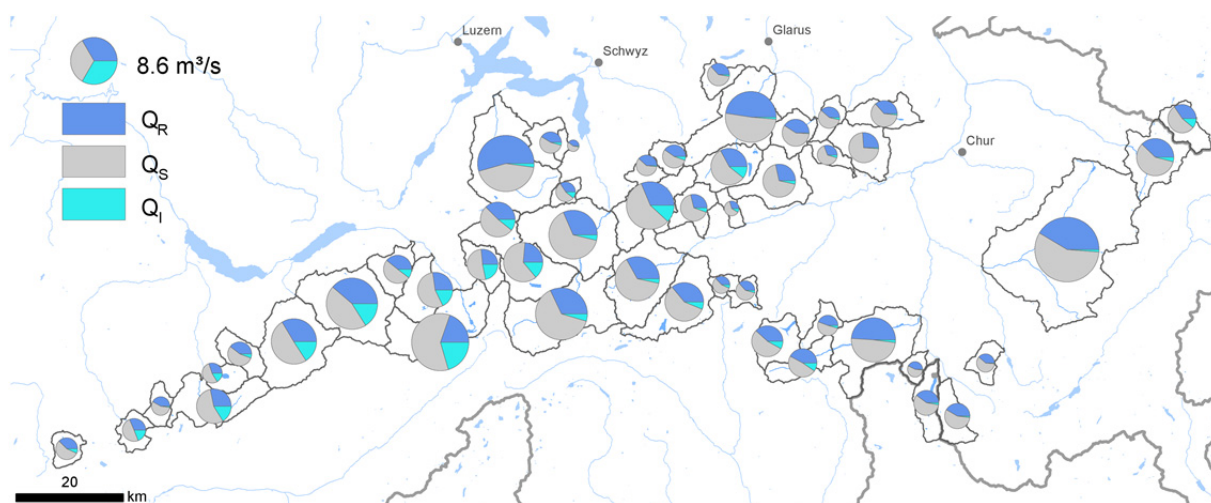


Figure 5.10: Mean of modelled streamflow (pie size) and its components  $Q_R$ ,  $Q_S$ ,  $Q_I$  in the individual glacierized headwater catchments over the simulation period 1901–2006.

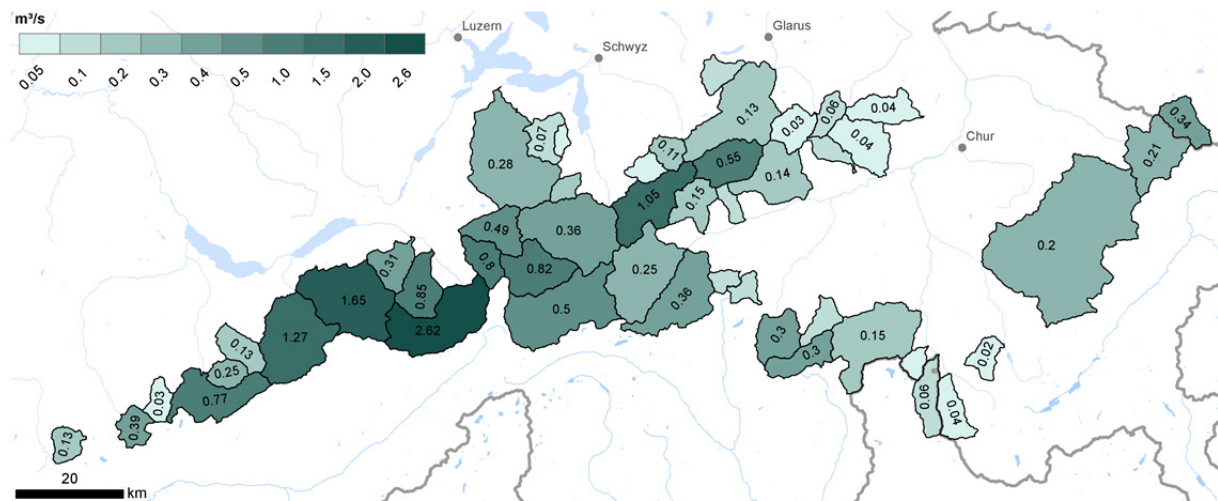


Figure 5.11: Mean of the modelled ice melt component of streamflow  $Q_i$  (in  $m^3/s$ ) in the individual glacierized headwater catchments for the simulation period 1901–2006.

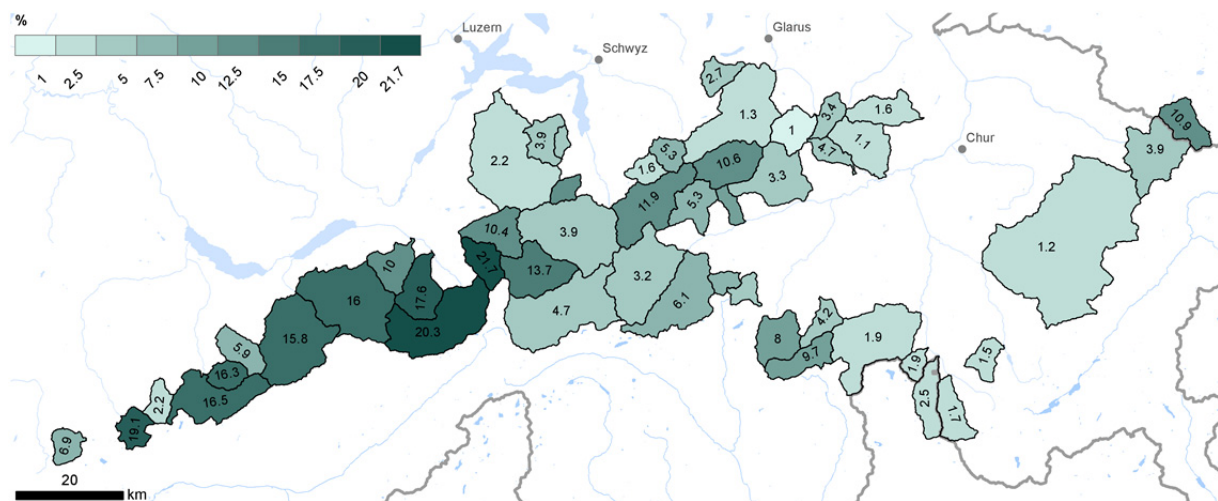


Figure 5.12: Mean fraction of the modelled ice melt component of streamflow  $Q_i$  (percentage of total streamflow) in the individual glacierized headwater catchments for the simulation period 1901–2006.

Table 5.3: Mean of the modelled components of streamflow (1901–2006) from all glacierized headwater catchments.

	$m^3/s$	mm/year	%
$Q_{sim}$	217.9	1655	
$Q_R$	78.7	598	36.1
$Q_S$	122.3	929	56.1
$Q_i$	16.9	128	7.8

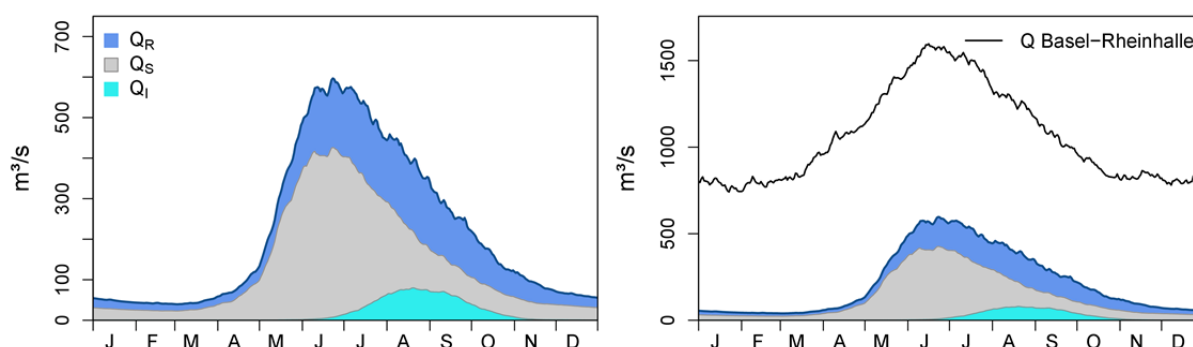


Figure 5.13: Modelling results for the streamflow components  $Q_R$ ,  $Q_S$ ,  $Q_I$  from all glacierized headwater catchments (see Figure 5.1). Left: hydrological regime (daily means 1901–2006). Right: the same illustration with the regime (daily means 1901–2006) at the River Rhine's gauging station in Basel ( $Q_{obs}$  data) for comparison.

As displayed in the long-term regime of the streamflow components (mean values for all days of the year in Figure 5.13), the snowmelt component of streamflow  $Q_S$  from the glacierized headwater is largest in June, whereas the ice melt component  $Q_I$  peaks in August. However, it should be noted that mean  $Q_I$  in September yields comparable amounts and, due to the decrease of total streamflow, even higher relative fractions. Over the period from November to June only marginal fractions of the  $Q_I$  component are present in the headwaters' streamflow. The regime of the observed streamflow at the gauge Basel (Rhine) in Figure 5.13 visualises the scale of the modelled streamflow components from the glacierized headwaters, and in particular the contribution of  $Q_I$ , in contrast to the average total flow of the River Rhine.

The mean annual streamflow components in the period 1901–2006 (Figure 5.14) show large intra-annual variations, yet distinct long-term trends are not evident. The mean of the streamflow components in the summer months June to August (Figure 5.14b) amount to:  $Q_S$ : 59%,  $Q_I$ : 8%, while averaging of the streamflow components for the months July to September yields a slightly larger fraction of  $Q_I$ , with  $Q_S$ : 47% and  $Q_I$ : 10%.

In individual years the streamflow components can differ significantly from the mean values, as is expressed in the range of the extreme (minimum and maximum) monthly mean values in Table 5.4. According to the ranges, the monthly mean fraction of  $Q_I$  reached a maximum of 63% (October 1921 compared to a mean fraction of  $Q_I$  in October of 13%). The lowest monthly mean fractions of  $Q_S$ , around 14%, were modelled for the months October, September, and August, thus in a period after the alpine snowmelt and during the dominating ice melt season. The mean fractions of  $Q_S$  in these months are considerably higher with values between 30 and 38%. The peak of the fraction of  $Q_S$  occurs in May with a mean and a maximum monthly fraction of 75.3% and 91.3% respectively. However, the fractions of  $Q_S$  for April and June are close to the values obtained for May.

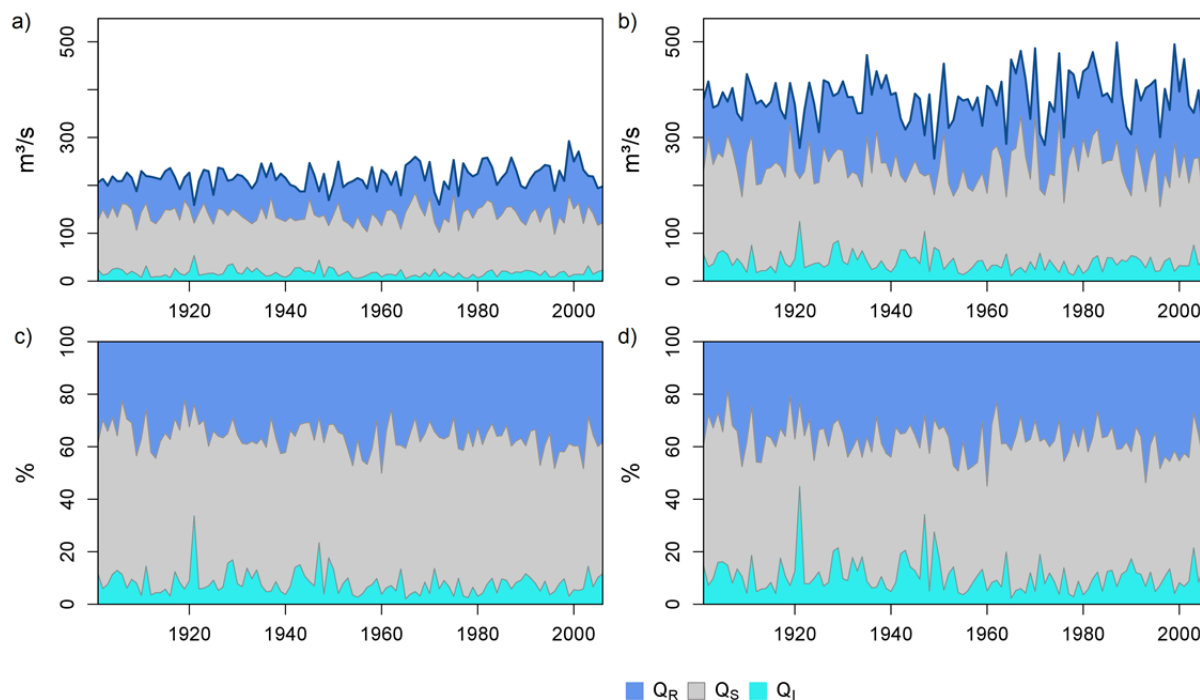


Figure 5.14: Modelled streamflow components  $Q_R$ ,  $Q_S$ ,  $Q_I$  from all glacierized headwater catchments (see Figure 5.1): a) annual means of the years 1901–2006, b) mean values of summer months (Jun, Jul, Aug) of the years 1901–2006, c) annual means of the years 1901–2006 as percentages of total streamflow, d) mean values of summer months (Jun, Jul, Aug) of the years 1901–2006 as percentages of total streamflow.

Table 5.4: Mean, minimum, and maximum monthly mean values (1901–2006) of modelled streamflow and its components from all glacierized headwater catchments.

		Jan	Feb	Mar	Apr	May	Jun	Jul	Aug	Sep	Oct	Nov	Dec
$Q$ [ $m^3/s$ ]	Mean	48.8	41.8	45.1	86.0	306.3	558.1	521.7	403.9	274.1	161.7	93.1	62.6
	Min	32.9	28.6	25.5	34.2	92.1	266.1	294.5	244.6	136.7	88.0	55.2	40.8
	Max	72.4	70.1	93.3	268.7	619.2	839.2	905.8	603.0	391.3	263.9	225.1	104.8
$Q_R$ [ $m^3/s$ ]	Mean	21.0	17.9	17.3	24.6	71.1	152.0	173.1	172.3	132.4	82.5	48.2	28.0
	Min	12.7	10.6	9.5	8.4	19.4	55.0	74.1	60.8	33.8	22.4	22.2	14.4
	Max	44.5	39.9	50.3	53.4	162.2	297.6	349.3	325.1	278.8	207.1	192.0	72.8
$Q_R$ [% of $Q$ ]	Mean	42.8	42.4	38.7	29.9	24.5	27.7	33.8	42.3	47.9	49.6	49.9	44.2
	Min	32.1	32.3	21.8	8.8	8.6	11.1	12.7	14.3	14.6	12.6	23.7	31.7
	Max	61.5	61.3	59.7	54.3	54.9	48.6	58.0	72.3	76.3	78.8	85.3	69.5
$Q_S$ [ $m^3/s$ ]	Mean	27.5	23.7	27.7	61.3	234.6	400.6	313.0	157.9	81.0	57.8	42.2	34.2
	Min	16.3	13.0	12.7	22.7	50.7	156.2	109.9	46.6	39.8	24.8	26.0	22.4
	Max	38.0	36.0	60.1	220.9	501.4	696.9	661.4	435.5	191.2	108.0	76.3	47.8
$Q_S$ [% of $Q$ ]	Mean	56.8	57.2	61.1	70.0	75.3	71.2	58.4	38.4	29.7	36.9	47.0	55.1
	Min	38.4	38.2	39.9	45.6	45.0	50.0	31.2	14.0	14.0	13.7	14.4	30.0
	Max	67.7	67.5	77.9	91.0	91.3	87.8	83.4	75.3	56.9	61.7	70.4	68.1
$Q_I$ [ $m^3/s$ ]	Mean	0.2	0.2	0.1	0.1	0.5	5.5	35.5	73.7	60.7	21.5	2.7	0.5
	Min	0.1	0.0	0.0	0.0	0.0	0.1	2.1	19.3	4.8	1.5	0.2	0.1
	Max	0.8	0.6	0.4	0.4	5.8	37.2	164.5	195.4	179.2	112.0	15.8	2.6
$Q_I$ [% of $Q$ ]	Mean	0.5	0.4	0.3	0.1	0.2	1.1	7.8	19.3	22.4	13.5	3.1	0.8
	Min	0.1	0.1	0.0	0.0	0.0	0.0	0.3	3.6	1.7	1.0	0.3	0.1
	Max	2.5	2.0	1.4	0.6	2.4	14.0	46.7	57.4	58.8	63.0	18.7	4.5

## 5.6 Modelled streamflow components in selected extreme years

The analysis of mean values (1901–2006) of the modelled streamflow components in the previous section confirm the generally relatively minor contributions of glacier ice melt to total streamflow similar to results found in (simple) water balancing exercises. In contrast, the perception that the ice melt component was of special relevance for the Rhine’s flow in historical low flow periods represents a widely spread hypothesis that matters particularly in the context of assessing the potential impacts of ongoing glacier retreat on future low flow events in the Rhine. Hence, the project aimed especially at the quantification of the range of extreme (maximum) fractions of  $Q_I$  during past low flow events of the Rhine. Consequently, the modelling results were analysed concerning the following questions:

- i) Which years and months in the period 1901–2006 were extreme in terms of low streamflows, negative glacier mass balances, and high values of the component  $Q_I$  at the scale of the glacierized headwater catchments (“headwater catchment scale“)?
- ii) What was the magnitude of the streamflow components (and particularly the ice melt component  $Q_I$ ) from the glacierized headwater catchments in specific years/periods which are selected as reference years/periods due to the occurrence of extreme low flow events at the scale of the entire Rhine basin (“downstream-perspective“)?

### 5.6.1 Extreme years and months at the scale of the glacierized headwater catchments

The maps below present the years (out of all years in the simulation period 1901–2006) for which the lowest streamflow (Figure 5.15), the largest ice melt component of streamflow  $Q_I$  (Figure 5.16), and the most negative glacier mass balance (Figure 5.17) in the glacierized headwater catchments were obtained. All three maps indicate a fairly consistent picture mostly dominated by few exceptional years across the headwater catchments. The two years (and also hydrological years), 1947 and 1921, are both characterized by intense glacier melt, thus heavily negative glacier mass balances, and large contributions of the  $Q_I$  component (Figures 5.16 and 5.17). Particularly in 1921 high relative fractions of  $Q_I$  were reached, since it is also the year with the lowest total streamflow in many catchments. For about half the catchments even lower total streamflow was simulated for 1972 (Figure 5.15). The more recent hydrologically extreme year of 2003 appears only on the map of the most negative glacier mass balances in single catchments at the western edge of the study area (Figure 5.17).

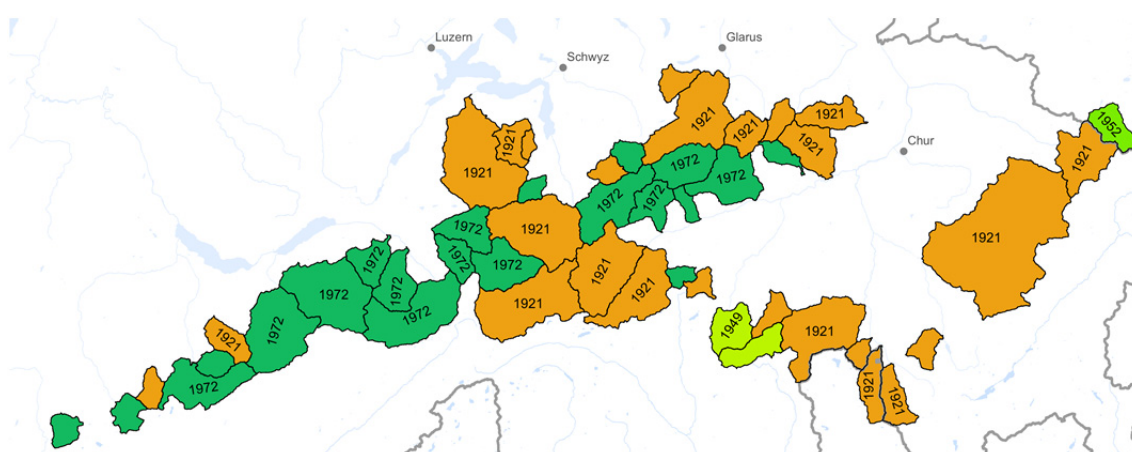


Figure 5.15: Year in the period 1901–2006 for which the lowest (mean annual) streamflow for each glacierized headwater catchment was modelled.

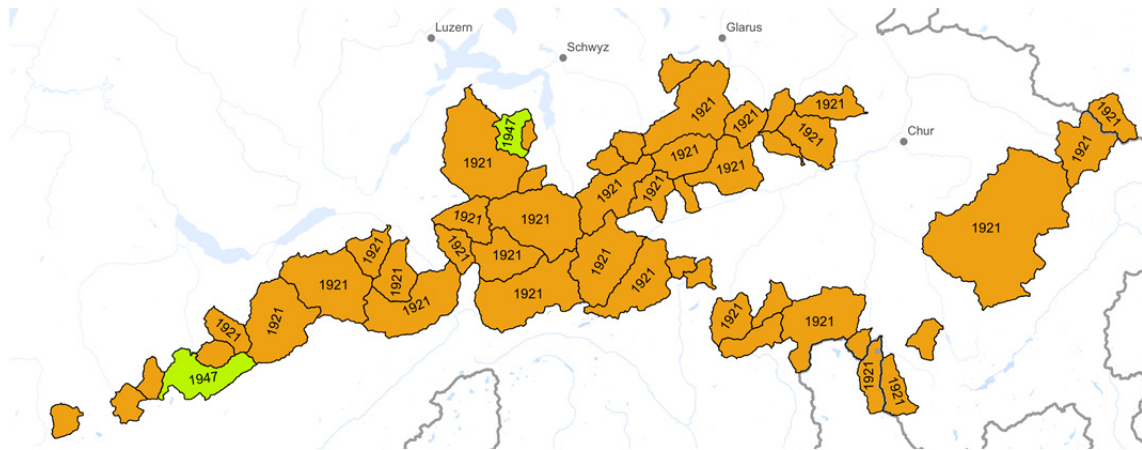


Figure 5.16: Year in the period 1901–2006 for which the largest ice melt component of streamflow  $Q_1$  (maximum annual mean of  $Q_1$  in  $m^3/s$ ) for each glacierized headwater catchment was modelled; the (here not shown) year, which resulted in the largest relative fraction of the ice melt component of streamflow  $Q_1$  (maximum annual mean of  $Q_1$  as percentage of  $Q$ ), is the year of 1921 for all glacierized headwater catchments.

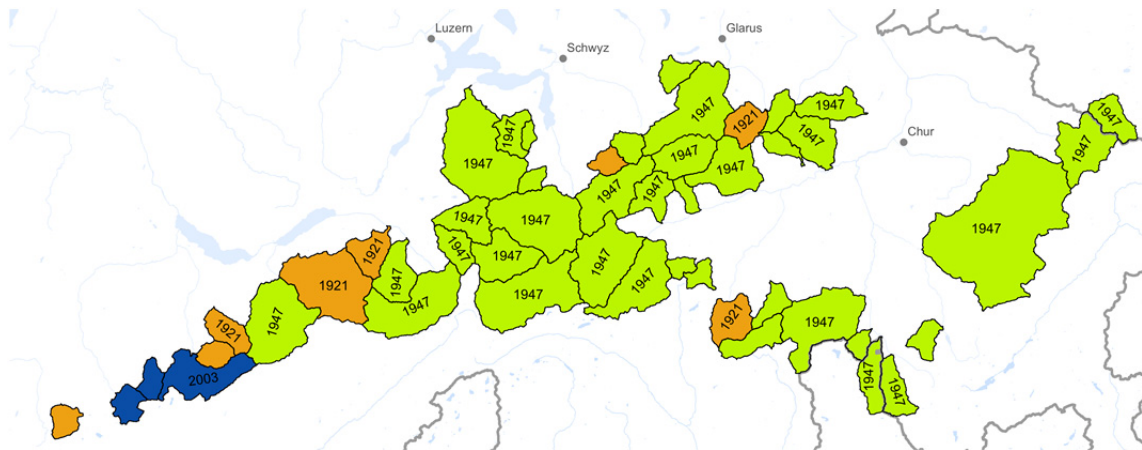


Figure 5.17: Hydrological year (Swiss definition: Oct to Sep) in the hydrological years 1902–2006 for which the most negative glacier mass balance for each glacierized headwater catchment was modelled.

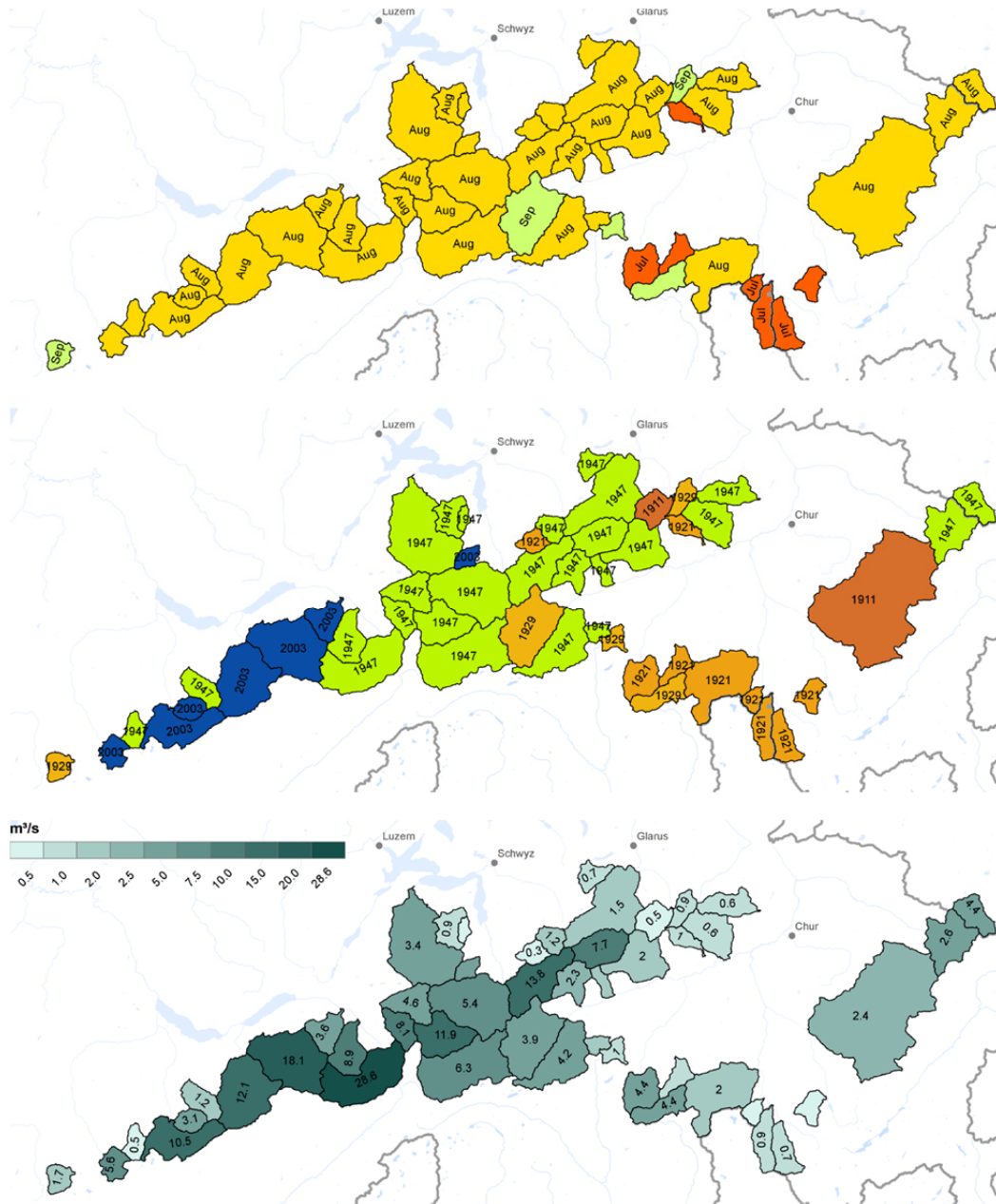


Figure 5.18: Maximum monthly mean of modelled  $Q_1$  of all months in 1901–2006 for each glacierized head-water catchment: month and year of occurrence (top and centre graph respectively) and  $Q_1$  value in  $m^3/s$  (bottom graph).

To discuss the quantitative modelling results, for instance the analysis of the mean  $Q_1$  values of all months in 1901–2006 (Figures 5.18 and 5.19), it is essential to differentiate in terms of absolute amounts of streamflow components versus their relative fractions (in %) given the latter's dependence on the dynamics of total streamflow. For most of the catchments the largest monthly means of  $Q_1$  (in  $m^3/s$ ) shown in Figure 5.18 was modelled for an August (either August 1921 or August 1947), whereas the largest monthly means of the relative fractions of  $Q_1$  (in % of  $Q_{sim}$ ), shown in Figure 5.19, were found mainly in September and October (again mostly in the years of 1921 and 1947). Hence, considering the underlying distinct seasonal pattern of alpine streamflow (Figure 5.5), the maxima of absolute  $Q_1$  correspond temporally to the innerannual peak of alpine streamflow, while the maxima of the

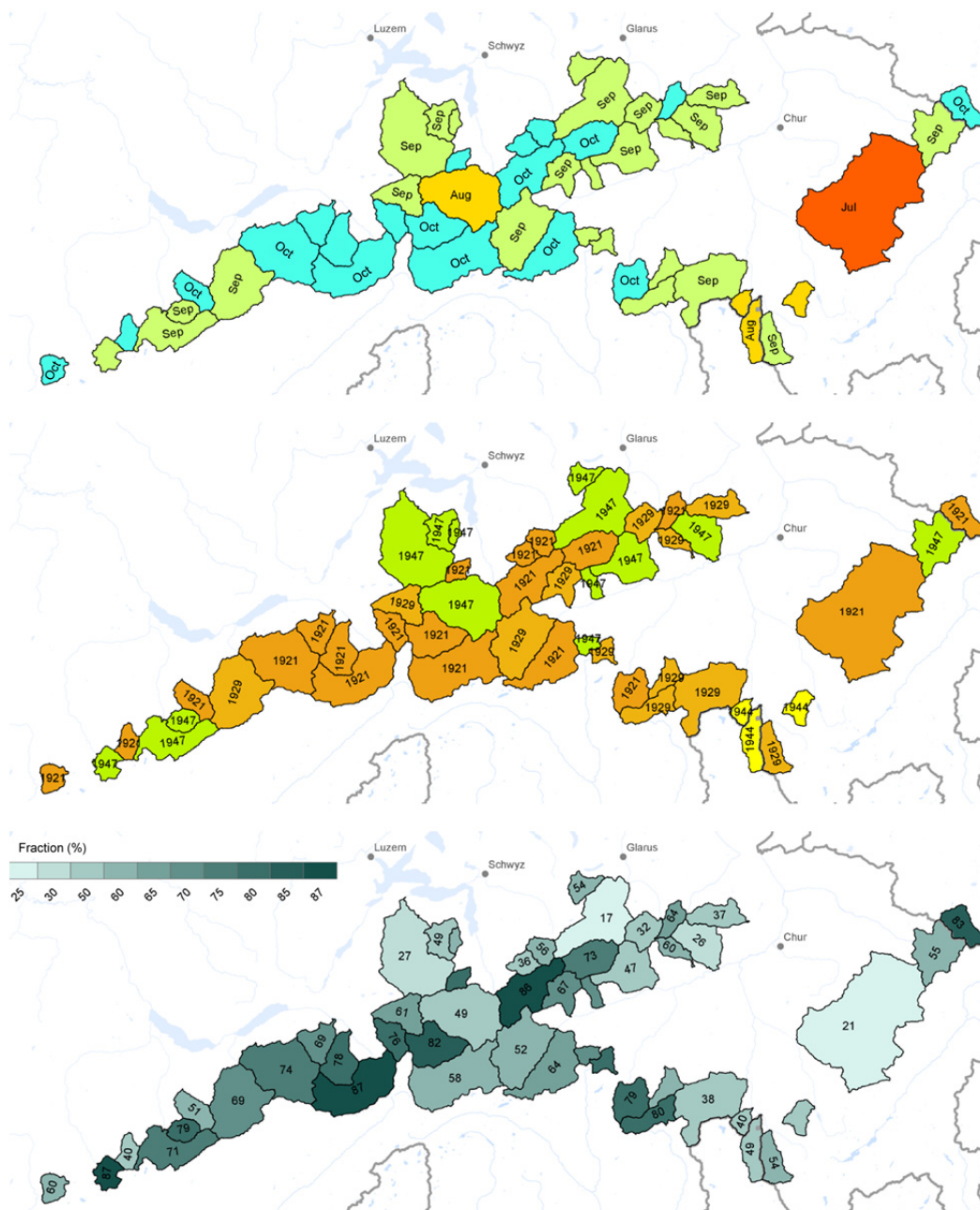


Figure 5.19: Maximum monthly mean of the modelled relative fraction of  $Q_1$  (as percentage of  $Q$ ) of all months in 1901–2006 for each glacierized headwater catchment: month and year of occurrence (top and centre graph respectively) and  $Q_1$  value in % $Q$ s (bottom graph).

$Q_1$  fractions coincide with the subsequent phase of receding streamflow. With regard to typical low flow events along the River Rhine the latter may be of even higher relevance (see also Chapter 6).

Among the “Top Ten“ months with the largest  $Q_1$  (based on monthly means) in the period 1901–2006 (Table 5.5) the recent past is only represented by August 2003 and August 2005, while all other listed most extreme months date back to the period prior to 1951. Particularly, the largest mean monthly relative fractions of  $Q_1$  (right column in Table 5.5) are closely linked to the occurrence of known historical drought and low flow years affecting Switzerland and adjacent regions.

Table 5.5: Ranking of the ten largest monthly mean modelled  $Q_i$  by absolute values in  $m^3/s$  and by relative fractions (in brackets in %), for 1901–2006, aggregated from all glacierized headwater catchments.

Ranking by absolute magnitude of $Q_i$			Ranking by relative fraction of $Q_i$				
Month	$Q_{sim}$	$Q_i$	$Q_s$	Monat	$Q_{sim}$	$Q_i$	$Q_s$
Aug 1947	340.5	195.4 (57.4)	72.7 (21.4)	Oct 1921	177.8	112.0 (63.0)	43.4 (24.4)
Aug 2003	349.7	179.3 (51.3)	85.8 (24.5)	Sep 1947	225.5	132.5 (58.8)	55.8 (24.7)
Sep 1929	307.3	179.2 (58.3)	75.5 (24.6)	Sep 1929	307.3	179.2 (58.3)	75.5 (24.6)
Aug 1911	416.0	164.9 (39.6)	184.6 (44.4)	Aug 1947	340.5	195.4 (57.4)	72.7 (21.4)
Aug 1928	406.1	164.8 (40.6)	109.4 (26.9)	Sep 1921	258.4	147.5 (57.1)	50.0 (19.3)
Jul 1921	352.2	164.5 (46.7)	109.9 (31.2)	Aug 2003	349.7	179.3 (51.3)	85.8 (24.5)
Aug 1921	335.1	161.1 (48.1)	86.6 (25.8)	Sep 1949	232.2	114.0 (49.1)	54.5 (23.5)
Sep 1932	350.4	152.1 (43.4)	78.3 (22.3)	Aug 1921	335.1	161.1 (48.1)	86.6 (25.8)
Sep 1921	258.4	147.5 (57.1)	50.0 (19.3)	Jul 1921	352.2	164.5 (46.7)	109.9 (31.2)
Aug 2005	479.3	146.6 (30.6)	112.5 (23.5)	Oct 1949	145.5	66.1 (45.4)	38.5 (26.5)

### 5.6.2 Modelled streamflow components in selected Rhine low flow years

Based on the analysis of discharge records from gauges at the Middle Rhine (Figure 5.20) the years of 1921, 1947, 1976, and 2003 were selected for a detailed assessment as reference years for low flow events. All these years are well-known as major historical European drought and low flow years and have already been investigated by numerous studies.

According to Grunow (1931, 1935) the **year 1921** was characterized by an exceptional meteorological drought peaking in July across Central Europe and even the entire continent (see also Briffa et al., 1994). Unusually dry conditions already dominated during October and November 1920 brought about by an anticyclone over Eastern Europe particularly for the alpine region. The resulting below average streamflow in the early autumn of 1920 contributed to the development of the extreme low flow conditions in 1921. Very mild winter temperatures often constrained the formation of a continuous seasonal snow cover. In fact, Swiss mean temperatures for January were the warmest on record at the time (recordings began in 1864) (Grunow, 1935). For the German Rhine basin Sassenfeld (1923) highlighted particularly the spring low flow conditions as being “unprecedented”. In Switzerland precipitation deficits up to 25% in spring were registered (Schorer, 1992). Linked to an atmospheric ridge from the North Atlantic Ocean (Azores High) this spring drought was followed by a hot summer in Central Europe (Grunow, 1931). According to a study of droughts at the European scale in the period 1892–1991 by Briffa et al. (1994), the drought of 1921 was a notable event not only because it is by far the most extreme when considering the spatial extent of severe drought conditions but also because its isolated occurrence during a sequence of nearly 3 decades of either normal or wet years.

Schorer (1992) provided a detailed study of the drought in the **year 1947** for Switzerland. The drought of 1947 has been considered as the climax of the so-called Central-European climatic optimum during a period from ca. 1940 to 1953. Schorer (1992) refers to it as “the exceptional drought disaster of the 20<sup>th</sup> century”. However, his rating appears to be less the result of the meteorological and hydrological extremes, but might be ascribed largely to the enormous impacts and damages of this event in the specific context of the post-war situation and following the “Hungerwinter of 1946/47” (see also Bundesrat, 1947). Schorer (1992) states the drought development in 1947 is mainly the result of long, persistent dry and warm spells, while discrete record-setting extremes (precipitation deficits or temperatures) on a short-term basis were less of an issue. According to the definition of drought intensity by

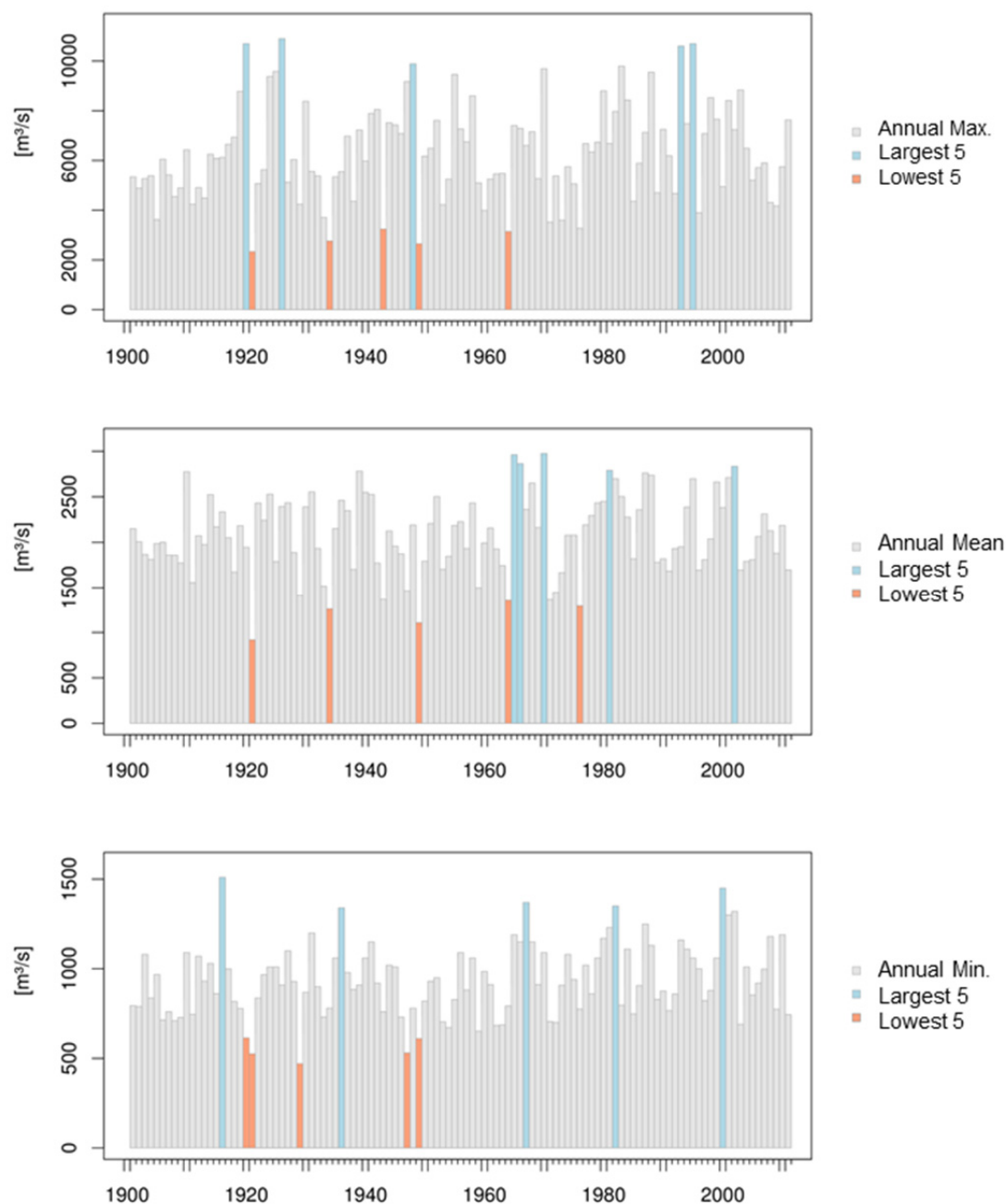


Figure 5.20: Annual maxima, means, and minima of the Rhine's streamflow at the gauging station in Cologne in the years 1901–2011 (streamflow observation record).

Pfister & Rutishauser (2000) the event of 1947 constitutes the most intense drought in the Swiss Plateau (Mittelland) for the period 1864–1995. Generally, regional differences are important for the understanding of drought propagation in 1947. Overall, the precipitation deficits affected the alpine areas, at least partially, slightly less than regions further to the north. Especially the Swiss Plateau and the region around Basel were affected by the precipitation deficits. In fact, the most severe deficits over the growing season and the largest impacts on surface water bodies in Switzerland were recorded there. In contrast, when focusing on the positive temperature anomalies, prevailing from April to October 1947 all over Switzerland, the alpine region was exposed to particularly large anomalies. This led to intensified snow and glacier melt and thus augmented streamflow, which, according to Schorer (1992), clearly had a larger effect on the mitigation of low flows than the regional contrasts in precipi-

tation deficits. Therefore, a considerable rise of the zero-degree isotherm is crucial: by exploring data series from representative alpine climate stations (station Grd. St. Bernhard at 2476 m a.s.l., station Jungfrauoch at 3578 m a.s.l., and station Weissfluhjoch at 2667 m a.s.l.) Schorer (1992) detected that the melt season (period with temperatures above 0 °C) in 1947 was prolonged by up to 2 months compared to the long-term mean duration (1901–60). Accordingly, the year of 1947 is also known for the occurrence of extremely negative glacier mass balances in the European Alps (Huss, 2012, see also Figure 5.17).

The characteristics and impacts of the drought in the **year 1976** have been addressed in studies by Schorer (1992) and by Courvoisier et al. (1977) for Switzerland, by Gerhard et al. (1983) for the Rhine basin, in numerous publications for further regions in Western Europe (e.g., Brochet, 1977; Dornkamp et al, 1980), and also at the continental scale (e.g., Tallaksen & Stahl, 2015). As was the case in the droughts of 1921 and 1947, the evolution of the event in 1976 was associated with the presence of a persistent atmospheric ridge (blocking pattern) over Europe. In contrast to the prolonged period of positive temperature anomalies characterizing the event of 1947, a short but intense summer heat wave at the end of June/begin of July aggravated the drought situation in 1976. Schorer (1992), however, argues that the overall (accumulated) surplus of heat linked to the temperature anomalies in 1976 was comparatively small, particularly in the higher altitudes of the Alps and the Jura region. Moreover, the second half of the summer was even cooler than the long term mean (in 1901–1960). Switzerland, where abundant rainfall in the second half of July terminated the meteorological drought, was not as heavily impacted as other regions in Western Europe, yet it became an alarming event for the national energy sector after Swiss energy companies, due to their reduced hydropower production, had been forced to acquire energy on the European market in a situation of exceptionally high price levels resulting from drought-related impaired power production in other European countries (Schorer, 1992). Regarding the cumulative streamflow deficit, the situation in 1976 was more severe than 1947. However, the flow of the Rhine (at Basel) during 1976 never dropped to the extremely low level of autumn 1947 (see also annual means and minima in both years at the gauge in Cologne in Figure 5.20). Schorer (1992) attributes the different character of the 1976 event mainly to the fluctuating weather conditions and a lower relevance of increased temperatures and glacier melt contributions (in 1976 compared to 1947). At the northern rim of the Alps near-average temperatures from March to May in altitudes above 2500 m.a.sl., intense precipitation in July, the cool late summer period, and an early onset of the snow accumulation season in autumn led to an only moderately increased ablation of glaciers, although 1976 overall ended with a negative annual net mass balance. It may be concluded that 1976 stands out among the four selected Rhine low flow years (1921, 1947, 1976, and 2003) due to a different drought development but also as an example case for a drought and low flow year that was not associated with substantial summer heat surpluses and significantly increased runoff contributions from glacier melt.

The evolution, progression, and impacts of the combined drought and heat in the summer of **2003** have been treated in a large body of reports and academic work. For instance, the report by BUWAL, BWG and Meteo-Schweiz (2004) contains information relevant to the alpine headwater catchments, whereas the reports by BfG (2006) and ICPR (2004) deal with the 2003 event for the Rhine basin. In Switzerland streamflows in 2003 mostly receded to levels lower than those in 1976, but were less extreme than in 1947 (BUWAL/BWG/MeteoSchweiz, 2004). The same applies to the annual minima of the Rhine's flow shown for the gauge at Cologne in Figure 5.20. Similar to the low flow situation in 1947 the Swiss Plateau was most severely affected, whereas abnormally high flows were recorded due to increased glacier melt in alpine streams.

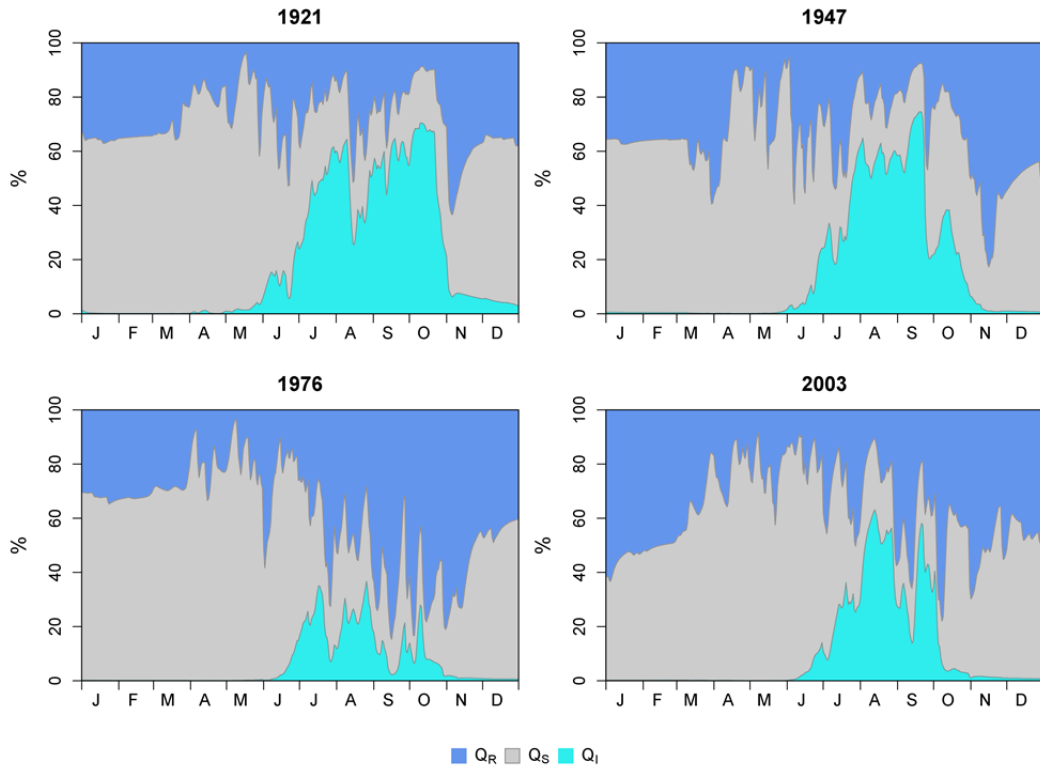


Figure 5.21: Fractions of the modelled streamflow components (percentage of total streamflow) from all glacierized headwater catchments (HBV-light model catchments, see Figure 5.1) for selected Rhine low flow years.

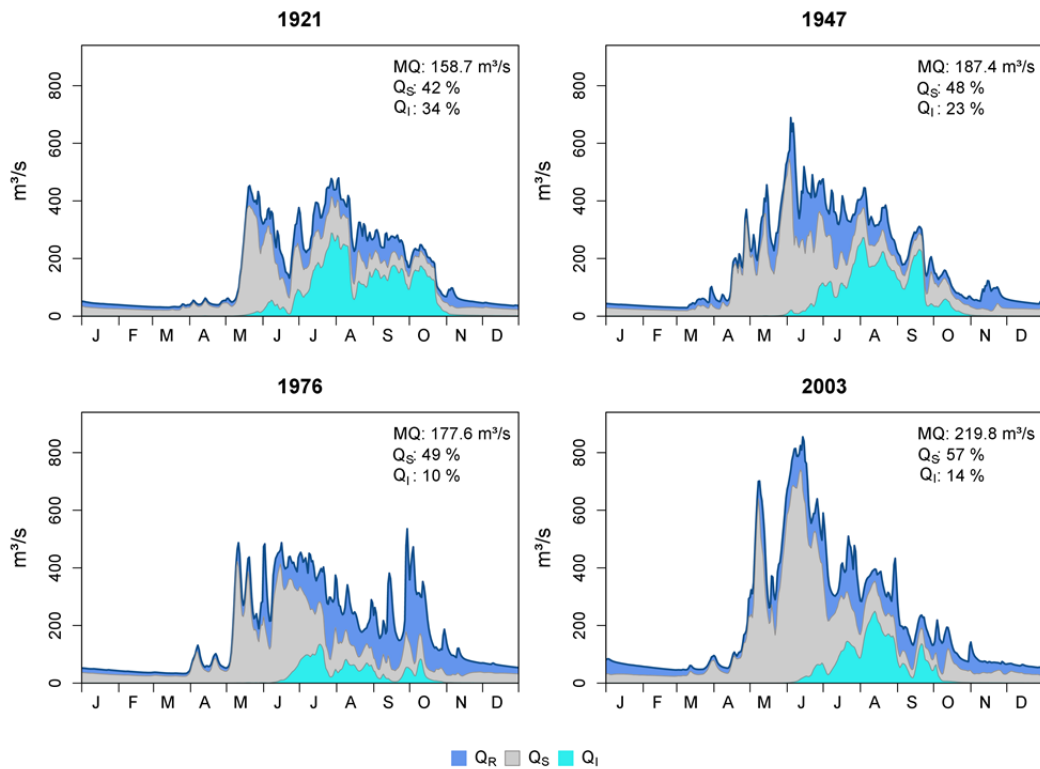


Figure 5.22: Modelled streamflow components from all glacierized headwater catchments (HBV-light model catchments, see Figure 5.1) for selected Rhine low flow years.

The modelled daily **components of the streamflow from the glacierized headwater catchments in the years 1921, 1947, 1976, and 2003** are shown in the Figures 5.21 and 5.22. Table 5.6 provides the corresponding mean streamflow components for all months in each of these years. In agreement with the brief characterisation of the years in the preceding paragraphs, a considerably smaller fraction of  $Q_I$  in 1976 compared to all three other years is clearly evident. In addition, the differing temporal dynamics and an earlier recovery and termination of low flow conditions in the autumn of 1976 are discernible in the modelling results. In contrast, for the other three years, 1921, 1947, and 2003, the magnitude of the ice melt component  $Q_I$  is remarkable. August of 1947 yielded the record of absolute monthly  $Q_I$  amounts (see Table 5.5). 1921, the year of the lowest mean flow of the simulation period not only had the highest relative fractions of modelled  $Q_I$  but also the largest annual totals of  $Q_I$  (in  $m^3/s$ ) of all the years in the simulation period.

Table 5.6: Monthly means of modelled streamflow and its components from all glacierized headwater catchments in selected Rhine low flow years, absolute values (in  $m^3/s$ ) and relative fractions of  $Q_{sim}$  (in %).

		Jan	Feb	Mar	Apr	May	Jun	Jul	Aug	Sep	Oct	Nov	Dec
1921	$Q_{sim}$	44.2	35.5	33.3	46.4	240.9	266.1	352.2	335.1	258.4	177.8	62.2	40.8
	$Q_R$	$m^3/s$ 35.7	12.4 34.8	10.2 30.7	8.4 18.1	40.0 16.6	72.8 27.3	77.8 22.1	87.4 26.1	60.9 23.6	22.4 12.6	30.4 48.8	14.4 35.4
	$Q_S$	$m^3/s$ 64	23.1 65.1	23.1 69.2	37.7 81.3	195.0 81	156.2 58.7	109.9 31.2	86.6 25.9	50.0 19.3	43.4 24.4	27.1 43.5	24.5 60.1
	$Q_I$	$m^3/s$ 0.3	0.0 0.1	0.0 0.1	0.2 0.5	5.8 2.4	37.2 14	164.5 46.7	161.1 48.1	147.5 57.1	112.0 63	4.8 7.7	1.8 4.5
1947	$Q_{sim}$	39.7	32.7	48.1	144.3	319.4	480.4	371.3	340.5	225.5	108.7	80.0	49.2
	$Q_R$	$m^3/s$ 36.4	11.7 35.8	21.0 43.6	25.8 17.9	70.5 22.1	163.9 34.1	127.4 34.3	72.4 21.3	37.2 16.5	25.8 23.8	52.5 65.7	23.9 48.5
	$Q_S$	$m^3/s$ 63.1	20.8 63.7	27.0 56.1	118.4 82	247.5 77.5	281.4 58.6	117.4 31.6	72.7 21.3	55.8 24.7	53.6 49.3	26.0 32.5	25.0 50.7
	$Q_I$	$m^3/s$ 0.5	0.2 0.5	0.1 0.2	0.1 0.1	1.4 0.4	35.1 7.3	126.5 34.1	195.4 57.4	132.5 58.8	29.3 27	1.5 1.8	0.4 0.9
1976	$Q_{sim}$	47.7	39.0	35.2	76.8	274.4	397.3	376.4	244.6	239.9	243	89.6	61.9
	$Q_R$	$m^3/s$ 32.1	12.6 32.4	10.0 28.5	14.8 19.2	46.4 16.9	100.2 25.2	145.6 38.7	113.1 46.2	158.8 66.2	165.8 68.2	57.6 64.2	27.3 44.1
	$Q_S$	$m^3/s$ 67.7	26.3 67.5	25.1 71.4	62.0 80.7	227.5 82.9	279.7 70.4	148.8 39.5	74.3 30.4	58.4 24.3	49.9 20.5	30.9 34.5	34.2 55.2
	$Q_I$	$m^3/s$ 0.2	0.1 0.2	0.0 0.1	0.0 0.1	0.5 0.2	17.4 4.4	82 21.8	57.2 23.4	22.7 9.5	27.3 11.2	1.1 1.2	0.4 0.7
2003	$Q_{sim}$	68.5	51.2	54.5	102.0	449.4	695.3	398.9	349.7	187.7	130.9	79.3	60.2
	$Q_R$	$m^3/s$ 56.1	25.8 50.4	18.3 33.7	20.1 19.7	97.8 21.8	113.6 16.3	136.6 34.3	84.6 24.2	78.1 41.6	65.4 49.9	42.8 54.0	27.0 44.8
	$Q_S$	$m^3/s$ 43.7	25.2 49.3	36.0 66.1	81.8 80.2	351.4 78.2	555.3 79.9	171.8 43.1	85.8 24.5	42.4 22.6	53.4 40.7	35.4 44.6	32.8 54.4
	$Q_I$	$m^3/s$ 0.3	0.1 0.3	0.1 0.2	0.1 0.1	0.2 0.0	26.3 3.8	90.4 22.7	179.3 51.3	67.2 35.8	12.2 9.3	1.1 1.4	0.5 0.9

Concerning the resulting streamflow components for 1921, especially the significant fractions of  $Q_I$  in October (monthly mean of 63% see Tables 5.5. and 5.6), already referred to in Section 5.6.1, and the seasonally very early emergence of the ice melt component of streamflow at the beginning of May are notable. However, a slightly earlier onset of the period with distinct fractions of  $Q_I$  (compared to the mean seasonal response pattern presented in Figure 5.13) is also found in 1947. This corresponds to the significant expansion of the alpine melt season in this year mentioned by Schorer (1992). Whereas in the Rhine low flow years 1921, 1947, and 1976, the total streamflow from the glacierized headwater catchments was below average, in 2003 it was slightly larger than the long-term annual mean (1901–2006). As in the years 1921 and 1947, the fractions of  $Q_I$  were considerable in August and September of 2003, yet, in contrast to the earlier drought years, they receded quickly and became minor early on in October (Figures 5.21/5.22 and Table 5.7).

## 5.7 Long-term behaviour of modelled streamflow components

Investigating long-term changes of the modelled streamflow components reveals interesting patterns. The modelled total streamflow from all glacierized headwater catchments shows a slight increase over the simulation period, and particularly during the most recent years. However, Figures 5.23, 5.24, and 5.25 demonstrate that the individual streamflow components are subject to different trends and variations.  $Q_R$  shows an increasing trend, while  $Q_S$  and  $Q_I$  seem to vary, with some phase delay, in opposing cycles of increasing and decreasing contributions within the investigated 20<sup>th</sup> century period. Herein, the known phases dominated by glacier retreat and the close to balanced conditions of the glaciers in the European Alps from the 1960s into the 1980s are reflected in  $Q_I$  by positive anomalies and negative anomalies respectively. The overall positive trend of total streamflow might be attributed to the increase of  $Q_R$  rather than to any positive trend of  $Q_I$ . This attribution corresponds to the findings of the study by Belz et al. (2007) about shifts in the hydrological regime of the Rhine and its tributaries in the 20<sup>th</sup> century. They inferred an increasing influence of pluvial elements on the alpine Rhine's regimes, caused by warming yet also due to trends in precipitation (regarding annual totals and particularly winter precipitation sums), and an only minor impact of glacier retreat on the dynamics of mean streamflow beyond the uppermost glacierized headwaters of the basin. Belz et al. (2007) related the detected increase of precipitation in the course of the 20<sup>th</sup> century to modifications of atmospheric circulations patterns and the frequencies of certain large-scale weather conditions.

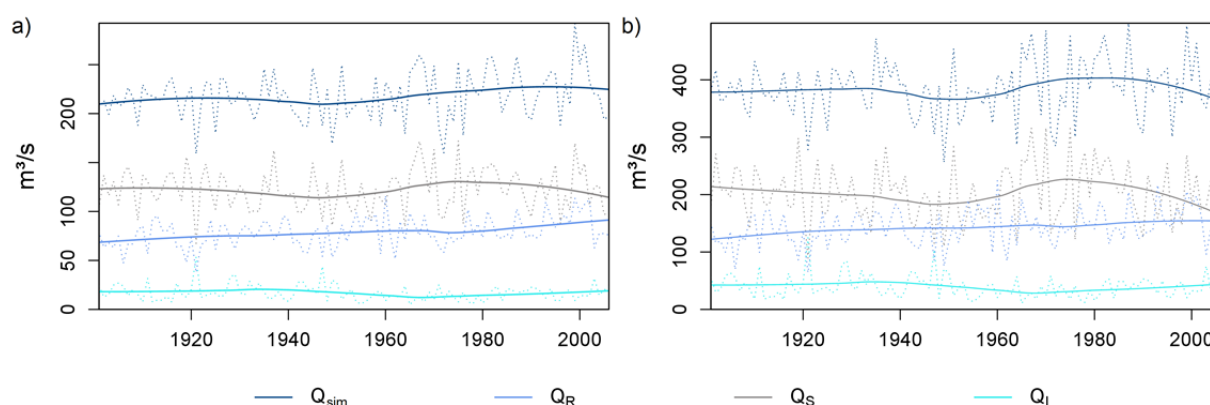


Figure 5.23: Long-term behaviour of modelled total streamflow and its components  $Q_R$ ,  $Q_S$ , and  $Q_I$  from all glacierized headwater catchments. Left: annual means. Right: mean values of summer months (Jun, Jul, Aug) for the years 1901–2006 (thin short-dashed lines) with LOESS- (locally weighted scatterplot smoothing) regression lines (solid lines).

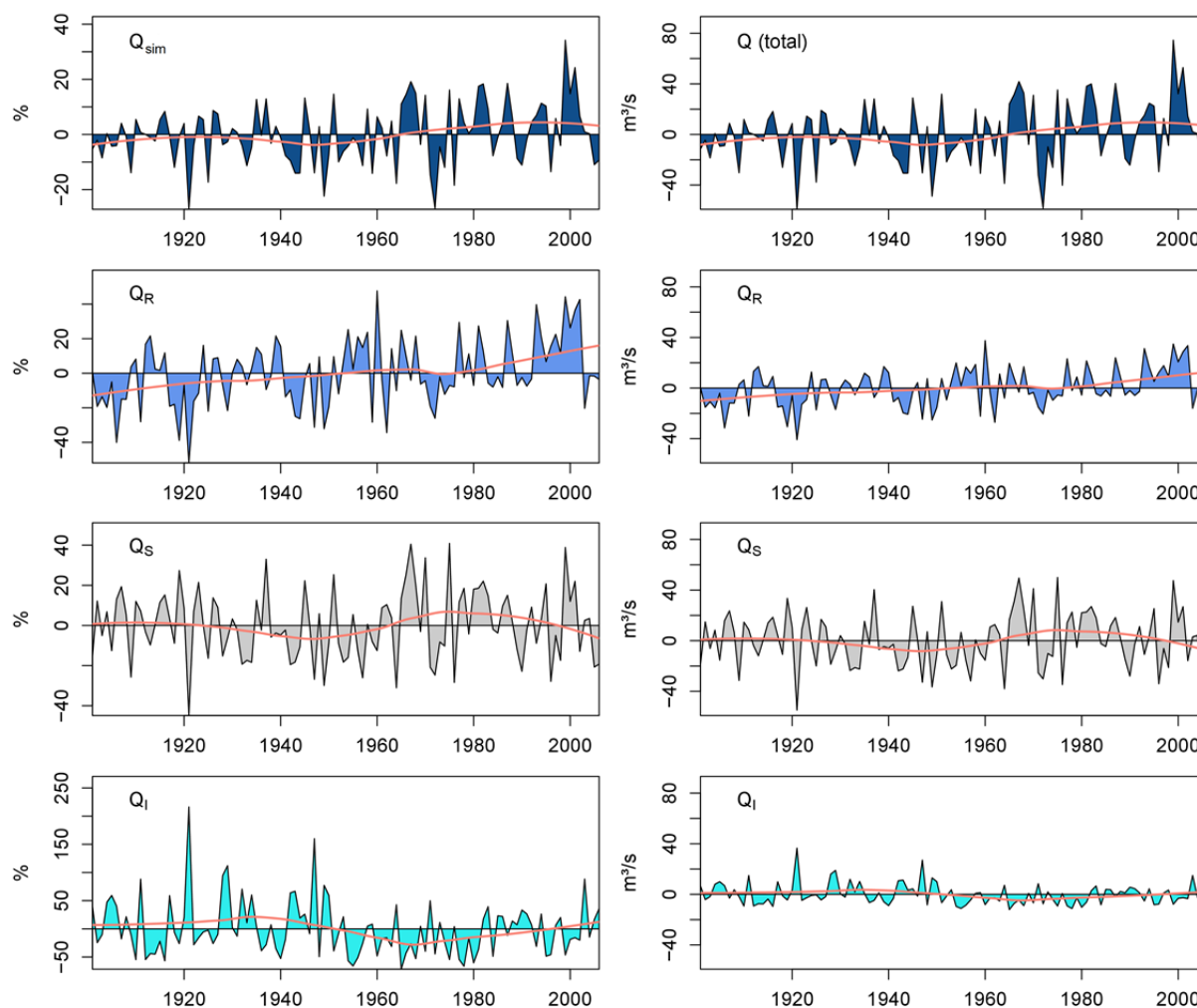


Figure 5.24: Long-term behaviour of total streamflow and its components  $Q_R$ ,  $Q_S$ , and  $Q_I$  from all glacierized headwater catchments. Relative (left) and absolute (right) deviation of annual mean from the long-term mean (1901–2006), both with LOESS-regression lines (orange line).

Looking in detail at the inner-annual changes of the streamflow and its components (Figure 5.25), a very high variability of the seasonal long-term trends becomes evident. Whereas the simulated changes of total streamflow, except for the winter period, are relatively moderate and rarely significant, the component  $Q_R$  shows mainly positive trends especially in winter when the trends are statistically significant. Particularly the presented seasonal trends of  $Q_S$  over the subperiod 1951–2006 (Figure 5.25) with considerable increases in spring and early summer shifting to clear decreases in summer and autumn are indications that snowmelt shifted to an earlier time. However, significant trends were detected only partially, namely at the beginnings of May and June and in September. Looking at the component  $Q_I$ , it is remarkable that the analyses over the two periods resulted in pretty distinct but contrary trend patterns. While the simulated changes of  $Q_I$  over the complete simulation period (1901–2006) are dominated by considerable negative trends until September, the analysis for the later subperiod from 1951 on resulted in positive trends nearly throughout the whole relevant time period from May to November. To interpret these trends again the characteristic phases of glacier development related to decadal climate variability over the course of the 20<sup>th</sup> century need to be considered. For instance, the quick transition from the near-stationary glacier extents, which characterized the 1960s to 1980s, to the intense glacier retreat in consequence of recent warming may explain the dominance of positive trends of  $Q_I$  over the subperiod of 1951–2006 in contrast to the mainly negative changes of  $Q_I$  over the

complete period 1901–2006. These results suggest that, generally, the results of any trend analyses are (heavily) dependent on the selection of time periods. Specifically in the present study potential inhomogeneities of the assembled meteorological input series (HYRAS-REC and HYRAS datasets) might also affect the trends shown here.

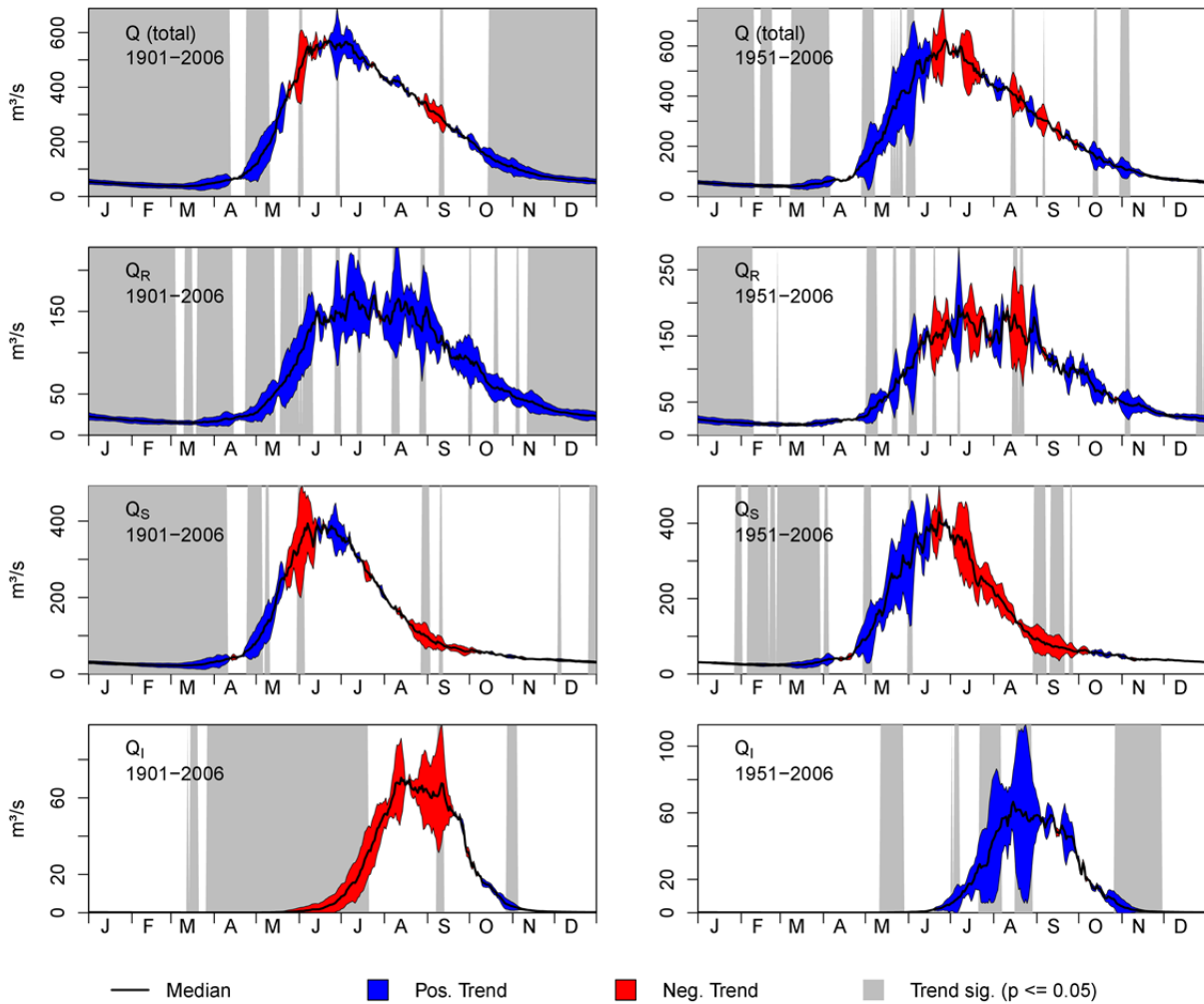


Figure 5.25: Regime changes of modelled total streamflow and its components  $Q_R$ ,  $Q_S$ , and  $Q_I$  from all glacierized headwater catchments: period 1901–2006 (left) and 1951–2006 (right). Trend magnitudes calculated as Sen Slope for each day of the year (based on moving averages over three days) and significance according to Mann-Kendall test.

The modelling results imply that so far (up to the year 2006) the retreat of the glaciers in the Rhine’s headwater catchments has been widely compensated by additional ice melt in response to increased temperatures. This is illustrated in the comparison of the glacier mass balances and the loss of glacier area (Figure 2.26a and b) with the temporal evolution of the specific streamflow component  $Q_I$  in mm based on the modelled glacier area in the corresponding hydrological year and the absolute  $Q_I$  component (in m<sup>3</sup>/s) in Figure 5.26c. The graph at the bottom (5.26d) demonstrates that a  $Q_I$  of 30 m<sup>3</sup>/s had been generated by a specific ice melt of about 1500 mm at the beginning of the 20<sup>th</sup> century, whereas towards the end of the simulation period about 2500 mm ice melt (corresponding to more negative mass balances) were required to generate the same flow ( $Q_I = 30$  m<sup>3</sup>/s) from the remaining glacier area.

It must be noted that this aggregated loss in glacier area and increase in the specific ice melt runoff contributions from the reduced glacier area of the 49 headwater catchments (Figures 5.24 to 5.26) is based on the modelling of many individual glaciers, ranging from very small up to fairly large ones, in different elevation zones and regions within the headwater area of the Rhine basin. Whereas the retreat of some of the (particularly small) glaciers may have progressed so far that the ice melt contribution to runoff from those glaciers is receding, for other glaciers (particularly the larger ones) the progressive loss of ice mass might still lead to increasing ice melt contributions or it might be compensated by increased melt rates resulting in the absence of a clear effect on the amounts of  $Q_I$ . However, for the case of an individual glacier and for longer time periods the latter seems to be a rather coincidental not very likely situation. According to a comprehensive study of more than 1000 small glaciers in the Swiss Alps by Huss & Fischer (2016) based on modelling and observations, the runoff from small glaciers with areas  $\leq 0.5\text{km}^2$  (which are especially common in the basins of Rhine and Rhône) has, after a sharp rise in the 1980s, already reached its maximum (peak water), depending on the glacier size class, between 1997 and 2004 and a continuous decline of the runoff from such small glaciers is to be expected over the next decades. In contrast, for several larger glaciers in the Swiss Alps investigated by Farinotti et al. (2012) the peak of the glacier runoff has not been reached yet and has been projected to be passed between 2020 and 2050 depending on the glacier, region, and the climate projection. Indeed, for the Trift and Silvretta glaciers, two among nine glaciers located in the Rhine basin studied by Farinotti et al. (2012), the typical pattern of initially increasing discharge followed by decreasing discharge was less pronounced compared to the other study areas with a larger glacier coverage. Overall, the findings of such studies point out that any assessment of the hydrological response to the currently ongoing retreat of glacier needs a rather detailed consideration of differences among subregions and individual glaciers. If the analysis of the development of the modelled streamflow component  $Q_I$  from all glacierized headwater catchments in Figure 5.23 or Figure 5.24 is focussed only on the latest subperiod since the last phase of quasi stable glacier conditions around the 1970s, it could be concluded that the Rhine's flow has still been profiting from increasing ice melt contributions due to glacier retreat. It can be assumed that the glacio-hydrological response at the scale of the Rhine headwater area is dominated mainly by the present medium-sized to large glaciers, because total  $Q_I$  volumes originating from all the scattered small glaciers make up for a minor part only. Hence, the modelling results achieved are in agreement with other glacio-hydrological studies, e.g., Farinotti et al. (2012), according to which the maximum glacier contribution to runoff in areas with considerable glacier coverage (presence of medium-sized and large glaciers) in the European Alps has not been reached yet.

The aforementioned findings, namely an increasing tendency of total streamflow and  $Q_R$  over the simulation period or the differing amounts of  $Q_I$  in the distinguished characteristic periods of the 20<sup>th</sup> century, are reflected in the mean values over each of these subperiods as well (Table 5.7).

Table 5.7: Mean of modelled streamflow ( $Q_{\text{sim}}$ ) and modelled streamflow components from all glacierized headwater catchments for subperiods (characterized by different glacier development stages, see Section 3.4).

Period	$Q_{\text{sim}}$		$Q_R$		$Q_S$		$Q_I$	
	$\text{m}^3/\text{s}$	$\text{m}^3/\text{s}$	%	$\text{m}^3/\text{s}$	%	$\text{m}^3/\text{s}$	%	
1901–1924	213.7	71.0	33.2	124.6	58.3	18.1	8.5	
1925–1954	212.2	76.4	36.0	116.4	54.8	19.5	9.2	
1955–1984	220.4	80.6	36.6	126.9	57.6	12.9	5.8	
1985–2006	226.6	87.7	38.7	121.5	53.6	17.5	7.7	

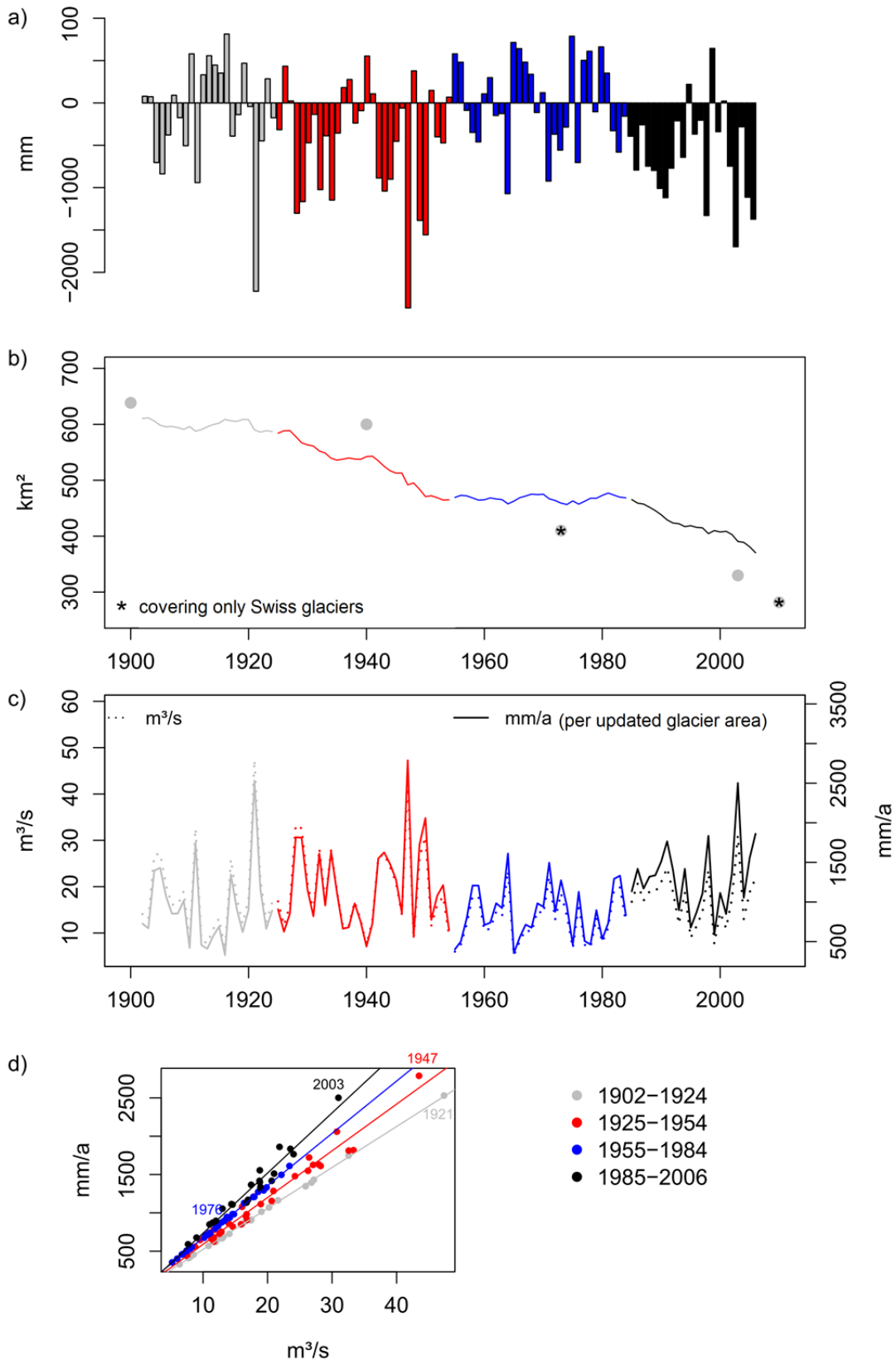


Figure 5.26: Modelled changes in all aggregated glacierized headwater catchments, colour coded for sub-periods (see also Section 3.4): a) glacier mass balances of Swiss hydrological years 1902-2006, b) modelled glacier areas (line) and glacier areas according to the different glacier area observation datasets, c) mean annual ice melt component of streamflow  $Q_i$  (for water years 1902-2006) as absolute value (in  $m^3/s$ ) and as runoff rate in  $mm/a$  in relation to the transient glacier area, d)  $Q_i$  in  $m^3/s$  (as in c) (x-axis) vs  $Q_i$  in  $mm/year$  per transient glacier area (as in c) (y-axis) and regression line for each sub-period.

An additional modelling experiment was carried out for the glacierized headwater catchments, in which the retreat of glaciers was disabled, i.e., the area covered by glaciers remained as initially set. Whereas many catchment-scale hydrological models now include glacier change routines, many conventional and operational hydrological models lack this feature and therefore do not consider representation of responses in glacier cover. Hence illustrating the effect will provide a ‘reference run’. The experiment shows an increase of streamflow, in particularly from 1980 on (Figure 5.27), which would be the result from the warming alone (assuming an unlimited glacier mass). As discussed above, the absence of such a clear increase of  $Q_i$  in the final modelling results can be explained by the combination of a decreasing glacier area with progressive glacier retreat.

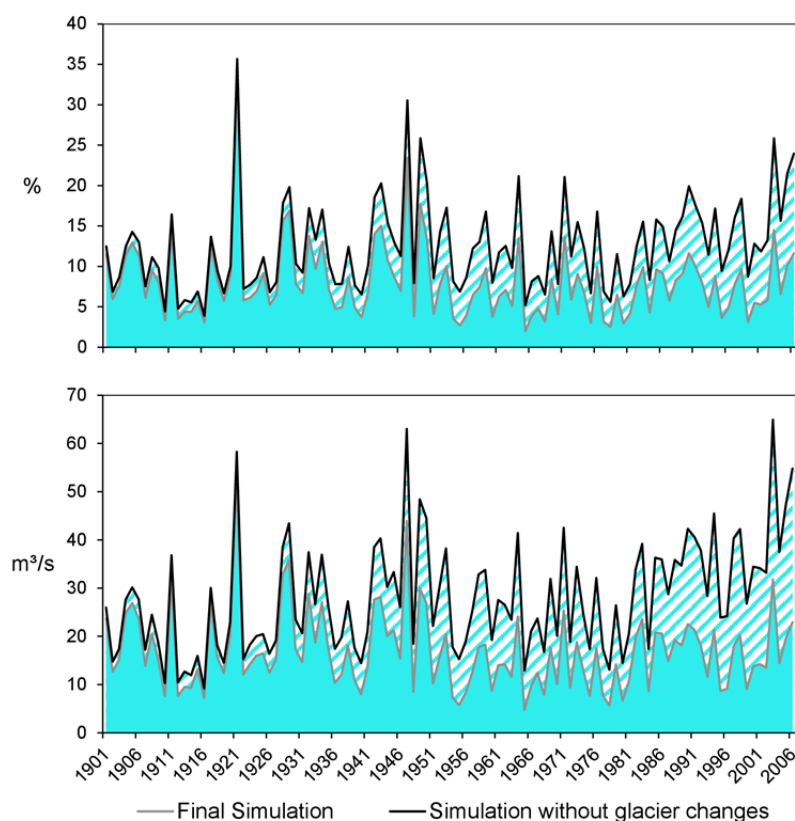


Figure 5.27: Annual mean modelled  $Q_i$  from all glacierized headwater catchments (HBV-light model catchment) (see Figure 5.1) from final model simulations (grey line) and from the modelling experiment with stationary glacier area (black line) as well as the resulting difference (hatched area): a) as relative fraction (percentage of  $Q_{sim}$ ) (top graph) and b) in absolute terms (bottom graph).

Figure 5.28 demonstrates the effect of this modelling experiment with stationary glacier areas on the simulation of streamflow in the year 2003. If glacier areas and volumes in 2003 corresponded to those present in the headwater catchments at the simulation start in 1901, the total flow from the glacierized headwater catchments in this low flow year would have been increased by roughly 15% (Figure 5.28b). Conversely, it can be shown that without any contribution of ice melt the annual flow in 2003 would have been decreased by about 15% (Figure 5.28c), which would have led to an aggravated low flow situation particularly in July, August, and September. A similar hypothetical modelling experiment was applied, e.g., by Koboltschnig et al. (2007) for the small and highly glacierized Goldbergkees catchment in the Austrian Alps, in which the application of the meteorological forcing of the year 2003 to the glacier extent of the year 1979 resulted in a 12% increase in annual discharge.

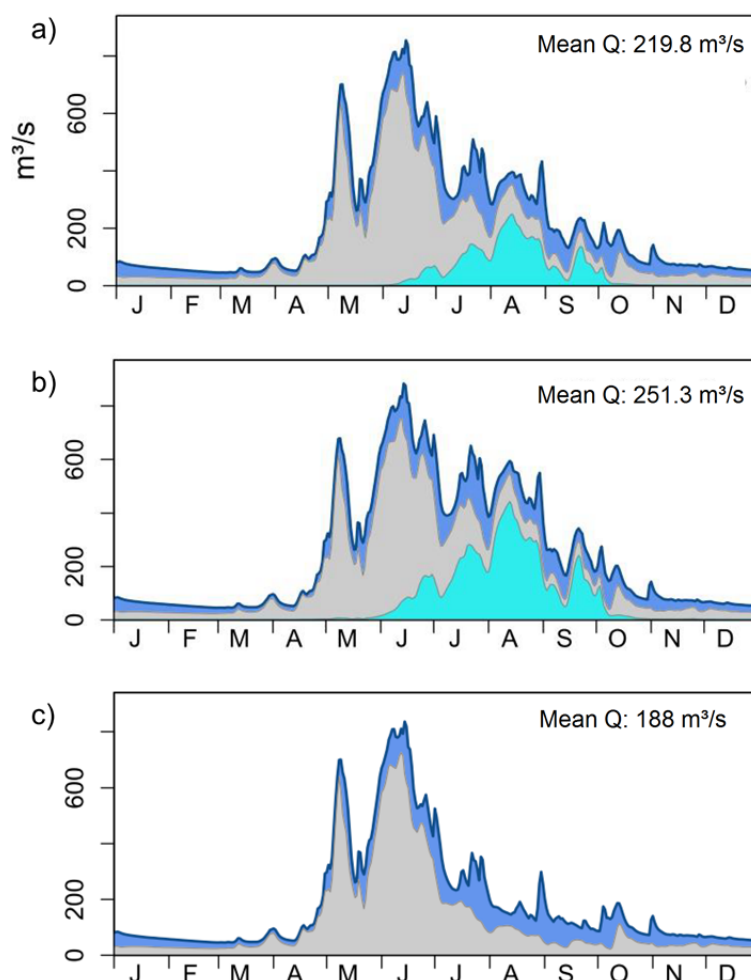


Figure 5.28: Modelled hydrographs and streamflow components from all glacierized headwater catchments for the extreme year of 2003: a) according to the final simulation (as in Figure 5.21), b) according to the reference run with stationary glacier coverage since 1901, and c) results of a) but with the ice melt component deducted ( $Q-Q_I$ ).

The presented analyses and discussion of the modelling results as well as the modelling experiment with stationary glacier coverage stress again the crucial role of the linkage between hydrology and glacier changes in determining the components of streamflow and in explaining trends and changes in streamflow behaviour. Moreover, the potential of advanced modelling scenarios to investigate the impact of coupled climate and land cover change is demonstrated.

## 5.8 Conclusions

Prior to the application of HBV-light for the delineated 49 glacierized headwater catchments several adaptations and extensions of the model were required to adequately capture the hydrological processes in these complex, high-elevation, catchments. In addition, the aim of basing the modelling on observational datasets, which cover all or at least the majority of the catchments, required the preparation of these data and methods for their use in the modelling steps. A particular focus was put on the appropriate representation of the glacier response. The ice melt component of streamflow ( $Q_I$ ) is generated only in this small part of the Rhine basin. Yet in the context of the long-term climate variability of the study its role is of key interest. By incorporating several benchmarks into the adapted multi-criteria calibration of the model, a good simultaneous agreement of the simulations with observations of streamflow, snow depth, snow coverage, and glacier volume, could be achieved over the 106-year

simulation period. The use of the spatially distributed snow and glacier datasets made it possible to also carry out a reasonable parameter optimisation for the 25 headwater catchments for which no streamflow observation data were available.

The results of modelling the streamflow components for the glacierized headwater catchments of the Rhine confirm the relatively small fraction of the ice melt component of streamflow, similar to the findings of water balance assessments for catchments in a similar scale range from other studies. Over the simulation period (1901–2006) the modelled  $Q_I$  amounts to a mean fraction of 8%. However,  $Q_I$  is characterized by a notably high inter-annual variability. Meteorologically extreme years and distinct decadal phases of glacier development in the 20<sup>th</sup> century are clearly reflected in the modelled ice melt component of streamflow. The occurrence of both, largest absolute amounts and largest relative fractions of modelled  $Q_I$ , with monthly mean fractions of up to 63% (aggregated results for all glacierized headwater catchments) coincides with historical low flow events at the River Rhine. The largest monthly means of the modelled  $Q_I$  are mostly found in the period before 1951 (subperiod with reconstructed climate input), and in particular in the drought years of 1921 and 1947. Yet, according to the modelling results for August during the dry and hot summer of 2003,  $Q_I$  contributed at similarly high levels as in earlier events. However, the evaluation of selected past Rhine low flow years also point at the occurrence of considerable low flow events in the Rhine for which increased contributions of ice melt played a rather minor role.

Analyses of long-term responses in the modelling results have not revealed a clear long-term signal (decreasing or increasing tendency) of  $Q_I$  amounts over the complete time period from 1901 to 2006, since enhanced melt and glacier retreat seem to largely balance each other at the scale of all headwater catchments. Hypothetical model runs, in which the glaciers were always kept at their initial state, visualise the considerable gain in  $Q_I$  which would result from the effect of warming climate alone (regardless of retreating glaciers). It should also be mentioned that analyses of shorter time periods than 1901–2006 (e.g., only the last decades since the last close to balanced conditions of the glaciers around 1970) or an extension of the simulations up to the present might result in different trends in streamflow. Overall, the modelling results match with findings of other studies, according to which the occurrence of the maximum glacier runoff contribution (peak water moment) can vary a lot among glaciers in the Alps, i.e., the moment of peak water discharge from small glaciers has been already passed at turn of the century, while in areas with larger glaciers it is expected to be reached within the next decades.

## 6 Modelling of the entire Rhine basin

### 6.1 Objectives and description of the LARSIM model

#### 6.1.1 The Water Balance Model LARSIM

The physically based water balance model LARSIM (Ludwig & Bremicker, 2006) is used to model the streamflow downstream of the glacierized headwater catchments. LARSIM is provided by the Landesanstalt für Umwelt, Messungen und Naturschutz Baden-Württemberg (LUBW) for this project. The water balance model enables a detailed, spatially distributed, process-based simulation of the surface water balance with a high temporal resolution (daily or hourly time steps). Daily time steps are used for this study.

LARSIM simulations are based on a variety of spatially distributed datasets (terrain elevation, slope, land use, soil conditions, channel geometry, etc.). As a first step, the river basin is subdivided into smaller subunits (either into hydrological subbasins or into regular grid cells). To better address sub-scale processes, these areas are then further subdivided according to land use classes. Pre-determined soil properties are assigned to these land use classes. The following processes are computed at a sub-scale level dependent on land use class and seasonally variable datasets:

- Snow accumulation, metamorphism, and ablation
- Evapotranspiration (incl. interception)
- Soil water balance

The following processes are dealt with at the subunit scale:

- Runoff generation using three or four parallel single linear storage reservoirs.
- Routing and retention of flow in the channel can be simulated with different hydrological processes. Alternatively, volume-discharge relations determined by hydrodynamic models can be implemented.

Additionally, flood retention basins, dams, diversions, and water transfers can be considered. LARSIM offers several different modules for the modelling of individual processes which can be used within a specific project (e.g., depending on data availability).

LARSIM includes many features that were specifically designed for its operational use as a flood forecasting model. High-resolution LARSIM water balance models are thus very well suited for operational purposes (Luce et al., 2006). Such operational, highly spatially distributed models are readily available for large parts of the River Rhine and for the German part of the Danube basin (Bremicker et al., 2013). Additionally, LARSIM runs are set up for a multitude of water management tasks including the operational use as well as offline applications. For example, LARSIM has also been driven with projected future climate variables to evaluate future changes in the water balance (Gerlinger & Meuser, 2013).

Different versions of LARSIM are available for the Rhine basin. These different versions are linked in the current project to determine the snow and ice melt contributions to runoff and to follow these inputs through the entire Rhine basin. In this system, LARSIM itself computes the snow processes within the non-glacierized catchments. The runoff contributions from the glacierized catchments are transferred to LARSIM as fluxes from the HBV-light model runs.

Existing operational flow forecast models along with offline models used for climate change impact simulations were adapted to calculate the snowmelt and ice melt contributions to runoff at a daily time step. Existing streamflow data are used to test and validate the models. The prediction of long-term changes in streamflow components as a result of changing climate conditions and land use will also be considered here by looking at the changes that occurred in the period from 1901 to 2006. The simulation and validation of the flow routing through the reservoirs as well as the regulated and unregulated lakes upstream of Basel within LARSIM includes a consideration of the changes in water management practices.

### 6.1.2 Combined Two-Scale Model for the Rhine Basin

The streamflow and streamflow components within the non-glacierized portions of the Rhine basin are modelled for selected gauges along the River Rhine to Lobith at the German-Dutch border using a combination of two model structures: Upstream of the gauge at Basel, high resolution 1x1km<sup>2</sup> LARSIM models are employed while downstream 5x5km<sup>2</sup> LARSIM models are used.

#### ***Rhine Basin upstream of the stream gauge Basel (1x1 km<sup>2</sup>- grid model (LARSIM-Hochrhein))***

Four high-resolution LARSIM models (1x1km<sup>2</sup>-grid models) were available for the Rhine basin upstream of Basel that were originally set up for the „Landesanstalt für Umwelt, Messungen und Naturschutz Baden-Württemberg (LUBW)“ and the „Amt der Vorarlberger Landesregierung (AVLR)“. Additionally to the LUBW model for the Swiss part of the Rhine basin, two LUBW models for tributaries to the Rhine and Lake Constance in Baden-Württemberg and the AVLR model for the Bregenzerach River were available (Figure 6.1). The combination of these four models used for modelling the Rhine upstream of Basel is referred to as “LARSIM Hochrhein” in this report.

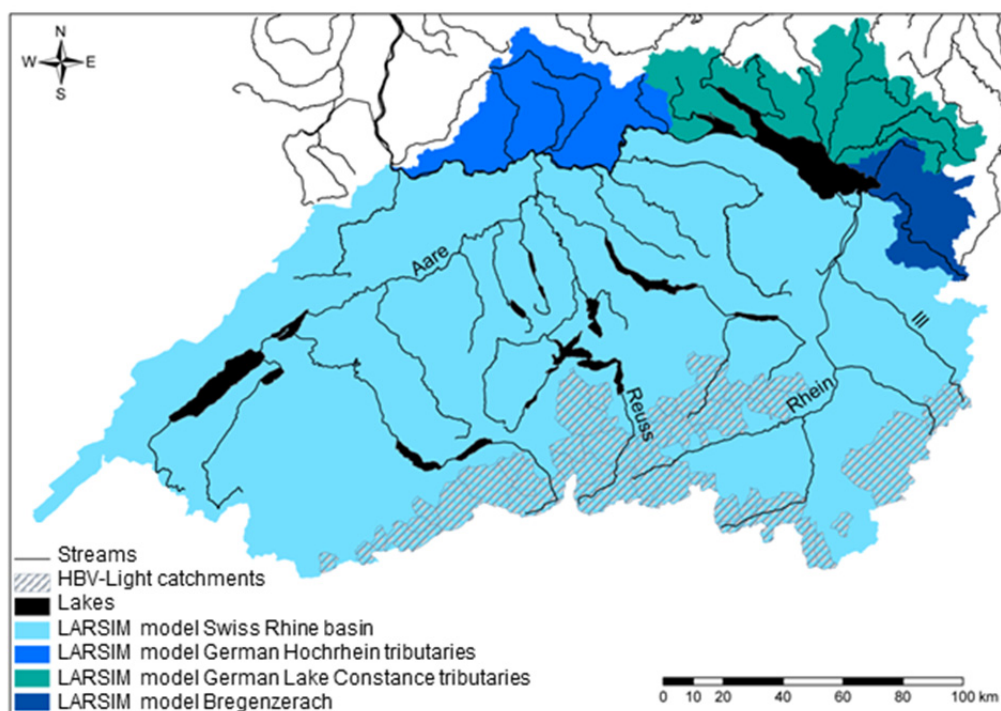


Figure 6.1: LARSIM water balance models (spatial resolution: 1x1km<sup>2</sup> grid cells) for the Rhine basin upstream of the gauge Basel.

The models are coupled. The resulting model chain allows the spatially high-resolution simulation throughout the basin upstream of the gauging station at Basel. At an hourly time step, the coupled models are currently used for the operational, real-time forecasts by the flood-forecasting centre (HVZ) of the LUBW. They can also be run at daily time steps. Daily model simulations of the LARSIM-Hochrhein model chain are also currently being used for long-term forecasts by the HVZ. Hence, the model chain used in this study represents an established modelling setup, proven in practice.

Previously the models relied on different geo-coordinate systems and the GMD format employed by LARSIM. For application in the ASG Rhine project all models were converted to the Swiss coordinate system (CH 1903) and adapted to use the LILA/KALA data input format, which will be used in any versions of LARSIM from now on.

#### ***Rhine Basin downstream of the gauge Basel (5x5km<sup>2</sup>- Grid model (LARSIM-ME-Rhein))***

A LARSIM grid model with a resolution of 5x5 km<sup>2</sup>, previously developed for the Bundesanstalt für Gewässerkunde (BfG, Federal Institute of Hydrology) to model several large river basins in Central Europe, was available. This model has been used with a daily resolution in BfG projects studying the impact of climate change on hydrological processes (Figure 6.2) and is generally referred to as LARSIM-ME. Within the ASG Rhine project the part of the model covering the Rhine basin was employed and in this report is referred to as LARSIM-ME-Rhein.

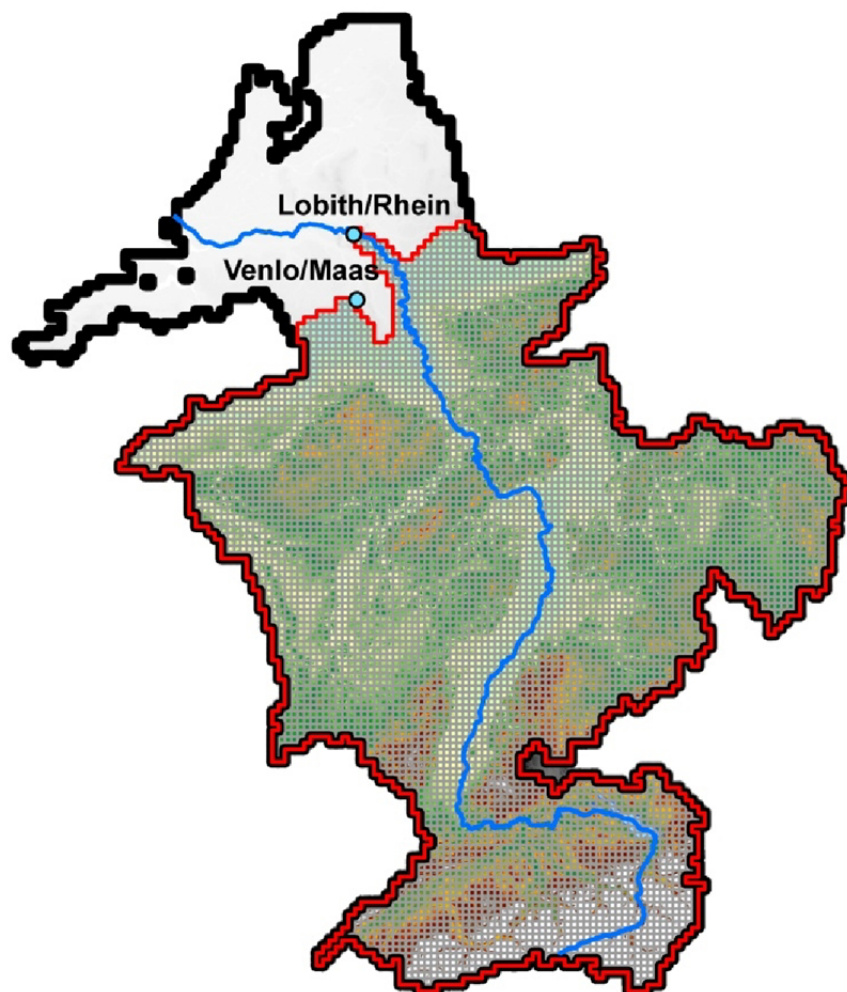


Figure 6.2: 5x5km<sup>2</sup> grid cells of the LARSIM-ME-Rhein model for the Rhine basin.

The 5x5 km<sup>2</sup> model differs from the high-resolution 1x1 km<sup>2</sup> model in several aspects:

- Evapotranspiration is calculated with the Penman/Wendling equation (instead of the Penman-Monteith approach).
- The snow simulation uses the degree-day approach (instead of an approach computing the complete energy balance of a snow cover including radiation).
- The surface topography is coarser due to the lower 5x5km<sup>2</sup> resolution.
- The LARSIM-ME is also available for the entire Rhine basin.
- Due to the use of less complex process descriptions (see above), only information on air temperature, precipitation, and global radiation are required as input data. This information is available from the HYRAS dataset.

The higher resolution 1x1km<sup>2</sup> LARSIM models require additional information on wind speed, relative humidity, and atmospheric pressure to calculate evaporation using the Penman-Monteith equation. Data for these variables for the LARSIM-Hochrhein model had to be acquired from quality controlled station data, but were not needed for the LARSIM-ME-Rhein model.

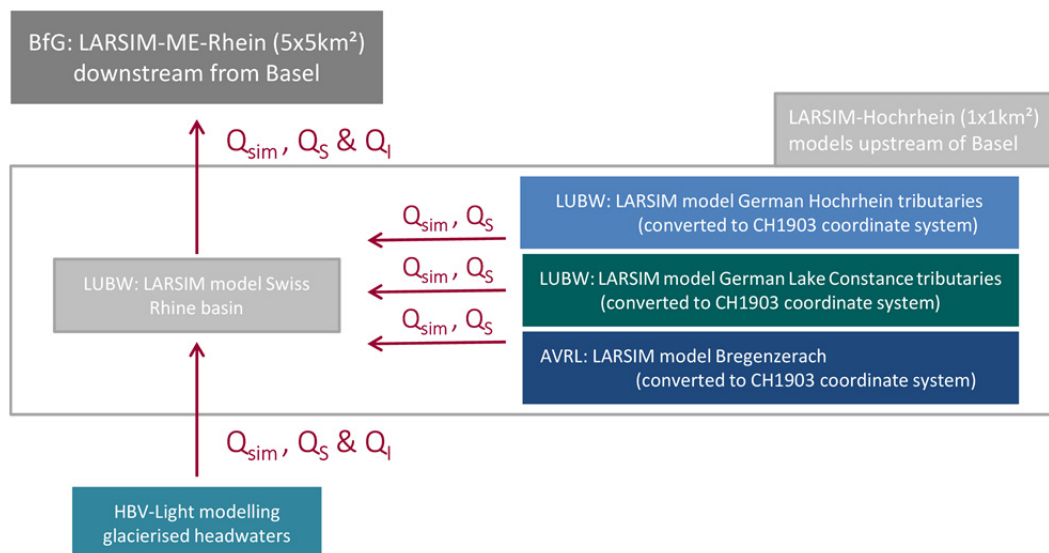


Figure 6.3: Coupled HBV- und LARSIM-Models including the handover of the streamflow components.

While the Rhine basin upstream of Basel was modelled with the higher resolution 1x1km<sup>2</sup> (LARSIM-Hochrhein), the availability of the 5x5km<sup>2</sup> model (LARSIM-ME-Rhein) allowed a computationally efficient simulation of the Rhine basin downstream of Basel at lower resolution. Hence, the ASG Rhine project employed a coupled two-scale modelling concept to simulate the entire Rhine basin as shown in Figure 1.4 and Figure 6.3:

- **LARSIM-Hochrhein:** the high resolution of the 1x1km<sup>2</sup> LARSIM model used for the Rhine basin upstream is particularly relevant for the determination of the melt water streamflow components. The higher resolution allows for a much better representation of the surface topography and surface relief in the 1x1km<sup>2</sup> model compared to the 5x5 km<sup>2</sup> model, thus supporting an accurate simulation of the snow cover processes in alpine areas. Additionally, more comprehensive modelling approaches are used in the high-resolution model setup to simulate snow processes and evapotranspiration, the effects of reservoirs and water manage-

ment practices at a higher level of detail, and a channel routing that is based on implemented  $dV/dQ$  relations for the most important rivers (e.g., Aare, Thur). The high-resolution model also incorporates the channel routing through the entire River network upstream of Basel. As the  $1 \times 1 \text{ km}^2$  resolution is not considered high enough to model the local details of the highest headwater areas in the Alps, the HBV models were employed for the glacierized headwater catchments.

- **LARSIM-ME-Rhein:** The detailed simulated daily streamflows from the Rhine basin upstream of Basel are then transferred as input fluxes into the LARSIM-ME-Rhein model. Snowmelt contributions from catchments downstream of Basel are thus obtained by the  $5 \times 5 \text{ km}^2$  LARSIM-ME-Rhein model.

For an improved representation of the relief within the large  $5 \times 5 \text{ km}^2$  model grid cells, elevation zones within the grid cells were identified and integrated into the model setup as part of a separate project (on behalf of the BfG) before running the model (BfG 2016). The elevation zones were identified from a digital elevation model and do not consider information about the land use in the individual zones. Fractions of land use within the elevation zones are considered similar to the fractions within the entire grid cell.

The snowmelt simulations within LARSIM are subsequently carried out separately for the specific elevation zones, which aimed to make the simulations more spatially precise. In high-relief terrain, this will allow modelling a much more realistic representation of snow accumulation and snowmelt.

## 6.2 Model adaptations and extensions

### 6.2.1 Adaptation of the LARSIM model

To accurately predict streamflow in operational flow forecasting as well as in the context of climate change impact assessments, a validation of the correct representation of runoff generation processes (including snowmelt) and a quantification of their contributions to streamflow is crucial. Therefore, within LARSIM, the simulation of the snowmelt contribution to streamflow, has been improved continually over the past years. The relevant effects of snowmelt (including the redistribution of snow from higher to lower elevations within the model areas) are included in LARSIM at a high spatial and temporal resolution. LARSIM also calculates the snow cover dynamics separately for each land cover class. Since LARSIM does consider all the factors important for a reliable simulation of the snow cover dynamic in its snow model algorithm, it is particularly well suited to calculate the snowmelt contribution to runoff and the resulting snowmelt component of streamflow. In all operational LARSIM applications, snowmelt simulations are continuously validated, employing satellite data, in-situ snow observations, and streamflow observations for different seasons and snowmelt periods.

Further adaptations to LARSIM were needed for application within the ASG Rhine project to model the snowmelt and ice melt components of streamflow. Thus, LARSIM was extended to accept streamflow (including the corresponding components  $Q_s$  and  $Q_i$ ) provided by the HBV model runs as a lateral input flux. Figure 6.4 shows the HBV model catchments and the streamflow input nodes into the river network for further simulation by the LARSIM-Hochrhein model.

As the HBV model does not include an explicit representation of the river network and therefore no channel routing scheme, the routing for a few river segments between HBV-modelled streamflow input nodes along the same river were performed by LARSIM (e.g., in the upper reach of the Hinterrhein River).

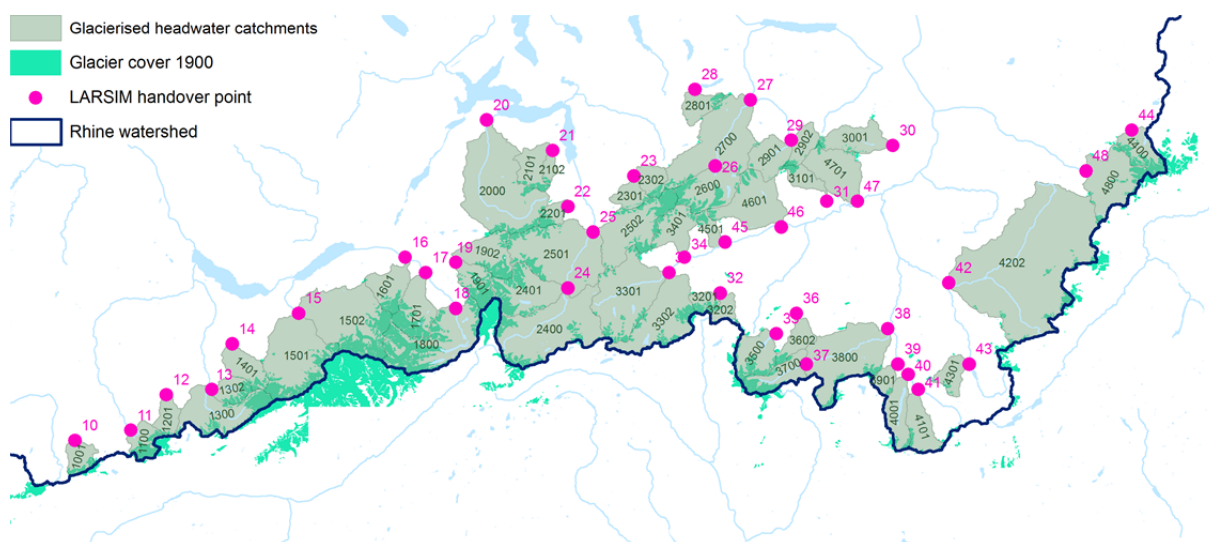


Figure 6.4: Schematic map showing the glacierized headwater catchments modelled with HBV-light (see also Figure 5.1 and Table 5.1) and including the handover points to the LARSIM-Hochrhein model. To transfer the modelled runoff components from the 49 individual catchments to the LARSIM-Hochrhein model, 39 handover points numbered 10 to 48 were determined.

Additionally, LARSIM was extended to handle the streamflow components originating from snowmelt and ice melt as separate model variables including their mixing, channel routing, and their retention throughout the catchment and within the drainage network. Thus, LARSIM is now able to differentiate into the contributions of rain and snowmelt to runoff and to route not only total streamflow but also its individual components  $Q_S$ ,  $Q_I$ , and  $Q_R$  through the entire channel network (including lakes and reservoirs) in the Rhine basin downstream of the glacierized headwater areas. The necessary model code adaptations to a complex model that is used for different tasks in operational as well as offline modes are particularly challenging.

To facilitate the simulation of the individual streamflow components, the mixing tank model described in Chapter 4 was also integrated into LARSIM. The mixing tank concept is used within LARSIM at two points: Firstly, to simulate the runoff generation and resulting streamflow components within each model element ( $1 \times 1 \text{ km}^2$  or  $5 \times 5 \text{ km}^2$  grid cell) and, secondly, to track the different components of streamflow through lakes and reservoirs. Thus, mixing tanks are realized for every model element as well as all lakes and reservoirs within LARSIM. The computation of the fractions of the components in the mixing tanks is performed in parallel to the streamflow simulations themselves in LARSIM. This means that the mixing tanks are only used to determine the relative fractions of the individual streamflow components within the model elements (or the lakes and reservoirs). The determined fractions from each model element (or lake or reservoir) then flow to the downstream element within the model.

The channel routing of the individual streamflow components along the river network is performed by the general routing routine in LARSIM. Similarly to the runoff generation, the fractions of the streamflow components determined from the mixing tanks along with the total streamflow are routed to the next downstream model element. The same applies to inflows and abstractions from water transfers.

The LARSIM simulations requires a file defining the initial state variables for every model subunit including, for instance, soil water storage, snow depth and snow water equivalent, and streamflow in the drainage network. To compute the streamflow components, this file must also include information about the initial water volume in each mixing tank as well as the relative fraction of the snowmelt

component within that water volume for each model element (or lake or reservoir). Additionally, the relative fractions of the  $Q_1$  component within mixing tanks that represent reservoirs, lakes, and flood retention basins have to be determined. A necessary extension to the initial state variable file was implemented during the ASG Rhine project.

As described in Chapter 4, the volume of the mixing tanks can be limited to avoid that the overall fractions of the streamflow components become virtually constant over a longer time period, which would prevent the desired effect tracking of the streamflow response to temporally variable contributions of snowmelt and ice melt. Principally, the limit for the maximum mixing tank volume of the model elements ( $MB_{elem}$ ) can differ from the maximum mixing tank volume for lakes, reservoirs, and retention basins ( $MB_{lake}$ ).  $MB_{elem}$  and  $MB_{lake}$  can be set specifically for each individual model element and each lake or reservoir respectively.

However, as stated in Chapter 4, for the final simulations in the project the volume for the mixing tanks of all model elements (grid cells) was generally limited to 25 mm, similar to the application with HBV-light. The maximum volume of the mixing tanks for lakes and reservoirs was also limited to 25 mm. A detailed sensitivity analysis looking at the effect of different dimensions of the mixing tank is shown in Chapter 7.

### 6.2.2 Integration of the summary changes of the water management practices

The model setup of the 1x1km<sup>2</sup> LARSIM-Hochrhein model included 12 lakes, some of them regulated. The regulation of individual lakes is simulated dependent on inflow, lake level, season, and operation rules. Such operation rules were available for Lake Zürich (Zürichsee), Lake Thun (Thunersee), and Lake Brienz (Brienzersee) as well as for the connected lake system of Lake Neuchâtel (Neuenburgersee), Lake Biel (Bielersee), and Lake Morat (Murtensee) in the Swiss Jura region. The known rules were implemented into the model. For the Lake Lucerne (Vierwaldstättersee), seasonal operation rules were derived from relationships of lake levels and volumes and from streamflow observations. The implemented operation rules were not changed over the modelling period 1901–2006. The five lakes: Lake Constance (Bodensee, consisting of two connected water bodies the so-called Obersee and the Untersee), Lake Sarnen (Sarnensee), Lake Sempach (Sempachersee), and Walensee are considered unregulated lakes in the model. Observed volume-discharge relationships of these five lakes are modelled.

Table 6.1: Lakes in the LARSIM-Hochrhein-Model

Lake	Regulation
Lake Constance (Obersee part)	unregulated
Lake Constance (Untersee part)	unregulated
Lake Brienz (Brienzersee)	operation rules given
Lakes Neuchâtel/Biel/Morat	operation rules given
Lake Sarnen (Sarnensee)	unregulated
Lake Sempach (Sempachersee)	unregulated
Lake Thun (Thunersee)	operation rules given
Lake Lucerne (Vierwaldstättersee)	operation rules approximated
Walensee	unregulated
Lake Zürich (Zürichsee)	operation rules given

Principally, changes in river regulation and water management such as the building of additional dams or a change in the management of an existing lake may be included in LARSIM, if the required data describing the quantitative changes in the management practice were provided by the operator or the local authorities. For example, before the start of the model runs the management practices for 17 res-

ervoirs in the Moselle River basin, eastern tributaries of the Rhine in Nordrhein-Westfalen, and in tributaries of the Main River were acquired as part of a separate project on behalf of the BfG. These practices and their changes were implemented in the LARSIM-ME-Rhein-Model (BfG, 2016).

Within the 106 year study period of the ASG Rhine project, newly built reservoirs were included at the time of their completion to adequately reflect the changing storage volume. For the Rhine basin upstream of Basel, it is very difficult to acquire the required information on water management changes due to the large number of changes and operators. After consultations with the CHR/KHR, it was therefore decided to forgo an integration of the exact reservoir volumes, management practices, outlet volumes, starting dates, and information about the exact timeline of river corrections (as, e.g., the Jura water correction from 1962 to 1973). Instead, it was decided to use a summary approach to the implementation of such changes based on observed data.

Consequently, four conceptual, cumulative “model reservoirs” were implemented into the LARSIM-Hochrhein model to represent the effects of the numerous hydropower reservoirs in the alpine part of the basin. The four model reservoirs simulate a summary of the anthropogenic influences on the streamflow by reproducing the collective effects of the numerous small reservoirs present in reality. The four cumulative model reservoirs were placed just upstream of the stream gauges Gisingen/III, Domat-Ems/Rhein, Brienzwiler/Aare und Seedorf/Reuss within the river network of LARSIM. The storage effects of these cumulative model reservoirs have proven adequate for the representation of temporary storage throughout the year at the daily model time step used. The barrage weirs along the Aare River and the Hochrhein (High Rhine, reach of the River Rhine between Lake Constance and Basel) are addressed by the implementation of  $dV/dQ$ -relationships within the LARSIM-Hochrhein model, to ensure a high quality of the channel routing calculations.

To represent the reservoirs and their temporal development within the modelling area, first the results of a study by Frielingsdorf (2013) were analysed. This study describes the temporal evolution of the reservoirs and their retention storage volume in the river basins of Aare, Reuss, and Rhine. The primary source of information for this project was the Swiss drainage system information network (GEWISS).

The study results were subsequently used to define the changes in the reservoir volume since 1901 upstream of the implemented theoretical reservoirs along the rivers Aare, Rhine and Ill. Figure 6.5 shows the retention volume upstream of the gauges Domat-Ems/Rhein, Brienzwiler/Aare, Seedorf/Reuss und Gisingen/III. The most important reservoirs are labelled in the Figure. When looking at the retention volume development, significant differences between the basins become evident. For example, no significant new reservoirs were built in the Reuss basin after 1960. Yet, in the Upper Rhine basin, several large reservoirs were built and put into operation between 1950 and 1970.

To better quantify the increasing retention volumes, the observed average monthly streamflow of the four relevant gauges was analysed:

Three time periods were defined:

- 1910–1924: time period without or with only minor influence of reservoirs or other anthropogenic influences
- 1940–1954: time period that shows a markedly increasing retention volume but overall retention volume still less than today
- 1997–2011: time period representing the current situation



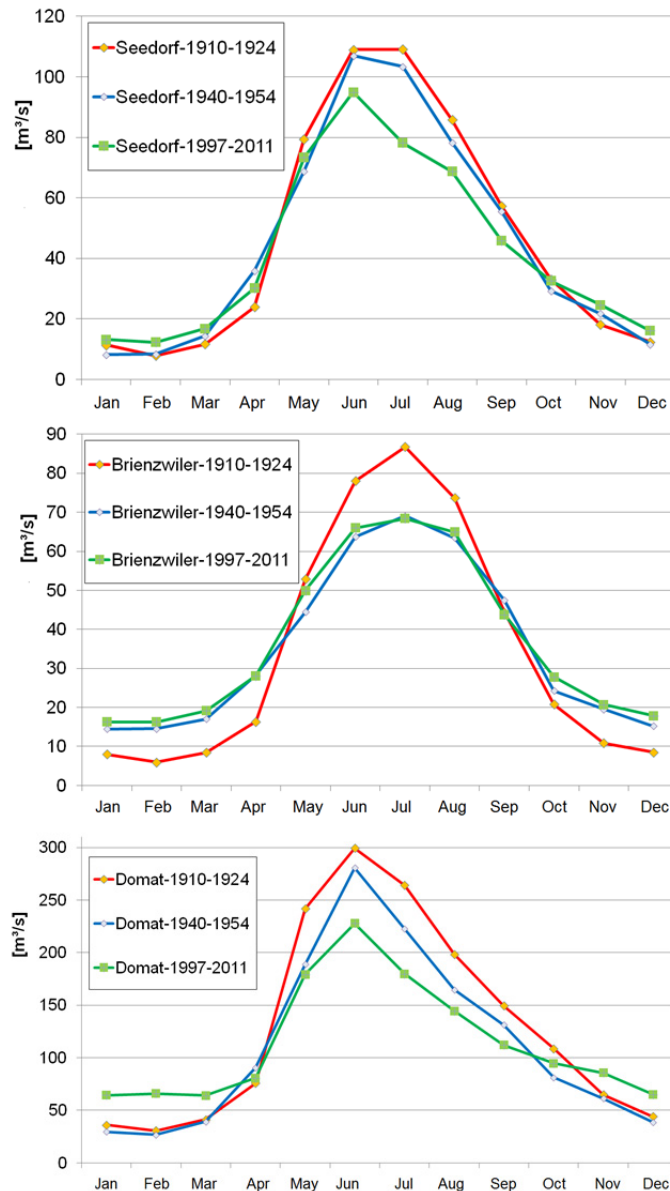


Figure 6.6: Average observed monthly streamflow (in m³/s) at the gauges Seedorf/Reuss (upper left), Brienzwiler/Aare (upper right) and Domat-Ems/Rhein (lower) for the time periods 1910–1924 (red), 1940–1954 (blue), and 1997–2011 (green).

In the final integration of the changes in water management practices into the LARSIM-Hochrhein model also the HBV modelling results from the glacierized headwater catchments were taken into consideration. Two to three dates were chosen to adjust the volumes of the implemented cumulative reservoirs to represent the development of the actual retention volume. The model reservoir retention volumes for the Swiss part of the Rhine basin were adjusted in 1932, 1954, and 1961. For the Ill basin, the adjustment was implemented in 1959, since the Lünensee reservoir, representing ca. 75% of the total retention volume in the Ill basin, was put into operation in that year.

To test the effects of the cumulative reservoirs, model simulations with and without these reservoirs were conducted. Figure 6.7 shows an example of this model experiment for the gauge Brienzwiler/Aare. The figure includes the model efficiency values (Nash-Sutcliffe-Coefficient) with and without the cumulative reservoirs. Again three time periods were chosen to represent the increase in retention volume upstream of the theoretical model reservoir (1901–1931, 1932-1953 and 1954-2006).

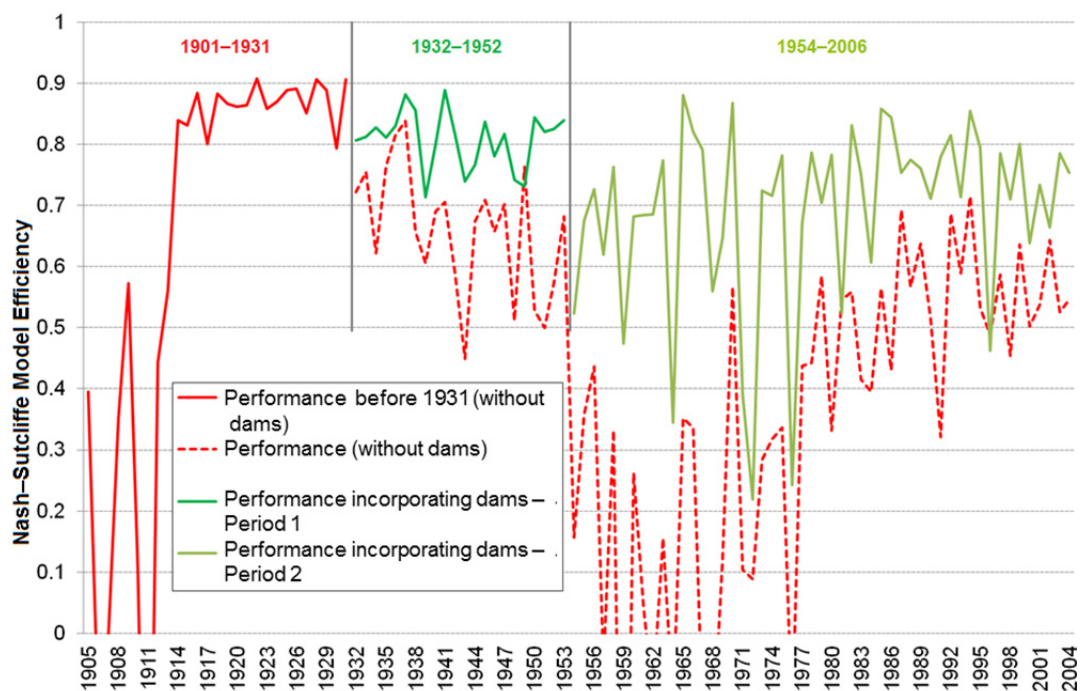


Figure 6.7: Annual model efficiency (Nash-Sutcliffe-Coefficients) at the gauge Brienzwiler/Aare with (green) and without (red) integration of the cumulative reservoir in the upper reach of the Aare for the time periods 1901–1931, 1932–1953, and 1954–2006.

It appears that for the time period until 1913 either the meteorological data of the HYRAS-REC dataset has some large discrepancies compared to the real values for the upper reaches of the Aare River or there are some errors in the streamflow observations. This leads to lower model efficiency values until 1913.

Overall however, Figure 6.7 shows that the integration of the cumulative reservoir has led to considerably better model performances compared to the model runs without the reservoir. It also becomes evident that the model performs best at the end of the 1901-1931 time period, when no major reservoirs existed. Model efficiencies are lower for more recent time periods even with the inclusion of the theoretical model reservoirs and with actually observed meteorological data (instead of reconstructed data). This suggests that the cumulative reservoirs within the model can only approximate the real conditions. Especially the current, more variable, reservoir operation rules result in a streamflow behaviour that cannot be predicted in detail by the model, thus leading to model efficiencies below 0.8.

### 6.2.3 Comparison of the snow water equivalent values from the simulations of the LARSIM-Hochrhein model against SLF data

LARSIM is already used operationally in many catchments in which snow plays a major role. These include catchments in the Alps (e.g., in the Swiss part of the Rhine basin, the Ill and Bregenzerach basins in Austria and the Iller and Isar basins in Bavaria) as well as basins in medium elevation mountain ranges such as the Jura, Black Forest, Vosges, and Swabian Alb. To test the results of the snow modelling of the high resolution LARSIM-Hochrhein model, a comparison of the modelled snow water equivalent values ( $SWE_{LARSIM}$ ) with the SWE product of the WSL Institute for Snow and Avalanche Research (SLF)  $SWE_{SLF}$  was conducted for the Swiss part of the Rhine basin (Hohmann, 2013; Hohmann, 2014).

This comparison was performed for the time period 1970 to 2006. It used the original data of the ASG Rhine project (without the correction for the systematic precipitation measurement error). The testing included the temporal as well as the spatial variability of the data by comparing maps of differences between  $SWE_{LARSIM}$  to  $SWE_{SLF}$  on certain dates for the entire model area, comparisons of the temporal evolution of  $SWE_{LARSIM}$  to  $SWE_{SLF}$  over certain subregions and over the catchments of 33 stream gauges over entire winters.

The first analysis of the comparisons between  $SWE_{LARSIM}$  and  $SWE_{SLF}$  indicated that LARSIM tended to predict a later melting of the snow cover. The LARSIM simulations were thus repeated using a temporally variable albedo algorithm. This algorithm considers the aging of the snow surface and associated decrease of the albedo closely following the approach of the "Utah Energy Balance Snow Accumulation and Melt Model" (Tarboton & Luce, 1996). The aging of the snow cover considers the changes in snow crystals due to water vapour diffusion and melting and refreezing processes as well as the deposition of dust on the snow cover. Implementing this snow aging decreased the differences between  $SWE_{LARSIM}$  and  $SWE_{SLF}$ .

Overall, the comparison of  $SWE_{LARSIM}$  to  $SWE_{SLF}$  showed over- as well as underpredictions by the model. Looking at the associated daily values for precipitation, temperature, and observed streamflow revealed that there were differences in the precipitation input. The spatially distributed precipitation input data of the LARSIM-Hochrhein-Model (HYRAS data) tends to predict lower precipitation values compared to the SLF product. However,  $SWE_{LARSIM}$  and  $SWE_{SLF}$  showed a good agreement for most of studied gauged catchments.

As a consequence of this analysis and the results of the HBV modelling of the headwater catchments (see Section 6.3.1.), all precipitation input to the LARSIM-Hochrhein-model as well as to the HBV models used a correction for the systematic error in precipitation observations based on Sevruk (1989).

#### **6.2.4 Model performance of runoff simulation at selected gauges**

To analyse the model performance for the streamflow simulations of the 106 year study period (1901-2006) the ratio of annual simulated and modelled runoff ( $Q_{sim}/Q_{obs}$ ) as well as the Nash-Sutcliffe model efficiency calculated from daily time series of observed and modelled streamflow were used. Figures 6.8 to 6.10 show the resulting annual values for the stream gauges Basel, Kaub, and Lobith.

The Figures show that the runoff ratios and efficiency values differ more from their ideal value of 1 for the time period 1901 to 1951 when the model was run with HYRAS-REC input. This product underestimates precipitation as discussed in Section 2.3. The values improve after 1951, when HYRAS input was used. It has to be noted, however, that the discrepancies between modelled and observed data are not extreme and that annual mean values were reproduced reasonably well by the model. It was concluded that the quality of the simulations using the LARSIM-Hochrhein and LARSIM-ME-Rhein can adequately reproduce the streamflow over the 106 year study period in the Rhine River basin, and thus the generated meteorological data products may be used.

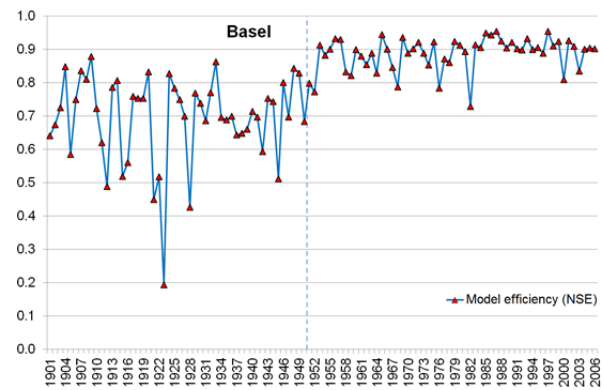
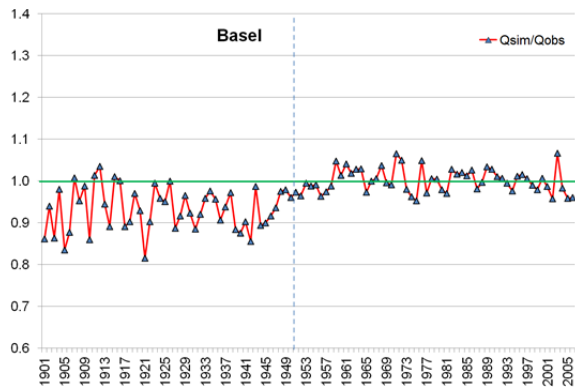


Figure 6.8: Annual ratios of Qsim to Qobs (left) and annual NSE values (right) at the gauge Basel/Rhein from 1901 to 2006 (LARSIM-Hochrhein).

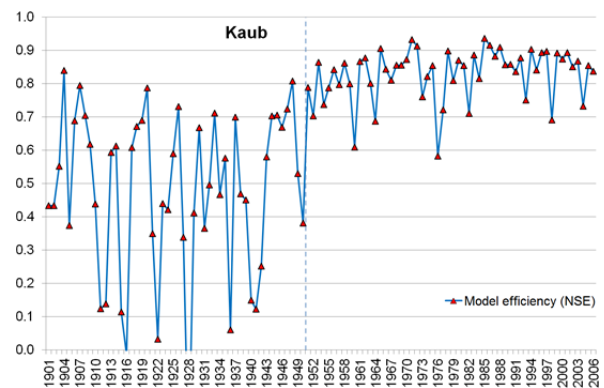
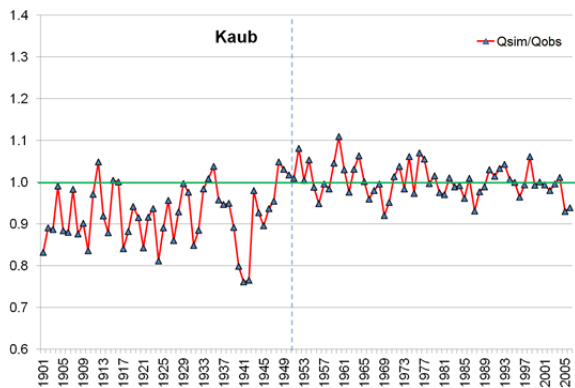


Figure 6.9: Annual ratios of Qsim to Qobs (left) and annual NSE values (right) at the gauge Kaub/Rhein from 1901 to 2006 (LARSIM-ME-Rhein).

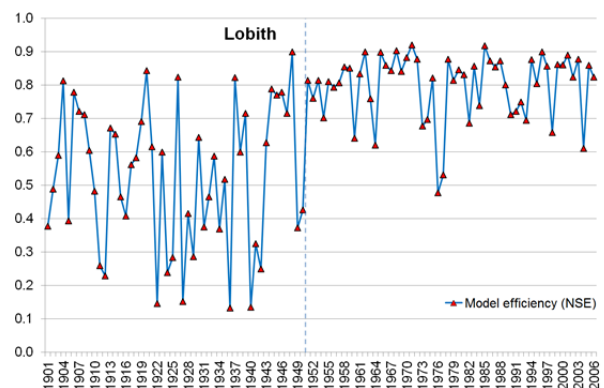
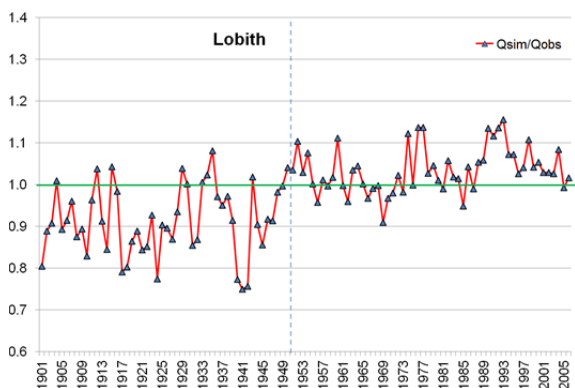


Figure 6.10: Annual ratios of Qsim to Qobs (left) and annual NSE values (right) at the gauge Lobith/Rhein from 1901 to 2006 (LARSIM-ME-Rhein).

### 6.3 Modelled components of streamflow (1901–2006)

#### 6.3.1 Average streamflow components

A first analysis looked at the computed average annual snowmelt and ice melt components of streamflow for the time period from 1901 to 2006. Figure 6.11 shows annual averages of the fractions of the streamflow components for major Rhine gauges for the time period 1901 to 2006. To determine the fractions, the annual averages of total streamflow and of the streamflow components (in  $m^3/s$ ) for the period 1901 to 2006 were calculated and then converted to relative fractions (in % of streamflow).

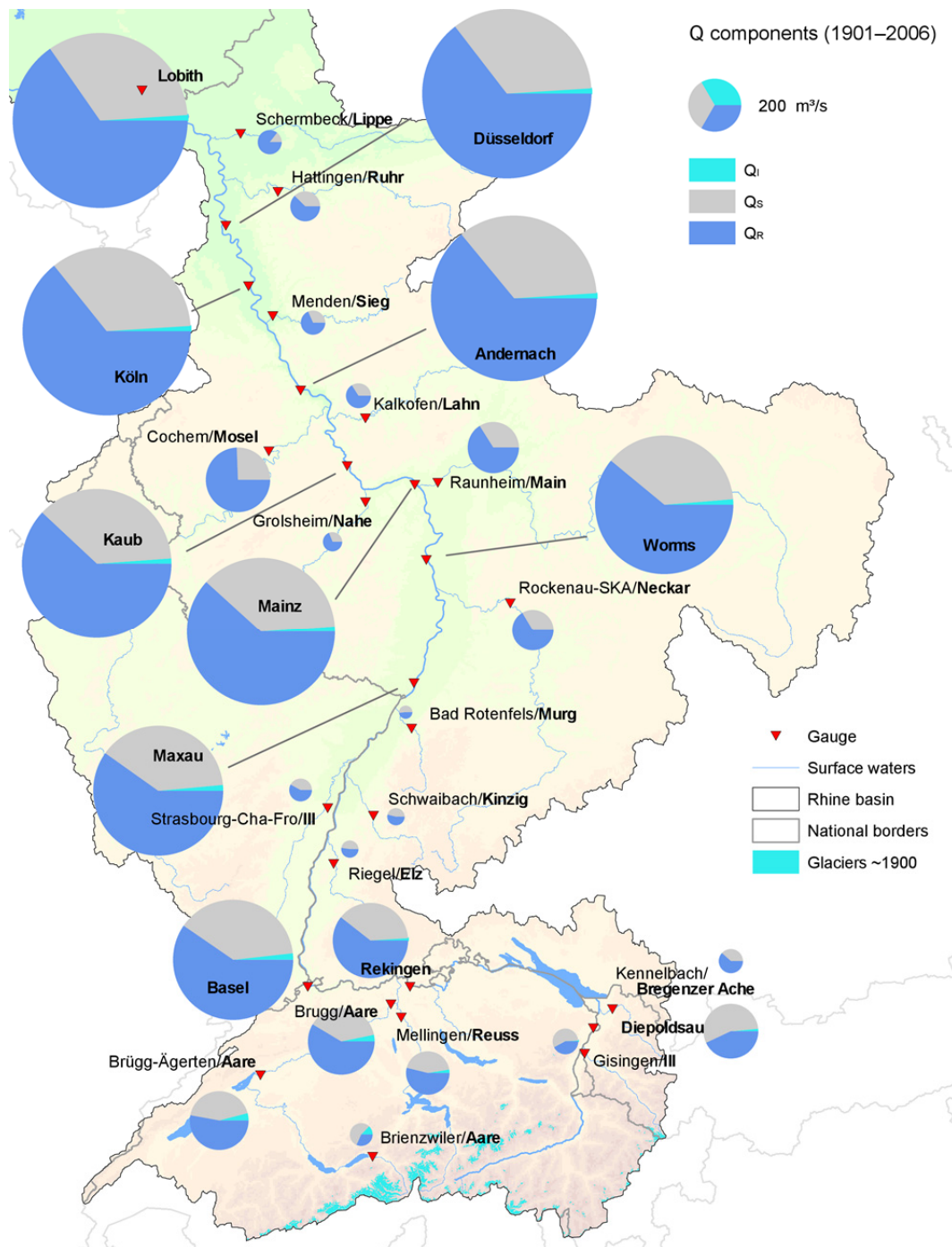


Figure 6.11: Fractions of rain ( $Q_R$ ), snowmelt ( $Q_S$ ) and ice melt ( $Q_I$ ) components of streamflow in the Rhine and its tributaries (annual averages over the time period 1901–2006).

Alternatively, the mean of the daily relative fractions of the components of all days in the period 1901–2006) could be specified. However, this option is omitted here to enable the comparison with results from other studies that modelled and determined streamflow components at lower than daily resolutions.

It becomes evident that especially the streamflow in the Aare region includes major contributions of ice melt. The relative fraction of the ice melt component of streamflow downstream of the gauge Basel and even in the Alpine Rhine (River Rhine upstream of Lake Constance) is only marginally detectable. Annual average fractions of ice melt (1901–2006) of fewer than 2% were calculated below the gauge Basel.

Figure 6.12 shows the hydrological regimes as well as the different streamflow components for 1901 to 2006 for the four gauges Brienzwiler/Aare, Basel/Rhein, Cochem/Mosel und Lobith/Rhein as an example. Aside from the absolute values, the Figure also shows the relative fractions of the streamflow components. The snowmelt component  $Q_S$  shows a decrease in the annual snowmelt component of streamflow from approx. 55% at the gauge Brienzwiler to 34% at the gauge Lobith, while the ice melt component  $Q_I$  decreased from approx. 13% at Brienzwiler to 0.8% at Lobith. The average snowmelt component at the gauge Cochem/Mosel amounts to about 26%, with no contribution from ice melt.

Figure 6.12 clearly exhibits the difference between the nival-glacial regime at the gauges Brienzwiler and Basel showing a summer maximum of streamflow and the pluvial regime at the gauges Cochem and Lobith with winter streamflow maxima.

Figure 6.12 shows the average simulated streamflow values along with the data observed at the stream gauges for the period 1901 to 2006. The values generally match fairly closely. However, a systematic underprediction of streamflow by the model downstream of Basel is evident.

- As was the case for the water balances shown in Figures 6.8 to 6.10, for the three gauges along the Rhine, precipitation appears to have been underestimated during the data reconstruction period by the HYRAS-REC dataset. This frequently leads to lower simulated than observed streamflow values for the time before 1951 as in the hydrological regimes in Figure 6.12.
- The underprediction of the observed streamflow data along the Rhine gauges is especially evident for the months March to May. One cause may be the modelled snow cover in LARSIM. LARSIM uses a fixed threshold temperature to distinguish between rain and snow. All precipitation is considered to be snow once the air temperature is below that threshold. Precipitation is considered to be rain if the air temperature is above the threshold. This leads to a water content of the snowpack that is often too low in the model and may be one cause for a delayed start of the snowmelt.

The most recent version of LARSIM therefore includes an algorithm that considers mixed precipitation. This algorithm considers a fluent transition between rain and snow for a certain temperature range and causes higher modelled water contents of the snow cover. First tests with the new algorithm indicate an improved dynamic in the modelled snowmelt. Thus, it can be expected that the underprediction of spring streamflow may be reduced in the future with this new snow routing, which was not yet available for the ASG Rhine project.

The fractions of snowmelt- and ice melt discussed so far were averaged annual values for the time period 1901 to 2006. The analyses of the **average monthly fractions of the ice melt streamflow component  $Q_I$**  show that the  $Q_I$  fractions (in % of total streamflow) are considerably higher during the summer months. This can also be seen in Figure 6.12.

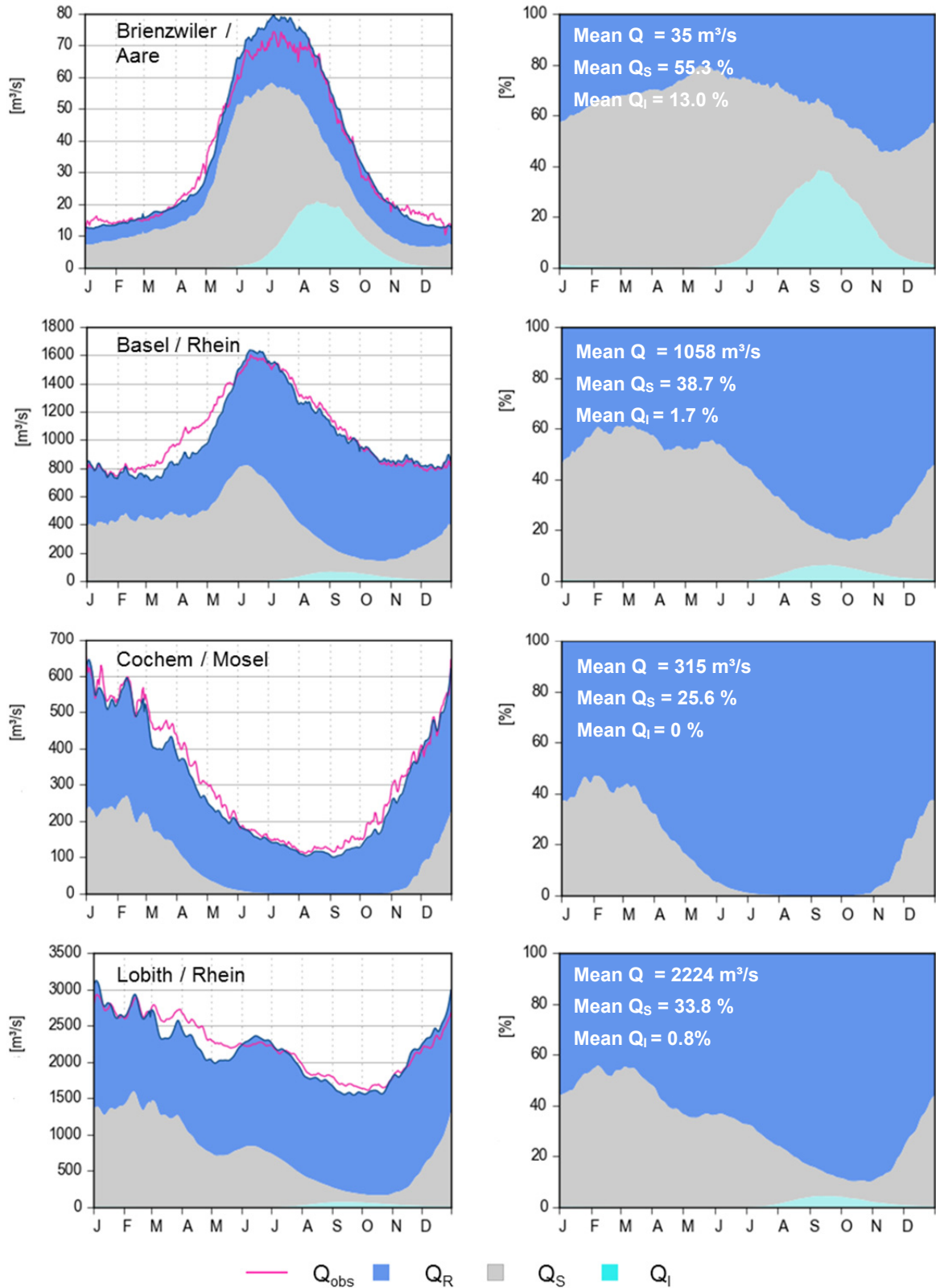


Figure 6.12: Hydrological regimes with modelled streamflow components  $Q_I$ ,  $Q_S$ ,  $Q_R$  (left: absolute values, right: relative fractions) for selected gauges in the Rhine basin (annual averages for the period 1901 – 2006)

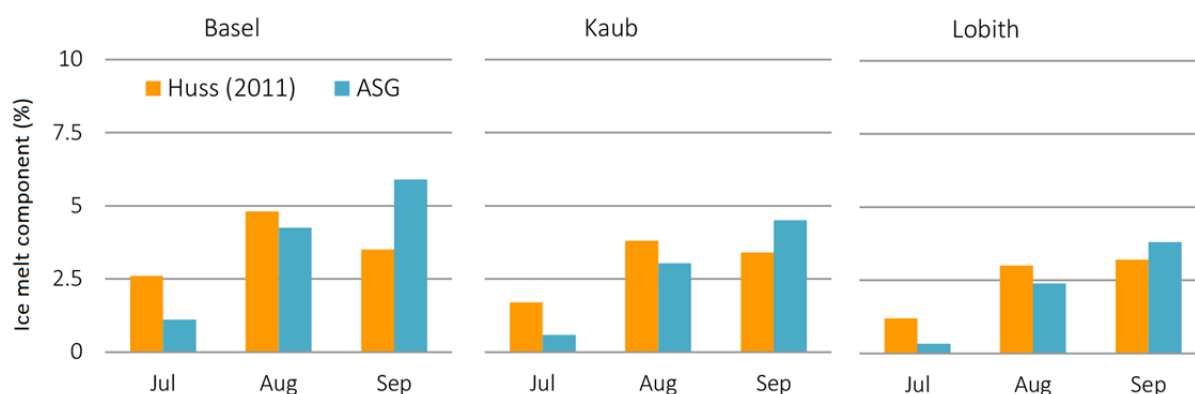


Figure 6.13: Fractions of  $Q_i$  (%) for the months July, August, and September at selected Rhine gauges (monthly averages for the period 1908–2006) compared to “contribution of the bare ice melt component” data from Huss (2011) for the period 1908–2008 (see Huss (2011): Table S2, supporting information). Percentages are for observed streamflow at the respective gauges.

An average fraction of the  $Q_i$  component of 4.5% for August and approx. 6% for September at Basel and 2.6% for August and 4.2% for September at Lobith were modelled. Modelled September values are higher than modelled August values, which can be attributed partly to the generally lower absolute streamflow in September compared to August, which, along with a sustained ice melt component amount, leads to a higher relative ice melt fraction. Additionally, the influence of the modelled retention in the reservoirs, lakes, and along the river reaches delay the maximum fraction of the ice melt contributing to runoff (also see the following Section 6.4).

Figure 6.13 also shows values modelled by Huss (2011) for the time period 1908 to 2008 for the three gauges. For better comparability, Figure 6.13 thereby shows the average monthly values obtained during the ASG Rhine project for the time period 1908–2006 instead of the entire study period 1901–2006 period. The values from Huss (2011) are slightly higher in July but lower in September.

One reasons for this difference may be the comparably simplified simulation of the storage processes and channel routing of the ice melt runoff from the glacier to the tributary and further along the main stem Rhine used by Huss (2011). The comparison with the study by Huss (2011), however, shows that the order of magnitude of the components modelled by the ASG Rhine project agree with those of other studies. The advantage of the values obtained during this project is the availability of the modelled component time series for further analyses as high-resolution daily values. Additionally, snowmelt and other runoff generating mechanisms were also modelled for the non-glacierized part of the basin for the same long-term period and their effect on streamflow can thus be tracked also.

The modelled maximum daily and monthly streamflow components are much higher than the averaged values depicted in Figures 6.12 and 6.13. Therefore, the following section will investigate the extreme values within the time period 1901 to 2006 in more detail.

### 6.3.2 Minimum and maximum runoff contributions

Table 6.2 lists the **average maximum and minimum monthly snowmelt components  $Q_s$**  for 29 selected gauges in the Rhine basin. The periods 1901–1951 (input dataset HYRAS-REC) and 1951–2006 (input dataset HYRAS) are shown separately.

Differences in the  $Q_s$  values for the two periods 1901–1950 and 1951–2006 are notably small. The average and minimum monthly values show slightly lower snowmelt components of streamflow for the latter period as may be expected due to the recent warming trend:

- The average monthly values of  $Q_S$  for 1901–1951 are between ca. 55.5% (in the Aare basin at the gauge Brienzwiler) and ca. 34.5% (for the Rhine basin at Lobith) whereas the slightly reduced values for 1951–2006 are 55.3% (Brienzwiler) and 33.4% (Lobith).
- The same can be seen for monthly minimum values with  $Q_I$  values of 12.7% (Brienzwiler) and 3.2% (Lobith) during the early and values of 11.5% (Brienzwiler) and 2.2% (Lobith) for the later period.
- The streamflow of those Rhine tributaries downstream of Basel with no headwaters in the Alps are dominated entirely by rain over several months; therefore their minimum  $Q_S$  values are 0%. However, even these catchments can have  $Q_S$  values of over 90% for the snowmelt season during the months of February and March.

The modelled maximum values of relative fractions of  $Q_S$  show a different picture for the two time periods 1901–1951 and 1951–2006:

- Whereas for the gauges upstream of Basel the maximum monthly average values for the later period are slightly lower compared to the earlier one, they are slightly higher for the gauges downstream of Basel. The maximum monthly averages of  $Q_S$  at the Rhine gauges generally fall in the 80 to 90% range.

The modelled maximum daily snowmelt component of streamflow  $Q_S$  reach values of over 90% at all gauges and 100% (or close to) at many, not exclusively alpine, gauges. It has to be noted, however, that these extreme rare daily values of up to 100% could, at least partially, be the result of the chosen conceptual approach to simulate the streamflow components with the limited volume mixing tank approach (see Chapter 4). The maximum streamflow component fractions are discussed in more detail in the following chapter.

Table 6.3 lists the average and maximum daily values of ice melt components  $Q_I$  for selected Rhine gauges upstream of Basel and important gauges downstream to Lobith. As in Table 6.2, the values are presented separately for the two time periods up to and after 1951:

- The highest  $Q_I$  values are modelled at all Rhine gauges for the known dry, hot, and low flow years 1947 (maximum during the first period up to 1951) and 2003 (maximum for the second period up to 2006). The maxima for the first period (1947) are higher with values of 33.4% at Basel and 26.4% at Lobith compared to the year 2003 during the second period, when maximum daily  $Q_I$  values reached 22.9% at Basel and 17.3% at Lobith.
- The absolute values of the modelled ice melt component (in  $\text{m}^3/\text{s}$ ) for the days with maximum  $Q_I$  in 1947 and 2003 at the gauges Basel and Lobith are very similar with values of around 150  $\text{m}^3/\text{s}$ . Some of the gauges in the middle and lower Rhine even show slightly higher absolute  $Q_I$  values for 2003 compared to 1947.
- Table 6.3 lists the maximum absolute  $Q_I$  that occurred on the day of the maximum relative fractions of  $Q_I$ . When looking at the maximum absolute  $Q_I$  values (and the associated relative  $Q_I$  values) for the two low flow years 1947 and 2003 a different picture emerges: The maximum  $Q_I$  at Basel occurred on 31 Aug 2003 with a value of 171.1  $\text{m}^3/\text{s}$  (1947: 23 Aug 1947 and 180.5  $\text{m}^3/\text{s}$ ) and at Lobith on 06 Sep 2003 with 162.3  $\text{m}^3/\text{s}$  (1947: 30 Aug 1947 and 173.4  $\text{m}^3/\text{s}$ ).

Table 6.2: Modelling results: mean, maximum and minimum monthly averages for the fractions of  $Q_s$  (% of  $Q$ ) for the time periods up to and after 1951 for selected gauges in the Rhine basin (ordered upstream to downstream, for location of the gauges see Figure 6.11).

Gauge/Stream	Period 1901–1950 (with reconstructed climate input HYRAS-REC)					Period 1951–2006				
	Mean (%)	Maximum (%)	Month	Minimum (%)	Month	Mean (%)	Maximum (%)	Month	Minimum (%)	Month
Gisingen / Ill	62.1	98.7	May 1917	1.1	Aug 1934	52.3	97.3	May 1982	1.0	Sep 1958
Bregenzer Ach	48.2	98.9	Feb 1922	0	Sep 1920	30.6	99.2	Mar 1956	0	multiple times
Diepoldsau / Rhein	57.5	94.2	May 1917	7.6	Sep 1950	53.9	90.0	Jun 1970	6.3	Oct 1953
Rekingen / Rhein	40.2	82.2	Jun 1919	4.3	Sep 1931	37.2	82.0	Feb 1982	4.3	Sep 2005
Mellingen / Reuss	45.0	85.0	Mar 1931	5.6	Sep 1950	42.5	83.8	Feb 1982	5.1	Sep 2005
Brienzwiler /Aare	55.5	90.9	May 1907	12.7	Sep 1921	55.3	87.5	Apr 1968	11.5	Oct 1990
Brügg-Ägerten /Aare	43.8	86.7	Apr 1931	6.5	Sep 1931	42.4	83.6	Mar 1985	5.6	Oct 2006
Brugg / Aare	38.9	86.0	Mar 1931	5.3	Sep 1931	37.9	85.6	Feb 1981	4.2	Oct 2006
<b>Basel / Rhein</b>	<b>39.9</b>	<b>82.3</b>	<b>Mar 1931</b>	<b>4.8</b>	<b>Sep 1931</b>	<b>37.9</b>	<b>84.9</b>	<b>Feb 1982</b>	<b>4.3</b>	<b>Oct 2006</b>
Riegel / Elz	49.7	96.1	Apr 1944	0	multiple times	46.7	97.9	Mar 1953	0	multiple times
Schwaibach / Kinzig	47.3	99.7	Feb 1922	0	multiple times	45.6	100.0	Feb 1982	0	multiple times
Strasbourg / Ill	43.5	90.4	Mar 1931	0	multiple times	41.2	91.5	Feb 1982	0	multiple times
Bad Rotenfels / Murg	54.3	99.4	Mar 1931	0	multiple times	50.3	99.9	Mar 1953	0	multiple times
Maxau / Rhein	39.9	84.1	Mar 1931	4.3	Sep 1931	37.9	87.4	Feb 1982	3.3	Oct 2006
Rockenau / Neckar	32.9	93.4	Mar 1931	1.5	Jun 1926	34.4	98.3	Mar 1953	1.0	Jun 1965
Worms / Rhein	38.7	84.7	Mar 1931	4.1	Sep 1931	37.1	89.1	Feb 1982	3.2	Oct 2006
Raunheim / Main	33.3	89.4	Feb 1941	1.2	Oct 1939	34.7	97.0	Mar 1970	0.7	Oct 1998
Mainz / Rhein	37.9	84.5	Mar 1931	3.9	Sep 1931	36.6	90.4	Feb 1982	3.1	Oct 2006
Grolsheim / Nahe	29.1	89.3	Mar 1931	0	Oct 1930	32.9	97.6	Feb 1970	0	multiple times
<b>Kaub / Rhein</b>	<b>37.7</b>	<b>84.3</b>	<b>Mar 1931</b>	<b>3.9</b>	<b>Sep 1931</b>	<b>36.5</b>	<b>90.4</b>	<b>Feb 1982</b>	<b>3.1</b>	<b>Oct 2006</b>
Kalkofen / Lahn	32.8	92.4	Feb 1941	0	multiple times	35.3	97.9	Mar 1970	0	multiple times
Cochem / Mosel	25.8	89.1	Jan 1924	0	multiple times	25.7	92.3	Feb 1981	0	Oct 1951
Andernach / Rhein	35.8	85.1	Mar 1931	3.5	Sep 1931	34.6	90.1	Feb 1982	2.3	Oct 2006
Menden / Sieg	30.3	93.9	Feb 1907	0	multiple times	32.9	97.4	Mar 1970	0	multiple times
Köln / Rhein	35.5	85.0	Mar 1931	3.4	Sep 1931	34.5	89.7	Feb 1982	2.3	Oct 2006
Düsseldorf / Rhein	35.2	84.5	Mar 1931	3.4	Sep 1931	34.2	88.8	Feb 1982	2.3	Oct 2006
Hattingen / Ruhr	38.0	96.1	Mar 1901	0	multiple times	37.7	96.9	Mar 1970	0	multiple times
Schermbeck / Lippe	14.0	81.2	Mar 1942	0	multiple times	15.1	78.3	Mar 1970	0	multiple times
<b>Lobith / Rhein</b>	<b>34.5</b>	<b>82.4</b>	<b>Mar 1942</b>	<b>3.2</b>	<b>Sep 1931</b>	<b>33.4</b>	<b>87.8</b>	<b>Mar 1953</b>	<b>2.2</b>	<b>Oct 2006</b>

Table 6.3: Modelling results: mean and maximum fractions (daily values) of  $Q_i$  (% of  $Q$ ) for the time periods up to and after 1951 for selected gauges in the Rhine basin (ordered upstream to downstream, for location of the gauges see Figure 6.11). Values that show considerable differences between simulated ( $Q_{sim}$ ) and observed ( $Q_{obs}$ ) (and therefore higher uncertainties for the calculation of the relative fraction of  $Q_i$ ) are highlighted in red.

Gauge/Stream	Period 1901–1950 (based on reconstructed climate input HYRAS-REC)							Period 1951–2006						
	Mean	Maximum relative fraction $Q_i$ (and corresp. absolute value)						Mittel	Maximum relative fraction $Q_i$ (and corresp. absolute value)					
	$Q_i$ (%)	Date	$Q_i$ (%)	$Q_i$ (m <sup>3</sup> /s)	$Q_{sim}$ (m <sup>3</sup> /s)	$Q_{obs}$ (m <sup>3</sup> /s)	$Q_i / Q_{obs}$ (%)	$Q_i$ (%)	Date	$Q_i$ (%)	$Q_i$ (m <sup>3</sup> /s)	$Q_{sim}$ (m <sup>3</sup> /s)	$Q_{obs}$ (m <sup>3</sup> /s)	$Q_i / Q_{obs}$ (%)
Gisingen / Ill	0.9	1947-9-20	67.8	5.7	8			1.0	1952-8-14	49.5	4.7	9.58	34	13.9
Diepoldsau / Rhein	1.9	1947-9-20	39.5	45.4	115	101	44.9	1.1	1952-9-9	20.6	28.4	138.0	147	19.3
Rekingen / Rhein	1.1	1947-9-23	19.7	31.7	161	188	16.9	0.6	2003-8-29	9.9	25.0	253.4	222	11.2
Mellingen / Reuss	3.0	1947-9-22	53.5	46.3	87	57	80.6	2.2	2003-8-27	38.2	34.3	89.8	76.2	45.0
Brienzwiler / Aare	15.2	1947-9-21	81.8	38.6	47	31	123.6	11.1	2003-8-13	73.8	52.6	71.3	71.1	74.0
Bügg-Ä. / Aare	4.7	1947-9-22	49.2	73.5	150	170	43.3	3.6	2003-8-28	41.8	82.8	198.1	189	43.8
Brugg / Aare	3.7	1947-9-22	43.6	72.8	167	180	40.5	2.7	2003-8-27	37.0	82.2	222.1	215	38.2
<b>Basel / Rhein</b>	<b>2.1</b>	<b>1947-9-22</b>	<b>33.4</b>	<b>158.1</b>	<b>474</b>	<b>481</b>	<b>32.9</b>	<b>1.4</b>	<b>2003-8-27</b>	<b>22.9</b>	<b>147.3</b>	<b>644.6</b>	<b>555</b>	<b>26.5</b>
Maxau / Rhein	1.8	1947-9-23	31.8	156.3	492	504	31.0	1.2	2003-8-27	22.0	148.4	675.2	573	25.9
Worms / Rhein	1.6	1947-9-23	30.8	155.2	504	550	28.2	1.1	2003-8-27	21.2	149.2	704.2	611	24.4
Mainz / Rhein	1.4	1947-9-23	29.2	153.8	526	660	22.6	0.9	2003-8-27	20.0	150.3	751.2	694	21.7
<b>Kaub / Rhein</b>	<b>1.4</b>	<b>1947-9-23</b>	<b>29.1</b>	<b>153.0</b>	<b>526</b>	<b>555</b>	<b>27.6</b>	<b>0.9</b>	<b>2003-8-27</b>	<b>19.9</b>	<b>150.8</b>	<b>758.6</b>	<b>723</b>	<b>20.9</b>
Andernach / Rhein	1.1	1947-9-23	27.8	151.7	546	640	23.7	0.7	2003-8-27	18.6	151.3	813.5	788	19.2
Köln / Rhein	1.1	1947-9-23	27.5	150.3	547	650	23.1	0.7	2003-8-28	18.4	151.3	822.9	804	18.8
Düsseldorf / Rhein	1.1	1947-9-23	27.2	149.2	548	660	22.6	0.7	2003-8-28	18.1	151.8	836.7	803	18.9
<b>Lobith / Rhein</b>	<b>1.0</b>	<b>1947-9-23</b>	<b>26.4</b>	<b>146.6</b>	<b>556</b>	<b>725</b>	<b>20.2</b>	<b>0.7</b>	<b>2003-8-28</b>	<b>17.3</b>	<b>152.6</b>	<b>884.3</b>	<b>901</b>	<b>16.9</b>

Figure 6.14 illustrates the relations between the relative and absolute ice melt component for the year 2003. Here it becomes evident why the absolute  $Q_I$  at the time of the maximum relative  $Q_I$  fraction was higher at Lobith than at Basel (Table 6.3). Section 6.4.2 looks at the  $Q_I$  component during the low flow situation 2003 in more detail.

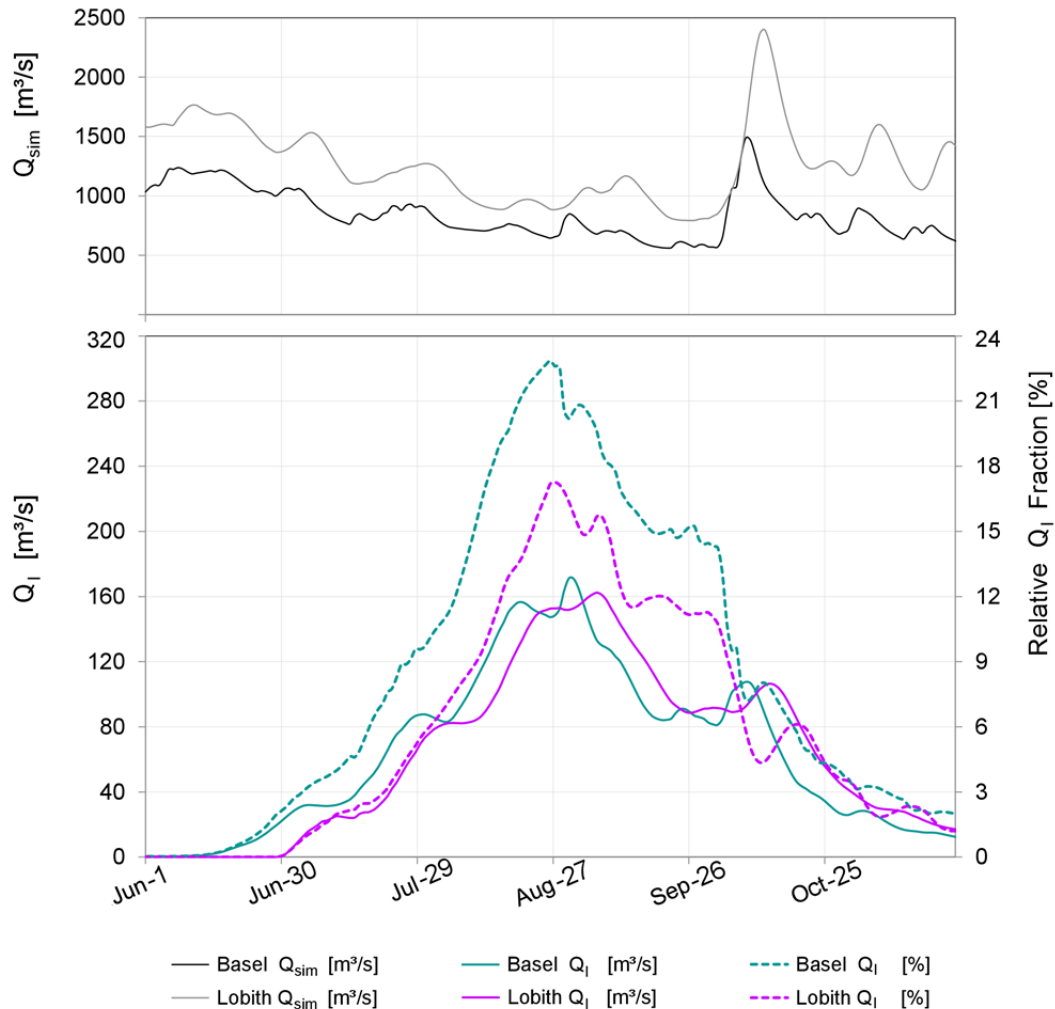


Figure 6.14: Modelled streamflow with absolute and relative fractions of  $Q_I$  for summer and autumn 2003 at the gauges Basel/Rhein and Lobith/Rhein.

When discussing single extreme daily values it has to be kept in mind that the relative streamflow component fractions depend directly on the modelled overall streamflow and are therefore subject to some uncertainty. For example, it was found that the model clearly underpredicted the observed total streamflow for the low flow year 1947 for virtually all gauges along the middle and lower Rhine (see the highlighted red numbers in Table 6.3, and Figures 6.14 and 6.15).

This bias then results in an overprediction of the relative  $Q_I$  values. Relating the modelled  $Q_I$  value instead to the observed streamflow ( $Q_I / Q_{obs}$  in Table 6.3) results in a lower fraction of ca. 20% instead of the 26.4% that was obtained in relation to the biased modelled streamflow.

The expected generally lower model performance for the period before 1951, when the HYRAS-REC input was used, has to be considered when interpreting the results especially concerning hydrological extreme events. Further aspects concerning the relevance and uncertainty of unusually high relative  $Q_I$  fractions in low flow years of the Rhine are discussed in detail in Section 6.4.

## 6.4 Modelled streamflow components in low flow years

### 6.4.1 Streamflow components in selected low flow years in comparison

Aside from analysing the behaviour of the average streamflow components from snowmelt and ice melt, it is of particular importance to look at their contributions during low flow years. Thus, the low flow years 1921, 1947, 1976, and 2003 were looked at in particular (see also Section 5.6). Figures 6.15 and 6.16 show the daily streamflow and streamflow component fractions for the two years 1947 and 2003.

The low flow year 1976 showed a comparably low average contribution of ice melt to runoff of about 2% and 1% at the gauges Basel and Lobith respectively. Those two gauges had  $Q_I$  values higher than 6% and 3% respectively for 1947. As stated in Chapter 5, in contrast to the other low flow years the year 1976 did not have particularly warm temperatures in the alpine regions of the Rhine basin. Consequently, the year 1976 will not be discussed further.

When looking at 1947 and 2003, it becomes evident from Figures 6.15 and 6.16 that the simulated fits the measured streamflow fairly well not only for the year 2003 (which used the HYRAS input dataset) but also for the year 1947 (which used the reconstructed HYRAS-REC input dataset). The underprediction of the modelled streamflow for the autumn of 1947 at the gauge Lobith was already noted (see Table 6.3). The weekly fluctuations in the hydrograph of the observations at the gauge Brienzwiler illustrate the influence of the upstream water storage for hydropower production. However, the cumulative model reservoir, which is included in the model upstream of that gauge, enables a good simulation of the streamflow at least for 1947 and 2003.

Figures 6.17 combines the average annual and average monthly values of the modelled snow- and ice melt components for three low flow years:

- Average annual values 1921, 1947, and 2003: The evolution of the streamflow components along the Rhine in the low flow years 1921, 1947, and 2003 shows that the snowmelt component in those years decreased from an approx. 45 % at the gauge Brienzwiler to 30 % at Lobith. The fraction of ice melt during the low flow years 1921, 1947, and 2003 declines along the Rhine from a range of 21 % to 45 % (gauge Brienzwiler) down to a range of 1.7 % to 5.8 % (gauge Lobith).
- Average monthly values in 1921, 1947, and 2003: For the summer months August and September during the low flow years the ice melt components at the gauges are much higher than their long-term means. The averages of the  $Q_I$  fractions at the gauge Lobith for the three low flow years range between 11% and 18% for August and between 13% and 24% for September. Remarkably, the October values during 1921 and 1947 are still relatively high (around 20% at the gauge Lobith). The October 2003  $Q_I$  values are considerably lower (5.5% at the gauge Lobith).

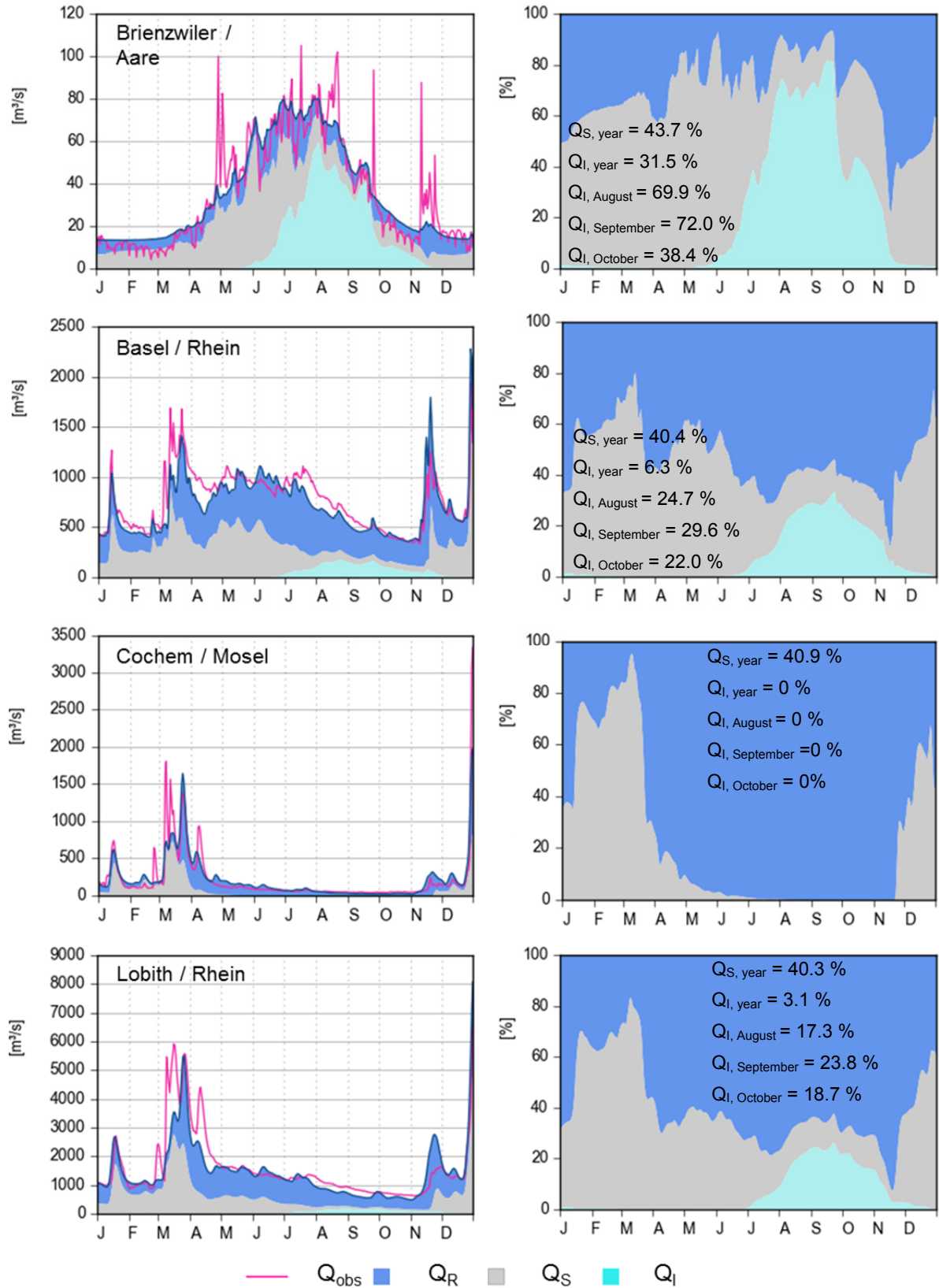


Figure 6.15: Observed and modelled hydrographs for the low flow year 1947 with the simulated streamflow components  $Q_R$ ,  $Q_S$ ,  $Q_I$  (left: absolute values; right relative fractions) at selected gauges in the Rhine basin (daily values 1947).

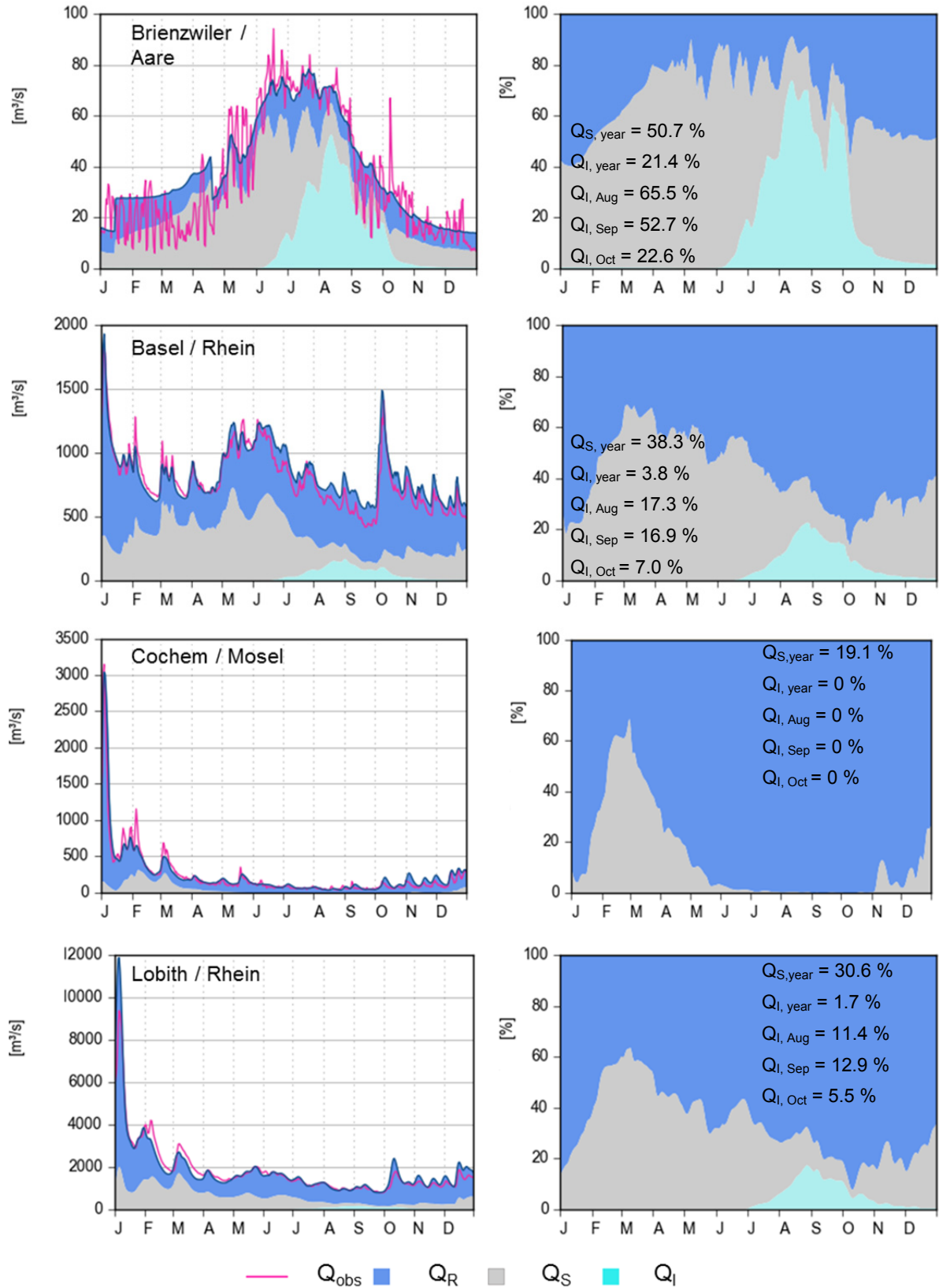


Figure 6.16: Observed and modelled hydrographs for the low flow year 2003 with the simulated streamflow components of  $Q_R$ ,  $Q_S$ ,  $Q_I$  (left: absolute values; right relative fractions) at selected gauges in the Rhine basin (daily values 2003).

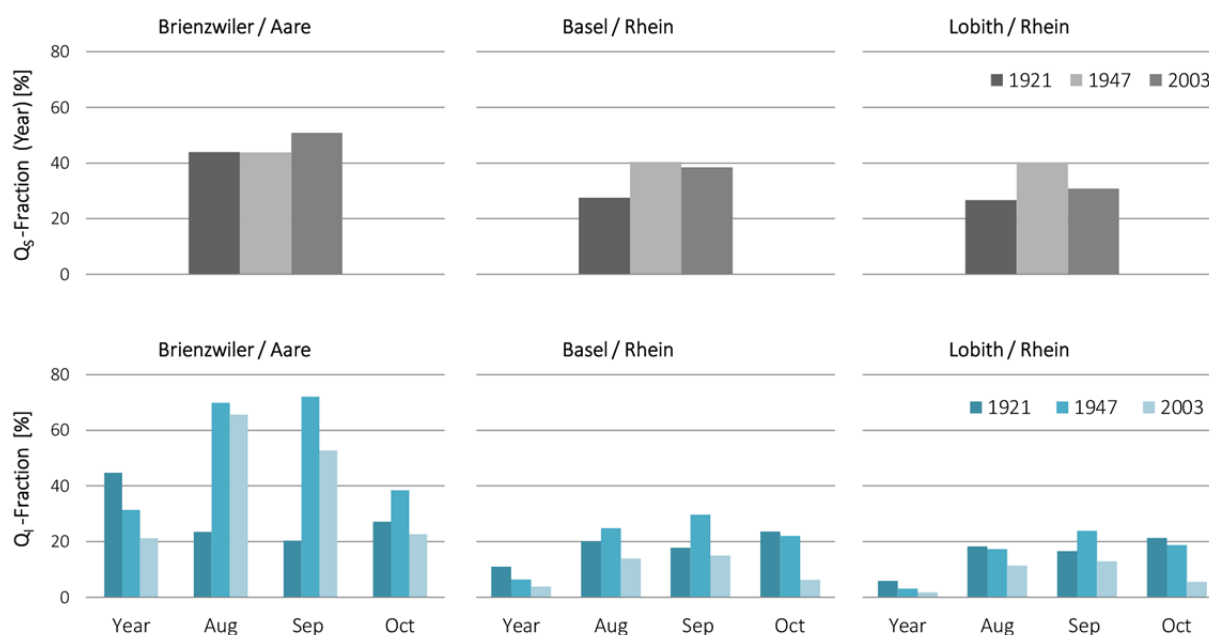


Figure 6.17: Fractions of  $Q_S$  (upper panel, average annual values) and  $Q_I$  (bottom average annual values and monthly values for August, September, and October) for the low flow years 1921, 1947, and 2003 at selected gauges in the Rhine basin.

The following aspects should be considered regarding the strikingly high  $Q_I$  values for October 1921 and 1947:

- The temporal evolution of the modelled ice melt components of streamflow at the gauges cannot be related directly to the temporal evolution of the glacial melt. Ice melt of glaciers will largely be finished in October. The ice melt components shown in Figure 6.17, however, are the response of the streamflow to the modelled glacier ice melt at certain locations along the river network. These values include the retention and storage within the modelled glacier storages, lakes, reservoirs and river channel routing.
- The high  $Q_I$  values for October 1921 and 1947 can at least partially be attributed to an intensive and prolonged ice melt season in those two extreme years (see Section 5.6.1).
- As is always the case when discussing relative fractions, it has to be considered that the low flows in the months of October 1921 and 1947 were among the most extreme of all time. This means that even average October  $Q_I$  values would have led to unusually high relative fractions of streamflow.
- The model generally underpredicts the total streamflow for the middle and lower reaches of the Rhine for the Octobers 1921 and 1947, which has the aforementioned effect on the relative fractions of  $Q_I$ .

Once again it should be stated, as a reminder, that the maximum daily values of the ice melt component can be much higher than monthly values (see Section 6.3). On individual days (in the time period 1901 to 2006) Rhine gauges down to Lobith showed an ice melt component of roughly one fifth of total streamflow.

Analysing the study results (see Figures in this chapter and the values listed in Tables 6.2 and 6.3) one finding stands out: the relative fractions of  $Q_I$  hardly decrease along the Rhine from the gauge at Basel to the Lobith gauge. This can be attributed to inflow from the tributaries of the Rhine being very low compared to the streamflow of the main stem Rhine, so that no considerable dilution and therefore no

significant decrease of the ice melt fraction takes place. For example, the average monthly streamflow for the August to October period in 1947 of the River Moselle at Cochem, the largest tributary to the Rhine below Basel, was 45 m<sup>3</sup>/s, while the Rhine's streamflow at the gauge Lobith was 895 m<sup>3</sup>/s (see Figure 6.15).

#### 6.4.2 Detailed analysis of the low flow year 2003

In many studies, 2003 has been considered a reference year or “benchmark event”, since it was the most extreme event in recent times. It also had numerous and partly far reaching impacts. The question what relevance the glacial ice melt had on the low flow in the Rhine was discussed with great controversy and was one of the reasons for the initiation of the ASG Rhine project. Thus, some results specifically concerning the modelled  $Q_I$  component for the low flow year 2003 are presented in detail.

Table 6.4 summarizes the average monthly absolute and relative  $Q_I$  for July, August, September, and October 2003 for selected gauges. Pronounced low flow conditions prevailed particularly in August and September along the middle and lower reaches of the Rhine. Streamflow recovered in October (see Figure 6.16). Thus, the most extreme low flow period in 2003 coincided with the annual maximum of  $Q_I$ . The monthly averages of the relative fractions of  $Q_I$  range between 10 and 15 % for the gauges along the middle and lower Rhine reaches for August and September, with the September values generally being slightly higher than the August values (Table 6.4). The monthly averages of the absolute  $Q_I$  values (in m<sup>3</sup>/s) only change marginally along the Rhine gauges.

Table 6.4: Average modelled  $Q_I$  values (absolute values in m<sup>3</sup>/s and relative fractions in % of  $Q$ ) for the months July, August, September, and October in the drought and low flow year 2003 for selected Rhine gauges (location for the gauges see Figure 6.11).

Gauge	July		August		September		October	
	(m <sup>3</sup> /s)	(%)						
Brienzwiler/Aare	23.7	32.9	42.9	65.5	21.5	52.7	5.9	22.6
Basel	49.0	5.5	126.9	17.3	109.2	16.9	64.1	7.0
Maxau	43.6	4.6	122.1	16.0	113.2	16.5	68.3	6.8
Worms	42.2	4.2	120.8	15.1	114.9	15.9	70.0	6.4
Mainz	40.7	3.8	119.5	14.0	116.7	15.0	71.8	6.2
Kaub	39.3	3.6	118.5	13.8	117.8	14.9	73.0	6.2
Andernach	37.7	3.2	117.1	12.7	119.0	13.6	74.4	5.8
Köln	36.1	3.0	116.0	12.3	120.6	13.5	76.1	5.7
Düsseldorf	34.6	2.8	114.8	12.1	121.6	13.4	77.3	5.7
Lobith	30.7	2.4	112.0	11.4	124.0	12.9	80.2	5.5

Similar to the long-term averages illustrated in the earlier Figure 6.13, Figure 6.18 shows the modelling results for the average  $Q_I$  in the months July, August, and September for the Rhine gauges Basel, Kaub, and Lobith in comparison to the results from the study by Huss (2011). As for the long-term average values shown in Figure 6.13, in this study the modelled ice melt component of the 2003 streamflow is accounted for with delay compared to the estimates by Huss (2011), i.e. lower values in July and higher values in September. Nevertheless, the two studies again model rather similar orders of magnitudes of the average monthly fractions of  $Q_I$  for this single, extreme year.

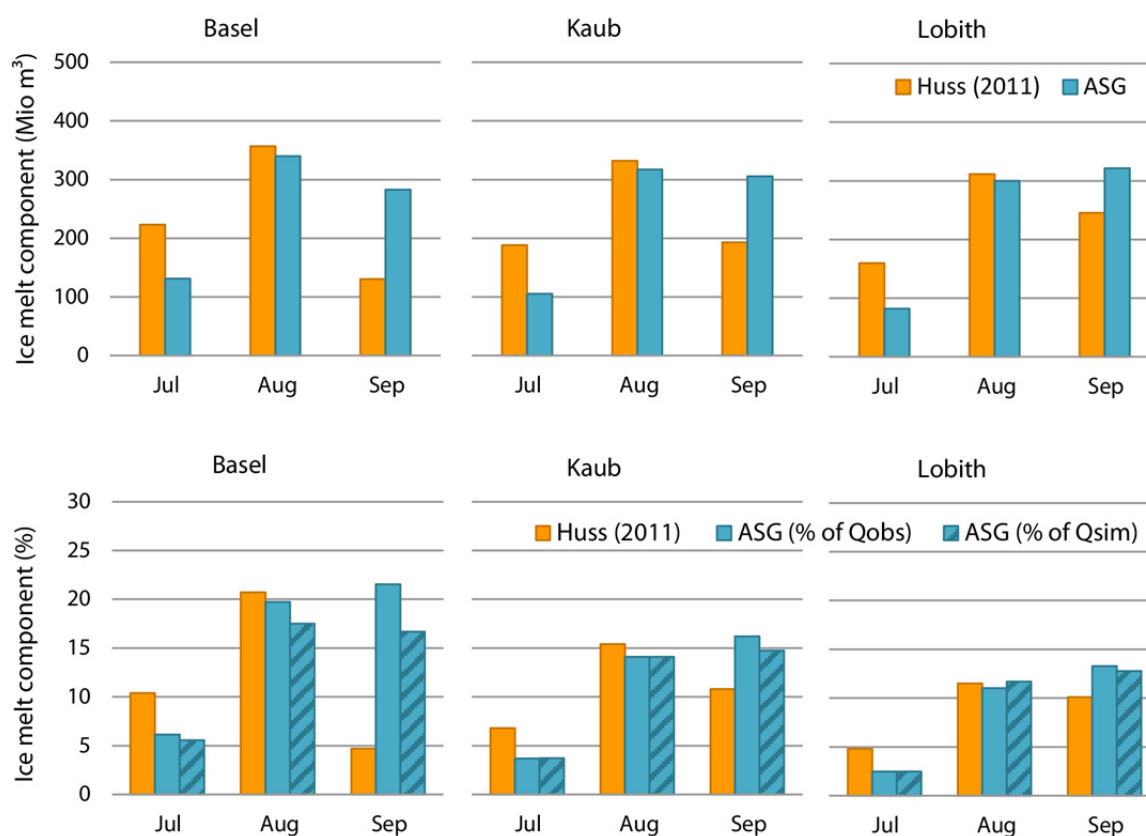


Figure 6.18: Monthly averages of the relative fractions of  $Q_1$  for the months July, August, and September 2003 at selected Rhine gauges from the ASG Rhine project in comparison to compared to “contribution of the bare ice melt component” data from Huss (2011) (see in Huss (2011): Table S2, supporting information).

Figures 6.19 and 6.20 as well as Table 6.5 look more closely at how high (maximally) the modelled daily  $Q_1$  fractions can be for the year 2003 for individual days at various gauges. The locations of the gauges can be seen in Figure 6.11. As was noted for the values listed in Table 6.3, the highest daily values of relative  $Q_1$  fractions for August of 2003 at most of the Rhine gauges also represent the highest daily  $Q_1$  values ever obtained for the entire (partial) simulation time period 1951–2006 with a value range around 20%. As evident from Figure 6.20, this maximum daily fraction in August 2003 generally resulted from a combination of two local  $Q_1$  peaks along with a local minimum in total streamflow.

In contrast to the low flow year 1947 discussed earlier (Section 6.4.1), the observed streamflow at the gauges for this low flow period is predicted rather well by the model for the middle and lower Rhine reaches, while the streamflow upstream of the gauge Maxau is slightly overpredicted by the model (Figure 6.20 and Table 6.5). Consequently, even higher relative  $Q_1$  fractions would result for some gauges, if the  $Q_1$  values were related to the (lower) observed streamflow values.

Table 6.5 shows the maximum values of absolute and relative  $Q_1$  for the two gauges Basel and Lobith. The evolution of these fractions over the year 2003 at the two gauges was already illustrated in Figure 6.15. The September days that showed the lowest modelled streamflow in 2003 had a  $Q_1$  component between 11 and 15% at the gauges from Maxau to Lobith.

The lowest simulated daily streamflow values listed in Table 6.5 and shown in Figure 6.19 illustrate nicely that the streamflow only increases slightly along the Rhine downstream of Basel during such

typical low flow situations. This also explains the remarkably little reduction of the relative  $Q_I$  fractions downstream.

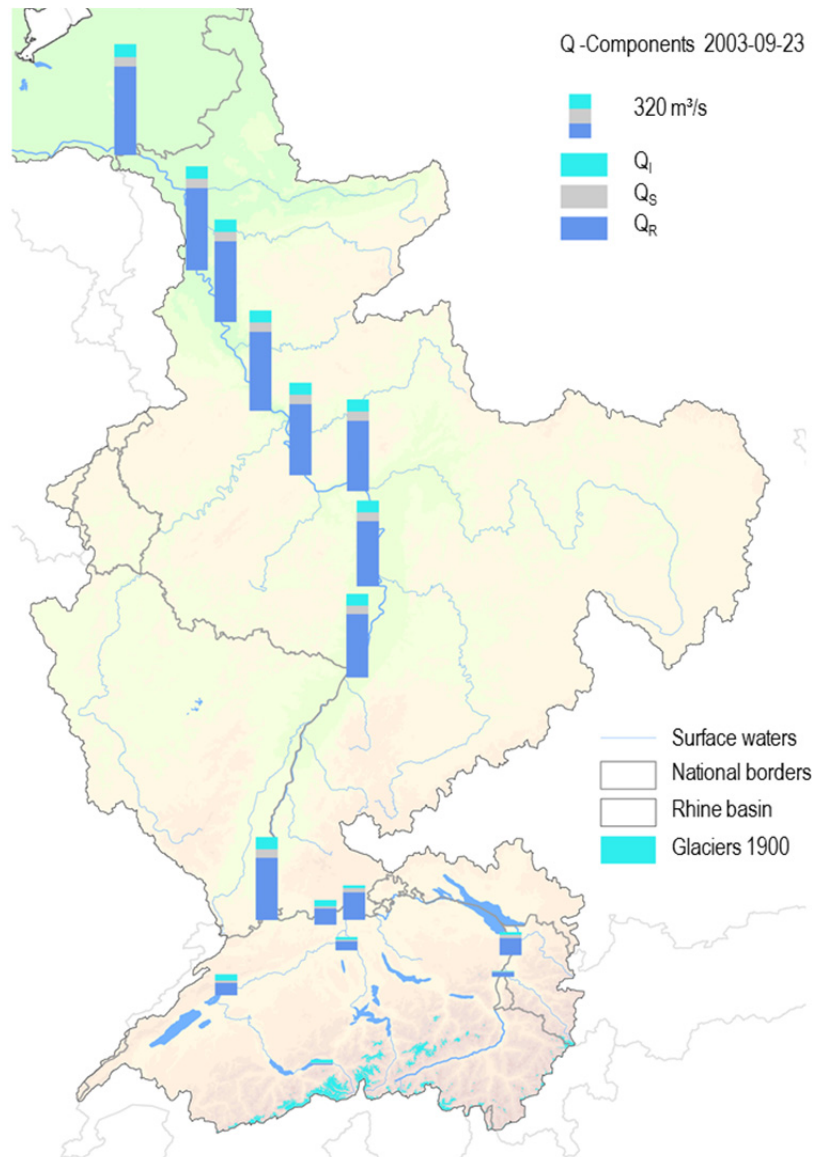


Figure 6.19: Modelled streamflow and streamflow components for the 23<sup>rd</sup> of September 2003 during the low flow period 2003 (minimum  $Q_{sim}$  was simulated on that date at the gauges Kaub, Andernach und Cologne, see also Table 6.5).

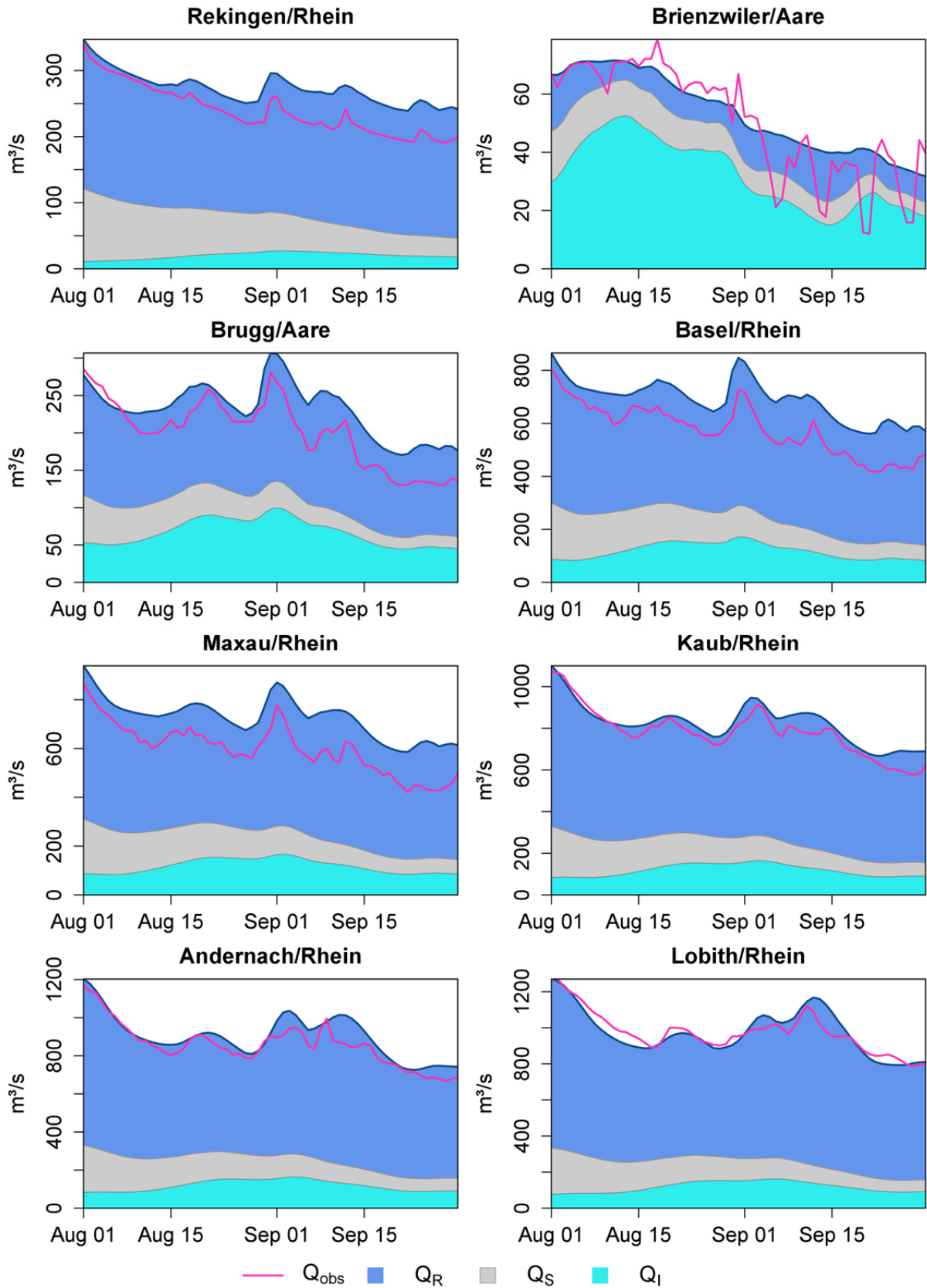


Figure 6.20: Temporal zoom into modelled and observed streamflow from August to September at selected gauges along the Rhine (from upper left to lower right, location of the gauges see Figure 6.11) during the low flow period in 2003.

Table 6.5: Dates of extreme daily values: lowest modelled total streamflow, highest absolute  $Q_I$  values, and highest relative  $Q_I$  fractions for the low flow year 2003 at selected Rhine gauges (Location of the gauges see Figure 6.11). Values are highlighted in red to indicate considerable differences between  $Q_{sim}$  and  $Q_{obs}$ .

Pegel	Minimum $Q_{sim}$				Maximum $Q_I$				Max. relativer $Q_E$ -Anteil			
	Day	$Q_{sim}$	$Q_{obs}$	$Q_E$	Tag	$Q_I$	$Q_I / Q_{obs}$		Day	$Q_I$	$Q_I / Q_{obs}$	
		m <sup>3</sup> /s	m <sup>3</sup> /s	%		m <sup>3</sup> /s	%	%		%	m <sup>3</sup> /s	%
Brienzwiler	Dec-31	<b>14</b>	7	1.4	Aug-13	<b>53</b>	73.8	74.0	Aug-13	<b>73.8</b>	52.6	74.0
Basel	Dec-12	<b>555</b>	507	1.3	Aug-31	<b>171</b>	<b>20.2</b>	<b>23.6</b>	Aug-27	<b>22.8</b>	147.3	26.5
Maxau	Sep-22	<b>586</b>	421	14.4	Sep-2	<b>167</b>	<b>19.5</b>	<b>22.7</b>	Aug-27	<b>22.0</b>	148.4	25.9
Worms	Sep-22	<b>610</b>	511	14.0	Sep-2	<b>166</b>	<b>18.4</b>	<b>20.4</b>	Aug-27	<b>21.2</b>	149.2	24.4
Mainz	Sep-22	<b>660</b>		13.1	Sep-3	<b>165</b>	17.7		Aug-27	<b>20.0</b>	150.3	
Kaub	Sep-23	<b>668</b>	621	13.0	Sep-3	<b>164</b>	<b>17.4</b>	<b>18.0</b>	Aug-27	<b>19.9</b>	150.8	20.9
Andernach	Sep-23	<b>726</b>	716	12.0	Sep-4	<b>164</b>	16.2	17.3	Aug-27	<b>18.6</b>	151.3	19.2
Köln	Sep-23	<b>742</b>	738	12.0	Sep-4	<b>163</b>	15.8	16.8	Aug-28	<b>18.4</b>	151.3	18.8
Düsseldorf	Sep-24	<b>751</b>	730	11.8	Sep-5	<b>163</b>	16.0	17.1	Aug-28	<b>18.1</b>	151.8	18.9
Lobith	Sep-26	<b>794</b>	820	11.2	Sep-6	<b>162</b>	15.7	15.9	Aug-28	<b>17.3</b>	152.6	16.9

#### 6.4.3 Ice melt component in relation to the flow duration curve

The flow duration curve is a well-established tool to illustrate the gauge-specific streamflow distribution, including extreme values. To illustrate the changes on streamflow without the ice melt component, especially on low flows along the Rhine, flow duration curves (for all values below the median) were created from the daily simulated streamflow values. The flow duration curves for the time periods 1901–1950 (using the reconstructed climate input data HYRAS-REC) and 1951–2006 were created separately. The Figures 6.21 and 6.22 show the following graphs:

- The flow duration curve for the observed streamflow data  $Q_{obs}$  (red).
- The flow duration curve of the simulated streamflow values  $Q_{sim}$  (blue) to illustrate how well the model can reproduce the flow duration curve and especially the extreme low flows.
- The flow corresponding to the difference between the simulated streamflow  $Q_{sim}$  and the  $Q_I$  values of each respective day (grey points): Each sorted  $Q_{sim}$  value is assigned the respective  $Q_{sim} - Q_I$  value of the respective day. These values represent the flow that would result if no ice melt component would be present on this day. This shows the variability of the effect of  $Q_I$  on the streamflow range.
- A line showing the moving median of the  $Q_{sim} - Q_I$  values: to relate the streamflow without ice melt component to the simulated streamflow, the median of the  $Q_{sim} - Q_I$  values over 105 values illustrates the temporal relation to the  $Q_{sim}$  value distribution.

An example from the gauge Brienzwiler clarifies the different relevances: since the ice component is 0 for low flow during winter (glacio-nival regime) the grey points showing  $Q_{sim} - Q_I$  up to a non-exceedance probability of ca. 2 % to 5 % lie directly on the duration curve of the simulated streamflow Figure 6.21. This means that the ice melt component  $Q_I$  plays no role for low flows at the gauge Brienzwiler. On the other hand, the effect of  $Q_I$  is clearly detectable for higher streamflow values with a non-exceedance probability of 50% or more: here the grey points of the lowest  $Q_{sim} - Q_I$  values amount to ca. 7 to 8 m<sup>3</sup>/s, while the blue line illustrating  $Q_{sim}$  shows values of ca. 50 m<sup>3</sup>/s. This indicates the considerable impact of  $Q_I$  on simulated summer streamflow, which would be much lower without the contribution of  $Q_I$ . The graph also shows the great variability of  $Q_I$  values at the gauge Brienzwiler.

When interpreting Figures 6.21 and 6.22 it must be kept in mind that the simulated ice melt component is deducted from the simulated streamflow to estimate a glacier-free streamflow distribution. However, there were no separate simulations run with and without glaciers, which would have resulted in a much more complex change. The  $Q_{sim} - Q_I$  values therefore do not represent the streamflow that can be expected after deglaciation of the Rhine basin but only give an indication about the magnitude and thus the importance of the  $Q_I$  component for the flow conditions shown in the flow duration curve.

The Figures show for both time periods, that the flow duration curves at gauges with a nival regime, that have the lowest streamflows in the winter, show almost no changes in the lowest streamflows due a subtracted ice melt component (gauge Brienzwiler, and partially gauge Basel in Figures 6.21 and 6.22). In contrast, gauges with a high pluvial influence (Kaub and Lobith) show a marked reduction of low flows when the ice melt component of streamflow is subtracted. At both of these gauges the cyan line showing the moving median of the  $Q_{sim} - Q_I$  values below a non-exceedance probability of 2 % is clearly below the flow duration curve of the  $Q_{sim}$  values.

The average reduction of  $Q_{sim}$  to  $Q_{sim} - Q_I$  at Lobith amounts to 11% for the 10 lowest streamflow values of the time period 1951–2006 (and 15% for the period 1901–1950) and to 6% for the lowest 100 streamflow values (18% for 1901–1950).

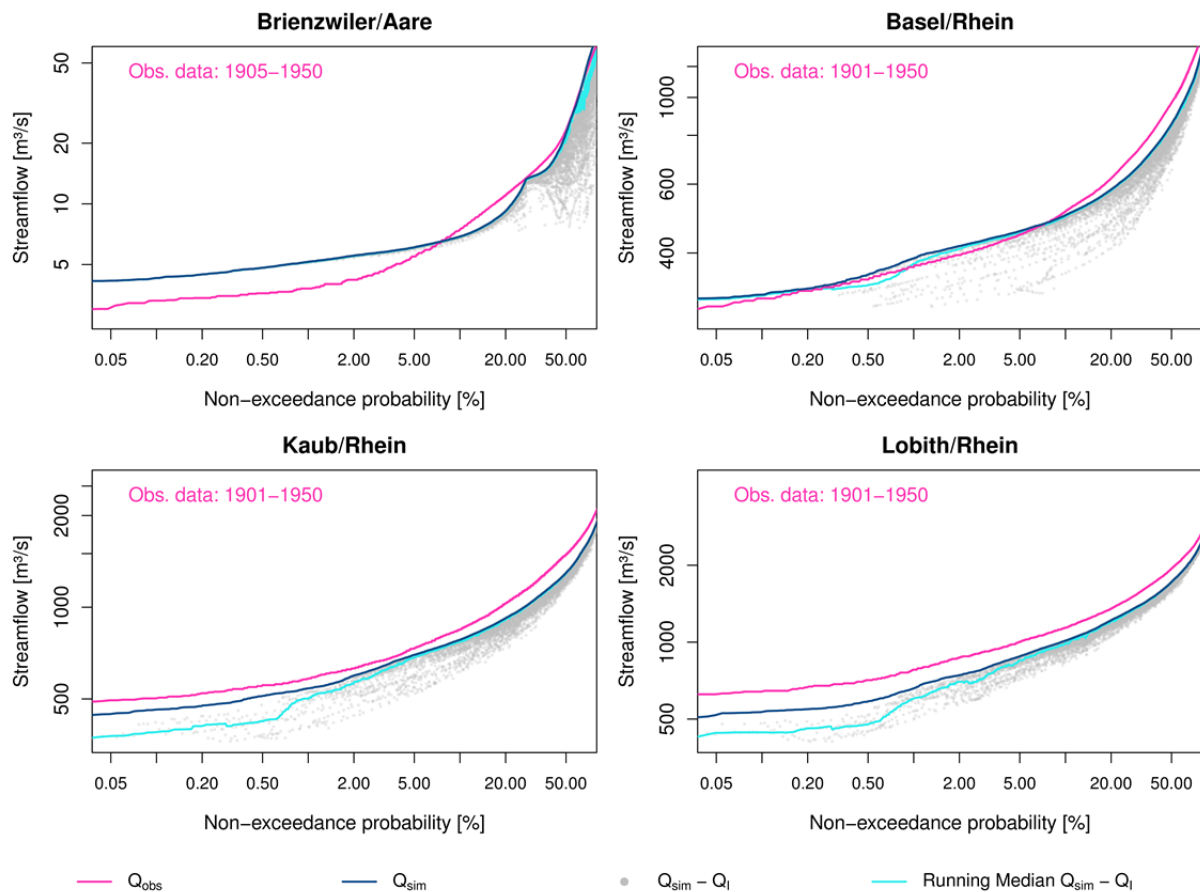


Figure 6.21: Flow duration curves of the observed streamflow  $Q_{obs}$  (pink) and modelled streamflow ( $Q_{sim}$ ) (blue) for selected gauges along the Rhine based on daily values of the time period 1901–1950 (using the reconstructed climate input data HYRAS-REC). Grey points indicate each individual  $Q_{sim} - Q_I$  flow value associated with the respective  $Q_{sim}$  value on the flow duration curve. The cyan line shows the moving medians of the  $Q_{sim} - Q_I$  values.

When comparing the flow duration curves of modelled versus observed streamflow for the Aare River at the gauge Brienzwiler some larger discrepancies for both time periods become evident. The modelled runoff at Brienzwiler is heavily influenced by the theoretical reservoir integrated into the model a few kilometres upstream of the gauge. For the second time period 1951–2006, a minimum outflow of 12–14 m<sup>3</sup>/s is assumed, which is held constant throughout the winter months. This results in the plateau of the  $Q_{sim}$  flow duration curve in Figure 6.22. However, due to the mentioned characteristic hydrological regime and the presence of noticeable  $Q_1$  values at times of high flow rates the somewhat larger model bias for medium and low streamflows within the upper Aare region does not considerably affect the interpretation for the relevant  $Q_1$  values during low flow situations for the non-alpine gauges along the middle and lower reaches of the Rhine.

A clear systematic underprediction of streamflow by the model is evident for the first time period 1901–1950 (using the reconstructed input climate data HYRAS-REC) for the gauges Kaub and Lobith (Figure 6.21). The flow duration curve for Kaub and Lobith is significantly better simulated for the latter period 1951–2006 (Figure 6.22). In contrast, model performance at Basel is better for the early period (Figure 6.21) compared to the latter (Figure 6.22) where the flow duration curve of the modelled streamflow shows a systematic overprediction. This has to be considered when interpreting the results of the modelled low flow events and the quantification of the relative  $Q_1$ -values and their uncertainty.

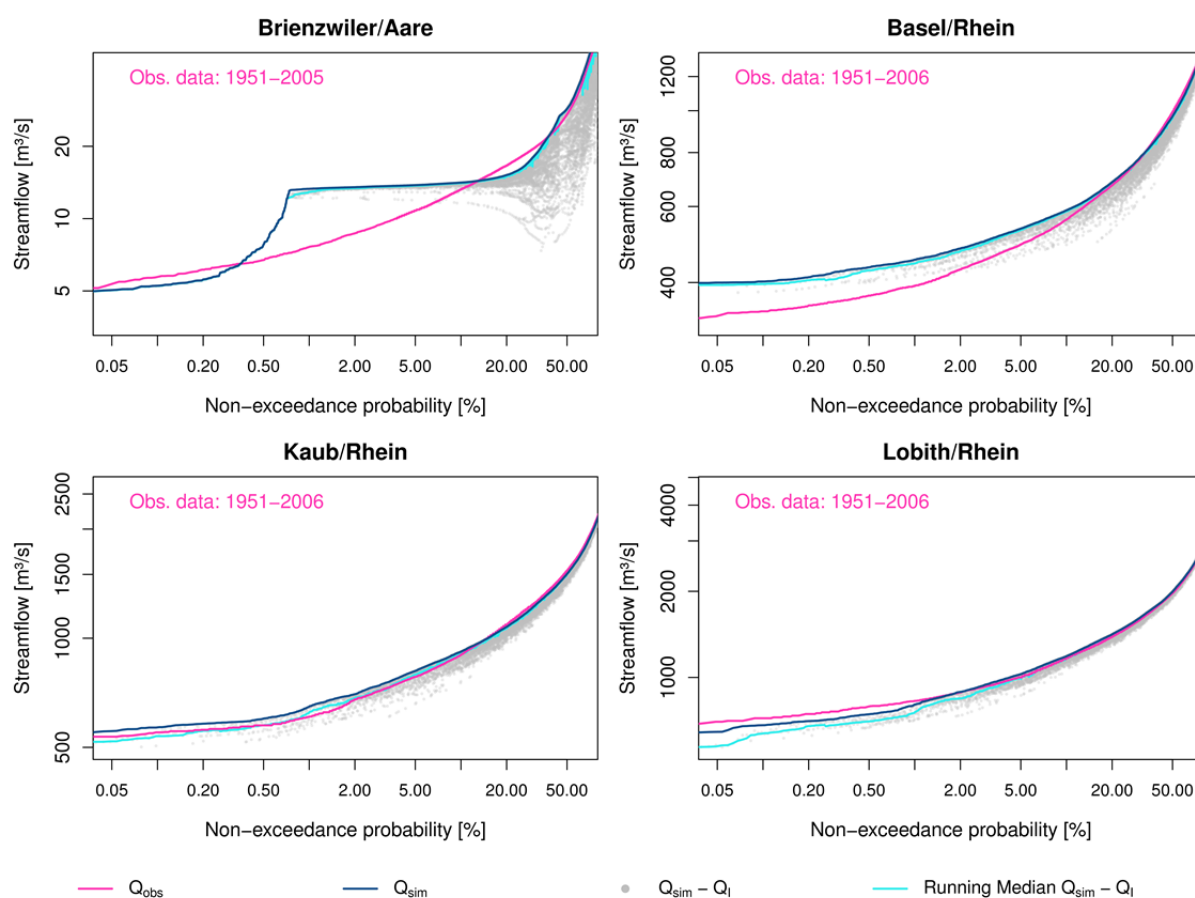


Figure 6.22: Flow duration curves of the observed streamflow  $Q_{obs}$  (pink) and modelled streamflow ( $Q_{sim}$ ) (blue) for selected gauges along the Rhine based on daily values of the time period 1951–2006. Grey points indicate each individual  $Q_{sim} - Q_1$  flow value associated with the respective  $Q_{sim}$  value on the flow duration curve. The cyan line shows the moving medians of the  $Q_{sim} - Q_1$  values.

## 6.5 Temporal changes of streamflow components

The ASG Rhine project also investigated the question how the rain, snow- and ice melt components of streamflow developed temporally over the phases of negative, balanced, and again negative mass balance of alpine glaciers over the last 100 years. Especially the question whether the “peak water” point, at which the river would receive the maximum contribution from glacial melt has been reached yet, is of interest for the Rhine basin. To provide a first impression of the temporal evolution, Figure 6.23 shows the ice melt component of streamflow for the month of August for each year from 1901 to 2006 for three Rhine gauges. The low flow years 1921, 1947, and 2003 clearly stand out. The Figure shows a high similarity to the curves for the headwater catchments in Figure 5.23, which also shows a trend line for the ice melt components of the glacierized regions.

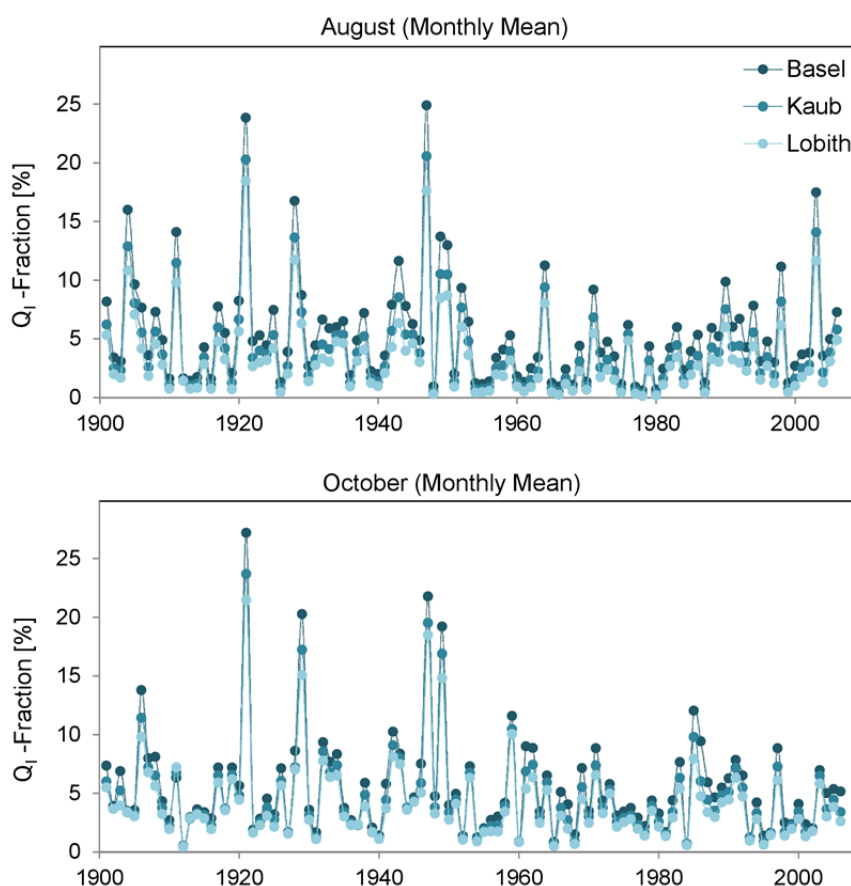


Figure 6.23: Mean monthly fractions of the ice melt component of streamflow at the gauges Basel/Rhine and Lobith/Rhine for the months August (upper) and October (lower).

As described in Chapter 5, phases of higher and lower  $Q_1$  are evident but no clear trend is detectable. Again the fractions have a high inter-annual variability with values ranging from a few percent to over 20% for August. The evolution for October is fairly similar, even though the years 1929 and 1949 stand out. October 2003 on the other hand is fairly average.

For an investigation of the decadal variability, fractions of snow- and ice melt were calculated for individual decades between 1901 and 2006 (Figure 6.24). The figure indicates that fractions of the snowmelt component were lower for the last two decades compared to earlier decades. This indicates a trend towards a lower snow pack due to higher air temperatures and consequently a less prominent snowmelt component of streamflow.

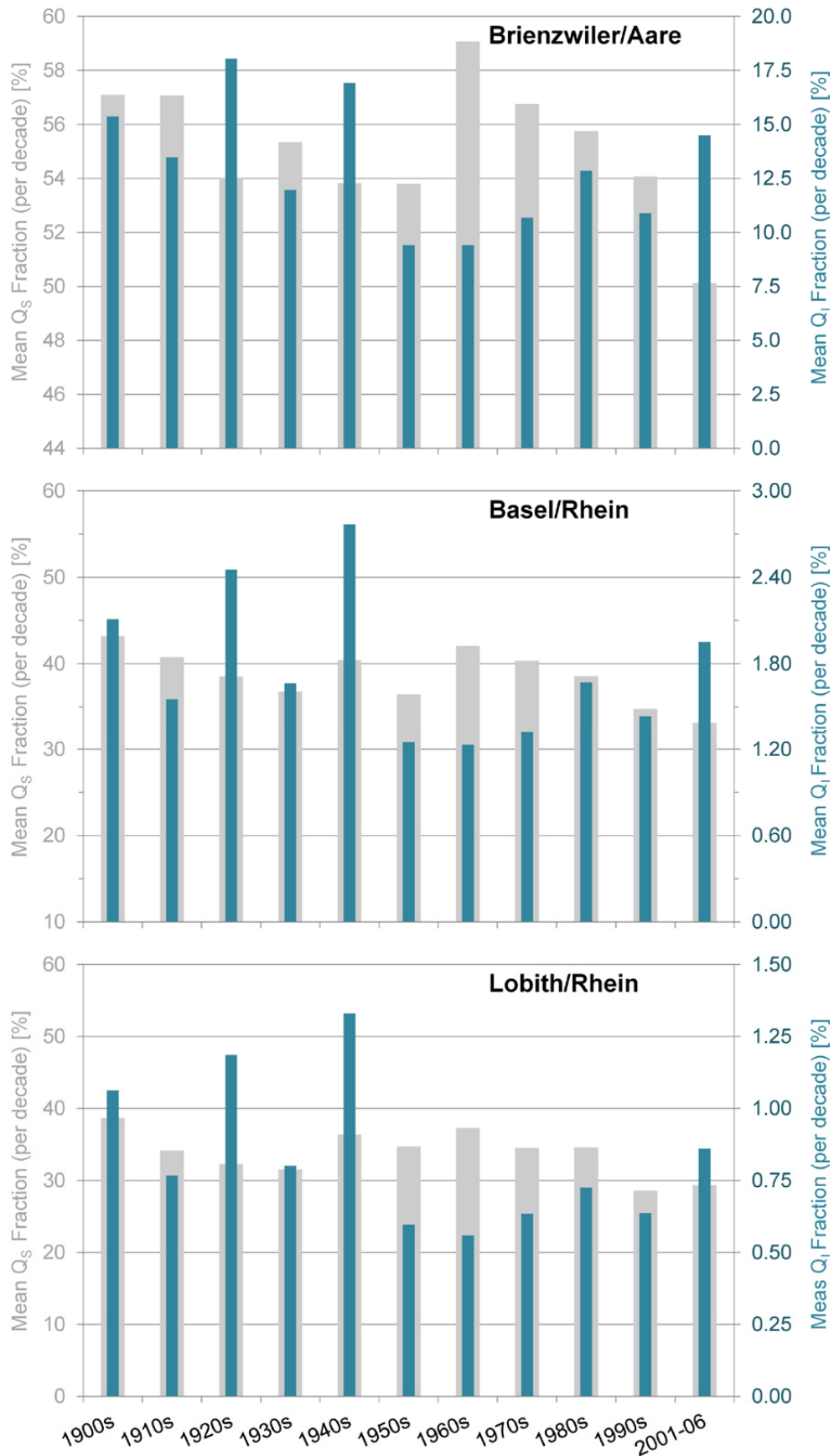


Figure 6.24: Average modelled fractions of snowmelt and ice melt streamflow components per decade at selected gauges in the Rhine basin for 1901 to 2006.

The ice melt component fractions in Figure 6.24 show particularly high values during the 1920s and 1940s, while values are lower for the 1950s. After the 1950s the values slowly increase particularly at the gauges Basel and Lobith. This evolution however, as discussed in Section 5.7, does not allow any conclusions whether the “peak water” point has been reached. As stated in Chapters 3 and 5, temperature dependent glacial melt increase and the reduction of the total glacier areas had approximately equal influence on the ice melt contribution to runoff at least until the beginning of the 21<sup>st</sup> century.

Extending the model period until today (or at least around 2015) as well as a simulation using climate projections may be able to allow further predictions and interpretations of the change. The model developments during the ASG Rhine project now provide the necessary tools for such experiments.

## 6.6 Conclusions

The project employed a set of different coupled models to simulate the streamflow in the Rhine River basin down to the gauge at Lobith: inflow from the glacierized headwater catchments modelled by HBV-Model transferred into the combined two scale LARSIM model (spatial model resolution to the gauge Basel 1x1km<sup>2</sup>, downstream of Basel: 5x5km<sup>2</sup>). The resulting hydrographs of the individual years showed that the observed streamflow at the studied gauges were represented reasonably well by the model. As expected, differences between modelled and observed streamflow were larger for the 1901–1950 time period, which used the reconstructed input climate data, compared to the time period 1951–2006.

The HBV models provided the streamflow components  $Q_S$  and  $Q_I$  from the glacierized areas, while LARSIM calculated the snow cover dynamics separately for each grid cell and land use class and provides snowmelt runoff contributions resulting in snowmelt components of streamflow  $Q_S$  in the LARSIM model areas. The implementation of the mixing tank concept, introduced in Chapter 4, allowed the calculation of the streamflow components  $Q_S$  and  $Q_I$  for each subunit within the model as well as for lakes and reservoirs along the river drainage network. The four cumulative model reservoirs in the alpine part of the Rhine basin, which were introduced into the model system to summarily reflect the anthropogenic influence due to reservoirs, allow for the representation of the temporal changes introduced by the building of reservoirs between 1901 and 2006 and to include their effects on streamflow in the model.

The following results were obtained for the modelled streamflow components:

- Mean annual values 1901–2006: a pronounced decrease of the average annual snowmelt and ice melt components of streamflow downstream between the gauges Brienzwiler/Aare and further down to Lobith/Rhein at the German / Dutch border ( $Q_S$  Brienzwiler: approx. 55%, Lobith: approx. 34%;  $Q_I$  Brienzwiler: approx. 13 %, Lobith 0.8%).
- Mean monthly values 1901–2006: the average  $Q_I$  fraction was considerably higher in summer ( $Q_I$  Basel: August approx. 4.5%, September 6.2%;  $Q_I$  Lobith: August approx. 2.6%, September 4.2%).
- Mean monthly values 1921, 1947, and 2003: in the low flow years 1921, 1947, and 2003 the  $Q_I$  fractions were even higher:  $Q_I$  Lobith: August (monthly means for 1921, 1947, and 2003) from 11% to 18%, September (monthly means for 1921, 1947, and 2003) from 13% to 24%, October (monthly means 1921 and 1947): around 20%; October 2003: 5.5%.
- Maximum daily values: The highest daily  $Q_I$  fractions for all Rhine gauges occurred during the low flow years 1947 and 2003 ( $Q_I$  1947: Basel 33.4%, Lobith 26.4%;  $Q_I$  2003: Basel

22.9%; Lobith 17.3%). Biases of modelled and observed streamflow have to be considered, when interpreting the relative maximum daily values of  $Q_I$  fractions uncertainties. The absolute amounts of  $Q_I$  for 1947 and 2003 are comparable at all gauges between Basel and Lobith and were about  $150 \text{ m}^3/\text{s}$ .

For certain days within the time period 1901–2006 about one fifth of modelled daily total river flow at the Rhine gauges down to Lobith are comprised of the response to ice melt in the Alps. It is interesting to note that the relative  $Q_I$  fractions show only a moderate decrease along the Rhine from the gauge Basel downstream to Lobith during autumn low flows. This marginal decrease can be attributed to the fact that during low flow situations the inflow from the Rhine tributaries downstream of Basel is very low compared to the flow of the Rhine itself, so that no significant dilution occurs.

The analysis of the snowmelt component of streamflow showed, that the  $Q_S$ -values were lower in the last two decades compared to the earlier decades. This decrease indicates a tendency towards a reduced snow pack due to increased temperatures and, consequently, lower snowmelt amounts.

No distinct trends were evident for the temporal changes of the ice melt component over the entire time period 1901 to 2006. As concluded in Chapters 3 and 5, the temperature dependent increase of glacial melt and the reduction of the glacier areas had approximately equal influence at least until the beginning of the 21<sup>st</sup> century.

## 7 Model validation and uncertainty analyses

### 7.1 Validation of selected modelling results

#### 7.1.1 Changes of glacier volume

Aside from data on glacier volume changes, which were directly used for the calibration of the modelled glacier retreat (see Chapter 5), some additional data were available for the independent validation of the simulated glacier changes.

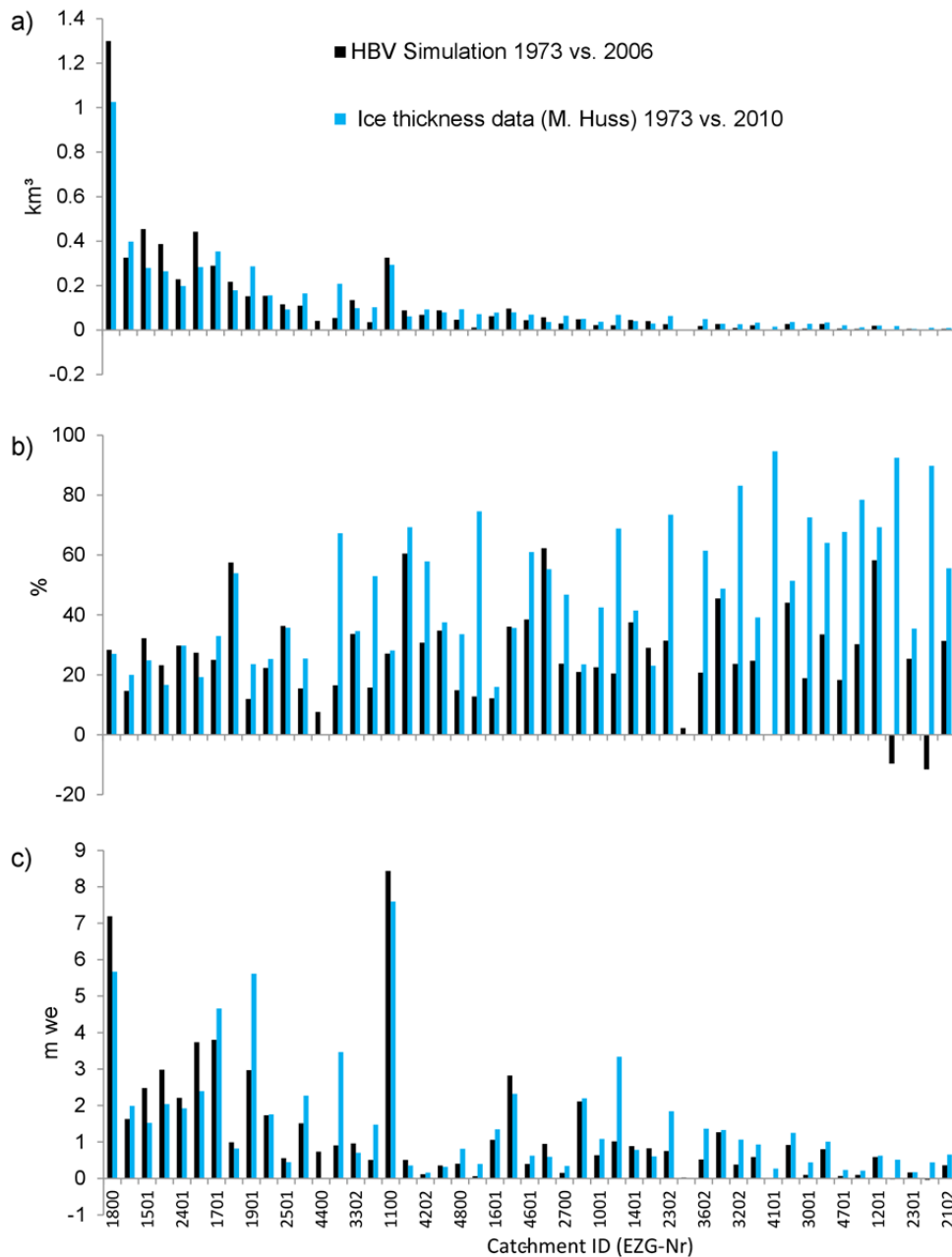


Figure 7.1: Comparison of the modelled loss of glacier volume from 1973 to 2006 with gridded data on glacier ice thickness for the years 1973 and 2010 (modelled data from Matthias Huss, calibrated with ice thickness observations). No ice thickness data were available for catchments 4001 and 4400 (which are outside of Switzerland) (for catchment numbers see map in Figure 5.1). Catchments are sorted by decreasing glacier area. Panels show a) loss of glacier volume in  $\text{km}^3$ , b) loss of glacier volume in % compared to the state of 1973, c) loss of glacier volume in m water equivalent related to the area of the modelled headwater catchment.

Figure 7.1 shows the modelled glacier volume reduction for the individual catchments (from 1973 to 2003) compared to grid data of glacier ice thicknesses for the years of 1973 and 2010. These data were calculated by Matthias Huss using empirical data on ice thickness and a method introduced by Huss & Farinotti (2012). The figure reveals a fairly good agreement for the headwater catchments that have a considerable glacier area, but clear increasing discrepancies for headwater catchments with smaller glacial areas. Catchments with smaller glaciers, however, only play a minor role for the uncertainty of the model results for the total  $Q_I$  component of streamflow from all glacierized areas in the Rhine basin (Figure 7.1c). In general, the rather large spatial differences in glacier volume reduction expressed as meter water equivalent by catchment area were reproduced well by the model (Figure 7.1c). This is especially important for the modelling of total catchment runoff.

The range of modelled relative changes in glacier volume in all modelled headwater catchments illustrates a strong spatial variability within the study area (Figure 7.2). The general temporal evolution of changes is very similar for the individual catchments. However, similar to Figure 7.1 the absolute values for the last 30 years are very different.

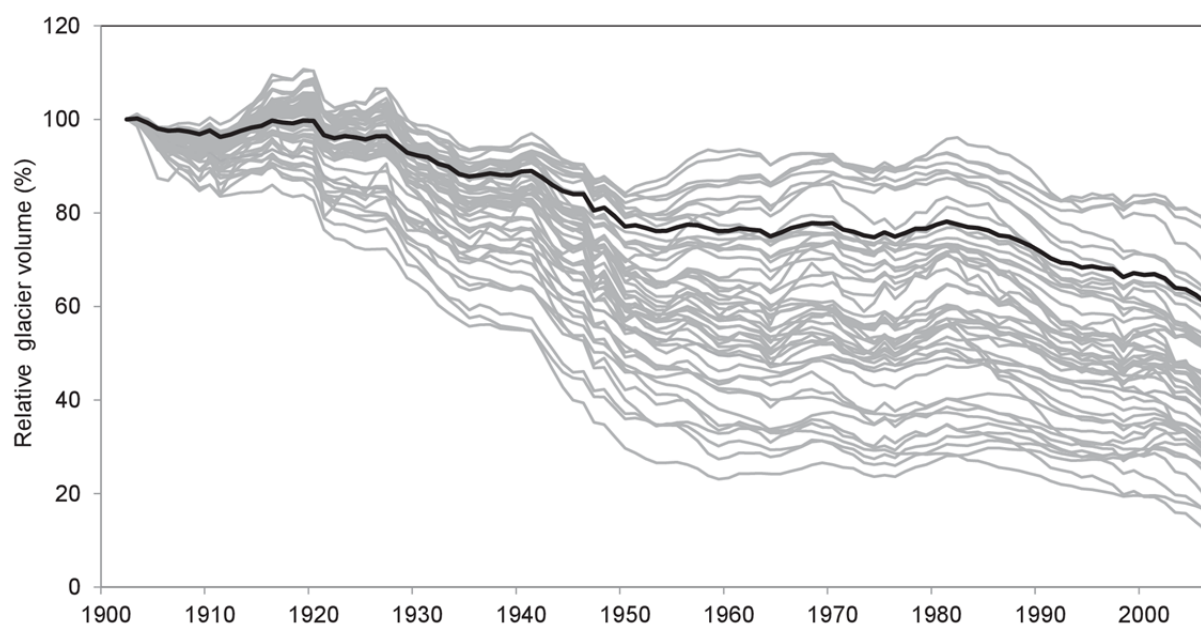


Figure 7.2: Modelled changes of glacier volumes relative to the 1901 volume for all 49 glacierized headwater catchments (grey). The area-weighted mean change is illustrated by the black line.

Another comparison of the glacier changes within all catchments is shown in Figure 7.3. It shows the evolution of the modelled glacier area as a sum over the entire Rhine basin against observed glacier areas in the years 1900, 1940, 1973, 2003, and 2010. The simulation clearly captures the known phases of stable and retreating glaciers in the 20<sup>th</sup> century. Simulated and observed glacier areas are in the same range. The model tends to underpredict glacier extent in the early part and overpredicts glacier extent later in the time series. Potential explanations for these biases, amongst others, may be the uncertain initial conditions or the winter temperatures used to drive the modelling of the early phases, with the reconstructed climate dataset (HYRAS-REC) exceeding observed temperatures. Considering the uncertainties of the glacier observations, which come from different sources and were obtained with different methods as well as the numerous challenges and the necessary assumptions in the HBV-light modelling of the glacier areas, the comparison shown in Figure 7.3 suggests a satisfactory agreement between modelled and observed glacier evolution in the Rhine basin over the last 100 years.

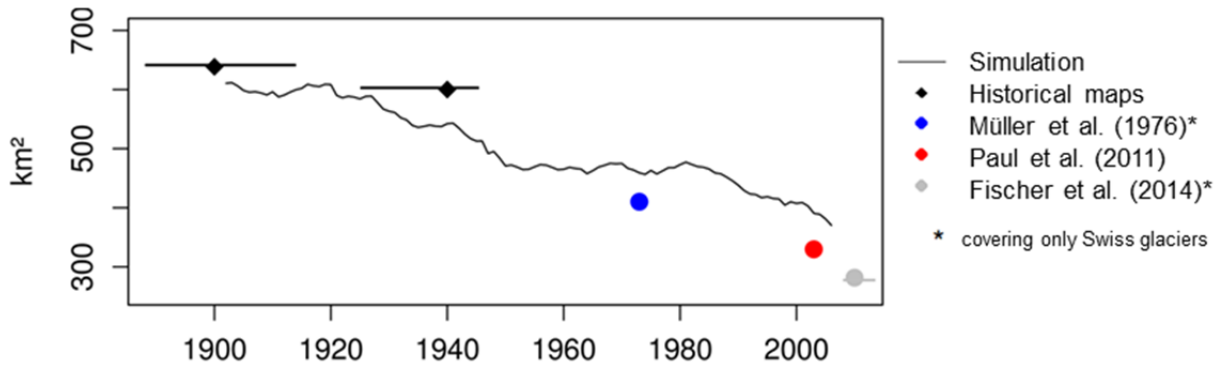


Figure 7.3: Modelled changes of the glacier areas in all 49 glacierized headwater catchments (black line) and observed glacier areas from different studies.

As mentioned in Chapter 3, few long-term observed mass balance data were available for the modelled catchments of the Rhine basin. One is a long-term dataset of the annual mass balances for the Clariden glacier in the basin of the Linth (newly analysed data from Huss et al., 2015). The Clariden glacier is the largest, but still only one of several glaciers in the modelled catchment, which makes a direct comparison of modelled and observed glacier area impossible. The same can be said for the Silvretta glacier in the catchment of the Landquart. However, Figure 7.4 shows that the simulation generally captures the positive and negative phases of the glacier mass balance over the last 100 years well, even if considerable differences in individual years are evident. These differences could be attributed, however, to the mentioned integrative modelling of several glaciers within the catchments.

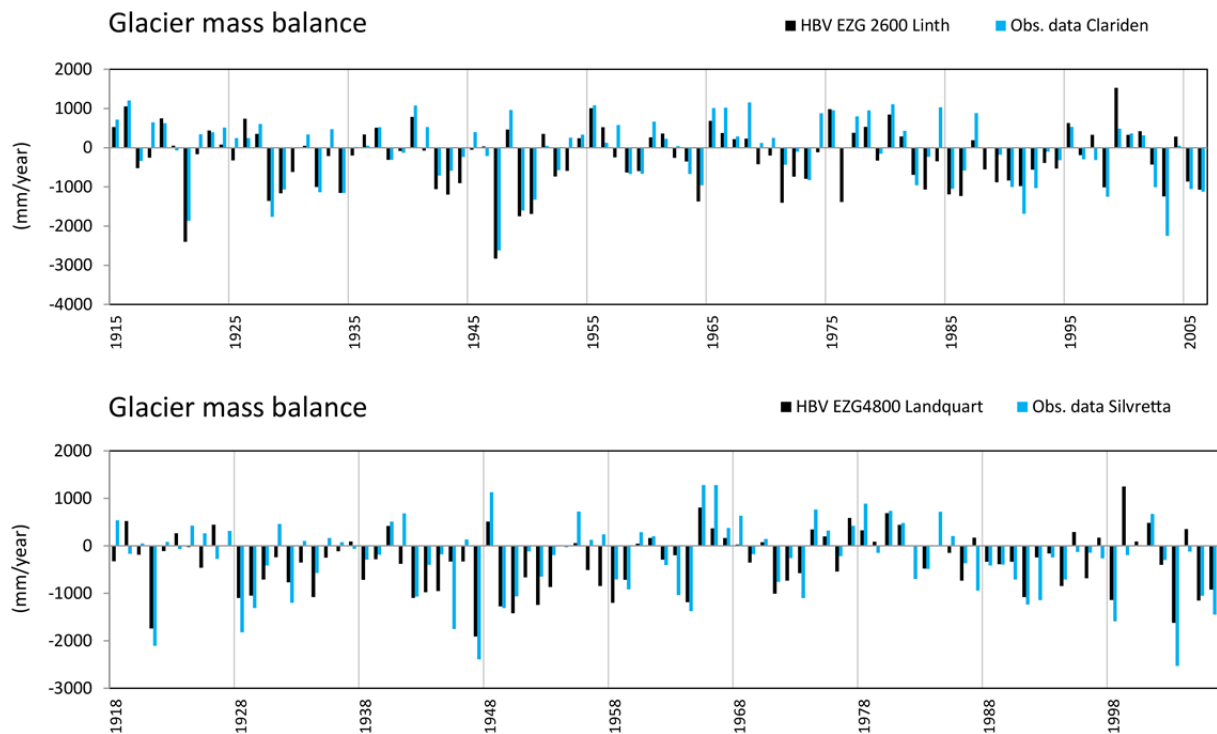


Figure 7.4: Observed annual mass balance for the individual Clariden glacier compared to the modelled annual mass balance of all glaciers in the Linth catchment (upper) and observed annual mass balance for the individual Silvretta glacier compared to the modelled annual mass balance of all glaciers in the Landquart catchment (lower). Data source: mass balance series Clariden and Silvretta: WGMS (2015); Huss et al. (2015).

In the part of the Rhine basin belonging to Vorarlberg/Austria, the glacierized Ill catchment is heavily influenced by water management applications. Thus no unregulated streamflow data, which could be used for model calibration, are available. Additionally, the glacier mass balance data only cover a short time period. Nevertheless, a qualitative comparison appears reasonable using this limited dataset. This comparison, shown in Figure 7.5, indicates that aside from some very well predicted years, the modelling did not reproduce the data well over several time periods. This is a good illustration of the usefulness of model calibration using a multi criteria approach (which was not possible here).

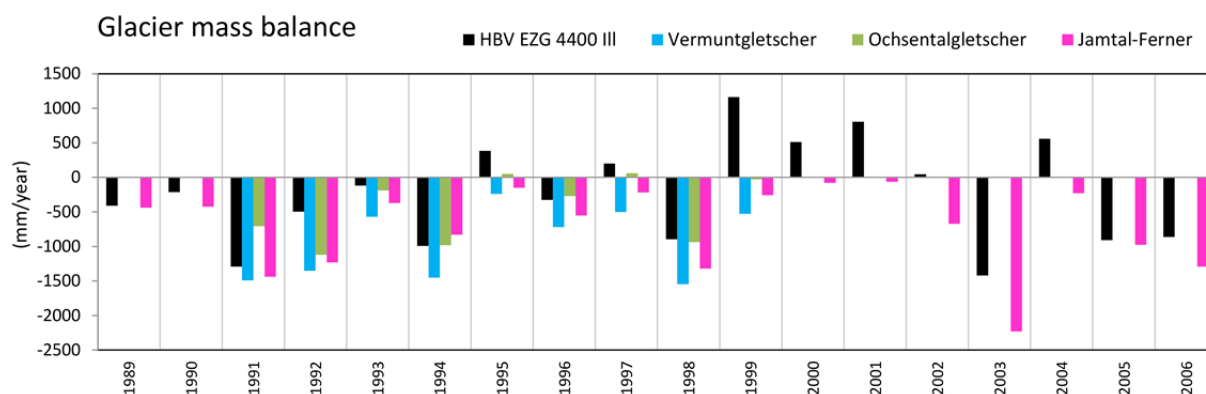


Figure 7.5: Modelled annual mass balance of all glaciers in the catchment of the Ill and observed annual mass balance for several individual glaciers in and just outside (Jamtal glacier) of the catchment. Data source: mass balance series Vermunt glacier, Ochsental glacier und Jamtal-Ferner: WGMS (2013).

### 7.1.2 Changes of the glacier length

As mentioned in Chapter 3, glacier length changes have been observed over a very long time for many glaciers. Thus, 56 time series of observed length changes for individual glaciers were available in the 49 simulated headwater catchments. As the HBV-light model only models glacier area and glacier volume but not glacier length, a semi-empirical formula relating length to area (Bahr, 1997) was employed to obtain a modelling-derived glacier length. The formula calculates glacier length ( $L$ ) as a function of glacier area ( $A$ ) as

$$L = A^{0.625} \quad (7.1)$$

The derived glacier lengths can then be converted to relative changes in length for comparison to the available observed length changes, which were grouped in three length classes and represented as median changes for each group (Figure 7.6). Even though these two glacier length values contain uncertainty due to the different methods of obtaining them (modelled data converted with empirical formula versus a group median change calculated from sometimes incomplete time series observations) they match rather well. Generally, the pattern of the annual changes is captured. However, the model tends to exaggerate the variations of glacier length changes, which may be attributed to the fact that the model does not consider a time-lag in the ice movement of the glaciers. Thus, the model simulates the areal changes especially of the larger glaciers too directly and too dynamically. The total modelled glacier length changes lie somewhere between the observed dynamic changes for midsize and small glaciers, which may be expected as most glaciers in the modelled catchments are in that size range.

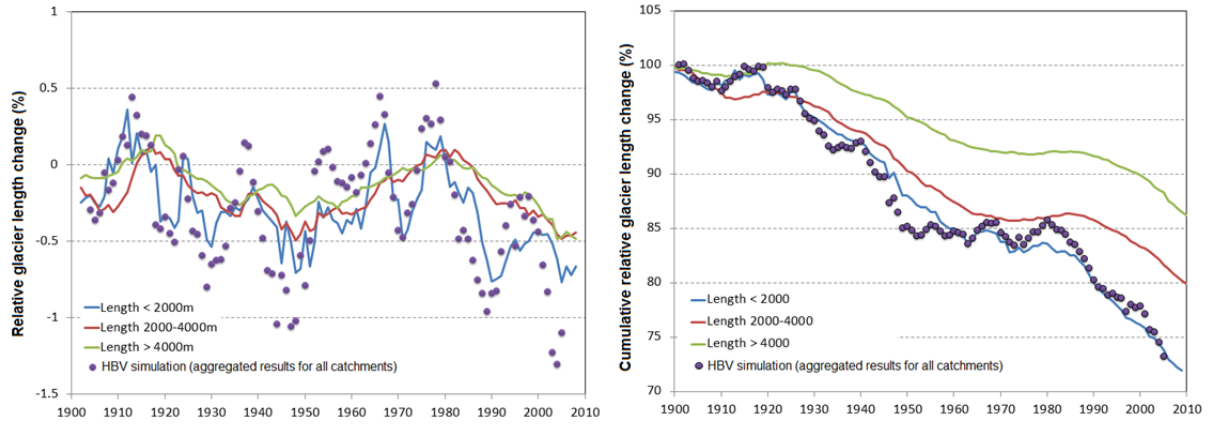


Figure 7.6: Modelled and observed annual relative change in the length of glaciers in the Rhine basin (left) and cumulative length change (right); shown are 5-year moving averages. Data source for observed length changes: WGMS (2013).

### 7.1.3 Comparison of the sensitivity of runoff to temperature and precipitation

The methodology developed to determine weekly sensitivity of catchment runoff to climate variability can also be employed to compare the estimated climate sensitivities based on the modelled streamflow with those derived empirically from observations as in Section 3.2. This validation was carried out for a selection of catchments using the daily temperature and precipitation data used as corrected model input with the resulting modelled streamflow data and in comparison with the observed streamflow data over the same period. Figure 7.7 shows the temperature sensitivities estimated based on modelled and observed runoff. In most example catchments, the temperature sensitivity of the modelled streamflow values, especially in early summer, is higher than the temperature sensitivity for the observed streamflows. However, overall the seasonality and the differences among catchments agree.

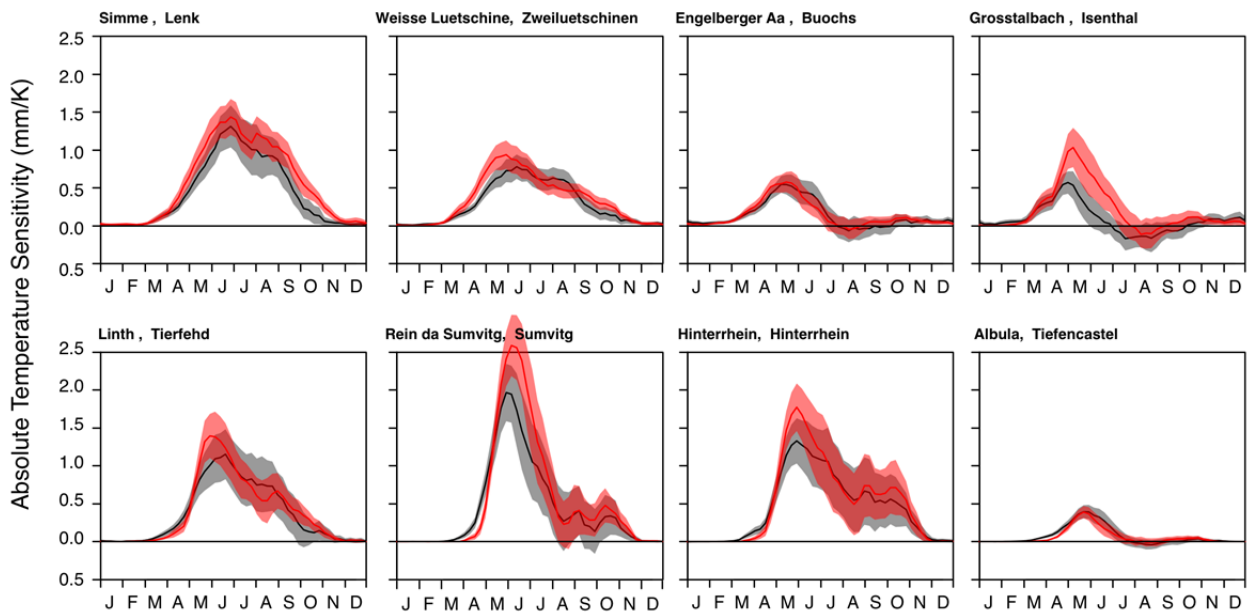


Figure 7.7: Weekly temperature sensitivity based on observed runoff (black) with confidence intervals (grey) and based on HBV-light modelled runoff (red) with confidence intervals (light red) for eight selected catchments.

The respective comparison of precipitation sensitivity (Figure 7.8) shows a good agreement for most of the catchments. For some catchments, the model-estimated precipitation sensitivity in early summer is higher. These results show that if the model would be used to simulate the effect of hypothetical climate change scenarios with defined temperature and precipitation increases, the model may simulate streamflow responses that are somewhat too strong.

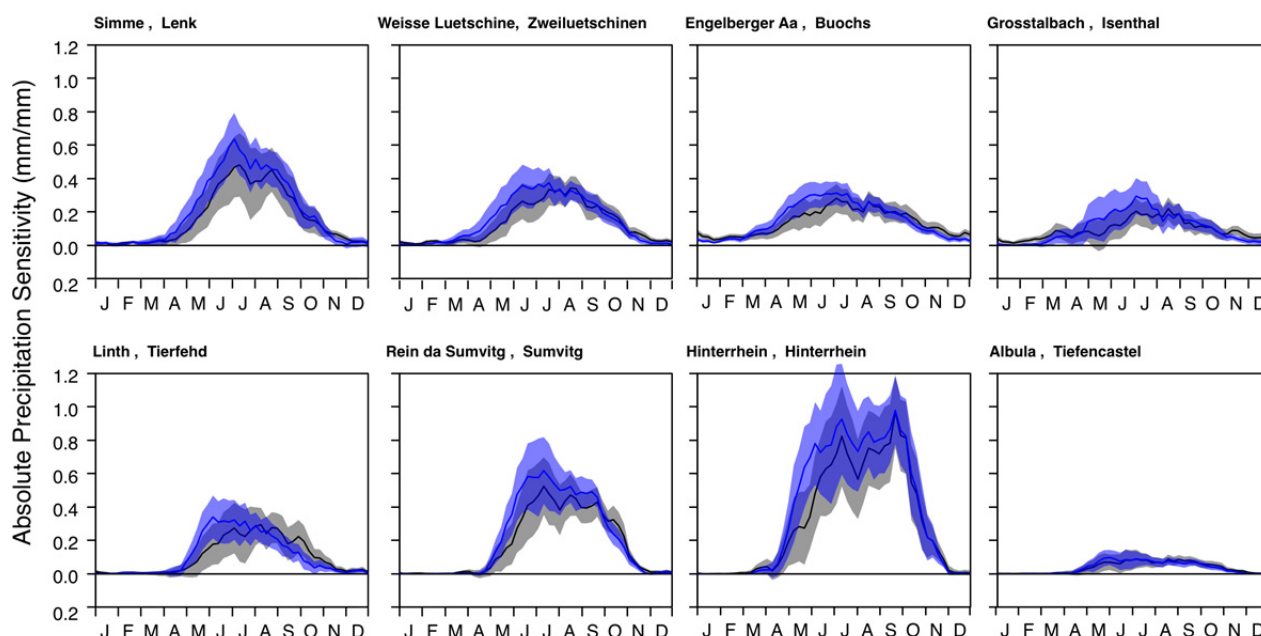


Figure 7.8: Weekly precipitation sensitivity for observed runoff (black) with confidence intervals (grey) and HBV-light modelled runoff (blue) with confidence intervals (light blue) for eight selected catchments.

## 7.2 Model parameter uncertainty

As any modelled hydrological variable, the streamflow components calculated by the work in the project are subject to uncertainties. This final section shows the results of analyses carried out to quantify the model parameter uncertainties and therefore provides the basis for an assessment of the overall uncertainties. Three aspects of the modelling process are looked at in particular:

- the limiting of the mixing tanks,
- the parameter uncertainty during model calibration, and
- the decisions made during the regionalization of the parameters and their effects.

With the exception of the analysis of the sensitivity limit on mixing tanks, the analyses of the parameter uncertainty were mainly carried out for the glacierized headwater catchments modelled with HBV-light. This was done, since only these models allow a suitable (in terms of run time and computational efficiency) number of model runs for the long study period. With the longer run-times of LARSIM model runs for the entire Rhine basin for the entire study period 1901–2006 that model was not suited for similar analyses.

### 7.2.1 Limiting of the mixing tank volume for the modelling of the streamflow components

As illustrated in Chapter 4 for an example catchment, a limit of the volume of the mixing tanks was introduced to prevent the development of a constant mix ratio of streamflow components over longer time periods. The limiting therefore enables the effect tracking of individual components on the

streamflow response. A sensitivity analysis during the development of the mixing tank methodology concluded that the effect tracking was best achieved, if the volume of the mixing tanks was limited to approximately the maximal daily throughflow in the model system.

The uncertainties resulting from such a definition of the mixing tank volume limits for the determination of the streamflow components are shown here employing the final calibrated model versions used in the study. A wide range (1–1000 mm) of the mixing tank volume limit shows clear effects on the simulated snowmelt component of streamflow (Figure 7.9). Variations in a narrower range (e.g., 10–20 mm in Figure 7.10) only reveal minor differences for the snowmelt component.

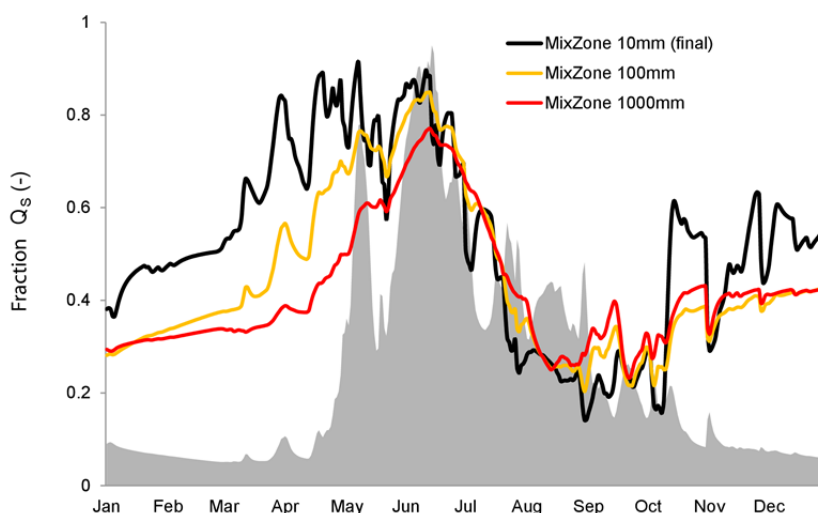


Figure 7.9: Influence of the mixing tank volume limit of 10 mm (black line identical to final model results), 100 mm (orange line), and 1000 mm (red line) on the fraction of  $Q_S$  modelled with HBV-light for all glacierized catchments (aggregated values) for the year 2003 (as an example). Grey area: hydrograph of total streamflow (as additional information for comparison).

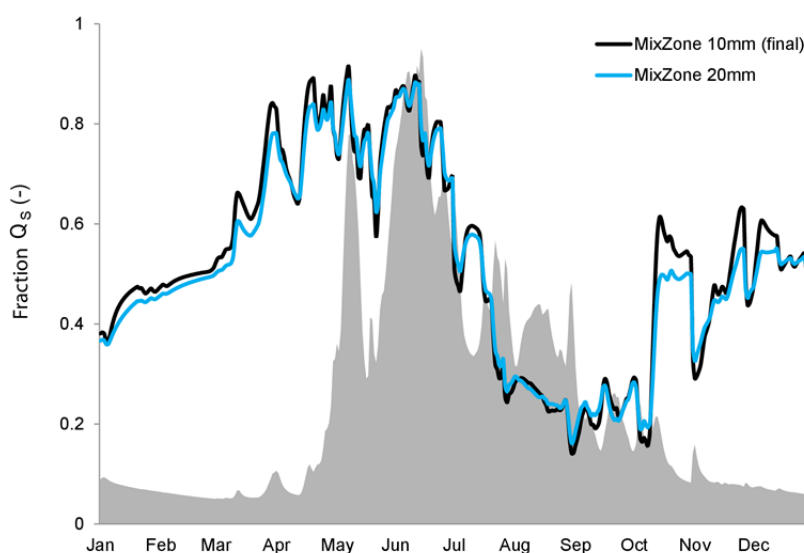


Figure 7.10: Influence of the mixing tank volume limit between 10 mm (black line identical to final model results) and 20 mm (blue line) on the fraction of  $Q_S$  modelled with HBV-light for all glacierized catchments (aggregated values) for the year 2003 (as an example). Grey area: Hydrograph of total streamflow (as additional information for comparison).

These sensitivity analyses were also carried out using the LARSIM model for the subunit of the Aare River upstream of Interlaken (catchment area ca. 1100 km<sup>2</sup>; i.e., ca. 1300 LARSIM model elements). This subunit also includes five HBV-modelled glacierized catchments that feed into the LARSIM-Hochrhein model. Additionally, the LARSIM simulations include a theoretical cumulative reservoir along the Aare River (placed just upstream of the gauge Brienzwiler/Aare) and the regulated lake Lake Brienz (Brienzersee). The sensitivity tests used different combinations of mixing tank volume limits for model elements and for lakes and reservoirs. Figure 7.11 shows the hydrographs for the year 1992 up- and downstream the cumulative reservoir, while Figure 7.12 shows the 1992 hydrographs before and after Lake Brienz (Brienzersee).

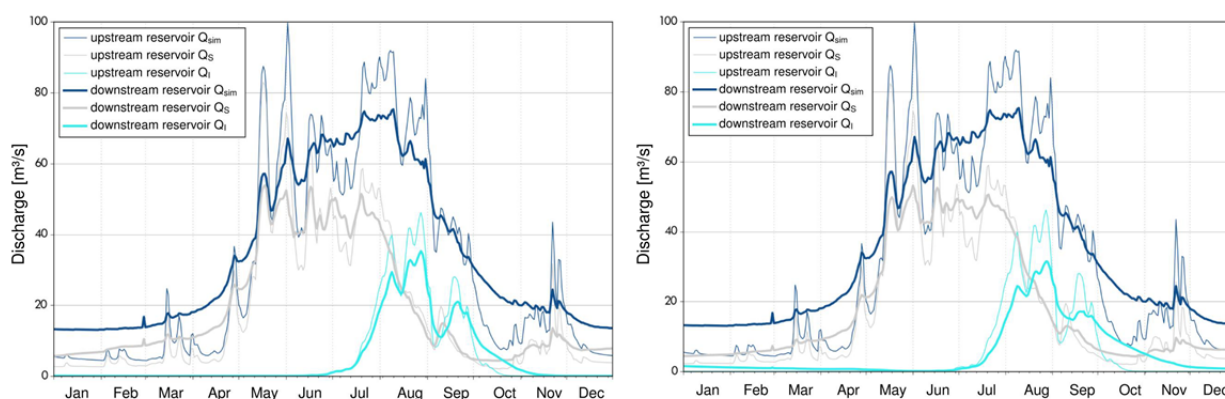


Figure 7.11: Simulated streamflow and streamflow components for the year 1992 upstream the cumulative model reservoir at the Aare (thin lines) and downstream the cumulative model reservoir at the Aare (thick lines) with a mixing tank volume limit of 25mm (left) and 100mm (right).

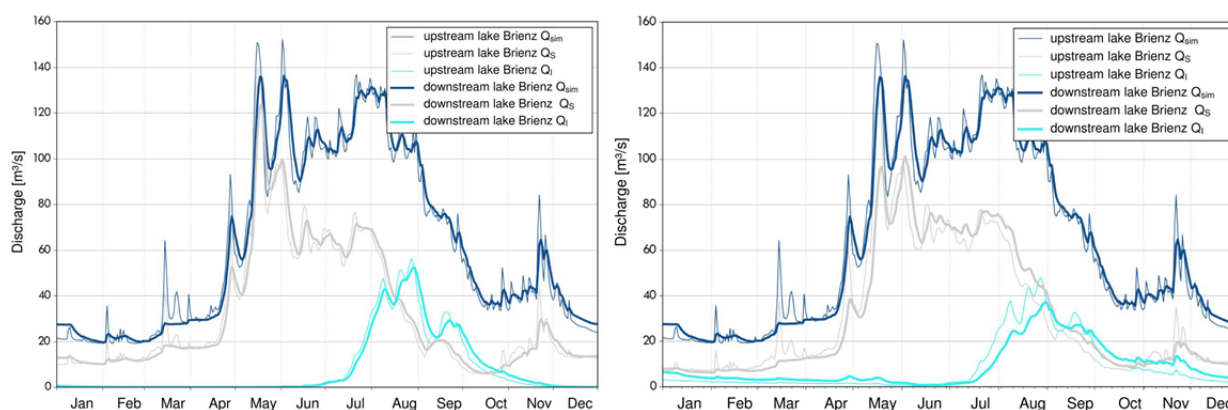


Figure 7.12: Simulated streamflow and streamflow components for the year 1992 upstream of Lake Brienz (Brienzersee) (thin lines) and downstream of the lake (thick lines) with a mixing tank volume limit of 25mm (left) and 100mm (right).

The total streamflow (dark blue lines) remains the same when using mixing tank volume limits of 25 mm or 100 mm, since the variation of the maximum volume of the mixing tanks only affects the relative fractions of snow and ice components but not the total flow volume. The retention effect of the reservoir and the lake can be seen clearly. It becomes evident that the cumulative reservoir at the Aare River has a much more pronounced effect on streamflow and its snowmelt and ice melt components,  $Q_S$  and  $Q_I$ , than Lake Brienz (Brienzersee). This is in particular the case for the peaks of the ice melt component, which are reduced markedly after the reservoir, especially for a mixing tank limit of 100 mm. In the case of Lake Brienz the 100 mm mixing tank volume limit causes a clear shift in the

streamflow components from summer to winter, and thus, a considerable retention effect on the ice melt component. In addition, the fraction of the snowmelt component in winter streamflow is lower for a 100 mm volume limit than for a 25 mm volume limit.

Overall, the figures indicate that the choice of mixing tank volume limit influences the component tracking for the lakes and reservoirs incorporated in the LARSIM model. However, the resulting differences are rather minor. The higher fraction of the ice melt component of streamflow during the entire winter for a 100 mm volume limit may be useful to study its reservoir retention, but appears less applicable for the desired effect tracking. Thus, the study eventually used a mixing tank volume limit of 25 mm for the LARSIM simulations, as was mentioned in Chapter 4.

**7.2.2 Parameter uncertainty**

Ten calibrations with a minimum of 3000 model runs each were performed using a genetic parameter optimization algorithm (GAP) implemented in HBV-light (see Seibert, 2000) for every glacierized headwater catchment (Chapter 5). The resulting 10 best parameter sets for each catchment represent another component of the uncertainty analysis.

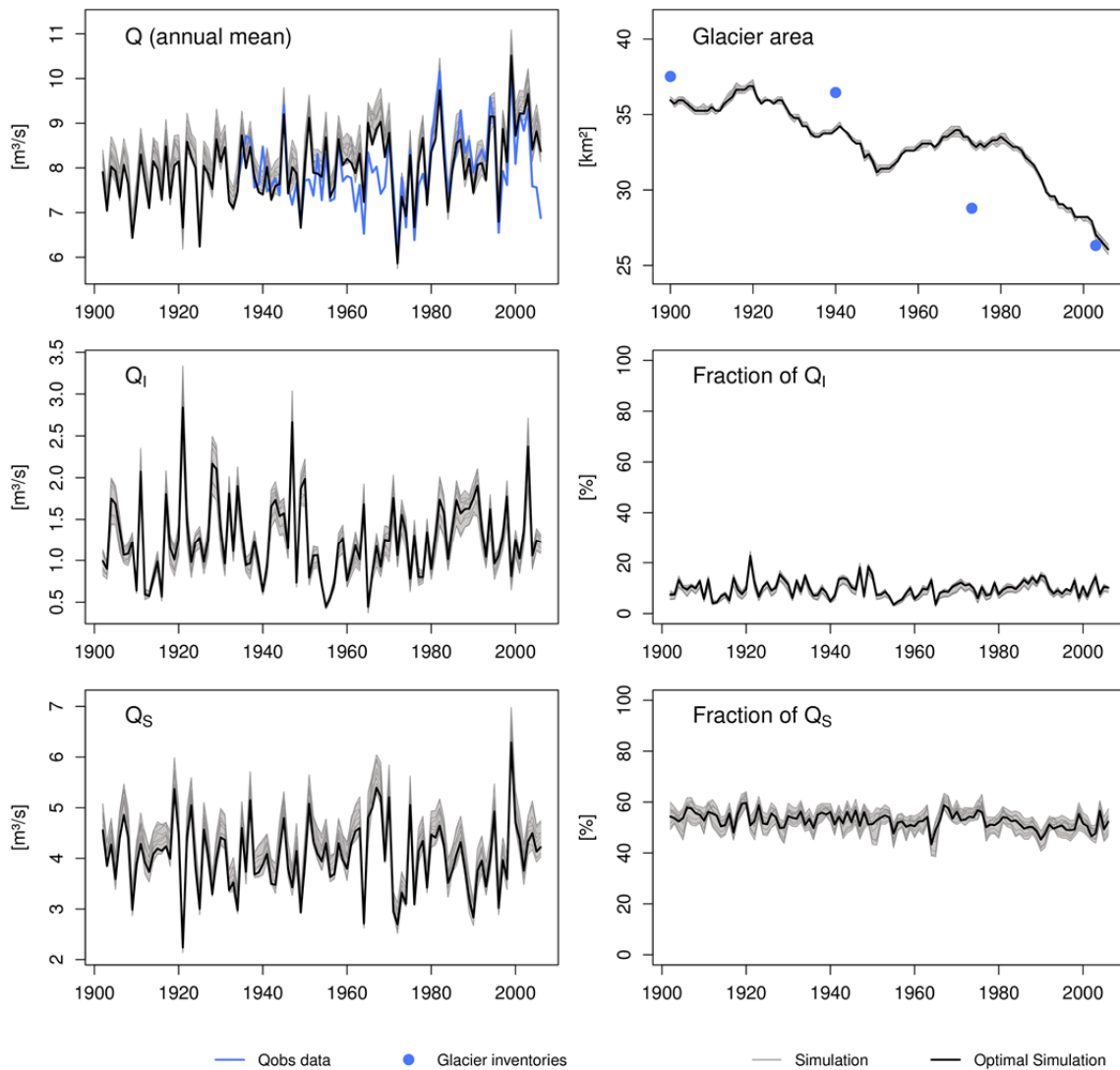


Figure 7.13: Mean annual simulation results for total streamflow, glacier area and streamflow components (black line) with illustration of the simulation results using the 9 additional parameter sets obtained during model calibration (grey lines) for the catchment “Weisse Lüttschine”, Gauge “Zweilüttschinen” (catchment # EZG1501) as an example.

Figure 7.13 shows the resulting parameter uncertainty for the water years 1902–2006 for one example catchment, while Figure 7.14 shows the aggregated uncertainty of all model runs for all glacierized headwater catchments. For each individual catchment as well as for the aggregated values, the uncertainties resulting from model calibration are minor, especially regarding glacier area. The uncertainty contained in the streamflow and especially the ice melt component  $Q_I$  is also very low. This strengthens the confidence in the study's conclusions about  $Q_I$  values throughout the entire Rhine basin. The parameter uncertainty for the snowmelt component is slightly higher but still less than 10% in any year. The same applies to the total streamflow from all catchments.

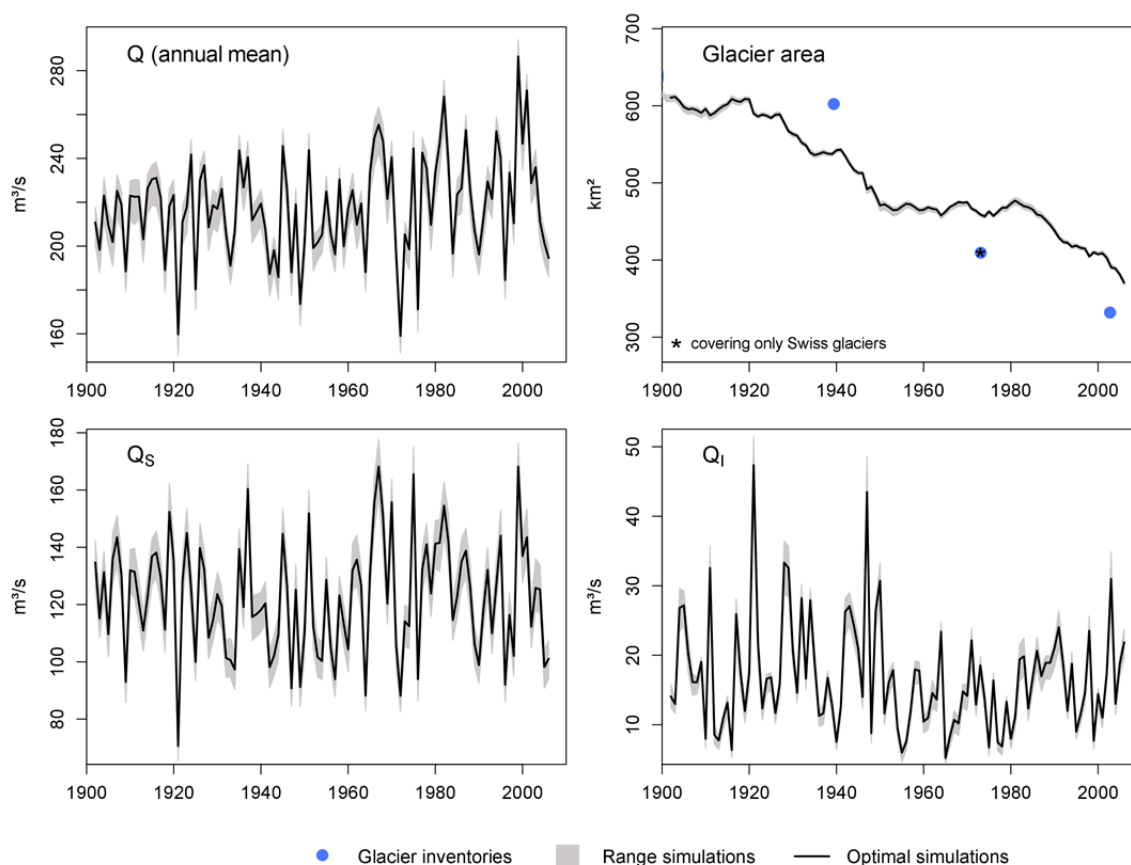


Figure 7.14: Mean annual simulation results for total streamflow, glacier area and streamflow components (black line) aggregated for all glacierized headwater catchments with the grey area showing the range of simulation results using the 9 additional parameter sets obtained during model calibration.

Figure 7.15 shows the spatial distribution of the uncertainty of the relative fraction of the ice melt component of streamflow. Generally, the mean parameter uncertainty is higher for catchments with higher glacier coverage since the fraction of  $Q_I$  is larger in these catchments.

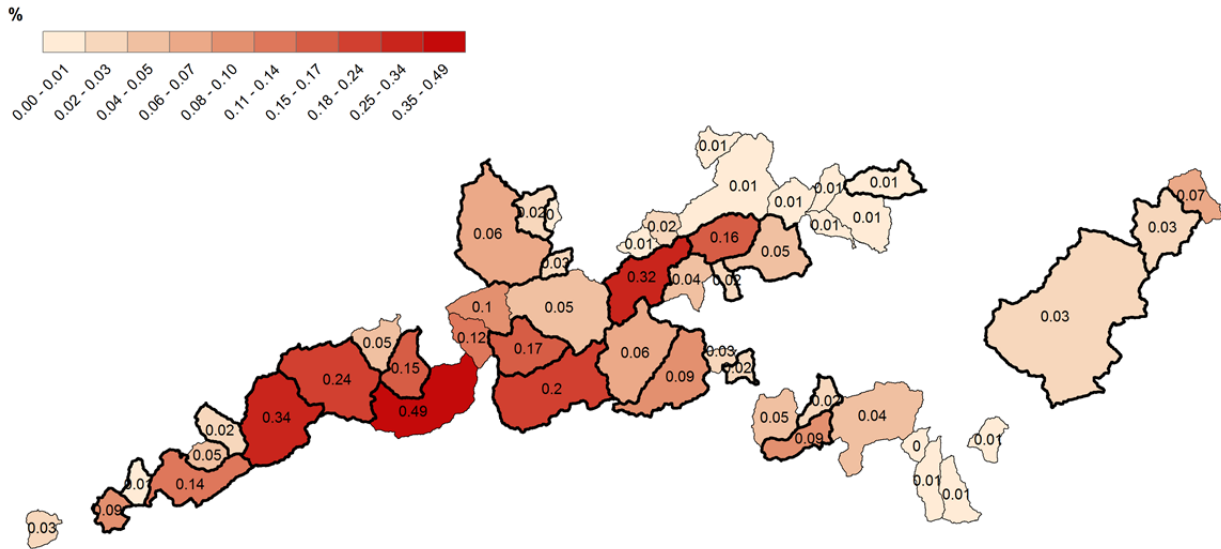


Figure 7.15: Mean parameter uncertainty of the  $Q_1$  fraction (% of total streamflow) for all individual glacierized headwater catchments obtained from 10 model runs each (using the 10 calibration parameter sets); thick borders around a catchment indicate that streamflow data were available for these catchments.

### 7.2.3 Uncertainty due to parameter transfer into catchments without streamflow data

Lastly, the uncertainty caused by the transfer of the model parameters to ungauged catchments was analysed. As described in Chapter 5, all catchments for which streamflow data were available were calibrated using the model efficiency (equation 5.2) as a first step. Based on the resulting parameter sets for these catchments, an approach was developed to transfer the parameters to the 25 glacierized headwater catchments without streamflow data. In this approach, similar catchments were identified based on a wide range of values describing area characteristics (see Figure 7.16).

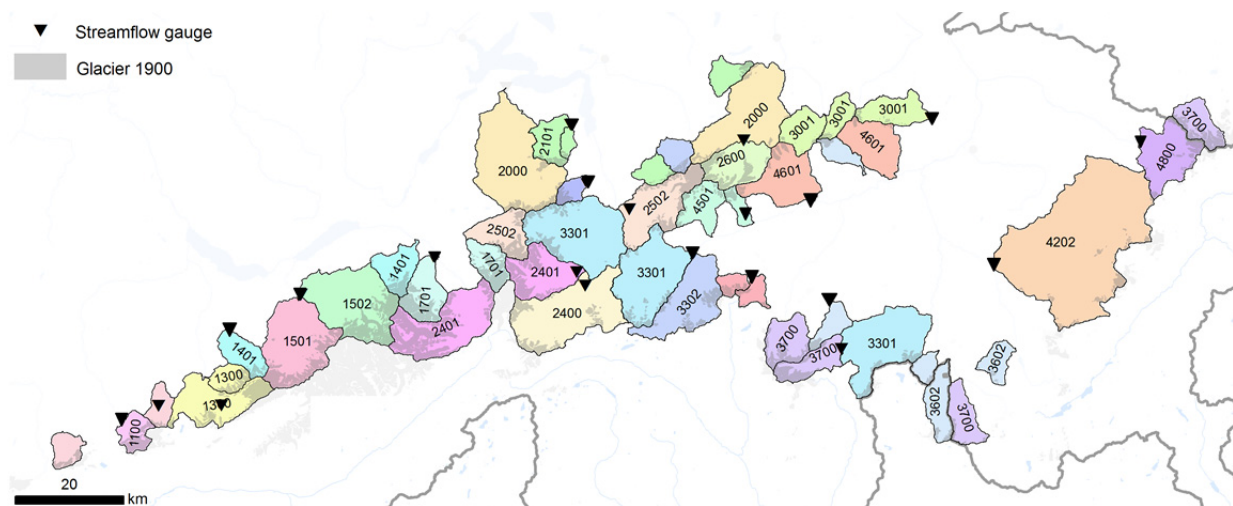


Figure 7.16: Map of the parameter regionalization over the glacierized headwater catchments; catchments without streamflow data and the corresponding most similar catchments, from which the parameters were transferred, are depicted in the same colour. Also shown is the ID number of the respective catchment with streamflow data (see Table 5.1).

Subsequently, those HBV-light model parameters that deal with runoff generation were transferred directly (i.e., set to the optimal, calibrated value). On the other hand, parameters within HBV-light dealing with the simulation of snow- and glacier processes were determined using multi-criteria calibration after equation 5.3. For this calibration of the ungauged catchments, the prior parameter ranges applied were constrained based on the optimized (final) parameter sets of all the catchments with streamflow data. To investigate the uncertainty or the improvement introduced by this additional calibration after parameter transfer, for each ungauged catchment a reference simulation was carried out. In this simulation the parameters were not calibrated additionally but the parameter set (all parameters including the snow and glacier parameters) of the most similar headwater catchment was adopted.

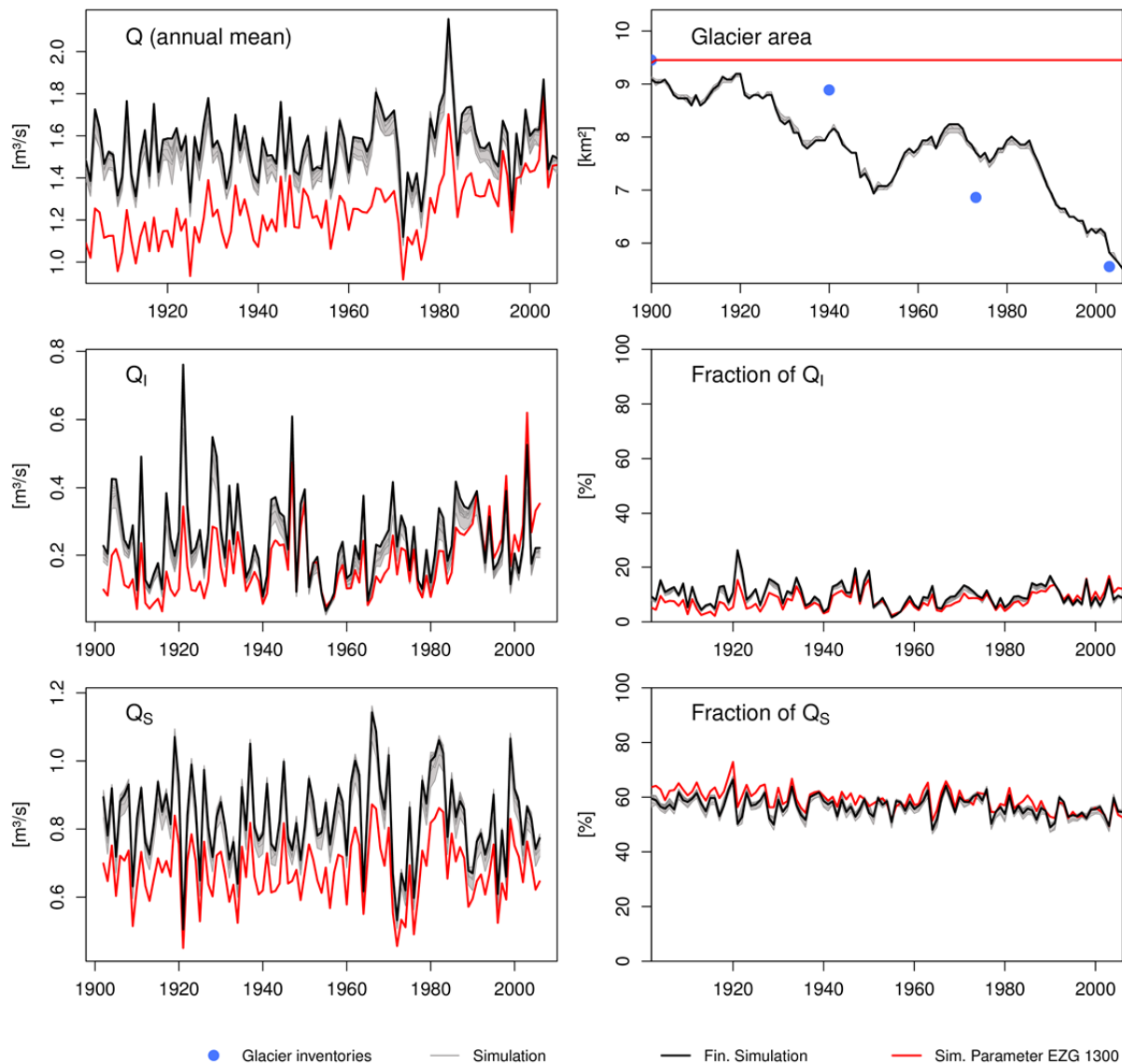


Figure 7.17: Exemplary model results for the catchment „Öschibach“ (EZG1302) showing the final simulation and the reference simulations using the 9 additional parameter sets and an additional reference simulation using the fully transferred parameters from the companion catchment “Kander” (catchment EZG1300) without additional calibration of the snow- and glacier parameters (red line).

Exemplary results from such reference runs for two ungauged catchments are illustrated in Figures 7.17 and 7.18. These examples clearly show that not carrying out an additional calibration using observed snow and glacier data would, at least in some parts, have led to a much worse simulation of the glacier evolution. The effect on the modelled streamflow and streamflow components is, in some regions, also considerable (Figure 7.17), while it is only minor in other regions (Figure 7.18). Overall, these examples show the generally great benefit of using observed data on snow and glaciers for limiting issues of equifinality especially in modelling the glacierized headwater catchments.

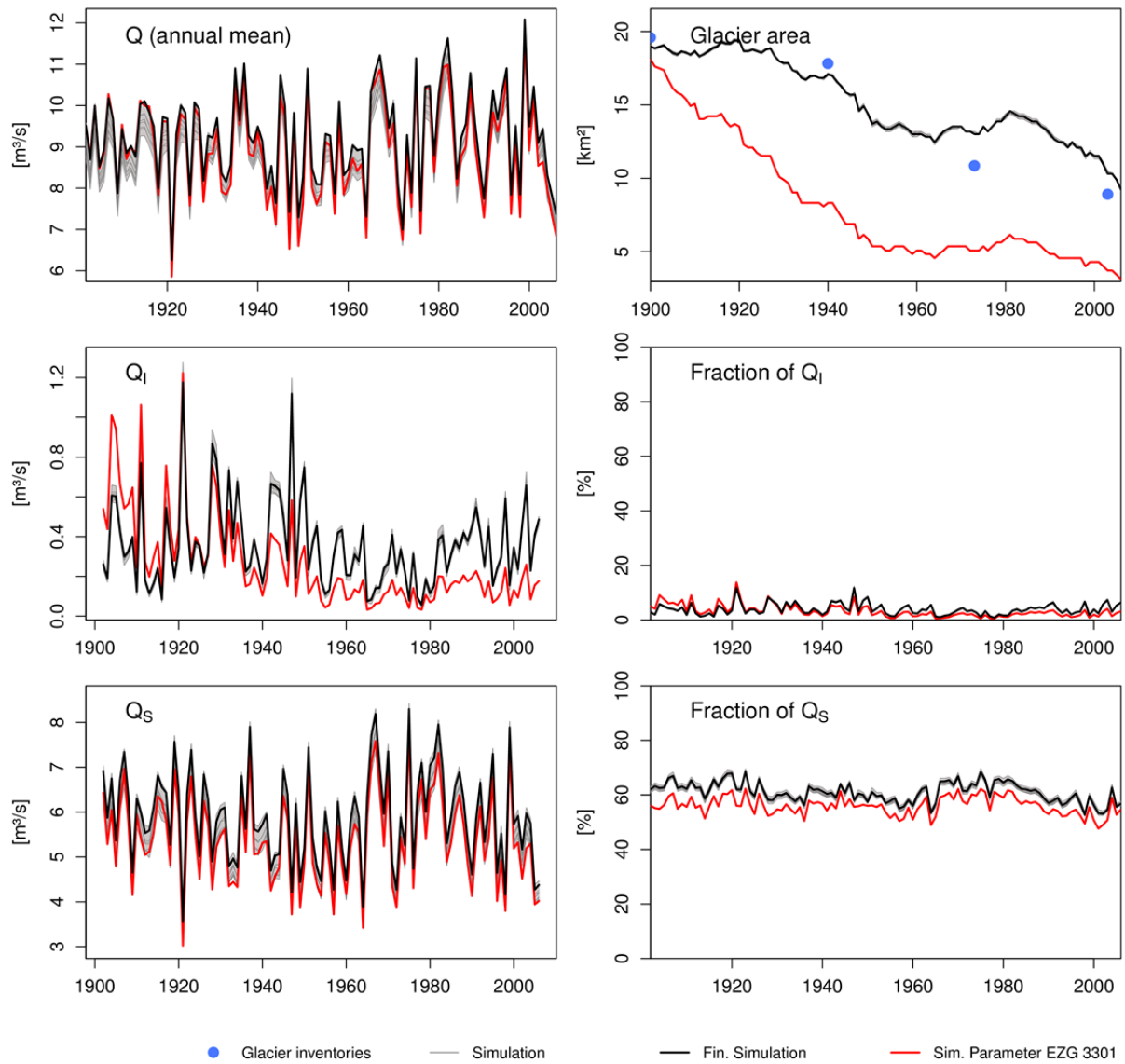


Figure 7.18: Example model results for the catchment „Reuss” (lower part of the Reuss catchment, EZG2501) showing the final simulation and the reference simulations using the 9 additional parameter sets and an additional reference simulation using the fully transferred parameters from the companion catchment “Vorderrhein” (catchment EZG3301) without additional calibration of the snow- and glacier parameters (red line).

### 7.3 Conclusions

The derived quantities of the streamflow components over the time period 1901–2006 cannot be validated directly, as they are understood as an effect tracking of the streamflow response to the contributions of the input of rain, snowmelt, and ice melt, and thus follow the specific focus and assumptions of the project. However, the ASG Rhine project followed the general strategy to include as many available observed datasets on streamflow, snow, and glaciers as possible to constrain the modelling. This in turn limited the opportunities to validate the model results with independent datasets. Nevertheless, all comparisons between model results and the various observations based (independent) glacier data products did not show any considerable (systematic) discrepancies. Instead, predominantly good agreements were obtained.

The seasonality of empirically determined temperature and precipitation sensitivities of streamflow from glacierized headwater catchments was also, in general, reproduced adequately. However, temperature and precipitation sensitivities were partially overestimated systematically for many of the glacierized headwater catchments. This tendency has to be considered when using the models for a study on the effects of climate change and interpret changes for different catchments and for different seasons.

Although a comprehensive quantitative analysis on uncertainty and sensitivity of the entire modelling chain used in the ASG Rhine project could not be carried out, all exemplary analyses on model sensitivity and model uncertainty as well as all comparisons with observed data suggest that the modelling results are suitable to elucidate the questions posed and the main conclusions of the study are unaffected. The analyses also indicate that the challenge of modelling the streamflow components in the entire Rhine basin over the time period 1901–2006 inevitably leads to some uncertainties that should be considered when interpreting the model results in detail.

## 8 Conclusions from the project considering climate change

The aim of the project was to quantify, for the first time, at a daily and monthly resolution, the fractions of rain, snowmelt, and glacier ice melt that comprised the streamflow of the River Rhine during the long study period 1901–2006. Three main results regarding this quantification have emerged as particularly important considering past and future climate conditions:

- High maximum daily fractions of glacier ice melt of up to one third of the streamflow in Basel and one fifth of the streamflow in Lobith during extreme drought events that affected Central Europe, e.g., in 1921, 1947, and 2003.
- Rather small to negligible changes in the glacier ice melt component over the entire period as a result of a compensation of increasing glacier melt and declining basin glacier coverage.
- A substantial snowmelt component of the streamflow along the entire River Rhine.

The first result is relevant with respect to the projected climatic changes towards drier and warmer summers in Central Europe. The results of the modelled daily flow components suggest that glacier ice melt to date still plays an important role for the augmentation of low flows in situations such as the extreme drought years referred to.

Related to this conclusion, is the study's result that due to the substantial glacier retreat, much more negative glacier mass balances are required nowadays to generate the same amount of glacier ice melt contribution as generated earlier in the study period. In other words: if the summer drought and heat-wave of the year 2003 had happened in earlier years, the glacier ice melt component would have been much larger and the low flow situation in the downstream reaches of the Rhine would have been less severe. In comparable situations in the future, ongoing glacier retreat will thus further reduce the ice melt component of the low flow.

These processes suggest that a potential compensation of the expected reduction of glacier ice melt contributions by a generally projected future increase in winter precipitation in Western Europe should be considered an important part of future changes to the streamflow of the River Rhine. The highly relevant contribution of snowmelt to streamflow even in the lower reaches also suggests that changes in snow cover and timing of snowmelt as a contribution to streamflow will play a most crucial role in the future.

Any assessment of the findings from this project needs to consider the novel methodological developments the results are based on – in particular the effect tracking of the three different contributions of rain, snow, and glacier ice melt through the modelled hydrological system and into streamflow components. Initially, it had to be specified what exactly was of interest with respect to climate change. In fact, from a particle tracking perspective, the streamflow of the River Rhine consists of all three components year-round, because the Rhine basin has large reservoirs (e.g., lakes, groundwater), where the input contributions will mix and reside. Therefore, assessing more specifically the effect of changes in the different contributions from rain, snowmelt, and glacier ice melt on total streamflow also required a tracking of the effect on the streamflow response instead. To simulate this effect, the developed mixing tank approach with a limited mixing volume was developed.

The mixing tank approach offers further potential for analyses of the mixing in lakes and reservoirs under specific conditions and constraints. These could be used to simulate scenarios of the effect of changes on particular streamflow components and one example of such potential model experiments was carried out: glaciers were kept their same size through the simulation period. The modelling capa-

bilities and model chain developed in this project for the propagation of the three components of streamflow now provide a reliable tool for further analyses of climate and regulation changes in the Rhine basin.

Another novel aspect of the study was the long multi-scale coupled glacio-hydrological modelling time period of 106 years in the past. The climate reconstruction carried out was a pragmatic but effective way to create a relatively consistent meteorological input over the entire study period. The analogue method has the advantage of a general applicability to other datasets. Although the validation of the reconstruction indicates an underestimation of precipitation during the early period, this bias appears not to have had a direct effect on the streamflow simulations. Nevertheless, the uncertainties of the modelled streamflow during the reconstruction period will be higher. The reconstruction method may also be applied to other meteorological datasets, e.g. those providing more recent updates. The recent drought year 2015 in particular may present an interesting further modelling case on the glacier melt contribution to extreme low flows along the Rhine.

Modelling long time periods in such an environment requires a correct representation of cryospheric and hydrological processes. Substantial model improvements were necessary, for example, to avoid a long-term accumulation of snow in high elevations without glaciers and thus a cumulative error in the water balance. Snow redistribution as well as a correctly coupled development of glacier mass balance, glacier volume, and glacier area in the accumulation and ablation zones of glaciers were thus given thorough attention through new extensions to the HBV-light model and the combination of various data in the multi-criteria calibration. All new model developments retain the conceptual semi-distributed structure of the HBV model, its computational efficiency, and applicability with commonly available data. The LARSIM models had to incorporate the successive increase in reservoir storage in the 20<sup>th</sup> Century in the Rhine basin and simulate the way this affects changes in streamflow variability. The simplified regulation scheme employed presents an effective approach that will benefit from further improvement of the details. The considerable effect found suggests that any study on long-term changes needs to consider this human alteration to streamflow in similar studies.

The ASG Rhine project had a number of data and modelling challenges to resolve and this naturally resulted in a wish list regarding data availability. If glacier, snow, hydrometric, and meteorological monitoring networks had more overlap and coordination, the modelling clearly could be improved. Currently, there are few long-term streamflow records available in catchments with glacier mass balance monitoring, snow monitoring and a weather station. This study showed that even a few years of data can help constrain the models and test their validity under changing conditions. Hence, a coordinated monitoring will be crucial to understand current and future changes.

In summary, the project's modelling results suggest that the streamflow components have not changed substantially over the entire study period. This can be attributed to the compensation of the reduction of glacier coverage by increased melt production from the remaining glacier area and possibly in addition from an increase in precipitation. With respect to climate change, the question of when the glacier ice melt component will notably decline will require further investigation. The study showed clearly that any assessment of future changes to the streamflow in the River Rhine needs to consider carefully the changes in all three streamflow components. The ASG Rhine project developed a number of models and tools that will allow scenario analyses of potential future developments.

## References

- Allen M., Funk M. (1999): Längen- und Massenänderungen der Gletscher seit dem letzten Höchststand um 1850. *Hydrologischer Atlas der Schweiz*, Tafel 3.7, Bern.
- Bahr D.B., Pfeffer W.T., Kaser G. (2015): A review of volume-area scaling of glaciers, *Reviews of Geophysics* **53**, 95–140, doi: 10.1002/2014RG000470.
- Bahr D.B., Meier M.F., Peckham S.D. (1997): The physical basis of glacier volume-area scaling. *Journal of Geophysical Research* **102**, 20–355.
- Baumgartner A., Reichel E., Weber G. (1983): Der Wasserhaushalt der Alpen. Niederschlag, Verdunstung, Abfluß und Gletscherspende im Gesamtgebiet der Alpen im Jahresdurchschnitt für die Normalperiode 1931 - 1960. Oldenbourg, München.
- Belz J.U., Brahmmer G., Buiteveld H., Engel H., Grabher R., Hodel H., Krahe P., Lammersen R., Larina M., Mendel H.-G., Meuser A., Müller G., Plonka B., Pfister L., Vuuren W. v. (2007): Das Abflussregime des Rheins und seiner Nebenflüsse im 20. Jahrhundert, Analyse, Veränderungen, Trends, Bericht Nr. I-22 der KHR, Lelystad.
- BfG (2016): Integration einer Höhenzonierung in LARSIM-ME Rhein/Maas und LARSIM-Simulationsläufe zur Unsicherheitsanalyse. Projektbericht der HYDRON GmbH im Auftrag der Bundesanstalt für Gewässerkunde (unveröffentlicht).
- BfG (2006): Niedrigwasserperiode 2003 in Deutschland. Ursachen-Wirkungen-Folgen. Autoren: Koehler G., Schwab M., Hauff M. v., Kluth K., Finke W., Belz, J.U., *BfG-Mitteilungen* **27**, Bundesanstalt für Gewässerkunde (BfG), Koblenz.
- Bookhagen B., Burbank D.W. (2010): Towards a complete Himalayan hydrological budget: Spatio-temporal distribution of snowmelt and rainfall and their impact on river discharge. *Journal of Geophysical Research: Earth Surface* (2003–2012), 115(F3).
- Briffa K.R., Jones P.D., Hulme M. (1994): Summer moisture variability across Europe, 1892–1991: an analysis based on the Palmer drought severity index. *International Journal of Climatology* **14**, 475–506.
- Bremicker M. (2000): Das Wasserhaushaltsmodell LARSIM –Modellgrundlagen und Anwendungsbeispiele. *Freiburger Schriften zur Hydrologie* **11**. Institut für Hydrologie der Universität Freiburg. [www.hydrology.uni-freiburg.de/publika/FSH-Bd11-Bremicker.pdf](http://www.hydrology.uni-freiburg.de/publika/FSH-Bd11-Bremicker.pdf)
- Bremicker M., Brahmmer G., Demuth N., Holle F.-J., Haag I. (2013): Räumlich hoch aufgelöste LARSIM Wasserhaushaltsmodelle für die Hochwasservorhersage und weitere Anwendung. *KW – Korrespondenz Wasserwirtschaft* **6** (9), 509–519.
- Brochet P (1977): La secheresse 1976 en France: aspects climatologiques et consequences. *Hydrological Sciences Bulletin* **22**, 393–411, doi: 10.1080/02626667709491733.
- Bundesrat (1947): Botschaft des Bundesrates an die Bundesversammlung über außerordentliche Maßnahmen zur Milderung der Notlage in den Trockengebieten (vom 26. September 1947). Bundesblatt XCIX/39, 189–211, Bern.
- Buttle J. M. (1994). Isotope hydrograph separations and rapid delivery of pre-event water from drainage basins. *Progress in Physical Geography*, **18**(1), 16–41.
- BUWAL, BWG, MeteoSchweiz, (2004): Auswirkungen des Hitzesommers 2003 auf die Gewässer, *Schriftenreihe Umwelt* Nr. 369., Bundesamt für Umwelt, Wald und Landschaft (BUWAL), Bern.

- Collins D.N. (2006): Climatic variation and runoff in mountain basins with differing proportions of glacier cover. *Nordic Hydrology* 37, 315–326, doi: 10.2166/nh.2006.017.
- Courvoisier H., Maeder F., Primault B. (1977): La sécheresse de 1976 et ses conséquences – Die Dürre 1976 und ihre Auswirkungen. *Arbeitsberichte der Schweizerischen Meteorologischen Zentralanstalt* 73. Schweizerische Meteorologische Zentralanstalt, Zürich.
- Déry S.J., Stahl K., Moore R.D., Whitfield P.H., Menounos B., Burfords J.E. (2009): Detection of runoff timing changes in pluvial, nival and glacial rivers of Western Canada. *Water Resources Research* 45, W04426, doi: 10.1029/2008WR006975
- Dornkamp J.C., Gregory K.J., Burn A.S. (Hrsg.) (1980): Atlas of Drought in Britain 1975-76. Institute of British Geographers, London.
- Engelhardt M., Schuler T.V., Andreassen L.M. (2014): Contribution of snow and glacier melt to discharge for highly glacierized catchments in Norway. *Hydrology and Earth System Sciences*, 18(2), 511–523.
- Farinotti D., Usselmann S., Huss M., Bauder A., Funk M. (2012): Runoff evolution in the Swiss Alps: projections for selected high-alpine catchments based on *ENSEMBLES* scenarios. *Hydrological Processes* 26, 1909–1924. doi: 10.1002/hyp.8276
- Finger D., Vis M., Huss M., Seibert J. (2015): The value of model complexity versus multiple data types for improving the performance of hydrological models in mountain catchments, *Water Resources Research* 51, 1939–1958.
- Finger D., Pellicciotti F., Konz M., Rimkus S., Burlando P. (2011): The value of glacier mass balance, satellite snow cover images, and hourly discharge for improving the performance of a physically based distributed hydrological model, *Water Resources Research* 47, W07519, doi: 10.1029/2010WR009824.
- Fischer M., Huss M., Barboux C., Hoelzle M. (2014): The new Swiss Glacier Inventory SGI2010: relevance of using high-resolution source data in areas dominated by very small glaciers. *Arctic, Antarctic and Alpine Research*, 46(4), 933–945.
- Fleig A. K., Tallaksen L. M., James P., Hisdal H., Stahl K. (2014): Attribution of European precipitation and temperature trends to changes in circulation types. *Hydrology and Earth System Sciences Discussions*, 11, 12799–12831.
- Franke J., González-Rouco J.F., Frank D., Graham, N.E. (2011): 200 years of European temperature variability: insights from and tests of the proxy surrogate reconstruction analog method. *Climate dynamics* 37(1-2), 133–150.
- Freudiger, D., Frielingsdorf, B., Weiler, M., Stahl, K., Steinbrich, A., Seibert, J. (2014): Teilbericht 1: Potential der meteorologischen Rasterdatensätze HYRAS und RhiresD für die hydrologische Modellierung alpiner Gebiete. In: Analyse der Unsicherheit der Niederschläge im alpinen Rheineinzugsgebiet in den HYRAS Produkten im Vergleich zu den Niederschlagsrasterdaten der MeteoSwiss (RHires) sowie zu den SLF SWE-Karten. Abschlussbericht vom 27.11.2014 zum Zusatzauftrag im ASG-Rhein-Projekt. Professur für Hydrologie, Universität Freiburg / HYDRON GmbH (unveröffentlicht).
- Frielingsdorf B. (2013) Veränderungen von Schmelzwasserereignissen im Abfluss des Rheins in den letzten 100 Jahren. *Masterarbeit an der Professur für Hydrologie*, Fakultät für Umwelt und Natürliche Ressourcen der Universität Freiburg (unveröffentlicht).
- Frick C., Steiner H., Mazurkiewicz A., Riediger U., Rauthe M., Reich T., Gratzki A. (2014): Central European high-resolution gridded daily s (HYRAS): Mean temperature and relative humidity. *Meteorologische Zeitschrift* 23, 15–32. doi: 10.1127/0941-2948/2014/0560.

- Gerhard H., van der Made J.W., Reiff J., de Vrees L.P.M. (1983): Die Trocken- und Niedrigwasserperiode 1976. La sécheresse et les basses eaux de 1976. Bericht Nr I-2 der KHR, 2. Auflage (1985). Internationale Kommission für die Hydrologie des Rheingebiets (KHR/CHR), Lelystad. [www.chr-khr.org/sites/default/files/chrpublications/rapport\\_i\\_-\\_2\\_0.pdf](http://www.chr-khr.org/sites/default/files/chrpublications/rapport_i_-_2_0.pdf)
- Gerlinger K., Meuser A. (2013): Modellierung des Wasserhaushalts unter Verwendung eines Klimaprojektions-Ensembles – methodisches Vorgehen und Ergebnisse. In AK KLIWA (Hrsg.): 5. KLIWA-Symposium 06.-07.12.2012 in Würzburg, Fachvorträge. *KLIWA-Berichte* Heft 19, 154–167. AK KLIWA, Karlsruhe/Mainz/Hof.
- Grömping, U. (2007), Estimators of Relative Importance in Linear Regression Based on Variance Decomposition, *The American Statistician*, 61, 139–147.
- Grunow J. (1935): Die Wasserklemmen der Norddeutschen Ströme in den Jahren 1891-1930. *Forschungen zur Deutschen Landes- und Volkskunde* 31, 1–74.
- Grunow J. (1931): Über die Ursachen großer Trockenheit in Mitteleuropa. Dissertation, Friedrich-Wilhelms-Universität Berlin, Berlin.
- Hirschi E., Auchmann R., Martius O., Brönnimann S. (2013): The 1945-1949 droughts in Switzerland. In Brönnimann, S. and O. Martius (Hrsg.): Weather extremes during the past 140 years. *Geographica Bernensia* G89, 81–90, doi: 10.4480/GB2013.G89.9.
- Hock R. (2005): Glacier melt: a review of processes and their modelling. *Progress in Physical Geography* 29, 362–391.
- Hohmann C. (2014): Teilbericht 2: Zusatzauftrag im Rahmen des ASG-Projekts: „Vergleich SWE<sub>sim-LARSIM</sub> mit aktualisiertem SWE<sub>SLF</sub>“. In: Analyse der Unsicherheit der Niederschläge im alpinen Rheineinzugsgebiet in den HYRAS Produkten im Vergleich zu den Niederschlagsrasterdaten der MeteoSwiss (RHires) sowie zu den SLF SWE-Karten. Abschlussbericht vom 27.11.2014 zum Zusatzauftrag im ASG-Rhein-Projekt. Hydrologie Universität Freiburg / HYDRON GmbH (unveröffentlicht).
- Hohmann C. (2013): Validierung der Schneedeckenmodellierung eines großskaligen hydrologischen Modells für alpine Einzugsgebiete. *Masterarbeit an der Professur für Hydrologie*, Fakultät für Umwelt und Natürliche Ressourcen der Universität Freiburg (unveröffentlicht).
- Huss M., Fischer M. (2016): Sensitivity of Very Small Glaciers in the Swiss Alps to Future Climate Change. *Frontiers in Earth Sciences* 4: 34. doi: 10.3389/feart.2016.00034
- Huss M., Farinotti D. (2012): Distributed ice thickness and volume of all glaciers around the globe, *Journal of Geophysical Research* 117, F04010, doi:10.1029/2012JF002523.
- Huss M., Jouvett G., Farinotti D., Bauder A. (2010): Future high-mountain hydrology: a new parameterization of glacier retreat. *Hydrology and Earth System Sciences* 14, 815–829.
- Huss M. (2012): Extrapolating glacier mass balance to the mountain-range scale: the European Alps 1900–2100. *The Cryosphere* 6, 713–727.
- Huss M. (2011): Present and future contribution of glacier storage change to runoff from macroscale drainage basins in Europe. *Water Resources Research* 47, W07511, doi: 10.1029/2010WR010299 .
- ICPR (2004): Wärmebelastung der Gewässer im Sommer 2003, Zusammenfassung der nationalen Situationsberichte, *IKSR-Bericht/ICPR-Report* 142d. International commission for the protection of the Rhine (ICPR), Koblenz.
- Jarvis A., Reuter H.I., Nelson A., Guevara E. (2008): Hole-filled SRTM for the globe Version 4, available from the CGIAR-CSI SRTM 90m Database (<http://srtm.csi.cgiar.org>).

- Jörg-Hess S., Fundel F., Jonas T., Zappa M. (2014): Homogenisation of a gridded snow water equivalent climatology for Alpine terrain: methodology and applications, *The Cryosphere* 8, 471–485, doi: 10.5194/tc-8-471-2014.
- Jonas T., Marty C., Magnusson J. (2009): Estimating the snow water equivalent from snow depth measurements in the Swiss Alps. *Journal of Hydrology* 378(1-2), 161–167.
- Jones, P.D., Harris, I. (2008): Climatic Research Unit (CRU) time-series datasets of variations in climate with variations in other phenomena. NCAS British Atmospheric Data Centre, 1.9.2015. <http://catalogue.ceda.ac.uk/uuid/3f8944800cc48e1cbc29a5ee12d8542d>
- Kendall M.G. (1975): Rank Correlation Methods. Charles Griffin, London.
- Kirchhofer W., Sevruck B. (1992): Mittlere jährliche korrigierte Niederschlagshöhen 1951-1980. *Hydrologischer Atlas der Schweiz*, Tafel 2.2, Bern.
- Koboltschnig G., Schöner W., Zappa M., Holzmann H. (2007): Contribution of glacier melt to stream runoff: if the climatically extreme summer of 2003 had happened in 1979. *Annals of Glaciology* 46, 303–308.
- Konz M., Seibert J., (2010): On the value of glacier mass balances for hydrological model calibration. *Journal of Hydrology* 385, 238–246.
- La Freniere J., Mark B.G. (2014): A review of methods for estimating the contribution of glacial meltwater to total watershed discharge. *Progress in Physical Geography* 38(2), 173–200.
- Lindström G., Johansson B., Persson M., Gardelin M., Bergström S. (1997): Development and test of the distributed HBV-96 hydrological model. *Journal of Hydrology* 201, 272–288
- Luce A., Haag I., Bremicker M. (2006): Einsatz von Wasserhaushaltsmodellen zur kontinuierlichen Abflussvorhersage in Baden-Württemberg. *Hydrologie und Wasserbewirtschaftung* 50(2), 58–66.
- Ludwig K., Bremicker M. (Hrsg.) (2006): The Water Balance Model LARSIM - Design, Content and Applications. *Freiburger Schriften zur Hydrologie* 22, Institut für Hydrologie der Universität Freiburg, Freiburg. [www.hydrology.uni-freiburg.de/publika/FSH-Bd22-Bremicker-Ludwig.pdf](http://www.hydrology.uni-freiburg.de/publika/FSH-Bd22-Bremicker-Ludwig.pdf)
- Mann H.B. (1945): Non-parametric test against trend. *Econometrica* 13, 245–259.
- Menzel L., Lang H., Rohmann M. (1999): Mittlere jährliche aktuelle Verdunstungshöhen 1973-1992. *Hydrologischer Atlas der Schweiz*, Tafel 4.1, Bern.
- Merz R., Parajka J., Blöschl G. (2011): Time stability of catchment model parameters: Implications for climate impact analyses, *Water Resources Research* 47, W02531, doi: 10.1029/2010WR009505.
- Moore R.D., Fleming S.W., Menounos B., Wheate R., Fountain A., Stahl K., Holm K., Jakob M. (2009): Glacier change in western North America: influences on hydrology, geomorphic hazards and water quality. *Hydrological Processes* 23, 42–61.
- Müller F., Caflish T., Müller G. (1976): Firm und Eis der Schweizer Alpen, Gletscherinventar. Vdf Hochschulverlag ETH Zürich, Zürich.
- OSHD-SLF (2013): Datenblatt zur SWE-Kartenserie 1972-2012 // KHR-Projekt. Stand 30.11.2013. Operationeller Schneehydrologischer Dienst des SLF (OSHD-SLF), Davos (unveröffentlichtes Dokument).
- Oudin L., Hervieu F., Michel C., Perrin C., Andréassian V., Anctil F., Loumagne C. (2005): Which potential evapotranspiration input for a lumped rainfall-runoff model?: Part 2—Towards a

- simple and efficient potential evapotranspiration model for rainfall–runoff modelling. *Journal of Hydrology* 303, 290–306.
- Paul F., Frey H., Le Bris R. (2011): A new glacier inventory for the European Alps from Landsat TM scenes of 2003: Challenges and results. *Annals of Glaciology* 52, 144–152.
- Pearce A.J., Stewart M.K., Sklash M.G. (1986): Storm runoff generation in humid headwater catchments: 1. Where does the water come from. *Water Resources Research* 22(8), 1263–1272.
- Pfister C., Rutishauser M. (2000): Dürresommer im Schweizer Mittelland seit 1525. In OcCC: Trockenheit in der Schweiz, Workshopbericht. Organe consultatif sur les changements climatiques (OcCC), Bern.
- Rauthe M., Steiner H., Riediger U., Mazurkiewicz A., Gratzki A. (2013): A Central European precipitation climatology – Part I: Generation and validation of a high-resolution gridded daily data set (HYRAS). *Meteorologische Zeitschrift* 22, 235–256, doi: 10.1127/0941-2948/2013/0436.
- Sassenfeld M. (1923): Die Trockenheit im Jahre 1921 im Rheingebiet. *Meteorologische Zeitschrift* 40, 93.
- Schorer M. (1992): Extreme Trockensommer in der Schweiz und ihre Folgen für Natur und Wirtschaft. *Geographica Bernensia* G40, Geographisches Institut, Universität Bern.
- Seibert J., Vis M.J.P. (2012): Teaching hydrological modeling with a user-friendly catchment-runoff-model software package. *Hydrology and Earth System Sciences* 16, 3315–3325, doi: 10.5194/hess-16-3315-2012.
- Seibert J., Rodhe A., Bishop K. (2003): Simulating interactions between saturated and unsaturated storage in a conceptual runoff model. *Hydrological Processes* 17(2), 379–390.
- Seibert J., McDonnell J.J. (2002): On the dialog between experimentalist and modeler in catchment hydrology: Use of soft data for multicriteria model calibration. *Water Resources Research* 38, 1241, doi: 10.1029/2001WR000978.
- Seibert J. (2000): Multi-criteria calibration of a conceptual runoff model using a genetic algorithm. *Hydrology and Earth System Sciences Discussions* 4, 215–224, doi: 10.5194/hess-4-215-2000.
- Sevruk B. (1989): Reliability of precipitation measurement. In Sevruk B. (Hrsg.): Precipitation measurements: WMO/IAHS/ETH Workshop on Precipitation Measurements, St. Moritz, 3-7 December 1989. ETH Zürich.
- Stahl K., Moore R.D. (2006): Influence of watershed glacier coverage on summer streamflow in British Columbia, Canada. *Water Resources Research* 42, W06201, doi: 10.1029/2006WR005022.
- Stahl K., Moore R.D., Shea J.M., Hutchinson D., Cannon A.J. (2008): Coupled modelling of glacier and streamflow response to future climate scenarios. *Water Resources Research* 44, W02422, doi: 10.1029/2007WR005956.
- Tallaksen L.M., Stahl K. (2014): Spatial and temporal patterns of large-scale droughts in Europe: Model dispersion and performance. *Geophysical Research Letters* 41(2), 429–434.
- Tarboton D.G., Luce C.H. (1996): Utah energy balance snow accumulation and melt model (UEB). bfg 2016Bfg (2016 Utah Water Research Laboratory).
- Theil H. (1950): A rank-invariant method of linear and polynomial regression analysis, *Indagationes Mathematicae* 12, 85–91.
- Uttinger H. (1949): Die Niederschlagsmengen in der Schweiz 1901-1940. Schweizerischer Wasserwirtschaftsverband, Zürich.

- Weber M., Braun L., Mauser W., Prasch M. (2010): Contribution of rain, snow-and icemelt in the Upper Danube discharge today and in the future. *Geografia Fisica e Dinamica Quaternaria* 33(2), 221–230.
- Weingartner R., Schädler B. (2001): Komponenten des natürlichen Wasserhaushalts 1961–1990. *Hydrologischer Atlas der Schweiz*, Tafel 6.3, Bern.
- Werner P.C., Gerstengarbe F.-W. (2010): Katalog der Großwetterlagen Europas (1881–2009) nach Paul Hess und Helmut Brezowsky, 7. verbesserte und ergänzte Auflage. *PIK Report* 119. Potsdam Institut für Klimafolgenforschung (PIK), Potsdam.
- WGMS (2013, updated, and earlier volumes): Glacier Mass Balance Bulletin No. 12 (2010–2011). Zemp, M., Nussbaumer, S. U., Naegeli, K., Gärtner-Roer, I., Paul, F., Hoelzle, M., and Haeberli, W. (eds.), ICSU(WDS)/IUGG(IACS)/UNEP/UNESCO/WMO, World Glacier Monitoring Service, Zurich, Switzerland, 106 pp. Data based on database version doi:10.5904/wgms-fog-2014-09.
- Zemp M., Paul F., Hoelze M., Haeberli W. (2008): Glacier fluctuations in the European Alps, 1850–2000. In Orlove B., Wiegandt E., Luckman B.H. (Hrsg.): *Darkening Peaks: Glacier Retreat, Science, and Society*, 152–167. University of California Press, Berkeley/Los Angeles.
- Zorita E., Von Storch H. (1999): The analog method as a simple statistical downscaling technique: comparison with more complicated methods. *Journal of climate* 12(8), 2474–2489.

## Acknowledgement

This report documents the results of the research project “Abflussanteile aus Schnee- und Gletscherschmelze im Rhein und seinen Zuflüssen vor dem Hintergrund des Klimawandels” –ASG Rhine (The snow and glacier melt components of the streamflow of the River Rhine and its tributaries considering the influence of climate change), which was initiated and funded by the International Commission for the Hydrology of the Rhine basin (CHR/KHR). We thank the following people for constructive criticism, thorough discussion, and advice throughout the three years of project duration: Jörg Uwe Belz (BfG), as CHR/KHR project leader, and Eric Sprokkereef (CHR/KHR secretary) as well as all members of the project steering group: Manfred Bremicker (LUBW), Peter Krahe (BfG), Gabi Müller (BMLFUW), Hans-Peter Nachtnebel (BOKU), Felix Naef (ETH Zürich), Petra Schmocker-Fackel (FOEN), Wolfgang Schöner (University of Graz), and Frederiek Sperna Weiland (Deltares).

The provision of data for project work and illustration in this report by the following institutions or persons is gratefully acknowledged:

- Climate datasets:
  - HYRAS data: DWD/BfG (see Rauthe et al., 2013; Frick et al., 2014)
  - RhiresD-/TabsD datasets: MeteoSwiss (see Frei et al., 2014; Isotta et al., 2014)
  - Long station records: DWD, MeteoSwiss, ECA&D (European Climate Assessment & Dataset (<http://eca.knmi.nl>))
  - Long gridded climate time series (for the validation of the reconstructed climate data): CRU (University of East Anglia Climate Research Unit, see Jones & Harris, 2008)
- Streamflow data records: “Amt für Wasser und Abfall des Kantons Bern” (water authority of the Cantone of Bern for supplying the streamflow record of the gauge Gündlischwand/Schwarze Lütschine), FOEN (Swiss Federal Office for the Environment), and BfG (German Federal Institute of Hydrology)
- Gridded SWE climatology “SLF-Schneekartenserie Winter 1972-2012”: SLF (WSL Institute for Snow and Avalanche Research, see OSHD-SLF, 2013; Jörg-Hess et al., 2014) with special thanks to Tobias Jonas and Nena Griesinger for attending ASG Rhine project meetings and helping with the use of this recently developed SWE map product.
- Data for glacier analyses:
  - “Siegfried maps” (for the digitisation of past glacier coverage): swisstopo
  - Previously available glacier inventories by Fischer et al. (2014), Maisch et al. (2000), Müller et al. (1976), and Paul et al. (2011)
  - Unpublished gridded glacier thickness data for the years of 1973 and 2010 (at 25m resolution for the spatial domain of Switzerland: Matthias Huss (Université de Fribourg / ETH Zurich). In addition, we are much obliged to Matthias Huss for his help and valuable advice related to glacier data and modelling.
  - Glacier length changes observation data: WGMS (World Glacier Monitoring Service, see WGMS, 2013 and <http://wgms.ch>)
  - Glacier mass balance data: WGMS / Matthias Huss (see WGMS, 2013; Huss et al., 2015)

The “LARSIM-developer community” consented to the use and enhancement of the model LARSIM for the ASG Rhine project. The required LARSIM-Modellgebietsdateien were provided by the following authorities:

- LUBW (“Landesanstalt für Umwelt, Messungen und Naturschutz Baden-Württemberg”: Institute for the environment, measurements, and nature conservation of the federal state of Baden-Württemberg): LARSIM models for the Swiss Rhine basin and the German tributaries of the Hochrhein (High Rhine) and Lake Constance
- AVLr (“Amt der Vorarlberger Landesregierung”: Office of the Government of the Federal State of Vorarlberg): LARSIM model for the Bregenzerach basin
- BfG: LARSIM-ME model for the Rhine basin. Furthermore, the BfG funded the supplementary project “LARSIM-Höhenzonierung” (elevation discretisation for the LARSIM-ME model).

Last, we thank the following staff/colleagues and (former) students who were temporarily involved in work related to the project:

Dirk Aigner (HYDRON), Damaris De (University of Freiburg), Simon Etter (M.Sc. thesis University of Zurich), David Finger (University of Zurich), Claudius Fleischer (M.Sc. thesis University of Freiburg), Barbara Frielingsdorf (University of Freiburg), Clara Hohmann (HYDRON/University of Freiburg), Nicole Henn (HYDRON), Robert Schweppe (HYDRON), Andreas Steinbrich (University of Freiburg), and Juliane Schillinger (B.Sc. thesis University of Freiburg). Dr. Stefan Pohl kindly helped with the translation and English proofreading of several chapters of this report.